The adaptive primary auditory cortex microcircuitry across brain states, scales, and species

for the degree of

doctor rerum naturalium (Dr. rer. nat.)

approved by Faculty of Natural Sciences of Otto von Guericke University Magdeburg

by

Katrina E. Deane, MSc.

born on January 12, 1992, in Marietta Georgia, USA

Examiners: Prof. Dr. Max Happel

Prof. Dr. Tania Barkat

Submitted on July 19, 2022

Defended on January 10, 2023

Abstract

The planet, society, a human, their brain, and even the primary auditory cortex (A1) are complex systems. The A1 is built up by canonical microcircuits of neurons, that interact to allow us to adaptively hear, respond, and learn about our acoustic environment. The research detailed here, explored auditory response profiles and population activity in A1 across several physiological boundaries and this thesis seeks to contextualize findings in the framework of complexity. These boundaries were between awake and anesthetized wholistic brain states, across microscopic and mesoscopic scales, and between three small species. There is an expanding movement, beginning decades ago, to compliment scientific reductionism with context-informed study design and interpretation of results. Here, we looked at the interpretation of results for three projects first in a self-contained way, and then within a wider scope and in consideration of their place in the overall A1 complex system.

The first project is about a critical shift in neuronal population activity after the application of ketamine-xylazine anesthesia. Ketamine, a common anesthetic, has been implicated, largely at a single or multi-unit level, in increased stimulus-locked excitability and inhibition of interneurons. We aimed to broaden understanding about the functional network mechanisms involved. I investigated the effects of an anesthetic dose of ketamine on Mongolian gerbil (*Meriones unguiculatus*) A1s after pure-tone stimulation using multichannel recordings across all cortical layers and subsequent analysis of the current-source density (CSD) profiles. Overall, we found a significant gain increase in granular input layers under ketamine. We ruled out a cross-trial coherence differences at the time of stimulus onset and could instead provide evidence for a granular layer broadband increase in magnitude, reflecting a stimulus-locked increase in recurrent excitation. Our findings on a population level supported the common hypothesis of cortical disinhibition via suppression of GABAergic interneurons.

The second project shows the suppression of population activity after a transient Cav2.1 voltage gated calcium channel (VGCC) clustering using a modern state-of-the-art optogenetic aggregation technique. The stochastic dynamics of each cell involved in population activity is dependent on the position of highly mobile, pre-synaptic VGCCs. When VGCCs were clustered in their respective active zones *in vitro*, it caused a more deterministic firing response profile per cell. To investigate the effects of reducing variability at a single cell level on a population *in vivo*, we used a new optogenetic tool to cross-link VGCCs via a photo-cross-linkable cryptochrome mutant, CRY2olig, in transgenic mice (*Mus musculus*). We found that clustering VGCCs suppressed cortical population activity dynamically, with greater suppression during sensory-evoked activity and greater still given highly synchronized distribution of synaptic inputs. Our results reveal that the mobility of VGCCs, which introduce variability into the network, is an important feature of sensory encoding via dynamic adjustment of activity across differing synaptic input strengths.

The third project explores the impact of the ecological niche of an organism on the organization and function of the A1. Therefore, we investigated laminar auditory response profiles of seba's short-tailed bats (*Carollia perspicillata*) and mice. Bats are a veritable auditory specialist, given their evolution to navigate 3-dimensionally with echolocation and sophisticated social communication, while mice are more specialized in other sensory systems. We investigated the differential recruitment of their respective A1 microcircuitry to auditory stimuli at set repetition rates. We generally found that mice had higher intrinsic background noise and that bats had a better signal to noise ratio, leading to a more temporally precise and lower-energy-cost cortical representation of consecutive stimuli. Despite methodological considerations, the phase coherence in bats was significantly higher across all oscillatory frequencies, indicating less inter-trial phase variability. These results indicate a possible loss of flexibility as a trade-off for higher temporal precision due to this specialization or hint at species-specific mechanisms to assist in dynamic adaptation.

Altogether, these studies are tackling fundamentally different topics through the exploration of A1 population activity in three small mammalian species. The balance of excitation and inhibition, introduction of variability, and differential recruitment for specialization underlie the successfully robust and adaptive A1—an integral complex system for our ability to perceive and interact meaningfully with the world we live in.

Der primäre auditorische Kortex (A1), das Gehirn, der Mensch, die Gesellschaft und der Planet sind komplexe Systeme. Die hier vorgestellten Forschungsarbeiten untersuchen auditorische Antwortcharakteristika von Nervenzell-Populationen über mehrere physiologische Grenzen hinweg. Ziel der vorliegenden Arbeit ist es, die Ergebnisse von drei separaten Studien im Kontext der Komplexität zusammen zu führen. Diese Studien thematisieren wache und narkotisierte Gehirnzustände, mikroskopische und mesoskopische Messbereiche und die Unterschiede der neuronalen Organisation des A1 zwischen drei Spezies. Seit Jahrzehnten gibt es eine wachsende Bewegung, den wissenschaftlichen Reduktionismus durch kontextbezogene Studiengestaltung und Interpretation der Ergebnisse zu ergänzen. In dieser Arbeit werden die Ergebnisse dreier Projekte vorgestellt, zunächst in einem eigenständigen Rahmen, um sie dann in einem größeren Zusammenhang und unter Berücksichtigung ihrer Stellung im komplexen Gesamtsystem A1 zu vergleichen.

Das erste Projekt befasst sich mit dem Einfluss einer Ketamin-Xylazin-Narkose auf die Aktivität neuronaler Populationen. Ketamin, ein gebräuchliches Anästhetikum, wird vor allem auf der Ebene einzelner oder mehrerer Einheiten mit einer erhöhten stimulusgebundenen Erregbarkeit und Hemmung von Interneuronen in Verbindung gebracht. Unser Ziel war es, das Verständnis auf der Ebene der beteiligten funktionellen Netzwerkmechanismen zu erweitern. Wir untersuchen die Auswirkungen einer anästhetischen Dosis Ketamin auf die Neuronen im A1 der Mongolischen Wüstenrennmaus (*Meriones unguiculatus*) nach Stimulation mit Reintönen mittels Multikanal-Ableitungen über alle kortikalen Schichten und nachfolgender Analyse der Strom-Quellen-Dichte-Verteilung. Insgesamt fanden wir unter Ketamin einen signifikanten Anstieg der Verstärkung in den granulären Eingangs-Schichten. Wir schlossen Kohärenzunterschiede über Messwiederholungen zum Zeitpunkt des Stimulusbeginns als Erklärung aus und konnten stattdessen zeigen, dass die Befunde durch eine stimulusabhängige Rekrutierung rekurrenter Schaltkreise erklärt wird. Unsere Ergebnisse auf Populationsebene unterstützen damit die gängige Hypothese der kortikalen Enthemmung durch Unterdrückung von GABAergen Interneuronen.

Das zweite Projekt zeigt die Unterdrückung der Populationsaktivität nach einer Aggregation von presynaptischen Cav2.1 spannungsgesteuerten Kalziumkanälen (VGCC) mittels modernster state-of-the-art Optogenetik-Technik. Die stochastische Dynamik jeder Zelle, die an der Populationsaktivität beteiligt ist, hängt von der Position der mobilen, präsynaptischen VGCCs ab. Wenn VGCCs in ihren jeweiligen aktiven Zonen in vitro geclustert wurden, führte dies zu einem deterministischeren Antwortprofil der Zelle. Um die Auswirkungen der Verringerung der Variabilität auf der Ebene einer einzelnen Zelle auf Populationsebene *in vivo* zu untersuchen, verwenden wir ein neues optogenetisches Werkzeug zur Vernetzung von VGCCs über eine photovernetzbare Cryptochrom-Mutante, CRY2olig, in transgenen Mäusen (*Mus musculus*). Die transiente Aggregation von VGCCs unterdrückt die Aktivität der kortikalen Population bei sensorisch evozierter Aktivität, je synchronisierter die synaptischen Eingänge, desto größer der Effekt. Unsere Ergebnisse zeigen, dass die Mobilität der VGCCs die Variabilität auf Netzwerk-Ebene ermöglicht und somit ein wichtiges Merkmal der sensorischen Kodierung durch dynamische Anpassung der Aktivität bei unterschiedlichen synaptischen Eingangsstärken darstellt.

Das dritte Projekt erforscht die Auswirkungen der ökologischen Nische eines Organismus auf die Organisation und Funktion des A1. Zu diesem Zweck haben wir die laminaren Antwortprofile von Seba-Kurzschwanzfledermäusen (*Carollia perspicillata*) und Mäusen verglichen. Fledermäuse sind wahre Hörspezialisten, da sie sich evolutionär entwickelt haben, um mit Hilfe der Echoortung dreidimensional zu navigieren und eine ausgefeilte soziale Kommunikation zu betreiben, während Mäuse eher auf andere Sinnessysteme spezialisiert sind. Wir untersuchen die unterschiedliche Rekrutierung ihrer jeweiligen A1-Mikroschaltkreise auf auditorische Reize bei bestimmten Wiederholungsraten. Im Allgemeinen konnten wir zeigen, dass Mäuse ein höheres intrinsisches

Hintergrundrauschen und Fledermäuse ein besseres Signal-Rausch-Verhältnis aufweisen, was zu einer zeitlich präziseren und weniger energieaufwändigen kortikalen Repräsentation aufeinander folgender Reize führt. Die Phasenkohärenz war bei Fledermäusen über alle Schwingungsfrequenzen hinweg signifikant höher, was auf eine geringere Phasenvariabilität zwischen den Versuchen hindeutet. Diese Ergebnisse deuten auf einen möglichen Verlust an Flexibilität als Kompromiss für eine höhere zeitliche Präzision aufgrund dieser Spezialisierung hin oder geben Hinweise auf spezies-spezifische Mechanismen zur Unterstützung der dynamischen Anpassung.

Insgesamt befassen sich diese Studien mit grundlegend unterschiedlichen Themen durch die Erforschung der Aktivität der A1-Population bei drei kleinen Säugetierarten. Das Gleichgewicht zwischen Erregung und Hemmung, die Einführung von Variabilität und die unterschiedliche Rekrutierung für die Spezialisierung bilden die Grundlage für ein erfolgreiches, robustes und anpassungsfähiges System des Hörkortex A1 - ein integrales komplexes System für unsere Fähigkeit, die Welt, in der wir leben, wahrzunehmen und sinnvoll mit ihr zu interagieren.

This PhD was one of many carried out during a global pandemic. My community, my partner, my supervisor, my lab, and my family gave me the strength through many stressful, despairing, and angry days to carry on. Despite setbacks, frustrating results, and equipment malfunctions, this process was a joy and an overall triumph. I have you all to thank that I could continue to pursue and foster my passion for this work. This is dedicated to you.

Everything could have been anything else and it would have

just as much meaning.

\- Mr. Nobody

Table of Contents

Chapter 1: Introduction; the A1 is a complex system

Complexity frames biological life

A complex system can be generally described with having three characteristics: complex collective behavior, signaling and information processing, and adaptation (Mitchell, 2011). Emergent chaos can develop from deterministic inputs, making these systems fundamentally unpredictable past a number of time-steps. Society, immune systems, ant colonies, and weather, to name a few, are complex systems. These all have a large number of units (members, T and B cells, ants, air pressure, etc.) that do not fall under the control of any central decision-making body. Their behavior becomes more than the sum of its parts and successfully transfers information to the collective in a meaningful way. Ants, for example, take on colony roles and make decisions about foraging behavior as separate units. However, the colony wide strategy turns into successful exploitation of found resources and parallel exploration for more without governance (the ant queen does not rule). The study of complexity is an emerging interdisciplinary domain of investigation to understand general principles of complex systems. Tenants of complexity sciences hope that learning about one complex system, like ants, will provide a window of insight into complexity in general. The ultimate hope would be to find some higher order language with which to understand all biological (and eventually artificial) life.

The brain is an excellent example of this—with many levels of nested complex systems. Zooming into the brain, you would find my region of interest: the auditory cortex, the primary auditory cortex (A1), and the microcircuitry within columns of the primary auditory cortex. Panning further in, you have a system that sits inside this region and spans the entirety of the cortex, which is the subtypes of neurons making up the microcircuitry and connecting regions. Further in, you would see a universal set of rules per neuron/interneuron, more or less represented in all subtypes, which is the motility of voltage gated calcium channels (VGCCs) in the ecosystem of the pre-synapse. Notice how we skipped a lot of steps. This is because, I would argue, nested complex systems are continuous rather than discrete and that makes choosing where to work and how to interpret data coming from one subsection of a system that much more precarious. Humans have a difficulty conceptualizing infinity, and therefore also continuous scales, because we realistically understand and communicate things at single scales and with discrete boundaries. Fortunately, some physiological boundaries do exist and help us compartmentalize function and structure, within which we can arbitrarily decide to work. These would be single neurons, cortical regions, whole brains, etc. These boundaries are easier to define because they have borders that can be perceived at the scales that we perceive in, not because they are truly discrete.

What if we zoom out? From a human brain, we step back to a human. A human has a gastrointestinal system, body-wide central and peripheral nervous systems stemming from the brain, not to mention its own boundary separating itself from others: skin. If we keep zooming out, we see that this human is connected to others through biology and relationship. These relationships are nested in larger and larger communities, up to societies and cultures. Society is connected to many other global complex systems because we made them, such as economic and political systems. Consider that, despite the human notion of "living with" nature, we are from and part of nature. Therefore, human-developed complex systems are connected to nature as well. For example, irrigation allowed more humans to live closer together which encouraged the spread of disease. Also, economies have been enacted that encourage unmitigated

exploitation of unrenewable resources, which has impacted all living things. Alongside our species, nature houses an unknowable number of complex systems. Nature uses a beautiful motif known as fractals, which are defined by having the same level of complexity no matter in which scale they are being viewed. For example, a shoreline, both bumpy seen from space and from the point of view of a crab, is a natural fractal. They exist in all scales, necessarily, and are what make the moving up and down scales continuous and difficult for us to actually parse.

In starting at such a broad topic, I would like to impart that there are countless complex nested systems connected to and influencing each other. I studied population activity, 1000s of neurons working together, in the A1 and then subsequently began developing curiosity for the framework around it all, complexity, throughout the course of these projects. We arbitrarily choose a starting point and a direction any time we try to study the contents of one of these systems. In studying a part of a system, the development of research and interpretation of the results benefits from an understanding of complexity and that we can never holistically understand its function by removing the system from the part to study it. As we start truly solving methodological discrepancies and the reproducibility problem, the scientific community can function more effectively in its signaling, information processing, and collective behavior. That is, the complex system of a network of interdisciplinary scientists may indeed piece together the mysteries of the brain—by coming at it from all scales and perspectives possible.

The complex auditory cortex

Cell diversity in the auditory cortex is vast. Mitani et al (1985) documented a beautiful variety of these from the cat A1 in the 80s. Populations in the A1, the activity of which is the domain of my research group, include pyramidal, somatostatin (SOM) interneurons, parvalbumin (PV) interneurons, and vasoactive intestinal peptide (VIP) interneurons which all interact to inhibit and disinhibit each other in complex relationships (Nelken, 2020). This diversity and complex collective action are an integral part of our ability to understand sounds and sort through our auditory scene. A mix of soundwaves at different frequencies and amplitudes enters through two identical, contralateral, points in our heads and is transformed into mechanical and then chemical signals, which preserve the information inside of them. Areas in the midbrain begin to tease out critical information, such as loudness, number of frequencies or harmonics, pitch, and location (G. Bidelman, 2013; G. M. Bidelman & Krishnan, 2010; Duron et al., 2020; González-Palomares et al., 2021; Houtsma & Goldstein, 1972; Langner, 1997; Nelken, 2004). This information is passed up through parallel pathways called lemniscal, through the ventral medial geniculate nucleus of the thalamus and primary auditory cortex and onto wider networks, and non-lemniscal, through the posterior thalamus to a variety of limbic structures. The pathways are thought to be responsible for different streams of processing and information gathering in an effort to sort through the constantly complex auditory scene (Bregman & McAdams, 1994; Hu, 2003). They inform each other along the way so that the A1 can use information coming laterally from supporting cortical areas and vertically from the thalamus to perform the important roles of processing, integration, and filtering.

If the sound is, for example, continuous, low, and behaviorally mundane, it can be filtered out. This is something we do constantly throughout our lives and the lesson at the beginning of every science communication talk about the auditory cortex. We tell the audience to notice that

they stopped noticing the ambient noise around them. It is incredibly important that we are able to not only sift through our auditory scene but also to passively, and without effort, understand behavioral relevance and irrelevance in our surroundings. The emergent phenomenon of these paths of sensory processing is not only in our ability to hear but in the dynamic filtering of what and how we hear given context and starting information. For example, neuronal response properties in the A1 under anesthesia can change due to influence from neurotransmitters, such as dopamine (Brunk et al., 2019; Happel, 2016; Happel et al., 2014), which is involved in reward prediction and learning (King et al., 2018).

If a sound is relevant to us, we can determine things about it through learned experience. If a person listens to a set of instruments, not only is emotional relevance often assigned based on an experience with music and the cultural context we find ourselves in, but we are more likely to be able to perceive individual instruments from a set if we have had experience hearing those instruments before. I played several instruments, and I am a trained singer. My auditory system can assign more information to a scene containing those instruments or vocalists than someone without that experience. I am absolutely not implying that the A1 does this task alone. However, I would argue that to say any one part of the pathway could be removed without loss is incorrect. The experience that allows me to understand the musical auditory scene is a part of not only my auditory cortex, but also the hippocampus, prefrontal cortex, the somatosensory cortex, and the motor cortex, etc. For example, when I hear singing, I understand how the throat should move to imitate the singer and can make those throat muscles clench in the right way to experiment with how it would sound in my voice (in my head). This provides information to my prefrontal cortex on my perception of the vocalist's skill level, which in turn informs how important this sound is to me, what emotional experience is assigned to it, how I focus on it, and if it should be filtered down in favor of another sound in the scene—a task done by corticothalamic feedback microcircuitry in the auditory cortex. Our research group and others have specifically explored how learned meaning or behavioral relevance of auditory cues changes A1 population response profiles (Happel, 2016; Ohl, 2015; Ohl & Scheich, 2005; Zempeltzi et al., 2020) and neuronal response profiles (David et al., 2012; Fritz et al., 2003; Jaramillo & Zador, 2011).

As a model system to understand sensory experience, the central auditory system is a unique region to study temporal processing, due to sound inputs being entirely temporal in nature. The auditory system is tonotopically organized up through to the A1 (J. Liu et al., 2019). There is high heterogeneity of tonotopic response profiles between individual cells in the A1, but closer cells are more likely to correlate behavior than farther cells (Rothschild et al., 2010), providing an organizational framework for this tonotopy. The main focus of this research is at the population level in the auditory cortex through laminar local field potential currents (LFP), a stationary signal based on dendritic input, and current source density (CSD) profiles. This has allowed us to explore response profiles down the depth of cortical columns with several populations acting upon each other in space and time.

Neurophysiology through scales

Neurophysiology is branch of science that studies the function, rather than structure, of the nervous system. The electrophysiological side of neurophysiology employs tools to understand specific mechanisms of activity in different scales in the brain with a focus on temporal precision. It is generally regarded as having three scopes: single unit or multi-unit recording

in the microscopic or molecular scale, population activity and microcircuit recording at the mesoscopic scale, or whole-brain population recording at the macroscopic scale. The signals attained therein overlap conceptually: that is, the movement of charged ions or change in polarity. Action potentials or spikes are recorded from cells *in vitro* or *in vivo* with single- or multi-unit electrodes. Electroencephalography (EEG) and magnetoencephalography (MEG) measure the movement of electrical and magnetic fields, respectively, across the whole brain from above the skull. Electrodes can record LFP from entire populations of neurons or from single neurons depending on their impedance and channel size. Despite consistency in the type of signal detected across scales, moving through them is always non-linear.

The LFP is generated from dendritic synaptic activity, calcium spikes, intrinsic currents, ephaptic effects, temporal scaling properties, and most importantly, network architecture and synchrony of neurons (Buzsáki et al., 2012). Strong spatial gradients in voltage are created by many perpendicularly aligned neurons synchronizing, especially when they have large dendritic trees which create a measurable open field. Extracellular activity is therefore resilient even though spiking, by nature, is highly transient, in part because it is the summation of postsynaptic current flow. Depolarization of one neuron from another input source causes an intake of positive ions, creating the negatively charged extracellular space called "sink". However, the depolarization of cells only probabilistically results in action potentials because excitatory and inhibitory inputs act on it in different locations and valences. Action potentials only probabilistically result in postsynaptic outputs to other cells due to the movement of molecules in presynaptic boutons (which will be discussed later). This nonlinear process of input to action potential to output is lost to the view of the mesoscopic electrode recording population activity. Thousands of neurons are within range of each channel, and they build to a crescendo of overall activity, of which the electrode only detects the outcome.

The research presented in this thesis deals largely with LFP recording in the mesoscopic scale (cf. Einevoll et al., 2013), which is nestled into a larger non-linear complex system. Our group uses CSD analysis, calculating the second spatial derivative, to analyze not only the already temporally precise map of neuronal activity but also a more spatially accurate map of local current flow (Happel et al., 2010; Mitzdorf, 1985). This provides laminar distinction of population activity down the depth of the auditory cortex, allowing us to quantify, for example, separate thalamocortical input sinks and more spatially sensitive changes in auditory response profiles (Happel, 2016). With these CSD profiles we can interpret population activity across the laminar structure shared between mammals (Douglas & Martin, 2004; Mitani et al., 1985; Mountcastle, 1997). From these sources, we know that the supragranular layers form a densely interconnected network across all cortical areas which communicate information to global systems. Granular layers are considered to be the main thalamic input layers to the sensory cortex, housing microcircuitry that contains pyramidal neurons, and a variety of interneurons which function to enhance or inhibit thalamocortical excitation. Infragranular layers act in coordination with the granular layers to mediate activity based on secondary thalamic input and also perform the important role of corticothalamic feedback. This feedback facilitates the adaptation of continued thalamocortical inputs through those specific pathways. The basic population dynamics, built on non-linear accumulation of signals at smaller scales, adapt, process, and filter a continuous stream of auditory information to allow us to derive meaning and behavioral relevance from external sound waves.

Robustness and redundancy in the cortex

Understanding complexity in any context means connecting with general principles and successful strategies that complex systems have been found to develop. My research touches on themes of variability in the brain. We will see this through the movement of microscopic elements (VGCCs) introducing variability across a full population of neurons in Chapter 4, and in comparison of variability between auditory and non-auditory specialist species in Chapter 5. I would like to set the stage for what purpose this serves in a complex system and how it might broadly benefit the brain.

A majority of neurons are silent in the brain (Shoham et al., 2006). Therefore, when we record in the scope of action potentials or postsynaptic output, only a fraction of neurons is visible. When we record in the scope of presynaptic activity, most of the neurons contributing to the summation of LFP signal are not then contributing to passing the signal further. The brain would have evolved to optimize some level of energy efficiency, especially due to its high energy cost relative to the rest of the body it's in. What then is the purpose of keeping a dense network of intrinsically active but silent cells in a population? Ovsepian (2019) proposed that circuits neutralized by persistent inhibition could adapt for the purpose of plasticity or new functionality when required. In the extreme, Ovsepian explored several cases where patients lost entire areas of their brains and were able to function regardless (Borgstein & Grootendorst, 2002; Feuillet et al., 2007). But we also very commonly introduce chemical and behavioral challenges to these networks in our scientific experiments. Those challenges only serve to either imitate behaviorally relevant scenarios or to test the limitations of function. Networks might keep dense reserves of silent neurons to call upon as needed even in these more common scenarios as well. If there is malfunction in a unit or a portion of the network, it could adapt and repurpose its reserves dynamically. Redundancy exists in large complex networks for this purpose.

Neurons that fire together wire together (Shatz, 1992) in a similar way that ants follow a trail to food due to concentrated pheromone, therefore further increasing the amount of pheromone. For ants, this occurs simultaneously while other ants randomly explore for new food sources. When an infant brain is born, it begins with an overabundance of synapses and then prunes them over years (Feinberg, 1982; Huttenlocher, 1979). Events occur which shape network connections, encouraging stronger bonds based on use—such as seeing or kicking—and letting go of unused synapses (Tierney & Nelson, 2009; Wiesel & Hubel, 1963). After the majority of the pruning process is done, the generation of new synaptic connections continues throughout adulthood and this contributes to plasticity (Kelsch et al., 2010). The exploitation of existing synaptic connections is occurring in parallel with largely random exploration in the form of new connections popping up which can be strengthened or not (see an investigation of this volatility in Mongillo et al., 2017). This creates a type of robustness in a population that would be impossible if a currently optimal strategy was exploited by the complete system. An amount of randomness or stochasticity must be exercised or an environmental change (such as loss of tissue or depletion of food) will destroy the network.

To expand on this, why is a tree not a series of perpendicular sticks? Why aren't branches perfectly spaced? Nature frequently uses fractals or fractal-like shapes, such as lightning, trees, roots, coastlines, and neurons. But they are rarely mathematically perfect. It's not because the perfect fractals wouldn't work best, but because having a functionally introduced randomness, which devolves deterministic systems into chaos, is evolutionarily advantageous. A system should never reach perfect marks on its solution to a problem in its environment.

Instead, it should reach a near-perfect solution (see *Robby The Robot Genetic Algorithm* described in Mitchell, 2011). If things change in the environment, the flexibility introduced by the random features and chance for random mutations allows the organism to adapt. On a longer timescale, evolution might select for new features. More immediately, single units or networks may adapt by reutilizing their redundant features. Neurons have a shorter shelf life than trees and are much more densely populated. Arguably, an internal brain-wide environment is more subject to change and has swifter state differences. The need to be adaptive is more important in this environment and therefore it seems flexibility and redundancy are built in at every scope in the brain, continuously.

Basic research as a unit of a complex theory building process

I have argued that everything is continuous and complex, but reductionism is still valid within this framework. Basic research has always been, by definition, foundational in the whole of science. Connected to my topics, for example, is that the most prevalent model for Schizophrenia is the hypofunction of N-methyl-D-aspartate (NMDA) channels. This theory was developed because ketamine and PCP, NMDA antagonists, induced psychotic states that resembled the disorder in key ways (Lodge & Mercier, 2015). The use of ketamine, my topic of Chapter 3, was not originally intended to find this connection to Schizophrenia, but now translational clinical science has a better path laid for finding cause and treatment. A connection to the topic of Chapter 4, is that altered calcium influx can lead to migraine aura (Plomp et al., 2001) ataxia, and epilepsy (Ophoff et al., 1998). Because of a shared root cause of P/Q VGCCs, anti-epileptics have been utilized as a possible migraine prophylaxis as well. Microscopic changes across a population sometimes build to disorders that can be better understood by reductionism—understanding specifically the part of the system that is causing malfunction. Beyond clinical, basic research on organisms that fill neuroethological niches, as seen in Chapter 5, give engineers and applied-scientists tools to creatively problem solve for the benefit of the environment and humanity. An example of this is that scientists have developed "ant colony optimization algorithms" to optimize cell-phone communications routing and delivery truck scheduling.

That being said, reductionist science must be done in community for it to serve higher purposes. We aspire to many great purposes in the advancement of knowledge, technology, and medicine and the data that we gather are components to construct those frameworks— like cathedrals that take generations and many hands and minds to build. Open science, clear methods, and reproducibility are paramount for the generation and continued life of datasets to this end. To stand on the shoulders of our predecessors, we must have access to what they created and be able to essentially trust their findings. The same is true of our peers as ideas grow and move around in a scientific community. In a complex world, I don't know the impact my findings will turn out to have. I don't know if my exploration of how the brain assigns meaning to sound will be utilized to cure the migraines that ail me. However, translational and clinical research need basic research to be done to make intellectual leaps in solving those problems.

Another translational reason to study the auditory cortex at a basic level is to understand sensory-driven behavior. Much of neuroscience is, necessarily, done in controlled spaces: under anesthesia, in boxes, with genetically identical animals. While this gives us data that is legible and analyzable, it makes for an insurmountable challenge. In a system that is non-linear

between and within all scales, it is impossible to say for certain that behaviors arise as we think they do and are completely applicable to natural environments. I will discuss in this dissertation how the results I have found over the last 5 years could be interpreted. However, there are always constraints to assigning meaning or causal links due to this complexity. Importantly, we don't do our work in a vacuum; it is through establishing sets of findings across many units in this network that have allowed us to reach the conclusions or make the technologies and medicines we now take for granted. It is through engaging in and strengthening this process that we will understand complexity in the brain.

The work at hand

I have hopefully sufficiently prepared you to think about my work in a larger context. So, here I will briefly describe the topics in this dissertation and what I may say about them. Chapters 3, 4, and 5 will more fully introduce and discuss these 3 projects in turn—in order to equip the reader with the necessary background to understand the results. Finally, in Chapter 6, I will conclude with a discussion of the three projects and how they may be considered together as different parts of the same complex system, spanning across the physiological boundaries of states, scales, and species.

Project 1: Ketamine anesthetized vs awake A1s

States: What effect does an anesthetic NMDA antagonist, ketamine, have on the microcircuitry that we study under it?

Because neurons and interneurons have a different concentration of NMDA channels, ketamine anesthesia affects them to different degrees. Most affected are parvalbumin releasing interneurons which act to suppress the excitatory and inhibitory feedback loop of thalamic input granular layers. This allows for rampant excitation in these layers after a presented stimulus that we do not observe in awake animals for the same stimulus. Seminal neurophysiological studies have provided groundwork for our understanding of basic properties of sensory response profiles in relevant cortical areas. However, we must acknowledge that data collected under anesthesia is not entirely applicable to awake subjects. There is a non-linear effect, and a sensory changing effect, due to the anesthetic agents we use to obtain these less complex, anesthetized, recordings. Knowing more specifically what the anesthesia is doing at a population level, allows us to at least conceptually account for this effect during the interpretations of population level findings under ketamine. It provides a wider context and allows us to step outside of the recording box for interpretation. This study illuminated the balance of excitation and inhibition in A1 microcircuitry, by disrupting it dynamically and considering this effect in the wider framework of sensory physiology across states.

Project 2: Voltage gated calcium channel aggregation and its impact on A1 microcircuitry function

Scales: How does a change from stochastic to deterministic output of individual neurons change the functional dynamics of a network of neurons?

In the first stage of our multistep research project, Prof. Martin Heine and Dr. Jennifer Heck clustered VGCCs in vitro (Heck et al., 2019). VGCCs facilitate the intake of calcium ions when the pre-synapse is depolarized due to an incoming action potential. Several calcium ions need to bind to calcium sensors on docked vesicles to initiate vesicle fusion and neurotransmitter release. However, VGCCs normally move around the pre-synaptic membrane, adding variability as enough calcium may then not reach the sensors. Heck et al. (2019) tagged the N-termini of VGCCs in the pre-synaptic terminal with a cryptochrome mutant, Cry2olig, which transiently snaps together under blue light (Taslimi et al., 2014). Optogenetically clustering VGCCs in their pre-synaptic active zones dramatically increased a neuron's excitatory post-synaptic response and produced a reliable paired-pulse depression to consecutive responses. The second stage of the project was to transfer this experiment across scales. We optogenetically clustered VGCCs across the distributed A1 *in vitro* (details on how in the methods and Ch 4), and recorded LFP at a mesoscopic scale across a longer time span. This study was a lesson in non-linearity. While the single neurons showed an increase in activity and a deterministic response profile, the full cortical column in the A1 revealed systemic and lasting suppression after VGCC clustering. This suppression was greater in conjunction with a higher density of neuronal recruitment. This may indicate a dynamic impact of VGCC motility on levels of synaptic input and possibly denotes a loss of robustness or flexibility due to clustering.

Project 3: Complexity in neuroethology; comparing two auditory niches in bats and mice

Species: How does the auditory cortex of an auditory or olfactory specialist diverge in recruitment of its shared laminar circuitry?

Black 6 mice have been an excellent and reliable model species to answer a variety of scientific questions, because they are a complex mammal that we have almost fully standardized. However, they do not have a neuroethological auditory niche in the way that echolocating bat species do. That is, they do not generally need very accurate auditory signal representation for behavioral success in their environments. The seba's short-tailed bat, an echolocating, fruit-eating bat, would need a more precise auditory representation of sound to successfully navigate. Both short-tailed bats and mice hear, and their auditory cortices, with the shared laminar architecture of mammals, are comparable in size. We collaborated with the Frankfurt Auditory Computation Lab to compare the A1 of these two species directly for the first time. We found, overall, clearer following in bats due to a better signal to noise ratio. What may have been predictable, is now partially confirmed. The bat auditory cortex can achieve greater temporal accuracy of signal response at lower metabolic cost than mice, which must contribute to the success in their echolocation-based navigation. It is through divergent recruitment of shared circuitry, and a difference in observed variability, that evolution has developed organisms to fill such alien niches.

What follows

Chapter 2 contains the full methods for all subsequent projects. Chapter 3 is an expansion on my first publication (Deane et al., 2020). Chapter 4 is an expansion on my second, which is currently available as pre-print (Deane et al., 2022a). Chapter 5 is a larger version of what is available as pre-print (Deane et al., 2022b) and sets the stage for the work I will continue to do in my future academic career—though with different bats. These topics were developed in parallel with my thoughts developing on what my scientific program would be. By the time I started fully stepping into the idea of studying the auditory cortex in terms of complexity, most of this work was done. This dissertation has given me the opportunity to turn around and look at my work within the bigger picture and attempt to convince you of the validity to do so. Chapter 6, then, is my final discussion on this research in terms of what was introduced in the current chapter. Please enjoy the colorful results to come; I welcome your questions at the defense of this work.

Chapter 2: Methodology

Ethical Approval

All experiments were conducted in accordance with ethical animal research standards defined by the German Law and approved by an ethics committee of the State of Saxony-Anhalt under the given license 42502-2-1394LIN or, in the case of our collaboration with Frankfurt, #FU-1126. They also conform to the principles and regulations as described in by Grundy (Grundy, 2015). All experiments were carried out with adult male Mongolian gerbils (*Meriones unguiculatus*, 4 to 8 months of age, 70-90g bodyweight, total acute: n=11, chronic: n=9), adult male mice (*Mus musculus*, acute: 8-13 weeks of age, 18-28 g body weight, total $n = 27$ or chronic: 6-13 weeks of age, 20-28 g body weight, total n=4) and adult seba's short-tailed bats (*Carollia perspicillata*, $n = 5$). Note that female mice or gerbils were not used as possible variances due to sex was not in the scope of our study. All bat experimental procedures were carried out at Goethe-University in Frankfurt (see García-Rosales et al., 2020) and will only be briefly described here.

Mouse Line and Optogenetic CRY2olig

The transgenic mouse line used in Chapter 4, C57BL/6J *Cacna1a*[^Citrine] (Mark et al., 2011), expresses a Citrine (YFP/GFP derivate) tag at the N-terminus of Cav2.1 voltage-gated calcium channels. This Citrine has been reported to be specifically detected by GFP antibodies (Mark et al., 2011). Here, we used a recently developed system that utilizes a feedback-controlled intracellularly expressed anti-GFP nanobody (called intrabody) to target the Citrine tag and at the same time equip the Cav2.1 N-terminus with a photo-cross-linkable cryptochrome mutant, CRY2olig (Taslimi et al., 2014). Under blue (477-488 nm) light exposure, CRY2olig snaps together transiently (Figure 2.1). As previously shown, CRY2olig reaches ~60 % clustering immediately after light stimulation and clusters decrease to ~30 % over 30-40 minutes and to ~0 % again in the duration of 160 minutes (see Taslimi et al., 2014 Fig. 1, Heck et al. 2019).

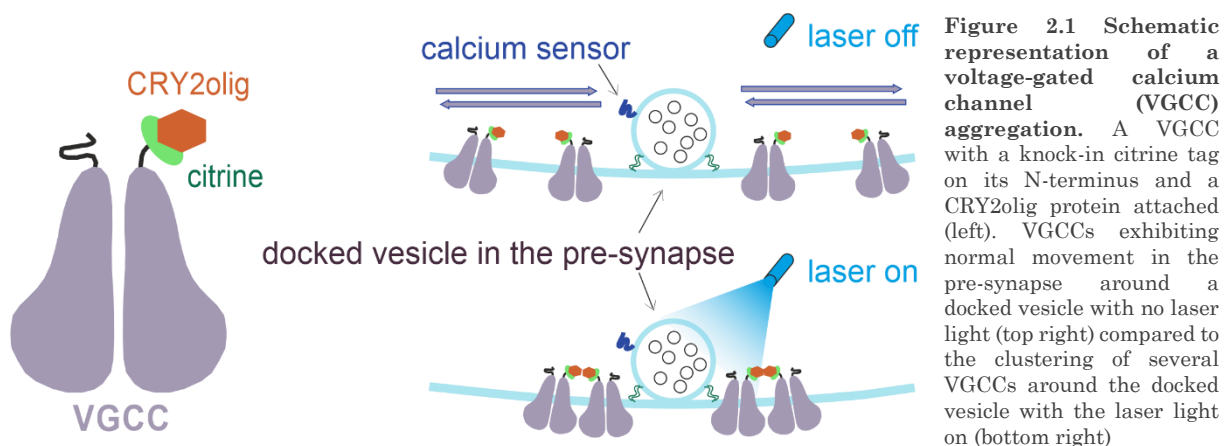**Figure 2.1 Schematic representation of a voltage-gated calcium channel (VGCC) aggregation.** A VGCC with a knock-in citrine tag on its N-terminus and a CRY2olig protein attached (left). VGCCs exhibiting normal movement in the pre-synapse around a docked vesicle with no laser light (top right) compared to the clustering of several VGCCs around the docked vesicle with the laser light on (bottom right)

Pharmacology

Recordings taken under anesthesia are henceforth labeled "acute" due to acutely placed electrodes for a single day of recording. Recordings taken in awake animals are henceforth labeled "chronic" due to implantations of chronic electrodes allowing for multiple days of recording.

Acute and chronic gerbil

Ketamine-xylazine was administered during surgery and throughout the experiment to maintain a steady level of anesthesia. Infusion of 45% v/v ketamine (50 mg/ml, Ratiopharm GmbH), 5% v/v xylazine (Rompun 2%, Bayer Vital GmbH, Leverkusen, Germany), and 50% v/v of isotonic sodium-chloride solution (154 mmol/1, B. Braun AG, Melsungen, Germany) was given intraperitoneally for an initial dose of 0.004 ml per 1 g bodyweight. A needle was place subcutaneously to maintain anesthetic status with an infusion rate of $22mg/kg^{-1}/h$ for deeper anesthesia during the surgery and a rate of $15mg/kg^{-1}/h$ during the experiment in anesthetized subjects. Anesthetic status was regularly checked (every 10-15 min) by paw withdrawal-reflex and breathing frequency. Body temperature was kept stable at 34°C.

In acute recordings, a final dose was administered subcutaneously at the end of the experiment and animals were sacrificed by decapitation. For chronic operations, animals received analgesic treatment with Metacam (2 mg/ml, Boehringer Ingelheim, Ingelheim am Rhein, Germany) substituted by 5% glucose solution 30 minutes before the end of surgery with 0.3 ml per 1 kg of bodyweight and for 2 days post-operatively with 0.2 ml per 1 kg of bodyweight.

Acute mouse

Electrode implantation and recording

Ketamine-xylazine was administered during surgery and throughout the experiment to maintain a steady level of anesthesia. Infusion of 20% v/v ketamine (Ketavet or Ketabel), 5% v/v xylazine, and 75% v/v of isotonic sodium chloride solution was given intraperitoneally for an initial dose of 4 ml per 1 kg of bodyweight. A needle was placed subcutaneously or intraperitoneally to maintain anesthetic status with an infusion rate of 0.2 mg per 1 kg of bodyweight per hour during the experiment. Anesthetic status was regularly checked (every 7.5–10 min) by paw withdrawal reflex, tail pinch, and breathing frequency. Body temperature was kept stable at 37°C. A final dose was administered subcutaneously at the end of the experiment and animals were sacrificed by decapitation.

Transduction of lentivirus

Ketamine-xylazine was administered once at the onset of surgery as described above for mice.

Isoflurane, administered in an isoflurane anesthesia system (Rothacher) in an O_2/N_2O mixture, was used for surgery, instead of ketamine, starting in the second half of 2020. Subjects were placed in an induction chamber and given 5% isoflurane for two minutes. They were then placed on a stereotactic frame (World Precision Instruments) with a heating pad,

for a stable 37°C body temperature, and given 1.5–2.0% isoflurane for maintenance. Breathing rate was kept between 80 and 100 bpm by adjusting the isoflurane rate.

Animals received analgesic treatment with Metacam substituted by 5% glucose solution 30 minutes before the end of surgery with 0.3 ml per 1 kg of bodyweight and for 2 days post-operatively with 0.2 ml per 1 kg of bodyweight.

Chronic mouse

Pentobarbital (Nembutal, H. Lundbeck A/S, Valby, Denmark) was administered at the onset of surgery with an intraperitoneal infusion of 50 mg per 1 kg of bodyweight and supplemented by 20% every hour. Anesthetic status was regularly checked (every 10-15 min) by paw withdrawal reflex, tail pinch, and breathing frequency. Body temperature was kept stable at 37°C. Animals received analgesic treatment with Metacam as described above for mice.

Chronic bat

Ketamine-xylazine was administered at surgery onset (ketamine: Ketavet, 10 mg/kg, Pfizer; xylazine: 38 mg/kg).

Surgery and electrophysiological recordings
Head-fixation Faraday cage

Common among several following protocols, we used a Faraday-shielded acoustic soundproof chamber with a speaker (Tannoy arena satellite KI-8710-32) located 1 m from the head-fixation platform. Recorded LFPs were fed via an Omnetics connector (HST/32V-G2O LN 5V, 20x gain, Plexon Inc.) into a PBX2 preamplifier (Plexon Inc.) to be pre-amplified 500-fold and band-pass filtered (0.7-300 Hz). Data were then digitized at a sampling frequency of 1000 Hz with the Multichannel Acquisition Processor (Plexon Inc.).

Stimuli in this setup were generated in Matlab (Mathworks, R2006b), converted into analog (sampling frequency 1000 Hz, NI PCI-BNC2110, National Instruments), routed through an attenuator (g-PAH Guger, Technologies), and amplified (Thomas Tech Amp75). A microphone and conditioning amplifier were used to calibrate acoustic stimuli (G.R.A.S. 26AM and B&K Nexus 2690-A, Brüel&Kjær, Germany).

Acute gerbil recordings and pharmacological silencing of the A1

For use in Chapter 3, n = 11. The surgical procedure for electrophysiological recording has been previously described in detail (Deliano et al., 2018). Briefly, the right auditory cortex was exposed by trepanation and the A1 was located by vascular landmarks. A small hole was drilled on the contralateral hemisphere for implanting a stainless-steel reference wire (Ø 200µm). Animals were head fixed with an aluminum bar, affixed by UV-curing glue (Plurabond ONE-SE and Plurafill flow, Pluradent).

Anesthetized animals were head-fixed in the head-fixation Faraday cage described above. Local field potentials (LFPs) were recorded with a 32-channel shaft electrode (NeuroNexus A1x32-50-413) implanted in the A1 perpendicular to the cortical surface (Happel et al., 2010). A series of pseudo-randomized pure-tone frequencies covering a range of 7 octaves (tone duration: 200 ms, inter-stimulus-interval (ISI): 800 ms, 50 pseudorandomized repetitions, 65 dB SPL, 7.5 min per measurement, 125 Hz – 32 kHz). We determined the best frequency (BF) as the frequency evoking the strongest response in the averaged granular CSD channels (see below).

Recordings of tone-evoked responses were taken after recording quality had stabilized: typically, 100+ minutes after implantation. After measuring the tonotopic tuning, 20 µl of the GABA$_A$ agonist muscimol (8.23 mM muscimol, TOCRIS bioscience, batch no: 9C/107090), dissolved in isotonic sodium-chloride solution, was applied topically onto the cortical surface, a method introduced and quantified by Edeline et al. (2002) to silence intracortical contributions of synaptic activity (Happel et al., 2010).

Chronic gerbil electrode implantation and in-vivo tonotopy recording

For use in Chapter 3, n = 9. Chronic implantation of a recording electrode followed similar surgical procedures to the acute implantation (above). Importantly, the trepanation was kept smaller in order to limit the region of exposed cortex to avoid tissue damage and to achieve stable fixation of the electrode. A recording electrode with a flexible bundle between shaft and connector (Neuronexus, A1x32-6mm-50-177_H32_21mm) was inserted and an initial recording was conducted in order to confirm that the implantation was within A1. Then, the electrode and the connectors (Neuronexus H32-omnetics) were both glued to the skull with a UV-curing glue. In order to protect the exposed region of the cortex, the hole was filled with a small drop of an antiseptic lubricant (K-Y Jelly, Reckitt Benckiser). Animals were allowed to recover for at least 3 days before the first recording.

Animals were then placed in a single-compartment box in an electrically shielded and sound-proof chamber. Recordings were performed with the head-connector of the animal through a preamplifier (HST/32V-G2O LN 5V, 20x gain, PlexonInc or RHD2132 Omnetics-Intan technologies) and a data acquisition system (Neural Data Acquisition System Recorder Recorder/64, Plexon Inc. or RHD2000 series, Intan Technologies), visualized online (NeuroExplorer, Plexon Inc. and RHD2000 interface GUI Software), and stored. Broadband signals were filtered offline to extract local field potentials (2000 Hz sampling frequency and later down sampled to 1000 Hz). Acoustic stimuli were presented with the same parameters, as in the anaesthetized group. Auditory stimuli were calibrated using a 1⁄2-inch condenser microphone (Brüel&Kjær) and presented with an intensity of 20 dB above a detectable averaged tone-evoked LFP component. Stimuli were digitally synthesized and controlled using Matlab (R2012b) and presented by Presentation® (Neurobehavioral Systems). Stimuli were delivered via an attenuator (g-PAH Guger Technologies), an amplifier (Lehmann Audio) and two electrostatic loudspeakers positioned 5 cm outside both sides of the box.

Acute mouse

Transduction of virus

For use in Chapter 4, n = 10 treated and n = 7 viral controls. Surgical transduction of the lentivirus in the A1 was performed as follows. The temporal bone was exposed via a single 3mm cut from ear to eye on the right side and the chewing muscle was gently removed from the temporal bone by scraping down for 2 mm. Three ~0.5 mm holes were created above the A1, 1 mm below the temporal suture through trepanation, 1 mm apart. Lentivirus, containing Cry2olig for the treated group or empty for the viral control group, was injected 300 and 600 µm deep at each of the three sites. Each of the 6 injection sites received 23 nl of virus 9 times every 3 seconds, totaling 207 nl of virus at each site and 1,242 nl across the A1. Lentiviruses have been shown as efficient in their role of infecting neurons *in vivo* in, amongst other species, rats (Naldini et al. 1996a; Naldini, et al. 1996b). While the spread of the virus is limited, it has been shown that 200 nl injection volumes diffuse within a spherical region with a diameter around 200-600 µm (Desmaris et al. 2001; Osten et al. 2006 see Figure 13.3). Therefore, between each subject, we can assume a large coverage of the A1 down the depth of the cortical column. The muscle was then replaced over the trepanned temporal bone and the skin was sutured.

The virus was allowed to express for 4 weeks before auditory recording. The naïve control group (n=10) received no surgery prior to electrode implantation.
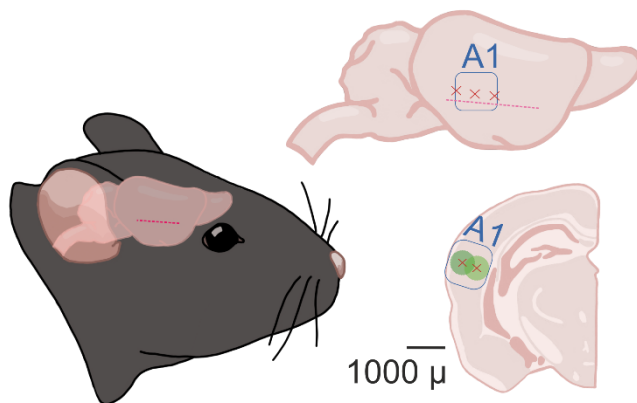

Figure 2.2 Schematic of lentivirus transduction. The temporal bone was exposed via a single 3mm cut from ear to eye on the right side and the chewing muscle was gently scraped down. Three ~0.5 mm holes were created above the A1, 1 mm apart. Lentivirus was injected 300 and 600 µm deep at each site. Each injection site received 207 nl of lentivirus, totaling 1,242 nl. An estimated 600 µm of viral spread (green) is represented in the frontal section centering around the two injection depths.

Electrophysiological recording, auditory stimuli, and blue light laser stimulation

For use in Chapter 4, n = 27. The surgical procedure for exposing the A1 and implanting the electrode in mice is the same as described above in the section: "Acute gerbil recordings and pharmacological silencing of the A1" and animals were head-fixed in the head-fixation Faraday cage described above. Note that the surgery took place in white light which may have caused some VGCC clustering in treated animals. After electrode implantation, the Faraday cage was kept in total darkness except for periods of red light for the experimenter to monitor and maintain anesthetic level. An hour of baseline tonotopy recording was taken in this condition to allow clustering to reverse before taking pre-laser measurements.

Three types of stimuli were provided during recording. The first was tonotopy: a series of pseudo-randomized pure-tone frequencies covering a range of seven octaves (tone duration: 200 ms; ISI: 800 ms; tone frequency: 1 to 32 kHz; 50 pseudorandomized repetitions; 70 dB

sound pressure level; 7.5 min per measurement). We determined the best frequency (BF) as the frequency evoking the strongest response in the averaged granular CSD channels. The second was click train measurement (Figure 2.3): a series of pseudo-randomized presentation-frequency noise-click trains with a carrier frequency of the determined BF (stimuli duration: 999 ms; click presentation-frequency: 5 and 10 Hz; ISI: 200 and 100 ms respectively; inter-trial-interval: 3 s; carrier tone: BF; 30 pseudorandomized repetitions before the laser and 50 after; 90 dB sound pressure level; 10 min before the laser and 15 min after per measurement). The third was an amplitude modulation measurement (Figure 2.3): a series of pseudo-randomized frequency modulations of a pure-tone at the determined BF (stimuli duration: 999 ms; modulation frequency: 5 and 10 Hz; carrier tone: BF; inter-modulation interval: 200 and 100 ms respectively; inter-trial-interval: 3 s, 30 pseudorandomized repetitions before the laser and 50 after, 70 dB sound pressure level, 10 min before the laser and 15 min after per measurement). Spontaneous activity was also recorded throughout the experiment in ~2-minute time chunks.

After tonotopy BF selection and the pre-laser click train, amplitude modulation, and spontaneous activity measurements were taken, blue light (power: 5mW; light duration: 20 s; light wave: 477 nm) laser was delivered to the cortex through a fiber suspended 5 mm above the cortical surface. One hour of click train measurements was taken, the laser was activated again, and one hour of amplitude modulation measurements were taken. Spontaneous activity was recorded directly before and after each laser presentation.
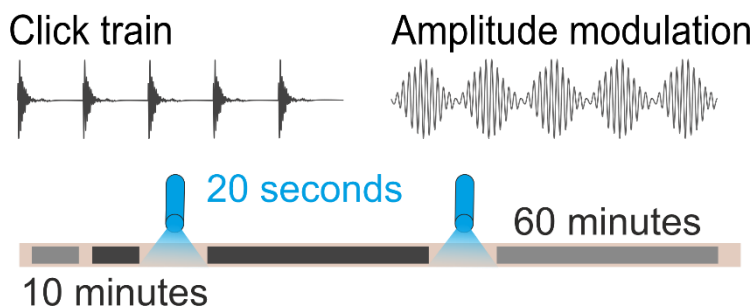

Click train   Amplitude modulation

20 seconds

60 minutes

10 minutes

Figure 2.3 Protocol of measurements. Top left: Click train waves, and Top right: amplitude modulated pure tones were each presented, Bottom: for one 10-minute measurement after an hour in total darkness and then for four 15-minute measurements after respective laser presentations.

Chronic mouse

For use in Chapter 5, n = 2. The surgical procedure for exposing the A1 and implanting the electrode in mice is the same as described above in the section: "Gerbil chronic implantation and in-vivo tonotopy recording" except for 2 key differences. First, pentobarbital was used as described above for anesthesia. Second, an additional headplate, 3D printed in the lab, was secured with dental cement over the cleared skull before the attachment of the Omnetics connector (Figure 2.4). This plate allowed head-fixation to 3D printed clamps on an in-house-designed head-fixation treadmill (Figure 2.4). This treadmill was placed in the head-fixation Faraday cage and mice were allowed 3 days of recovery post-operation and 5 days of habituation (from 15 to 75 minutes) on the treadmill.

After habituation, mice were head-fixed on the treadmill for 7 consecutive days to record cortical response to tonotopy (for BF calculation), amplitude modulated pure tones at the BF and off-BF frequencies, click trains, and spontaneous activity as described in the previous section. They were exposed to blue light laser stimulation between 15-minute measurements due to their initial purpose as the control group for an awake VGCC aggregation experiment.

However, pre- and post-laser measurements were considered equivalent and counted together for Chapter 5, meaning each subject had 14 measurements for each condition.
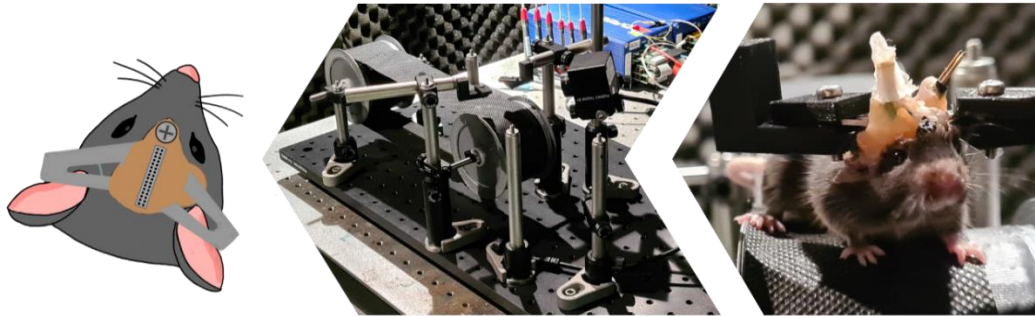

Figure 2.4 Head-fixated, freely moving mice. During chronic implantation of the electrode, mice were also given a headplate for head-fixation onto a home-made treadmill device. Head-fixation was secured via two 3D printed clamps and the subject was able to run forward or backward on the treadmill. Note that a wider tread was produced for later experiments but was not yet used.

Chronic bat

For use in Chapter 5, n = 5. Bat A1s were exposed through craniotomy (ca. 1 mm²) performed with a scalpel blade and were allowed to recover for at least two days before recording.

Bats were placed in a custom-made holder in a Faraday sound-proof chamber and kept at a constant body temperature of 30°C with a heating blanket (Harvard, Homeothermic blanket control unit). A speaker (NeoCD 1.0 Ribbon Tweeter; Fountek Electronics) was positioned 12 cm away from the bat's right ear. Recordings were made in the left A1. A laminar probe (NeuroNexus A1x16-50, impedance: 0.5–3 MΩ) was inserted perpendicularly into the A1 until the uppermost channel was barely visible at the cortical surface. The probe was connected to a micro preamplifier (MPA 16, Multichannel Systems MCS GmbH, Reutlingen, Germany), connected to an integrated amplifier and analog-to-digital converter with 32-channel capacity (Multi Channel Systems MCS GmbH, model ME32 System, Germany).

Acoustic stimulation, delivered by Matlab (R2009b), were trains of a single distress syllable (representative of this bat's distress repertoire) repeated at a rate of 5.28 or 36.76 Hz for a period of 2 s. Stimuli were presented 50 times each, in a pseudorandom order, with an inter-trial-interval of 1 s. Auditory stimuli were digital-to-analog converted using a sound card (M2Tech Hi-face DAC, 384 kHz, 32 bit; sampling frequency: 192 kHz due to technical reasons) and amplified (Rotel power amplifier, model RB-1050). Spontaneous activity was also recorded at the beginning of each session for 2+ minutes.

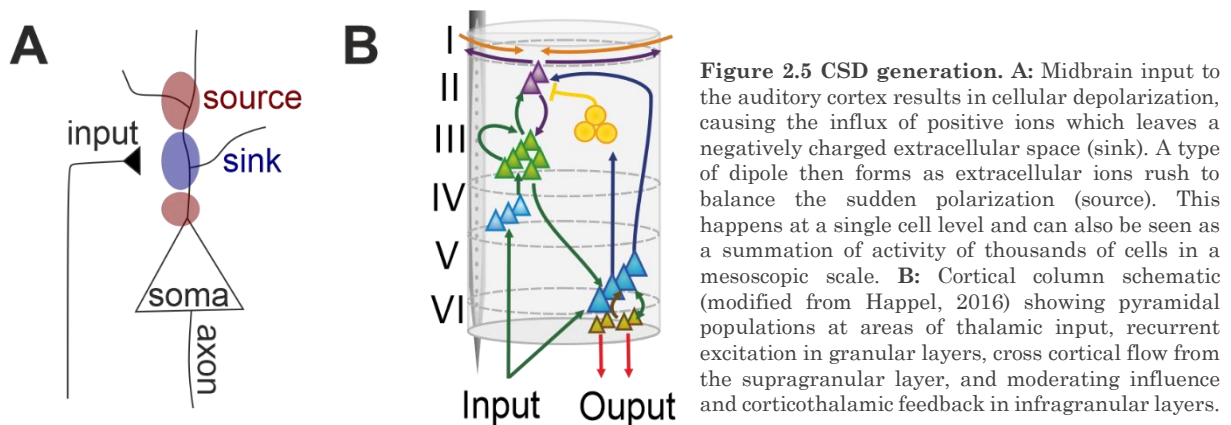## Current source density analysis

Based on the recorded laminar local field potentials, the second spatial derivative was calculated in Matlab (R2016a-R2022a), yielding the CSD distribution as seen in equation 2-1:

$$\text{2-1)} \quad \textbf{CSD} \approx \frac{\delta^2\Phi(z)}{\delta z^2} = \frac{\Phi(z+n\Delta z) - 2\Phi(z) + \Phi(z-n\Delta z)}{(n\Delta z)^2}$$

where $\mathbf{\Phi}$ is the field potential, z is the spatial coordinate perpendicular to the cortical laminae, $\mathbf{\Delta z}$ is the sampling interval, and n is the differential grid (Mitzdorf, 1985). LFP profiles were smoothed with a weighted average (Hamming window) of 9 channels which corresponds to a spatial kernel filter of 450 μm (Happel et al., 2010). CSD distributions reflect the local spatiotemporal current flow of positive ions from extracellular to intracellular space evoked by synaptic populations in laminar neuronal structures (

Figure 2.5A). Current sinks thereby correspond to the activity of excitatory synaptic populations, while current sources mainly reflect balancing return currents. Early synaptic thalamocortical inputs persist after intracortical silencing with the GABA_A-agonist muscimol related to thalamocortical projections on cortical layers III/IV and Vb/VIa (Brunk et al., 2019; Deane et al., 2020; Happel et al., 2010, 2014; Happel & Ohl, 2017) in accordance with reports by others (Schaefer et al., 2015). Early current sinks in the auditory cortex are therefore indicative of thalamic input in granular layers III/IV and infragranular layers Vb/VIa (Happel et al., 2010; Szymanski et al., 2009).

Figure 2.5B shows a schematic of an auditory column and a simplified spatial distribution of neuron and interneuron populations, modified from Happel (2016). Mouse, gerbil, and bat CSD profiles are discussed in this work and group averages for each species are shown in Figure 2.6. Layer distinctions are discussed below.

Figure 2.5 CSD generation. A: Midbrain input to the auditory cortex results in cellular depolarization, causing the influx of positive ions which leaves a negatively charged extracellular space (sink). A type of dipole then forms as extracellular ions rush to balance the sudden polarization (source). This happens at a single cell level and can also be seen as a summation of activity of thousands of cells in a mesoscopic scale. **B:** Cortical column schematic (modified from Happel, 2016) showing pyramidal populations at areas of thalamic input, recurrent excitation in granular layers, cross cortical flow from the supragranular layer, and moderating influence and corticothalamic feedback in infragranular layers.

Average rectified and relative residuals CSD

CSD profiles were further transformed by averaging the rectified waveforms of each channel by equation 2-2:

$$2\text{-}2) \quad AVREC = \frac{\sum_{i=1}^{n} |CSD_i|(t)}{n}$$

where n is the individual channel and t is time in ms. This measure gives us the overall temporal local current flow of the columnar activity (Givre et al., 1994; Schroeder et al., 1998). The relative CSD residues were calculated by equation 2-3 as the sum of the channels divided by the absolute values of the channels:

$$\text{2-3)} \quad RELRES = \frac{\sum_{i=1}^{n} CSD_i(t)}{\sum_{i=1}^{n} |CSD_i(t)|}$$

This measure reflects the disbalance in sinks and sources (Harding, 1992) and therefore gives us an indication of lateral (intracortical) vs vertical (thalamic) contribution to the signal (Happel et al., 2010).
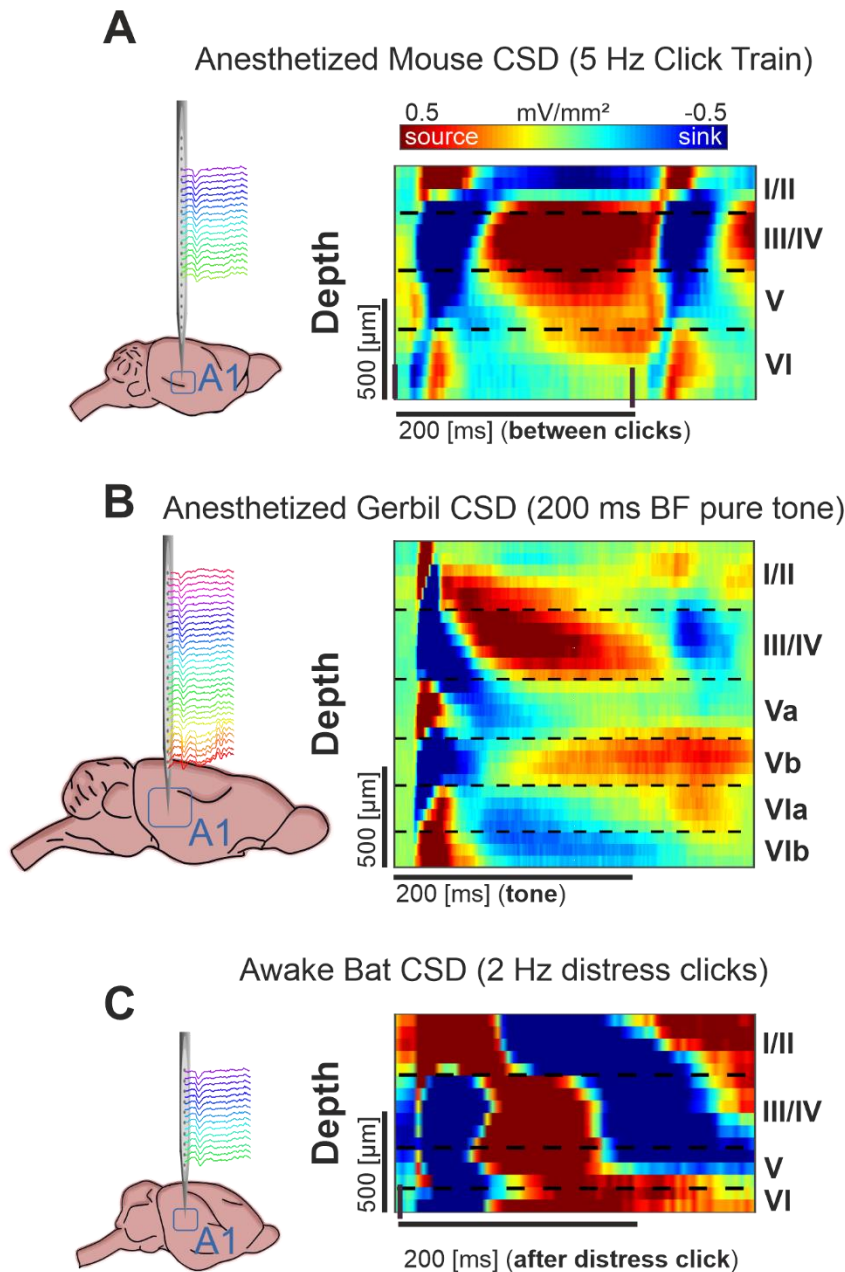

Figure 2.6 Animal Averaged CSDs. Each CSD average is scaled exactly the same in time (300 ms) and space (species dependent). CSDs show neuronal activity down the cortical depth of the auditory column over time. **A: left:** A mouse brain, highlighting the A1, with LFP signal being drawn from ~20 channels of a 32-channel electrode. **right:** Group average of anesthetized naïve mice (n=10) CSD profiles of cortical response to 5 Hz click train. Clicks are represented at time points 0 and 200 ms on the x axis in brown. **B: left:** A Mongolian gerbil brain, highlighting the A1, with LFP signal being drawn from all 32 channels of the electrode. **right:** Group average of anesthetized naïve gerbils (n=11) CSD profiles of cortical response to a 200 ms pure tone at best frequency per subject. **C: left:** A seba's short-tailed bat brain, highlighting the A1, with LFP signal being drawn from all 16 channels of the electrode. **right:** Group average of awake naïve bats (n=5) CSD profiles of cortical response to 2 Hz distress clicks. Clicks are represented at time point 0 ms on the x axis in brown.

Cortical layer traces

Based on tone evoked CSD distributions, we assigned the main sink components to the cortical anatomy as follows: the early dominant sink components are attributed to lemniscal

28

thalamocortical input, which terminates in cortical layers IV and the border of V and VI. Note that we performed CSD analysis on Mongolian gerbils, mice, and seba's short-tailed bats (Figure 2.6). Mongolian gerbils have a thicker A1 and subsequently more distinguishable layer sink components than the other two species (Deane et al., 2020; Happel et al., 2010); we distinguished layers I/II, III/IV, Va, Vb, VIa, and VIb in gerbil cortices. In the mouse A1, we distinguished layers I/II, III/IV, V, and VI as primary sink component layers based on mouse A1 CSD from Yamamura et al. (2017). Bat cortices were labeled in the same way as the mouse A1, but it should be noted that we did not have anesthetized recordings from this species. Each layer was transformed into layer sink traces by averaging sink activity of each channel attributed to the layer as seen in equation 2-4:

$$2\text{-}4) \quad \textbf{\textit{Layer trace}} = \frac{\sum_{i-1}^{n} \textbf{\textit{Layer}}_i(t)}{n}$$

where *Layer* } x<0 (only sink activity is taken), n is the number of individual channels attributed to the layer, and t is time in milliseconds. This layer trace gives us the temporal local current flow of sink activity per cortical layer for which it is calculated.

Staining protocols

H&E staining

Hematoxylin and Eosin (H&E) staining was done according to Mayer's protocol. Briefly as follows: 5 minutes in Finished Hematoxylin-solution (Sigma-Aldrich Inc., St. Louis, MO USA), shortly rinsed in distilled water, 10 minutes under running tap water, 10 minutes in Eosin (Sigma-Aldrich Inc.; 0.1% in distilled water), 10 minutes in tap water to wash out, replacing the water every few minutes, 5 minutes in in 80% alcohol, 5 minutes 2x in 100% alcohol, 5 minutes 2x in Xylene (Sigma-Aldrich Inc.). Slices were then mounted onto Merckoglas (Merck KGaA, Darmstadt, Germany)

Immunohistochemistry

Several protocols were attempted during the course of Chapter 4's study on VGCC clustering in the A1. Summarized here are common or representative elements. Slices were made 40 µm thick and stored in PBS. They were 20 minutes on a shaker in 1% Sodium Borohydride (NaBH4) in 1xPBS, washed 30 minutes in 1xPBS, washed every 10 minutes until solution was bubble-free with 1xPBS, incubated for 45 minutes on a shaker in 5% bovine serum albumin (BSA) + 0.3% Triton X-100 in 1xPBS, washed 10 minutes 3x in 1xPBS, and finally incubated in primary antibodies overnight on shaker at 4°C in 1% BSA + 0.03% Triton X-100 in 1xPBS. On the second day, they were washed 10 minutes 3x in 1xPBS, incubated in secondary antibodies for 2 to 4 hours on a shaker in 1% BSA + 0.03% Triton X-100 in 1xPBS, washed 10 minutes 3x in 1xPBS, and mounted with Mowiol (Sigma-Aldrich Inc.).

Antibodies are listed in Table 2-1. The first co-localization staining attempt was done with antibodies against Ca2+ channels and Synaptic Systems GFP – FluoTag-Q. The second

attempt was done with antibodies against Bassoon and ChromoTek GFP – Booster. Slices were taken from *Cacna1a^{Citrine}* and wild type C57BL/6J mice.

Primary Antibodies	Secondary Antibodies
Rabbit polyclonal Ca2+ channel *P/Q-type, a-1A subunit* - 152 203; 1:250 (Synaptic Systems GmbH)	Donkey anti-Rabbit Alexa Fluor™ 488 **Catalog #** A-21206; 1:200 (ThermoFisher Scientific)
Mouse monoclonal purified Bassoon antibody - 141 111; 1:1000 (Synaptic Systems)	Rabbit anti-Mouse Alexa Fluor™ 647 **Catalog #** A-21239, 1:200 (ThermoFisher Scientific)

Nanobodies
GFP - FluoTag-Q N0301-At647N-S; 1:300 (Synaptic Systems)
GFP - Booster Alexa Fluor® 488 gb2AF488-10; 1:500 (ChromoTek GmbH)

Table 2-1 List of antibodies and boosters used in the course of the study described in Chapter 4

Statistical Tools

CSD-derived Tuning curves

Tuning curves of layer-wise tone-evoked activity were centered on the BF response of each respective layer. Tuning curves were calculated for peak latencies and root mean square (RMS) values. Values were detected automatically when the sink activity crossed 1.5 standard deviation (STD) below the measured baseline activity. Candidate sink components were detected within each layer for an early time window (1-65 ms after tone onset) and a late time window (66-400 ms after tone onset). Based on the root mean square power, when the activity crossed 1.5 STD multiple times, the strongest sink activation was selected per time window.

Tuning curves of the AVREC CSD were centered on the BF of the granular thalamocortical sink (layer III/IV). Tuning features at the columnar level: RMS amplitude, peak amplitude, and peak latency, were calculated within the first 100 ms of tone presentation.

Repeated Measures ANOVA

A repeated measures Analysis of Variance (ANOVA) was calculated in Matlab on layer and AVREC tuning curves in Chapter 3 and on Vector Strength (see below) in Chapter 4. The repeated measures ANOVA is a tool to compare means across variables based on repeated observations and is used to determine causal relationships between independent and dependent variables. In the case of tuning curves in Chapter 3, this was performed with 2 factors: Groups and Frequencies, over 5 levels: tone frequencies centering octaves around the BF (-2 -1 BF +1 +2). Results determined if differences were significant due to—or dependent upon—groups, frequencies, or an interaction between those two. Post-hoc tests performed were Student's *t* tests and Cohen's d effect sizes (described below)

Single trial Student's *t* tests and Cohen's d

Student's *t* tests were calculated throughout this work at a single trial level. Single trial *t* tests are necessary to disentangle differences between groups on the basis of the natural variability within and between subjects, trial to trial. The logic of using these and the basis for trusting them is as follows. A more conservative method was considered first, such as repeated measures ANOVA or linear mixed model (LMM, see below), in order to gauge the basic shape of differences between or within groups. After determining that overall group differences existed at a high enough level to be picked up by these methods, the more sensitive *t* tests could be performed. To get a more conservative measure of these higher sensitivity differences, *t* tests were either subject to clustermass permutation (in the case of matrix comparisons, see below) or they were Bonferroni correct (*n* is stated with each test) and paired with Cohen's d Effect Size calculations. Cohen's d provides a measure of the magnitude of difference between the groups—or the strength of relationship of the dependent to independent variables. A Cohen's d effect size of medium, for example, would mean that ~70 % of one group fell below the other group's mean. *p* value results from single-trial *t* tests are thus best interpreted in conjunction with effect size results.

Continuous Wavelet Transform

Spectral analysis was performed in Matlab using the wavelet analysis toolbox function *CWT* (short for Continuous Wavelet Transform) for the following variables: animal, condition, stimulus, and recorded signal. Important parameters fed into the CWT were as follows: layer channels from CSD profiles, frequency limits: 5 to 100 Hz (below the Nyquist), and wavelet used: analytic Morse (Figure 2.7; Lilly & Olhede, 2012; Olhede & Walden, 2002).
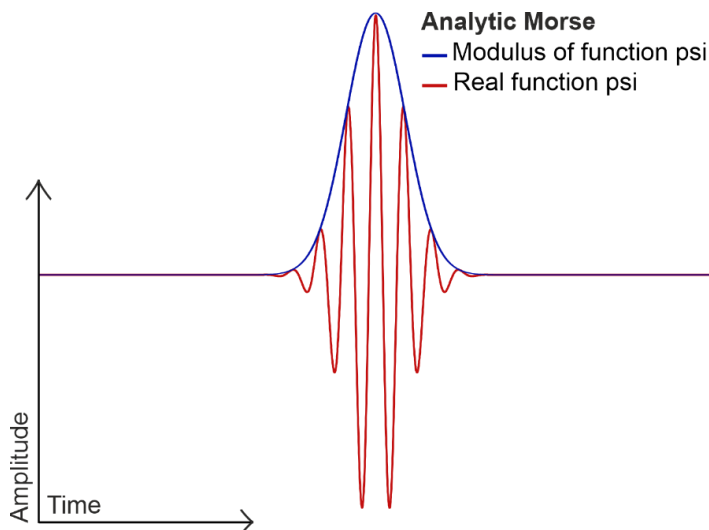
Figure 2.7 Morse wavelet; A common wavelet for continuous wavelet analysis on signal. This wavelet can be varied by two parameters to change time and frequency spread.

For layer-wise wavelet analysis, 3 channels centered on the middle channel of each layer were averaged and fed into the CWT. A trial-averaged scalogram was calculated for each cortical layer and wavelet magnitude—per frequency, per time point—for each subject with equation 2-5.

$$2\text{-}5)\quad \boldsymbol{Magnitude = |a + b_i|}$$

where a + b$_i$ represents the complex number output of the trial-averaged CWT analysis (Lachaux et al., 1999). Magnitude was calculated in Chapter 3 and Power was calculated in Chapter 4 with equation 2-6. The reason for this is that they are nearly the same metric and calculation, but power is conventionally used to show the strength of spectral response rather than magnitude, so we switched to power on later tests.

$$2\text{-}6)\quad \boldsymbol{Power = |a + b_i|^2}$$

Single trial scalograms were calculated for each animal as well and, on these, phase coherence—per frequency, per time point—for each subject was computed with equation 2-7:

$$2\text{-}7)\quad \boldsymbol{Phase\ coherence = |\frac{\Sigma^{(a+b_i)}/_{|a+b_i|}}{n}|}$$

Magnitude and phase coherence data were averaged pointwise (frequency and time bins were consistent across averages) for group plots. Clustermass permutations (as above) were performed for the difference between spectral representation in each layer at the BF and two octaves below (BF -2). Frequency bands were split as follows: theta 4-7 Hz, alpha 8-12 Hz, low beta 13-18 Hz, high beta 19-30 Hz, low gamma 31-60 Hz, and high gamma 61-100 Hz. For magnitude/power calculations: the test statistic for permutation was the student's t test and a Cohen's D matrix was generated to indicate effect size per frequency at each time point. For phase coherence calculations: the test statistic for permutation was the non-parametric Mann-Whitney-U (MWU; Cardillo, 2009; Maris et al., 2007) test and effect size, r, was indicated with the z score output as in equation 2-8:

$$2\text{-}8)\quad \boldsymbol{r = |\frac{z}{\sqrt{n}}|}$$

Clustermass permutation analysis

To compare matrix profiles (i.e., CSD profiles, scalograms from continuous wavelet analysis, and phase amplitude coupling result profiles (see below)), clustermass permutation analysis was performed. This test is specifically suited to control for a familywise error rate (FWER; cf. Groppe et al., 2011). The groups were averaged and then a difference was calculated for the observed matrices. We extracted a t (parametric) or u (non-parametric) statistic pointwise across matrices of groups. We selected a significance t or u threshold based on a two-tailed p-value < 0.05. Any statistic result at or above this significance threshold was converted to a 1 and anything below was converted to a 0—creating a binary matrix of 0s and 1s, where 1 is a possible point of significance in the comparison of those matrices. The 1s were then summed to create our observed clustermass value. Next, we permuted the groups 500 or 1000 times;

condition containers were created, equal to observed group sizes, and the matrices from both groups were combined and randomly allocated into those containers. The same point-wise statistic-and-threshold-calculated binary map was produced for each permutation with the total sum of 1s for each taken as a permutation clustermass value. This created a distribution of 500 or 1000 permutation clustermass values to which the observed clustermass could be compared. A p-value was calculated according to where the observed clustermass value fell onto the permutation distribution. A clustermass permutation test then tells us if the difference in the observed conditions is significant above chance—or put another way, it tells us how reliable the observed results are. This entire process was performed on full matrices, or within pre-selected regions of interest, such as layers, early and late sink components, spectral bands, etc. Note that phase coherence comparisons were non-parametric, MWU tests were calculated pointwise instead. Cohen's d or r (non-parametric) effect size was also calculated for each test.

Linear mixed models

After calculation of CSDs and traces for click train and amplitude modulation measurements in Chapter 4, the RMS was calculated along each trial trace within the time window: stimulus onset to 1000 ms / frequency presentation (200 ms for 5 Hz stim, 100 ms for 10 Hz stim). Peaks were also detected during this time window; highest peak prominence was selected as the relevant peak feature selected for that trial after it crossed an arbitrary threshold of peak prominence of at least 0.00008 (according to the findpeaks function in Matlab). This allowed us to exclude trials where no cortical activity after the stimulus onset was detected. RMS and peak amplitude features are comparable as metrics of cortical strength and therefore much of the analysis was computed with RMS.

Data was analyzed using LMMs due to the presence of repeated measurements within subjects which could be dealt with using a random effects structure. LMMs have several advantages, such as dealing with missing values and the ability to add various configurations of random effects, such as crossed or nested (Alday et al., 2017). For a full description of LMMs see Alday et al. (2017) and Harrison et al. (2018).

LMMs were implemented using R (version 3.6.1) and the *nlme* package (Pinheiro et al., 2021). The dependent variable, *RMS*, was log-transformed in order to meet the model assumptions (normality of residuals in particular). Independent categorical variables, *Group* (three levels: naive control, viral control, and treated) and *Measurement* (two levels: pre-laser and post-laser) were encoded using treatment coding and were added in the model with an interaction. The treated group post-laser measurement was selected as an intercept and each level of the categorical variables was compared to it (for example, naïve control group post-laser versus treated group post-laser). Separate models for each combination of signal frequency (5 Hz, 10 Hz) and layer (AVREC, I_II, IV, V, VI) were built in a following structure **2-9**:

$$\textbf{2-9)} \quad RMS \sim Group * Measurement + (\,1\,|\,Animal\,/\,TrialNumber\,)$$

where *Group* and *Measurement* are the fixed effects and *Animal* and *TrialNumber* are the random effects. Random effect for *Animal* controls for the assumption that each animal has a different baseline activity, while the rate of change (slope) is the same. Nested random effect (*Animal / TrialNumber*) controls for the dependence of trials for the same animal and assumption that observations between trials for the same animal are more similar to one another than to trials from the other animals. In this way, variability within the same animal carries less weight on the outcome.

Vector strength

To test for synchronicity of cortical activity to ongoing rhythmic stimuli, we computed vector strength. This was done by matching the latency of the most prominent peak in each time window across to the phase of the amplitude modulated signal at those time points. Each phase result was considered a unit vector with the orientation of the given phase. Vector strength was the resultant length of summing those unit vectors (c.f. Middlebrooks, 2008). This analysis was performed on the AVREC of each click train and amplitude modulation of 5 and 10 Hz in Chapter 4. Note that click trains do not have a phase; therefore, synchronicity of the click train results was calculated using the supposed phase of an amplitude modulated tone at those latencies. One 10-minute measurement was recorded pre-laser and four 15-minute measurement were recorded post-laser presentation wherein vector strength was calculated for each of them. With this, we compared the vector strength of groups and measurements as factors in a repeated measures ANOVA (see above).

Delta gamma cross frequency coupling

Low oscillation phase coupled to high oscillation amplitude has been implicated in information transfer across neural tissue (Bonnefond et al., 2017; Gourévitch et al., 2020). We performed cross frequency coupling (CFC) to determine if there were differences in the level of information transfer capacity between groups in Chapter 4. For each single trial, the center channel per layer was filtered for delta, low gamma, and high gamma. Instantaneous amplitude [A(t)] was taken for gamma bands and instantaneous phase [φ (t)] was taken for the delta band. At each repeated phase value, gamma amplitude was paired and averaged (for example, if a phase of 1 was reached 5 times, 5 amplitude values were found at those time points and averaged). A value, h, was assigned as the maximum minus the minimum amplitude of the generated distribution of averaged amplitudes over phase. Higher h would mean better coupling, wherein certain phases were associated regularly with higher amplitudes and other phases associated with lower amplitudes, making a greater distance between max and min. The observed h was compared against a surrogate distribution created by randomizing the filtered signals per trial and calculating h for each surrogate test. Where the observed h fell on this distribution, the z score was taken. z was averaged across groups for the final score and compared between and within groups pre- and post-laser. See Figure 4.11, placed in the results section for clarity in discussing implications. This analysis was conducted with both theta and delta for the low spectral frequency, but results were comparable. Therefore, only delta is shown in this work.

Phase amplitude coupling

Phase amplitude coupling (PAC) was calculated for each stimulus frequency and on spontaneous activity for groups in Chapter 5 per measurement, based on methodology by Kikuchi et al. (2017) and García-Rosales et al. (2020). LFP signals were filtered in the following low frequency bands with a 4th order bandpass Butterworth filter (Matlab function *filtfilt*): 1 to 3, 3 to 5, … 13 to 15 Hz. LFP signals were also filtered in the following high frequency bands: 25 to 35, 30 to 40, … 95 to 105 Hz. Hilbert transform was applied during the time window of stimulus presentation and, in the stimulus conditions, the average of across trials for the current stimulus and measurement was subtracted from the individual response of each trial to reduce the effect of stimulus-evoked cortical response. Instantaneous phase [φ (t)] for low frequencies and amplitude [A(t)] for high frequencies was then extracted.

To minimize the effect of phase non-uniformities (clustering) in the signal caused by non-oscillatory periodicities in the field potentials, the mean vector of the phase angles was linearly subtracted from the instantaneous phase time series with equation 2-10:

$$\textbf{2-10)} \quad \phi'(\text{t}) = e^{i\phi(\text{t})} - \frac{1}{n}\sum e^{i\phi(\text{t})}$$

where $\phi'(t)$ denotes the corrected (de-biased) phase at time t, and n represents the number of series time points. With $\phi'(t)$ and $A(t)$, a composite time series $z(t)=A(t) \times \phi'(t)$ was constructed. From $z(t)$, the modulation index (MI) was quantified with the following equation 2-11:

$$\textbf{2-11)} \quad \textbf{\textit{MI}} = |\frac{1}{n}\sum \textbf{\textit{z(t)}}|$$

PAC is susceptible to number of biases in how it is calculated and on the structure of the input signal. A direct comparison between species resulted in obviously extremely different MI scores across PAC calculations at different frequency pairings. We therefore also computed a surrogate MI by matching the phase series of a given trial with amplitude series of another trial and recalculating surrogate MIs (n = 500) to create a distribution against which we compared observed MI scores (see García-Rosales et al., 2020 Figure 3a). Observed MI scores were z-normalized to the surrogate distribution to obtain the z-scored MI (zMI). If no effect of PAC existed in the data, zMI values would hover around 0, whereas coupling effects would yield zMIs significantly higher than 0 (z-score > 2.5). These zMI values were then arranged into a matrix of high frequency amplitude over low frequency phase PAC pairings and these matrices were used for measurement-normalized comparisons between species over cortical layers. Direct species comparisons and region of interest (ROI) clustermap permutation tests were calculated where PAC appeared strongest per species.

Model fit analysis

In Chapter 5, a model fit analysis was performed on the averaged peak amplitudes after peak detection on measurement-averaged traces. Peak detection was calculated with the *nanmax* function in Matlab within detection windows after each stimulus in a presented stimulus train (e.g. for 5 Hz click stimulus, 5 peaks were detected—1 peak after each click). For each of the AVREC and layer trace peak amplitude datasets, 2 models were fitted: exponential decay seen in equation 2-12 and linear regression seen in equation 2-13.

$$\text{2-12)} \quad \boldsymbol{Exponential\ Decay = ae^{-b\,O} + c}$$

where $a + c$ is the intercept (the first observed peak amplitude), meaning a is depth or the distance between the first observed amplitude and c, b is the rate of decay (the greater the value, the steeper the decay), c is the offset (the value at which the model attenuates), and O is the order of peak amplitudes.

$$\text{2-13)} \quad \boldsymbol{Linear\ Regression = b_0 + b_1 O}$$

where b_0 is the intercept, b_1 is the slope, and O is the order of peak amplitudes. We used the function *minimize* from the Python SciPy package (Virtanen et al., 2020) to estimate the model parameters. The function used Broyden-Fletcher-Goldfarb-Shanno algorithm to minimize the root mean square error (RMSE), in equation 2-14:

$$\text{2-14)} \quad \textbf{RMSE} = \sqrt{\frac{\sum_{i=1}^{N}(y_i - \hat{y}_i)^2}{N}}$$

where y_i is the actual value, $\hat{y}_i$ is the estimated value by the model, and N is the number of data points. Model fits and detected peaks were then plotted with overlaid model parameters and RMSE value. Note that indexing in python meant the models started at index 0 but plotting starts at value 1 call or click.

Chapter 3: Ketamine anesthetized vs awake A1s

This is a summary, description, and expansion of the publication, *Ketamine anesthesia induces gain enhancement via recurrent excitation in granular input layers of the auditory cortex* by Deane et al. 2020. There is additional content but much of this chapter overlaps with the paper.

Background

Anesthesia induces wholistic changes to every scale of neuronal function. For the purpose of conducting surgeries or experiments on other parts of an organism, it is well-suited to reducing the risk of complications due to pain and conscious awareness. However, when studying the organ of conscious awareness, discussion of its use becomes more nuanced. Trade-offs are made and were heavily relied upon during seminal neurophysiological studies (e.g. Deweese and Zador 2003; Hubel and Wiesel 1959, 1962, 1965, 1969; Petersen et al. 2003): that the physiological recording from any brain region would be cleaner and clearer to understand, at the expense of real-world application and functional connection between regions. Research under anesthesia can be remarkably useful in teasing out parts of organs, circuits, processes, perception, or neuronal firing to understand them in a proverbial vacuum—as close to it as we can get. However, the whole is greater than the sum of its parts. While technical advances have increasingly allowed us to explore the physiology of cortical functions in awake and behaving animals, more could be known about the functional change in anaesthetized states, particularly with respect to the interaction between external stimuli and intrinsic cortical dynamics (Pachitariu et al., 2015).

My Master's thesis was written on a comparison between ketamine-anesthetized and awake, passively listening Mongolian gerbils (*Meriones unguiculatus*). The first year of my PhD, while organizing the project set out in Chapter 4, was spent further investigating the effects of ketamine on the auditory cortex and the implications this would have on research conducted under its influence. Ketamine is an N-methyl-D-aspartate (NMDA) receptor antagonist, which enters the open receptor channel, inhibiting ionic exchange (Anis et al. 1983; MacDonald et al. 1987), and it is a commonly used anesthesia for neurophysiological experiments. It has more recently gaining ground as an optimistically effective treatment for chronic depression at subanesthetic doses (Murrough et al., 2013). It is a World Health Organization approved anesthetic for surgical intervention in humans but does have the side effect of unsettling hallucinations (Marland et al., 2013) and it is used as an illicit recreational drug—albeit at hopefully lower doses—for that side effect. A main effect of ketamine in the brain, is the persistent increase in cortical glutamate which renders cells more excitable (Miller et al. 2016; Zhang et al. 2019). This induces high stimulus-locked excitability in the cortex. One mechanism thought to enact this is the disinhibition of the cortex through biased suppression of Parvalbumin- (PV-) releasing GABAergic interneurons (Behrens et al., 2007; Homayoun & Moghaddam, 2007; Miller et al., 2016; Schobel et al., 2013). Some single and multi-unit studies using ketamine anesthesia have also specifically implicated a lack of inhibitory modulations from supragranular populations to cortical recurrent excitation (Kato et al. 2017; Wehr and Zador 2003). What was needed, then, was a functional circuit level understanding of the effects of ketamine at anesthetic levels to support such a hypothesis.

We sought to provide this by comparing tone-evoked current source density (CSD) distributions in the awake and ketamine-anesthetized (15mg kg^{-1}/h i.p.) gerbils. Recordings

were taken from the primary auditory cortex (A1) using a chronically, in the case of awake animals, or acutely inserted 32-channel tungsten electrodes. Continuous local field potentials were recorded down the depth of the A1 and later converted to CSD profiles to provide a spatiotemporal map of cortical response pattern to auditory stimuli. Profiles were further analyzed on the average rectified signal, the layer sinks, or areas of population activity, and through spectral continuous wavelet analysis.

Overall, we found that the spatiotemporal flow of tone-evoked activity in the A1 was very comparable across both conditions, demonstrating that previously observed cortical population activity is largely conserved in under ketamine (Luczak & MacLean, 2012). Despite this, there were key differences in layer contributions to the overall cortical response. Particularly in granular layers III/IV, ketamine led to a significant frequency-specific gain increase by a multiplicative, rather than additive, intracortical amplification (cf. Ferguson and Cardin 2020). While signal strength increased, peak latencies were shorter, and less variable compared to the awake cortex – indicating higher synchrony of tone-evoked cortical inputs. With a continuous wavelet analysis, we further revealed that ketamine increased the time duration of phase coherence but not its strength at the time-point of cortical response, especially in the granular layer, and that it significantly increased the broadband spectral magnitude in this layer. We surmise, in agreement with proposed hypothesis, that due to the disproportionate inhibition of PV-interneurons under ketamine anesthesia, recurrent excitation in layer IV is allowed to run rampant through the mechanism of cortical disinhibition. This increases the spectral response across all frequencies due to the almost artificial strength and veracity of response in this layer and an echoing phase coherence in a highly synchronized micro-circuit with ineffective mitigation.

Results of project 1

An altered spatiotemporal profile in the A1 induced by ketamine anesthesia

We compared the tone evoked laminar CSD profiles in the A1 of Mongolian gerbils under three conditions in two subject groups. The CSDs, shown in Figure 3.1, expose spatiotemporal current flow in cortical depth over time—wherein blue areas, sinks, correspond to population activity. The first group (n=9) was awake with a chronically implanted laminar probe, passively listening to pure tones while freely moving in a small field (Figure 3.1A). The second group (n=11) was anesthetized with ketamine-xylazine (Figure 3.1B) and then had its cortices silence by topical application of GABA$_A$-agonist, muscimol (Figure 3.1C). For awake and anesthetized conditions, CSD profiles share the classic characteristics of the spatiotemporal flow of sensory information across cortical layers in line with previous findings (Atencio & Schreiner, 2010; Barth & Di, 1990; Sakata & Harris, 2009; Steinschneider et al., 1992, 1998; Szymanski et al., 2009). Around 15-20 ms after tone onset, an initial sink component appeared in granular layers III/IV as well as infragranular layers Vb and VIa, originating from thalamocortical projections to the A1 (Happel et al., 2010). From there, synaptic population activity propagated to supragranular and infragranular layers, yielding later sink components (Atencio & Schreiner, 2010; Chen et al., 2007; Sakata & Harris, 2009; Schroeder et al., 1998). Best frequency (BF) was then determined, based on the tonotopic nature of the auditory pathway, to be the tone with the most robust thalamocortical activation response (Happel et al., 2010; Metherate et al., 2005).

In order to disentangle thalamic input to the cortex from further corticocortical processing, muscimol was applied topically to the auditory cortex following precedent set in our lab by Happel et al. (2010). Muscimol functionally silences all intracortically generated activity in the cortex by increasing the supply of GABA$_A$ to the local circuitry. The thalamocortical input generates short sinks in granular and infragranular layers (Figure 3.1C) because extracellular, subthreshold activity still reflects the input from distanced, unaffected midbrain circuits regardless of local inhibition, which then discontinued further processing. Therefore, the strength of the early granular sink activity is strongly reduced and shorter under muscimol, inversely reflecting the strong intracortical amplification of early thalamic input under ketamine.

Overall, Figure 3.1A and B reveal a comparable spatiotemporal pattern of auditory-evoked responses with respect to the order of current sinks across layers and time in awake and under ketamine anesthesia. Figure 3.1C shows a consistent granular and a slightly varied infragranular thalamocortical input between BF and off-BF frequencies (2 octaves below) and confirms immediate intracortical processing directly after thalamocortical input. In the awake condition, CSD profiles reveal a weaker and spatially narrower early granular sink component and more temporally spread supragranular and infragranular sink components. Figure 3.1D shows a diagram of hypothesized granular recurrent excitation effects corresponding to CSD profiles which will be supported by following results.
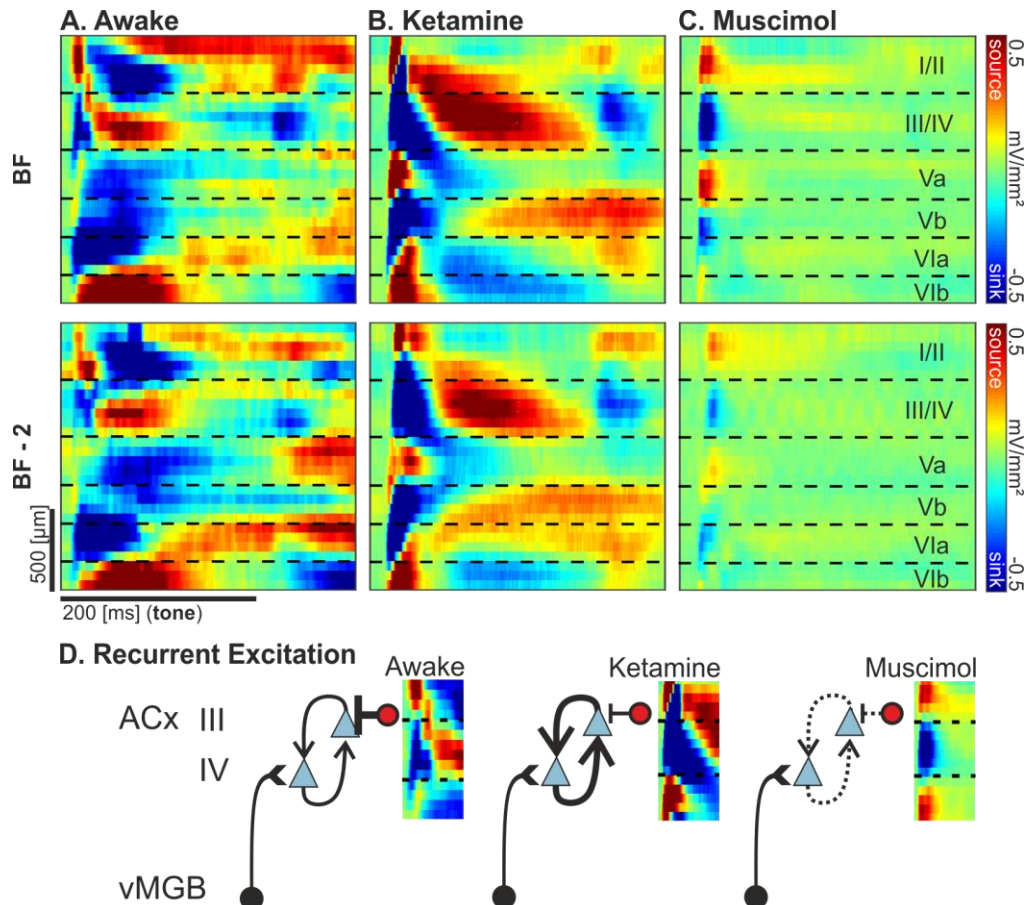
Figure 3.1 Grand average current-source density profiles. For BF and BF-2 below in **A:** awake, **B:** ketamine, and **C:** muscimol conditions (n=9, n=11, and n=11, respectively). Top, Best frequency response. Bottom, Response 2 octaves below the best frequency. The CSD profiles show the pattern of temporal processing (ms) within the cortical depth (μm). Representative layer assignment is indicated with horizontal dashed lines. Pure-tone stimuli were presented for the first 200 ms. Current sinks (blue), represent areas of excitatory synaptic population activity, while current sources reflect balancing currents (cf. Happel et al., 2010). **D:** Diagram of the potential contribution of cortical recurrent excitation in layers III/IV and its presumed balance differences in each of the 3 tested conditions. Figure and caption taken from Deane et al. 2020.

Spatiotemporal differences between the awake and ketamine groups (Figure 3.2A) were compared via a clustermass permutation test (Figure 3.2B, Table 3-1), where significant results in a point-wise Student's *t* test between groups counted toward an overall "clustermass" count and the observed clustermass result was compared against a distribution of permuted test results (n=1000) with randomized subjects into each group per permutation. A comparison of the entire CSD profile between groups showed that there was a significantly higher clustermass in the observed measurements than in the permutation distribution, for both BF and off-BF. This pointed to a reliable difference between groups above chance. An analysis of cortical layer activity, in both early (1 to 100 ms) and late (101 to 300 ms) sink components, separately reveals that activation in layer III/IV is highly significantly different across conditions. There is also significant difference between early I/II and VIa sink components at the BF and VIa and late Vb sink components off-BF. Early Vb is comparable across groups, as are late sink components in the BF and supragranular layers off-BF. Table 3-1 shows the consistency of these results across frequencies above and below the BF but shows that the late infragranular significant difference is only found at BF − 2 octaves. This permutation test validates that further statistical methods are unlikely to be randomly produced, especially in the highly significantly different granular layer.
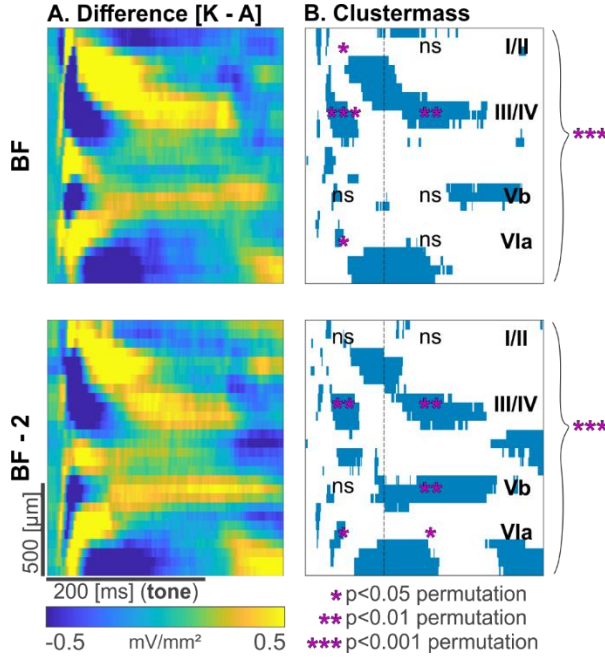
Figure 3.2 CSD clustermass permutation test. A: The difference (ketamine - awake) between the grand averaged CSD profiles for BF and BF − 2 octaves. **B:** Observed clustermass of significant differences (p<0.05) are plotted in blue (verified by a two-sample Student's *t* test). Permutation test results (*=p<0.05, **=p<0.01, ***=p<0.001) are indicated by magenta asterisks. Comparisons of the permutation test have been performed for early (1-100 ms) and late (101-400 ms) signals on a layer-wise (I/II, III/IV, Vb, VIa) and columnar level (indicated by braces on the right side). Figure and caption taken from Deane et al. 2020.

CSD permutation *p* values

	Full CSD	I/II early	III/IV early	Vb early	VIa early	I_II late	III/IV late	Vb late	VIa late
-2	**0**	**0.046**	**0.003**	0.104	**0.028**	0.479	**0.005**	**0.005**	**0.022**
-1	**0**	**0.036**	**0.001**	0.099	**0.002**	0.234	**0.002**	0.056	0.15
BF	**0**	**0.023**	**0.001**	0.156	**0.017**	0.152	**0.002**	0.102	0.077
1	**0.001**	0.116	**0**	0.13	**0.014**	0.087	**0.007**	0.263	0.06
2	**0.006**	**0.016**	**0.001**	0.127	0.115	0.075	0.111	0.245	0.115

Table 3-1 CSD permutation test results. A comparison between ketamine and awake group CSD profiles via a clustermass permutation test. *p* is bold where the observed clustermass in the region of interest (Full and early and late sink components across layers) was significantly above the permutation distribution generated with randomizing subjects into groups and calculating clustermass 1000 times. Results shown for the BF and +/- 1 and 2 octaves from the BF.

We sought to clarify internal consistency within the condition groups through a single condition permutation test (**Figure 3.3**). We calculated a clustermass permutation test on each group individually by splitting them in half and randomizing measurements into each half-bin. There were almost no clustermass counts found above chance, attesting to a level of internally stable variability in the groups. The significant effects in the permutation test described above can therefore be attributed to differences across the groups, and not within.
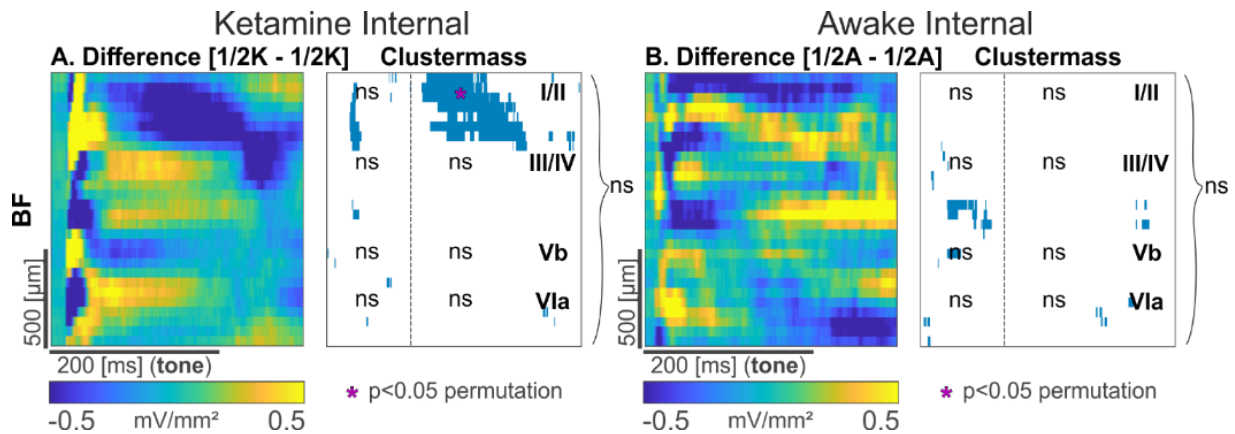
Figure 3.3 Permutation Clustermass Test within groups. The clustermass test was accomplished by splitting each group in half to test against itself. **A**: Difference plot (left) of half of the ketamine group against itself and observed clustermass of significant differences (right, p<0.05) are plotted in blue (verified by a two-sample Student's t test). Permutation test results (*=p<0.05, ns=not significant) are indicated by magenta asterisks or text. **B**: Difference plot of half of the awake group against itself and observed clustermass plot overlaid with permutation clustermass test results. Specific p value results not shown.

Foundation of muscimol silencing in the cortex

The topical application of the GABA$_A$-agonist muscimol on the cortical surface to induce silencing of intracortical synaptic activity has been introduced and quantified by Edeline et al. (2002) and used by Kaur et al. (2004). Happel et al. (2010) combined this approach with CSD analysis for the first time and connected residual current sink activity after intracortical silencing to the isolated thalamocortical inputs in cortical layers III/IV. In the current study, we tracked the temporal diffusion of muscimol across all cortical layers by a time-binned analysis of CSD distributions after topical application (Figure 3.4; see Figure 1 in Happel et al. 2010). The example subject shown in Figure 3.4 corroborates previous findings and indicates reproducibility of this silencing approach. Silencing was typically accomplished within 45 minutes and left behind only thalamocortical input sinks, as previously described.
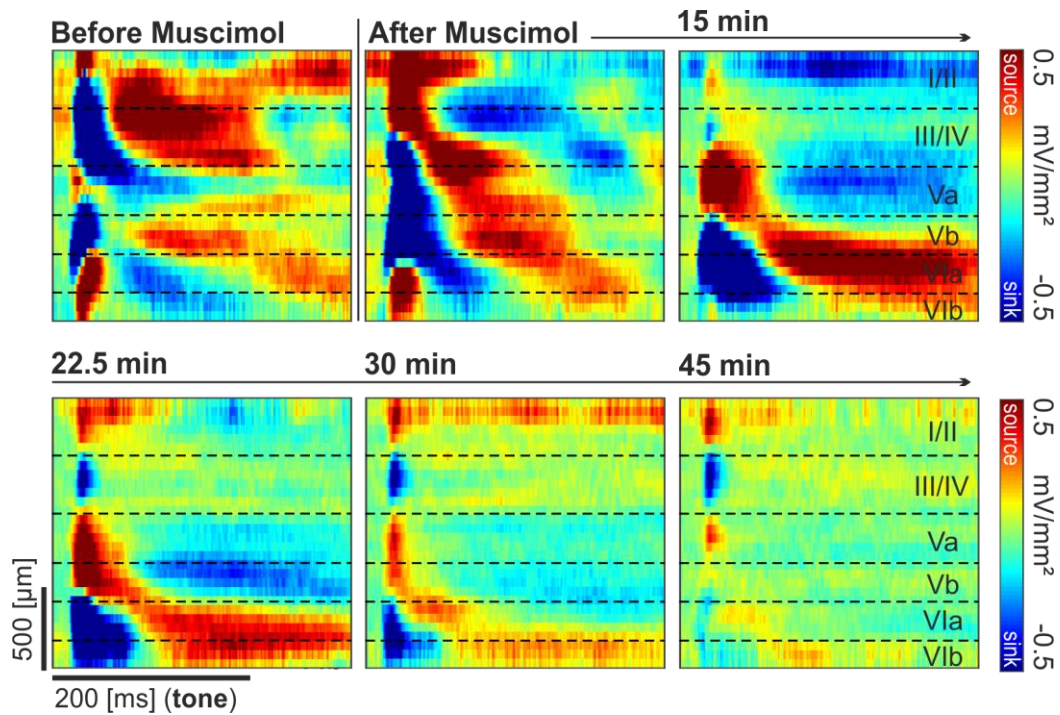
Figure 3.4 Single subject CSD over muscimol silencing. Tonotopic measurements of 50 trials each take 7.5 minutes. Consecutive measurements were trial-averaged up to the 45 minute mark for this subject. At 45 minutes, this CSD profile indicated that muscimol had sufficiently diffused through the A1 and the measurement was taken for comparison with the other two conditions. Per subject, 30 to 45 minutes was needed to see full muscimol diffusion.

Ketamine strengthens stimulus-locked activity by reduced temporal variability of tone-evoked input

The CSD profiles of all three groups indicated temporal differences in tone-evoked activity (Figure 3.1). To explore this, we compared the grand-averaged AVRECs (Figure 3.5A) as a measure of the temporal, columnar current flow per group. Ketamine-anesthetized subjects showed stronger AVREC onset response peaks, during the first 100 ms of tone stimulation. This is indicative of a more stimulus-onset-locked activation of the cortical microcircuitry. Muscimol reduced the response strength but demonstrated a similar pattern of time-locking with BF stimulation. Stimulation with frequencies 2 octaves apart from the BF generated only a slightly detectable tone-evoked component in the muscimol condition. Awake subjects showed a broadened response after stimulation with both the BF and the off-BF. In order to quantify these effects, we further calculated AVREC tuning parameters at a single-trial level (Figure 3.5B, ANOVAs in Table 3-2, t and Cohen's d in Table 3-3). Consistently, under ketamine, single-trial peak amplitudes were significantly higher compared to the awake group for all stimulation frequencies (Figure 3.5B, *left*), showing at least a Medium Cohen's d effect size across each.
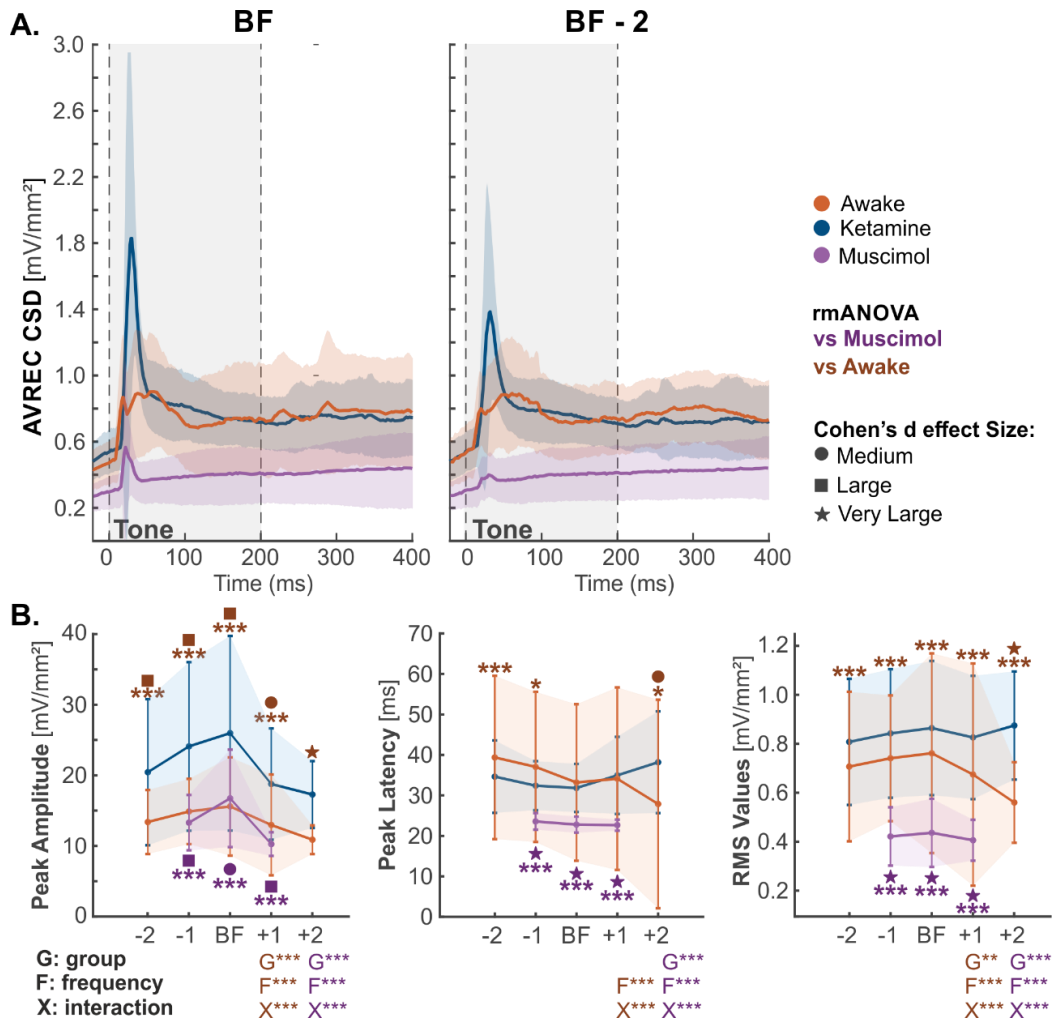
Figure 3.5 Group-wise comparison between columnar tuning properties. A: A window of 1-100 ms was selected to detect for the most prominent peak within each single trial and the latency and height of that peak was taken for each group (orange: awake, n=9; blue: ketamine, n=11; purple: muscimol, n=11). Shown are the grand-averaged AVREC CSD (± standard deviation (STD)) traces for stimulation with the BF (left) and BF -2 octaves (right). **B:** Tuning curve (±STD) of mean peak amplitude (left), mean latency (middle), and the mean RMS of the AVREC trace between 1-100 ms (right). Statistical results are a repeated measures ANOVA, showing group (G), frequency (F), or interaction (X) effects between both ketamine vs. awake (dark orange), or ketamine vs. muscimol (dark purple). * =p<0.05. ** =p<0.01, *** =p<0.001. Cohen's d indicates effect sizes with a circle for Medium, a square for Large, and a star for Very Large. A group effect size was also calculated for each stimulus bin. Confidence intervals indicate the standard deviation. Figure and caption taken from Deane et al. 2020.

	Peak Amplitude			Peak Latency			RMS		
	G	F	X	G	F	X	G	F	X
Ket vs Awake	**0**	**0**	**0**	0.073	**5.02E-08**	**1.14E-05**	**1.06E-12**	**1.64E-03**	**9.76E-11**
Ket vs Musc	**0**	**0**	**0**	**8.71E-07**	**0**	**1.67E-05**	**0**	**3.86E-07**	**0**

Table 3-2 Repeated measures ANOVA results table for AVREC tuning curves. Group (G), frequency (F), and interaction (X) results for ketamine vs awake and ketamine vs muscimol comparisons of the peak amplitude and latency and RMS of the first 100 ms of tone presentation. In bold are significant results where p<0.05.

Ketamine vs Awake

		-2	-1	BF	1	2
Peak Amp	p	**4.44E-16**	**0**	**0**	**1.63E-06**	0.151
	Cohen's d	**-0.80**	**-0.88**	**-0.88**	**-0.75**	**-1.39**
Peak Lat	p	**5.17E-04**	**0.021**	0.262	0.850	**0.030**

		-2	-1	BF	1	2
RMS	Cohen's d	0.34	0.42	0.11	-0.06	**-0.75**
	p	**2.08E-08**	**8.69E-09**	**1.05E-07**	**2.80E-05**	**0.036**
	Cohen's d	-0.37	-0.39	-0.31	-0.49	**-1.45**

Ketamine vs Muscimol

		-2	-1	BF	1	2
Peak Amp	p	~	**0**	**0**	**3.99E-11**	~
	Cohen's d	~	**-0.98**	**-0.72**	**-1.14**	~
Peak Lat	p	~	**0**	**3.33E-15**	**6.43E-10**	~
	Cohen's d	~	**-1.58**	**-1.65**	**-1.36**	~
RMS	p	~	**0**	**0**	**3.19E-11**	~
	Cohen's d	~	**-1.72**	**-1.67**	**-1.75**	~

Table 3-3 Post-hoc single trial tests for AVREC tuning curves. p value and Cohen's d effect size results shown for ketamine vs awake and ketamine vs muscimol comparison of the peak amplitude and latency and RMS of the first 100 ms of tone presentation. In bold are significant results where p<0.05 and Cohen's d results of at least Medium d>0.5.

The higher overall AVREC peak amplitude, narrower peak latency SEM, and small Cohen's D of RMS activity under ketamine anesthesia might be explained by a more synchronized recruitment of synaptic circuits. We therefore hypothesized that the variance of evoked amplitudes would be higher under ketamine-anesthesia, while response peak latencies would be more distributed in awake recordings. We applied a Brown-Forsythe test of variance to characterize noticeable differences in the variance of latency and amplitude of the peaks of each group (Figure 3.6A, results in Table 3-4). Under ketamine-anesthesia, there is a significantly larger variance in peak amplitude compared to both awake (p<0.001) and with muscimol (p<01; Figure 3.6B). Conversely, awake subjects had significantly higher variance at peak latencies (p<0.001; Figure 3.6B). This analysis accounts for the temporally broader shape of the averaged AVREC responses in the awake condition compared to ketamine-anesthetized subjects exhibiting a more stimulus-locked pattern of activity.
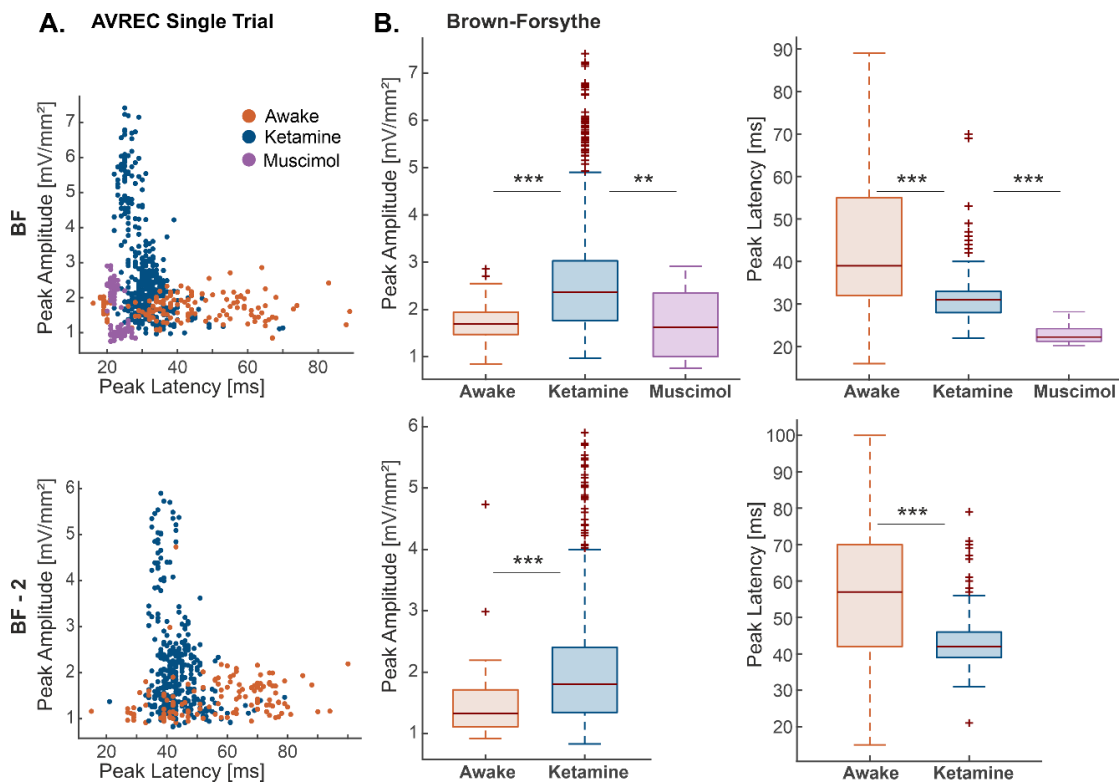
Figure 3.6 Brown-Forsythe test of variance for peak amplitude and latency. A: Single trial scatter plots of amplitude against latency of detected AVREC CSD peaks at BF (top) and BF -2 (bottom). **B:** Brown-Forsythe variance plotted as boxplots for awake (orange, n=9), ketamine (blue, n=11), and muscimol (purple, n=11) groups for peak amplitudes (left) and latencies (right). Boxes represent the 25%-quartiles, the bar represents the median, and whiskers represent the full range of data except outliers plotted as crosses. Note that cortical silencing via muscimol reduces measurable activity in non-BF stimulations. *** = p<0.001, ** = p<0.01. Figure and caption taken from Deane et al. 2020.

	Ket vs Awake		Ket vs Musc	
	p value	brown-forsythe stat	p value	brown-forsythe stat
BF Amplitude	**0**	62.0733	**0.0025**	9.2022
BF - 2 Amplitude	**0**	32.2621	~	~
BF Latency	**0**	240.849	**0**	25.2682
BF - 2 Latency	**0**	258.554	~	~

Table 3-4 Brown-Forsythe test of variance results for AVREC. p value and brown-forsythe (F) results shown for ketamine vs awake and ketamine vs muscimol comparisons of variance for peak amplitude and latency at the BF and BF – 2 octaves. In bold are significant results where p<0.05.

Ketamine-induced gain increase is due to amplitude-effects on granular input layer activity

To identify the source of the overall columnar differences, laminar tuning curves were calculated for RMS and peak amplitude and latency parameters of detected current sinks for each animal at thalamocortical input layers III/IV, Vb, and VIa, and supragranular layer I/II (Figure 3.7). Peak amplitude and RMS were both analyzed but, at the layer sink level, they were nearly identical in their results; therefore, only RMS is shown. Note that the muscimol group is not present in the supragranular layer due to lack of sink detection in silenced cortices.

The main effect on the evoked peak amplitude described for the AVREC waveform was reflected by the strength of the granular input layer. Here, ketamine anesthesia also led to an increase across all stimulation frequencies compared to the awake group, shown with a repeated measures ANOVA significant group effect (Table 3-5 contains all ANOVA results and Table 3-6 contains all stimulus frequency Cohen's d comparison results). Infragranular layers Vb and VIa showed no clear difference of the evoked RMS value between groups (Figure 3.7A). In contrast, the longer peak latencies of the AVREC waveform were reflected mainly in the temporal activity of supragranular layers. Peak latency comparisons in this layer had large or very large effect sizes for most stimulation frequencies (Figure 3.7B). Peak latencies of other sink components show only minor differences. This analysis of layer-specific sink activity reveals that the main drive for the time-locked columnar activity and higher peak amplitudes under ketamine is a strong excitation in cortical input layers III/IV. The increase of layer III/IV RMS value appears to be mostly a modulation of gain paired with only a minor difference in tuning sharpness between the awake and ketamine group. In order to reveal the frequency-specificity of such multiplicative gain, we calculated RMS values of current sink activity measured in individual layers binned for stimulation frequencies with 1 or 2 octaves distance to the BF and normalized to the BF response strength (Figure 3.7C). Sink activity in cortical layers I/II, III/IV, and Vb showed a corresponding frequency-specific gain increase. Repeated measures ANOVA results reflected a significant group difference only in the granular layer.
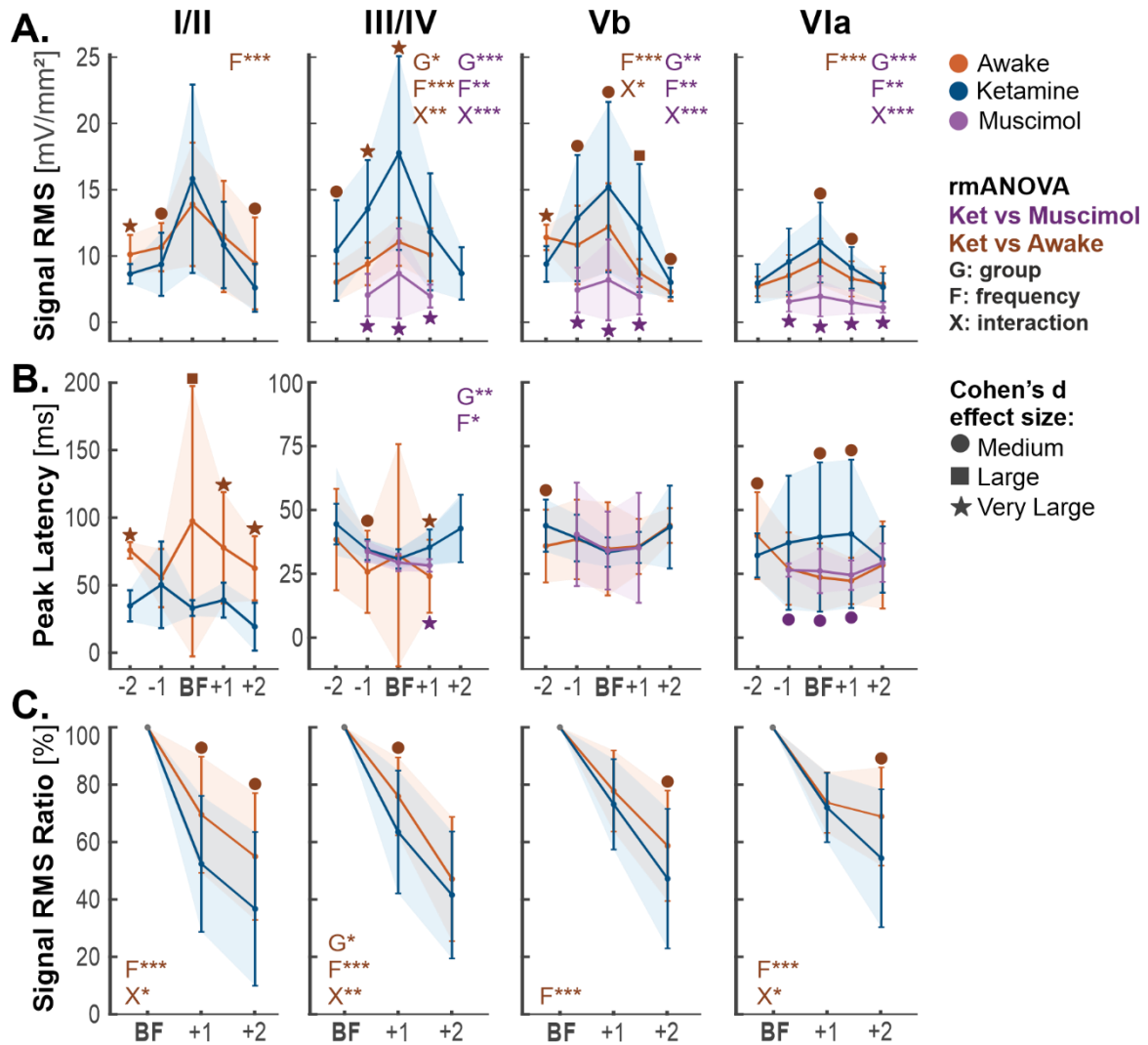
Figure 3.7 Early sink tuning curves. Tuning curves (±STD) of semiautomatic detected sink activity within each layer sorted according to the layer-wise BF tuning for each subject (orange: awake, n=9; blue: ketamine, n=11; purple: muscimol, n=11). **A:** Tuning curves of the layer-specific mean RMS values. **B:** Mean latency of the peak amplitude. **C:** Mean RMS values measured in individual layers were binned for stimulation frequencies with 1 or 2 octaves distance to the BF and normalized to the BF response strength. Statistics are based on an rmANOVA, which shows group (G), frequency (F), or interaction (X) effects between both ketamine vs. awake (dark orange), or ketamine vs. muscimol (dark purple). * =p<0.05. ** =p<0.01, *** =p<0.001. Cohen's D indicates effect sizes with a circle for Medium, a square for Large, and a star for Very Large. Confidence intervals indicate the standard deviation. Figure and caption taken from Deane et al. 2020.

		RMS			Peak Latency			Normalized RMS Ratio		
	Layer	G	F	X	G	F	X	G	F	X
Ket vs Awake	I/II	0.109	**4.87E-06**	0.073	**0.038**	0.259	0.475	**0.03**	**3.52E-08**	**0.014**
	III/IV	**0.023**	**3.47E-05**	**0.002**	0.139	**0.0095**	0.402	**0.043**	**9.60E-08**	**0.046**
	Vb	0.595	**3.51E-07**	**0.046**	0.503	0.182	0.607	0.191	**5.37E-09**	0.115
	VIa	0.858	**8.12E-06**	0.125	0.175	0.279	0.297	0.595	0.045	0.386
Ket vs Musc	I/II	**0.031**	**1.09E-04**	**0.0006**	0.215	0.12	0.741	**0.01**	**1.20E-06**	**0.001**
	III/IV	**0.0006**	**2.76E-03**	**2.84E-06**	**0.014**	**0.0023**	0.619	0.085	**5.18E-08**	0.051
	Vb	**0.004**	**9.09E-03**	**6.10E-05**	0.80	0.315	0.4	**0.006**	**7.63E-06**	**0.001**
	VIa	**0.0008**	0.055	**1.63E-05**	0.153	0.31	0.291	0.3	0.401	**0.046**

Table 3-5 Repeated measures ANOVA results table for sink tuning curves. Group (G), frequency (F), and interaction (X) results for ketamine vs awake and ketamine vs muscimol comparisons of the sink RMS, peak latency, and normalized RMS ratio of early sinks (starting before 100 ms of tone presentation). In bold are significant results where p<0.05.

Sink RMS Cohen's d

		-2	-1	BF	1	2
Ket vs Awake	I/II	**-1.36**	**-1.63**	0.13	**-0.76**	**-0.93**
	III/IV	**0.76**	**1.23**	**1.43**	**0.94**	~
	Vb	**-1.58**	0.15	0.45	0.43	0.25
	VIa	~	0.25	0.13	0.16	**-0.76**
Ket vs Musc	I/II	~	~	**1.72**	**1.20**	~
	III/IV	~	**2.17**	**1.96**	**1.80**	~
	Vb	~	**1.70**	**1.78**	**1.70**	~
	VIa	~	**2.08**	**2.41**	**2.50**	~

Peak Latency Cohen's d

		-2	-1	BF	1	2
Ket vs Awake	I/II	**-2.34**	**-2.23**	-0.24	**-1.84**	**-2.10**
	III/IV	**1.72**	**0.50**	0.39	0.44	~
	Vb	**1.26**	0.09	0.164	0.33	-0.03
	VIa	~	0.32	**0.77**	**1.02**	**0.60**
Ket vs Musc	I/II	~	~	-0.41	-0.28	~
	III/IV	~	**0.93**	0.35	**1.12**	~
	Vb	~	0.01	0.38	-0.26	~
	VIa	~	**0.54**	**0.65**	**0.63**	~

Normalized Sink RMS Ratio Cohen's d

		-2	-1	BF	1	2
Ket vs Awake	I/II	-0.46	**-1.05**	~	**-1.60**	**-2.12**
	III/IV	0.27	-0.18	~	**-1.20**	~
	Vb	-0.48	-0.23	~	-0.42	**-0.60**
	VIa	~	**-0.62**	~	**0.59**	-0.34
Ket vs Musc	I/II	~	~	~	**-1.18**	~
	III/IV	~	**0.64**	~	-0.18	~
	Vb	~	0.33	~	0.04	~
	VIa	~	0.44	~	0.25	~

Table 3-6 Single trial Cohen's d tests for sink tuning curves. Cohen's d effect size results shown for ketamine vs awake and ketamine vs muscimol comparison of the sink RMS, peak latency and normalized RMS ratio of early sinks (starting before 100 ms of tone presentation). In bold are Cohen's d results of at least Medium d>0.5.

Spectral magnitude was stronger and phase coherence was longer in the granular layer

To differentiate effects of amplitude and phase-locking on the described gain increase under anesthesia, we conducted continuous wavelet analysis at a laminar level (BF magnitude in Figure 3.8 and BF phase coherence in Figure 3.10). Overall, the spectral magnitude in granular layers III/IV revealed the highest difference between both groups with a broadband— across all spectral bands—increase in magnitude in the ketamine group for BF stimulation (Figure 3.8A, Table 3-7). This broadband significant increase between ketamine anesthetized and awake CSD scalograms was not present in the same capacity at BF - 2 octaves in layer IV (Figure 3.9, Table 3-7), indicating more similar spectral magnitudes for both groups at frequencies off of the BF. The significant increase in magnitude for BF stimulation was revealed by a high Cohen's D effect size area and with significant permutation clustermass test results for all spectral frequencies: from theta (4-7 Hz) to high gamma (60-100 Hz). The nature of this broadband magnitude increase in cortical layers III/IV induced by ketamine is consistent with the immediate recruitment of synaptic activity indicating stimulus-locked gain increase. In other layers, magnitude effects were less pronounced. In Figure 3.8B, the supragranular I/II and infragranular VIa clustermass permutation tests revealed no areas of

significant magnitude increase above chance. Layer Vb shows an increase across low beta and low gamma.

In conjunction, we analyzed single trial phase coherence for the corresponding individual layer-wise CSD traces (Figure 3.10, Table 3-7). While ketamine increased the stimulus-induced magnitude most prominently at stimulus onset, its effects on phase coherence were mainly surrounding the time of stimulus-induced columnar response. A corresponding broadband increase in phase coherence across all spectral frequencies as well as a strong increase in the lower beta range proceeded during stimulus presentation above chance according to permutation (Figure 3.10A). Phase coherence was also significantly increased above chance in layers I/II, Vb, and VIa across spectral frequencies (Figure 3.10B). However, the shape of clustermass significance and Very Large Cohen's d results was the most remarkable in layer IV. From high beta to high gamma spectral bands, the difference between awake and ketamine anesthetized subjects is not significant around the time of stimulus transmission to the A1 (~15-20 ms). Yet phase coherence is increased across a wider timescale and in lower spectral frequencies under anesthesia. Infragranular layers echo but do not fill out this shape in relationship between conditions. This indicates that phase coherence for higher spectral frequencies is comparable in awake brains during onset tone processing, but that phase coherence is maintained over a broader spectral and temporal area under ketamine due to the unmitigated recurrent excitation.
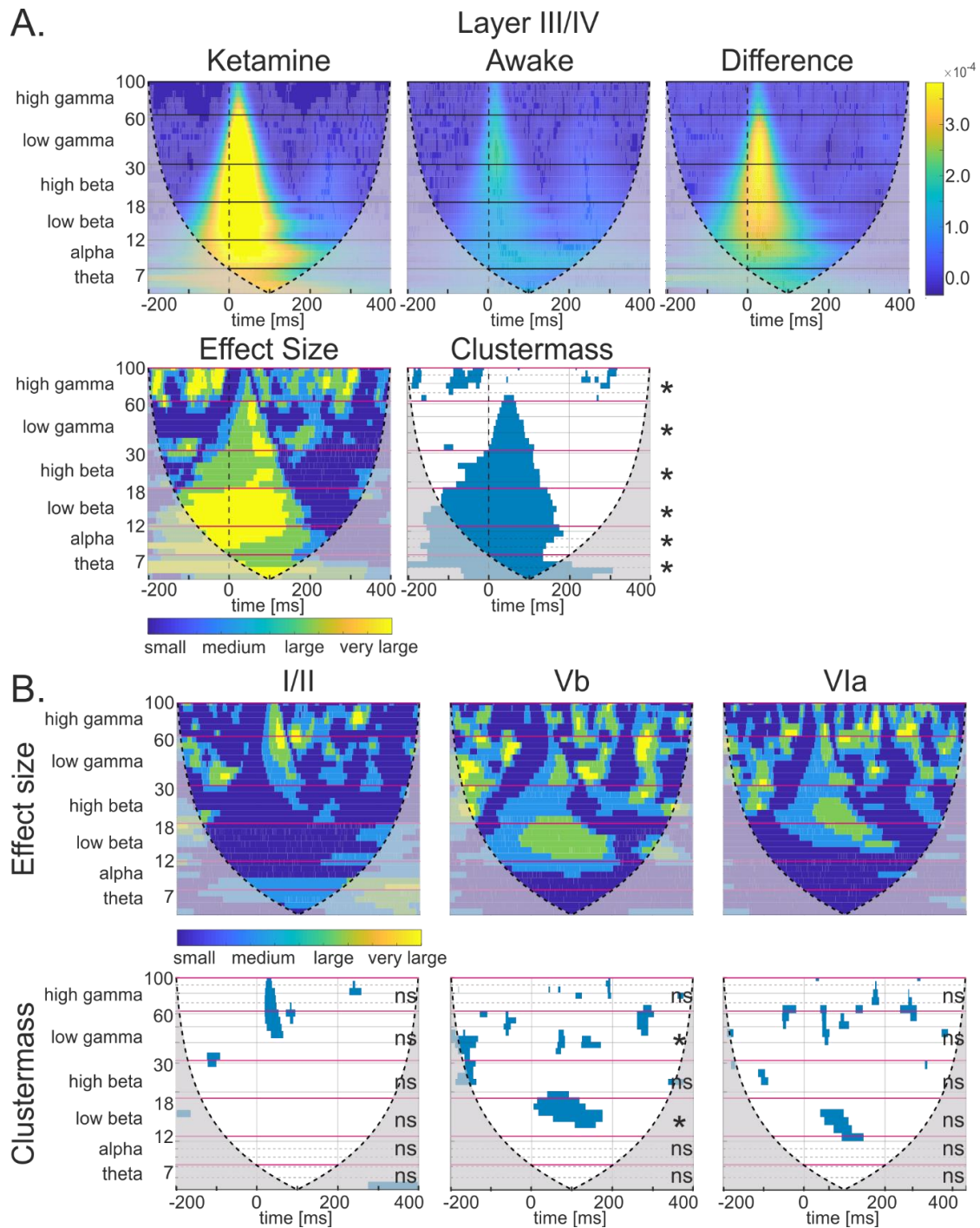
Figure 3.8 Magnitude scalograms of continuous wavelet transform and analysis from trial-averaged subject CSD profiles. A: BF response of layer III/IV; scalograms of ketamine group (left, n=11), awake group (middle, n=9), and the absolute difference between both groups (right); Effect size (Cohen's D) matrix showing small through very large effect size and clustermass matrix showing significance below p<0.05 (verified by two-sample Student's t test). Magenta lines indicate binning borders of frequencies for wavelet analysis and permutation test (left, *=p<0.05, **=p<0.01, ***=p<0.001, or ns=not significant) of the clustermass. **B:** Effect size (Cohen's D) matrix, clustermass matrix, and permutation test results for layers I/II, Vb, and VIa at their respective BF. All graphs show the cone of influence overlaid as a dashed line and muted areas which extend outward. This shows where the wavelet transform was likely affected by boundary conditions. Figure and caption taken from Deane et al. 2020.
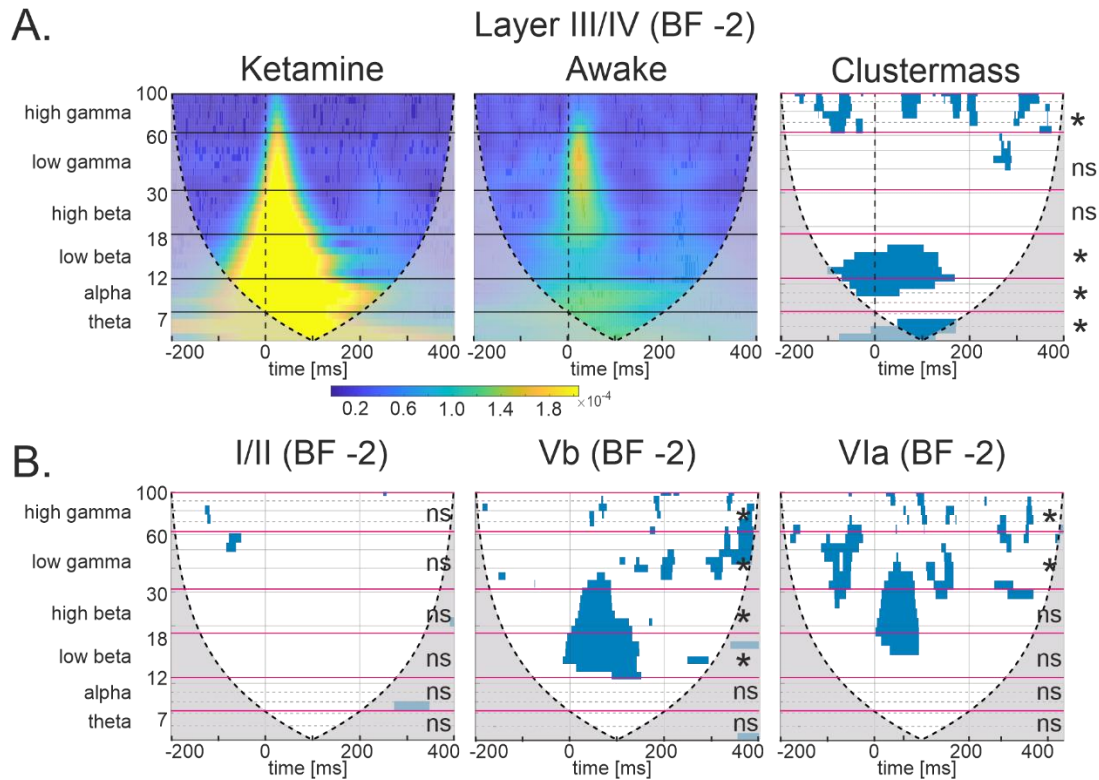
Figure 3.9 Magnitude scalograms of continuous wavelet transform and analysis from trial-averaged off-BF CSD profiles. A: BF – 2 octaves response of layer III/IV; scalograms of ketamine group (left, n=11), awake group (middle, n=9), and clustermass matrix showing significance below p<0.05 (verified by two-sample Student's t test). Magenta lines indicate binning borders of frequencies for wavelet analysis and permutation test (left, *=p<0.05, **=p<0.01, ***=p<0.001, or ns=not significant) of the clustermass. **B:** clustermass permutation test results for layers I/II (left), Vb (middle), and VIa (right) at their respective BF – 2 octaves. All graphs show the cone of influence overlaid as a dashed line and muted areas which extend outward. This shows where the wavelet transform was likely affected by boundary conditions.

Scalogram Magnitude at BF

Spectral Frequency	Layer I_II	Layer IV	Layer Vb	Layer VIa
Theta	0.203	**0.011**	0.159	0.304
Alpha	0.188	**0.018**	0.278	0.469
Beta low	0.353	**0.019**	**0.034**	0.138
Beta high	0.499	**0.023**	0.063	0.093
Gamma low	0.307	**0.033**	**0.02**	0.15
Gamma high	0.165	**0.018**	0.128	0.069

Scalogram Magnitude at BF - 2

Theta	0.356	**0.026**	0.163	0.316
Alpha	0.283	**0.024**	0.252	0.468
Beta low	0.129	**0.032**	**0.018**	0.401
Beta high	0.568	0.463	**0.036**	0.08
Gamma low	0.676	0.284	**0.007**	**0.005**
Gamma high	0.345	**0.008**	**0.025**	**0.007**

Scalogram Phase Coherence at BF

Theta	**0.003**	**0.023**	**0.018**	**0.001**
Alpha	**0.016**	**0.012**	**0.001**	**0.009**
Beta low	0.051	**0**	**0.003**	**0.013**
Beta high	**0.015**	**0.012**	**0.007**	**0.005**
Gamma low	**0**	**0**	**0**	**0.011**
Gamma high	**0**	**0**	**0**	**0.001**

Table 3-7 Continuous wavelet scalogram clustermass permutation test results. Shown are *p* values corresponding to where the observed clustermass fell on the distribution of permutation clustermass results after point-wise Student's *t* test for magnitude and Mann-Whitney *U*-test for phase coherence scalograms. In bold are where *p* is significant at p<0.05.
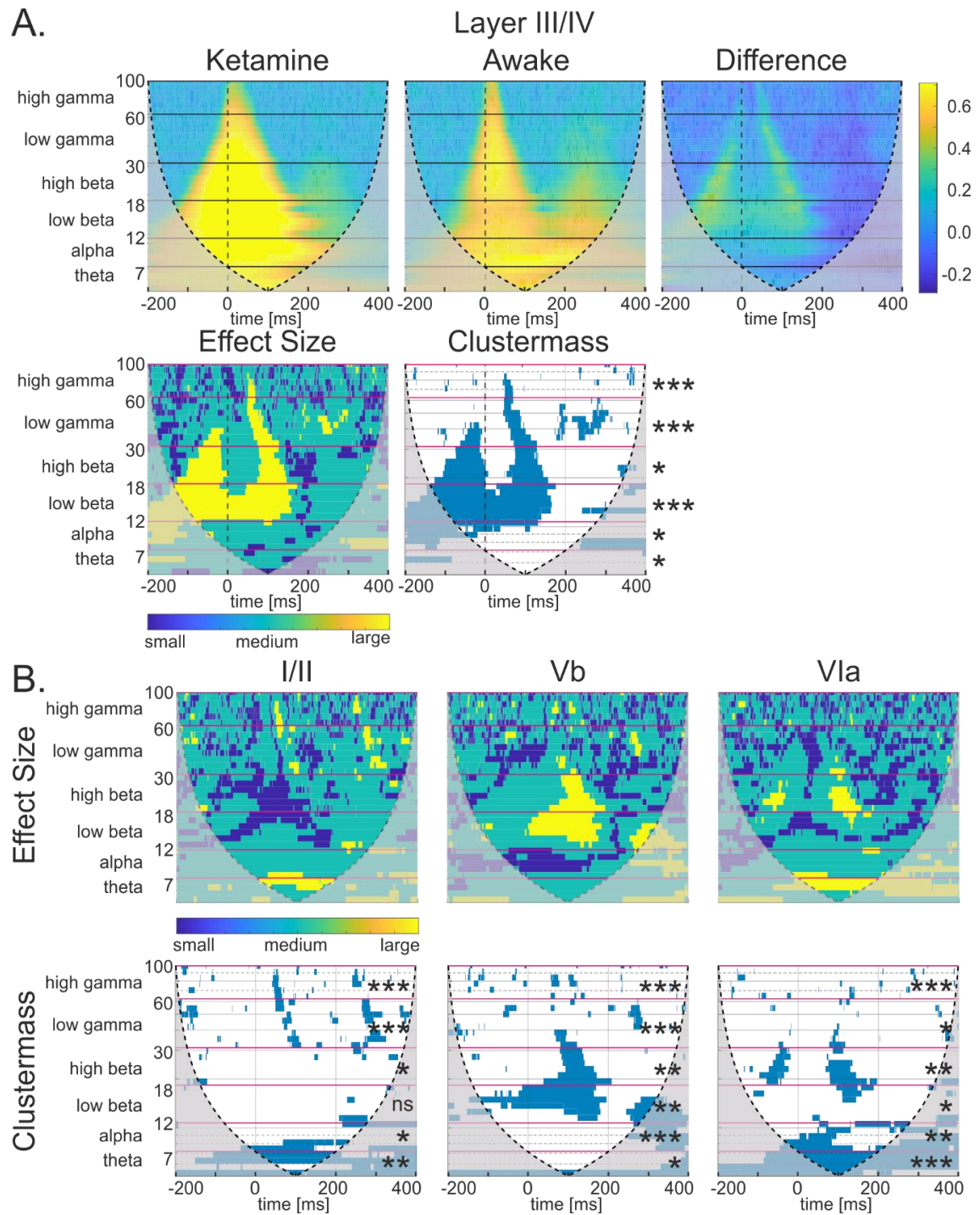
Figure 3.10 Phase coherence scalograms of continuous wavelet transform and analysis from single trial subject CSD profiles. A: BF response of layer III/IV; scalograms of ketamine group (left, n=11), awake group (middle, n=9), and the absolute difference between both groups (right); Effect size matrix showing small through large effect size and clustermass matrix showing significance below p<0.05 (verified by two-sample Student's t test). Magenta lines indicate binning borders of frequencies for wavelet analysis and permutation test (left, *=p<0.05, **=p<0.01, ***=p<0.001, or ns=not significant) of the clustermass. **B:** Effect size matrix, clustermass matrix, and permutation test results for layers I/II, Vb, and VIa at their respective BF. All graphs show the cone of influence overlaid as a dashed line and muted areas which extend outward. This shows where the wavelet transform was likely affected by boundary conditions. Figure and caption taken from Deane et al. 2020.

Population-based onset latencies reflect slower stationary signal were unaffected by ketamine at the BF

There was a discrepancy between onset latencies of spike data (~10-12 ms) and LFP-based measures (~15-20 ms). This was mainly due to the onset latency calculation of a rising curve that defines the onset latency as a crossing of a defined threshold (1.5 standard deviation in our case), which requires multiple cells to pool their activity. Such 'population-based' onset of activity is necessarily longer than the first spike that arrives in the cortex (see Happel et al., 2010; Schaefer et al. 2015). We checked for multiunit onset latencies in our data sets, and these were also slightly shorter in agreement with other spike-derived studies.

We observed minor group variations and slightly shorter mean onset latencies in the awake group. However, when comparing the onset latency tuning curves between awake and ketamine-anaesthetized animals, we did not observe a significant difference for the onset latency of the granular sink in layer III/IV (Figure 3.11). Differences of the mean onset latency after BF stimulation were in the range of around 1-2 ms showing robust onset latencies and only minor across-group differences.
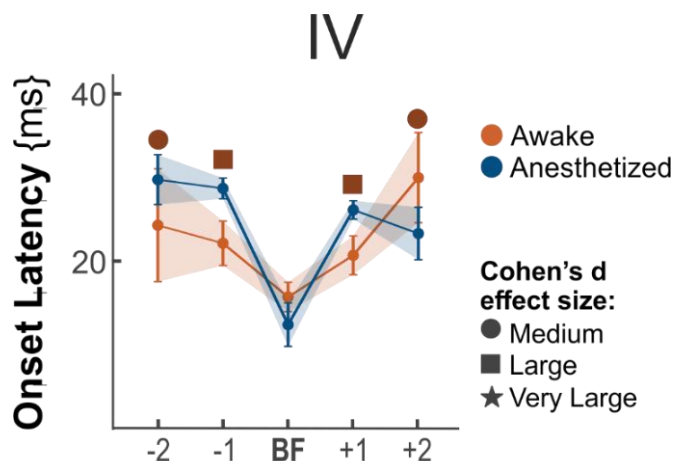

Figure 3.11 Tuning curve of the averaged onset latencies of the dominant layer IV sink between the awake and anesthetized group. (±SEM) We did not observe a significant difference of the earliest activity onset between both groups derived by an onset latency analysis of the dominant layer III/IV sink after stimulation with the frequency with the shortest onset latency. ANOVA and Cohen's d results shown at the bottom of figure.

Between subject comparison of awake and anesthetized gerbil A1

We performed an analysis on data from the awake group, called "chronic" for this section, that was collected under anesthesia to confirm placement of the electrode during the implantation surgery. We compared the results of the chronic group with its own data from those ketamine-anesthetized recordings and found that these results resembled the results

from the separate anaesthetized group, called "acute" for this section (
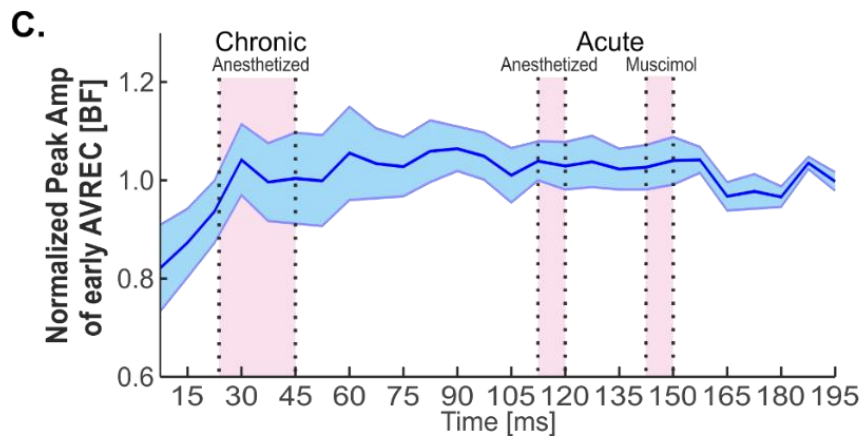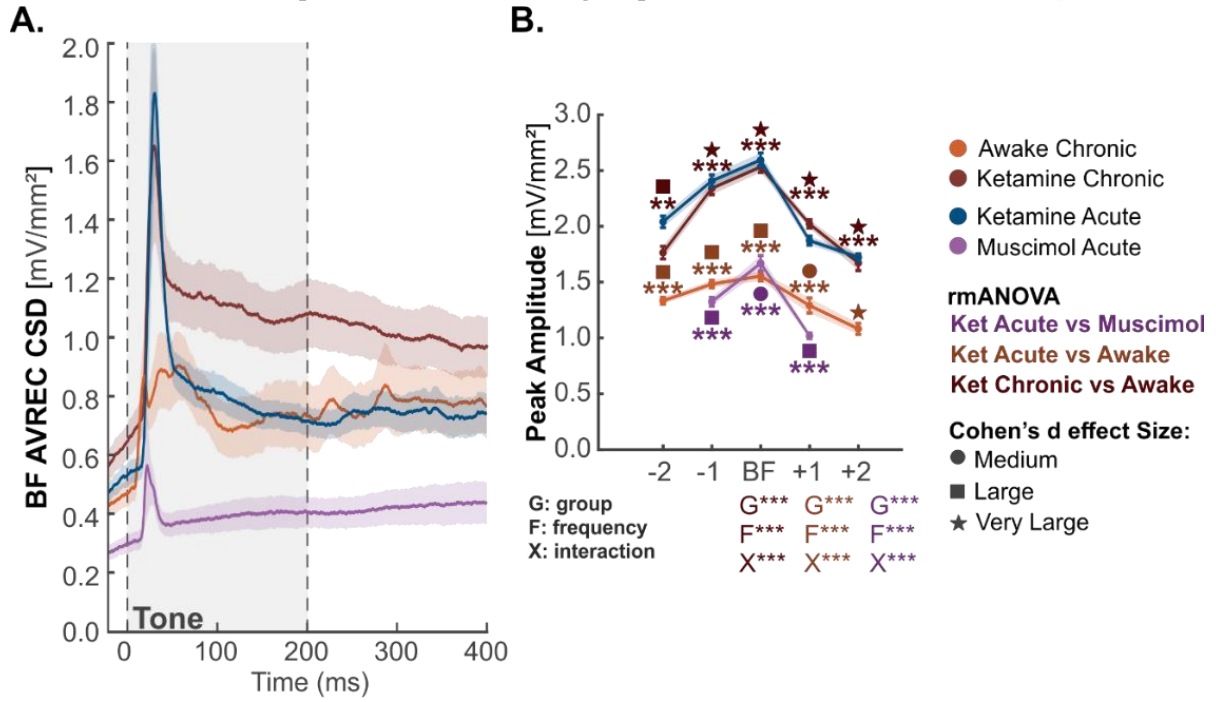
Figure 3.12, ANOVA in Table 3-8, *t* and Cohen's d in Table 3-9). Specifically, we compared the BF-evoked AVREC waveform in
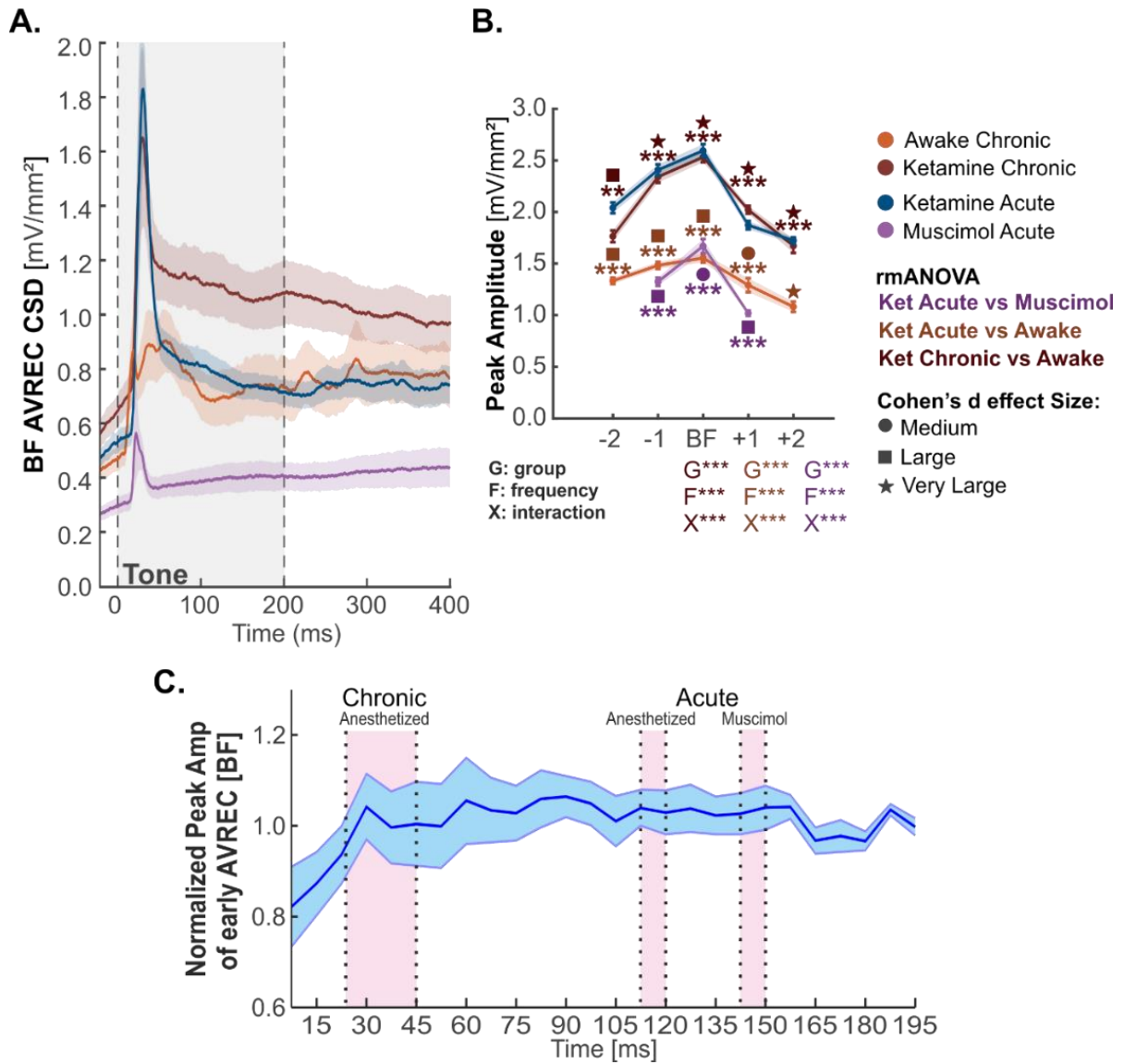
Figure 3.12A and the tuning curves for the AVREC peak amplitude for both groups/all four
conditions in
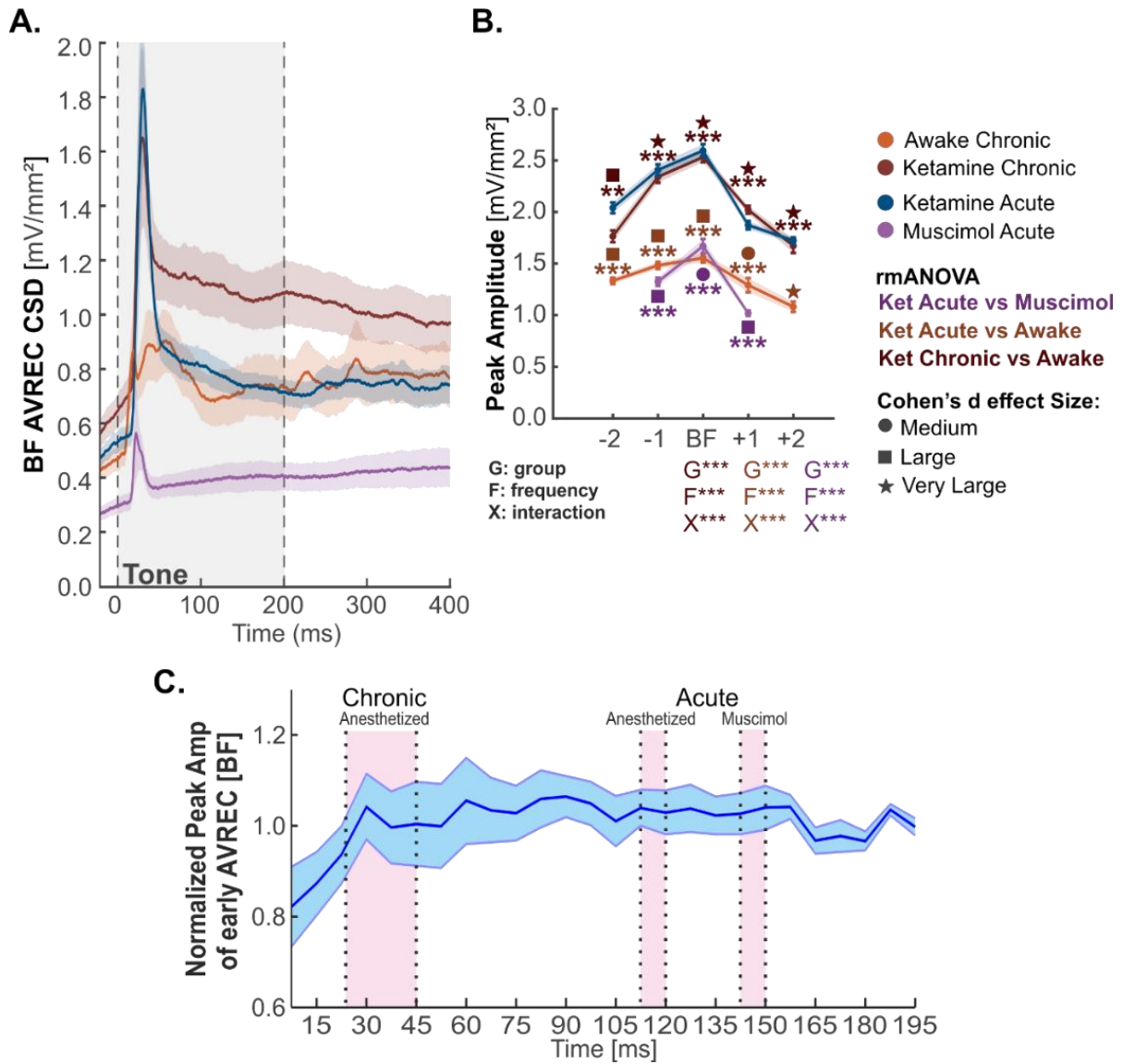
Figure 3.12B. We showed that the acute anesthetized group (blue) and the chronic
anesthetized group (red) were very similar in the BF-evoked AVREC waveform and peak
amplitude tuning. Further, tuning curves of both groups showed a similar significant
difference compared to the awake group, with even higher Cohen's d in the chronic
anesthetized vs awake comparison.

Figure 3.12 Averaged rectified CSD evoked by BF stimulation and group comparability. A: Averaged AVREC curves (±SEM) evoked by BF stimulation revealed that animals from the acute anaesthetized group are more similar to data from the awake group recorded under ketamine anesthesia during implantation of the chronic electrode. **B:** Tuning curves of the peak amplitude of the AVREC (±SEM) consistently showed the comparability of both groups under ketamine anesthesia. These show the same data for the three s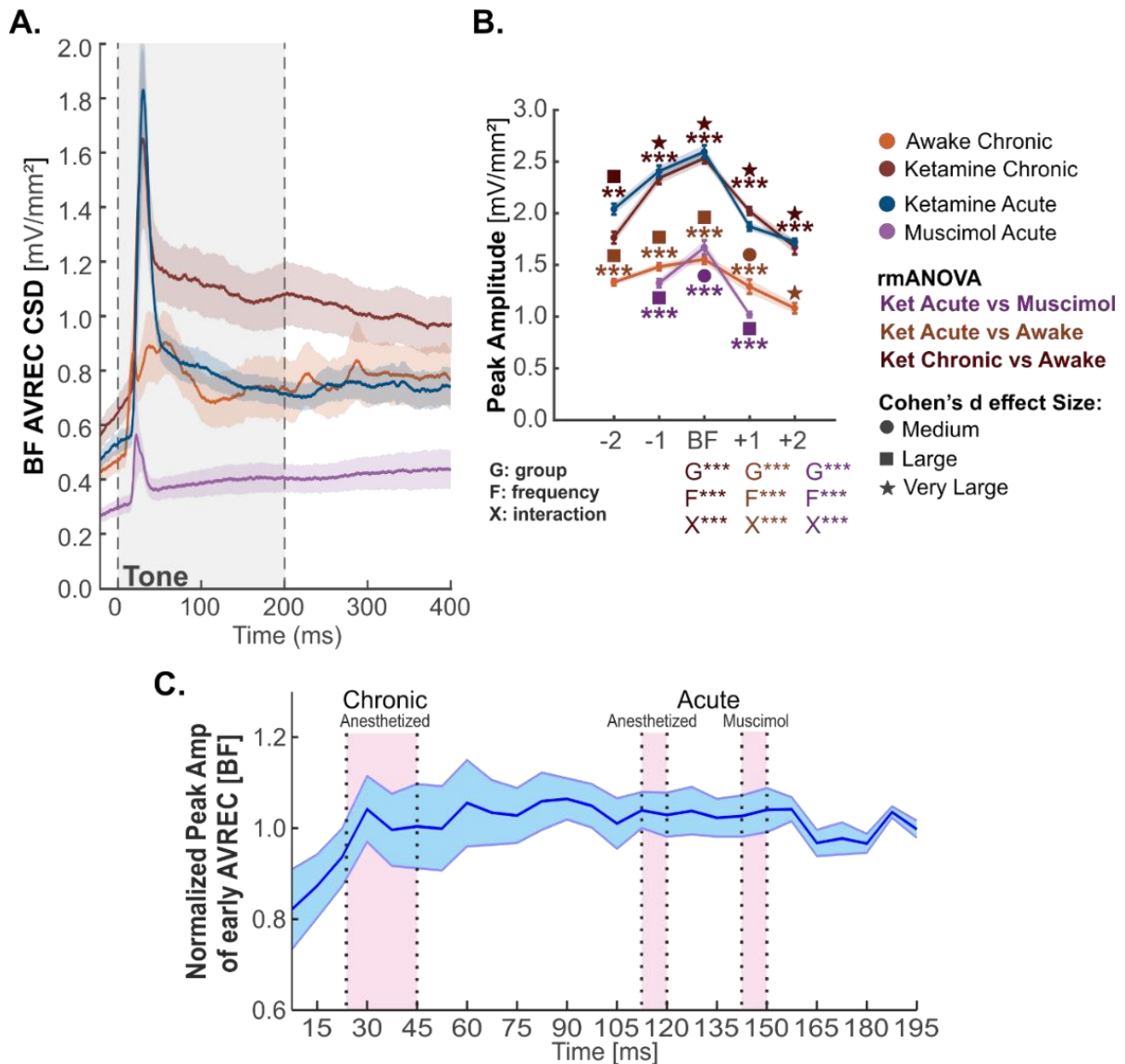tudy groups as Figure 3.5B *left* except confidence intervals are SEM to avoid visual obstruction. **C:** Timeline of the normalized peak amplitude of the AVREC waveform measured in the acute ketamine anesthetized group (±SEM). The AVREC peak amplitude increased over the first 30 minutes after implantation and stabilized in variance over 60 minutes after implantation.

	Peak Amplitude			Peak Latency			RMS		
	G	F	X	G	F	X	G	F	X
Ket Chronic vs Awake	0	0	0	0.042	0.0001	5.28E-05	0	1.33E-08	4.14E-11

Table 3-8 Repeated measures ANOVA results table for AVREC tuning curve within group comparison. Group (G), frequency (F), and interaction (X) results for ketamine chronic vs awake comparisons of the peak amplitude and latency and RMS of the first 100 ms of tone presentation. In bold are significant results where p<0.05.

Ketamine Chronic vs Awake (within subject)

		-2	-1	BF	1	2
Peak Amp	p	0.016	0	0	3.94E-08	0.0006
	Cohen's d	-0.94	-1.26	-1.29	-1.22	-1.76
Peak Lat	p	9.24E-10	0.035	0.835	0.532	0.406
	Cohen's d	0.23	0.24	-0.00	-0.26	-0.30
RMS	p	8.14E-06	0	0	2.34E-14	9.85E-04
	Cohen's d	-1.05	-1.33	-1.18	-1.51	-1.81

Table 3-9 Post-hoc single trial tests for AVREC tuning curves within group comparison. p value and Cohen's d effect size results shown for ketamine chronic vs awake of the peak amplitude and latency and RMS of the first 100 ms of tone presentation. In bold are significant results where p<0.05 and Cohen's d results of at least Medium d>0.5.

Discussion of project 1

Intracortical contribution to sink components in the A1

The group averaged CSD profiles (Figure 3.1) demonstrated a distinguishable pattern difference in cortical current flow over time between anesthetized and awake subjects. Muscimol treated CSD profiles contained only thalamocortical input, short and low-strength sinks time-locked to tone onset in layers III/IV and Vb/VIa (Happel et al., 2010). These thalamic-driven sinks in an otherwise intracortically silenced A1 indicate the spatiotemporal contribution of the thalamus and insinuate that much of the following signal in non-silenced conditions is then of cortical origin. This can be seen also in Figure 3.4 with the diffusion of muscimol over time in a single subject and a consistent tone-onset thalamocortical sink component after intracortical silencing down the depth of the cortical column. Muscimol would not have reached the mid-brain or there would have been no sinks in the cortex at all. It is still possible to see those sinks because the GABA$_A$, which floods the cortex under muscimol, is not inhibiting subthreshold contribution to the LFP signal, the intake of positive ions to a depolarizing population of cells. However, the population being activated by mid-brain afferents was then unable to further process or pass along the signal due to the strong local silencing. This revealed that intracortical processing is the main mechanism that contributes to the peak, strength, and duration of even early signal processing in the A1.

To validate that the cortical differences across awake and anesthetized groups were significant above chance, we performed a clustermass permutation test between these groups (Figure 3.2). At the columnar level and across the early and late time bins of layer III/IV, there was a high degree of significant difference. This analysis revealed a similarity (lack of significant difference) in early layer Vb and less strong significant difference in early layer VIa. It is notable already that the granular thalamic-driven sink component was the most significantly different across layers and that this difference was distinct from the more comparable infragranular thalamic-driven sinks between groups.

We further confirmed within group consistency by artificially halving the groups and randomizing subject selection to each half group in a permutation clustermass test (Figure 3.3).

Ketamine induces a higher time-locked stimulus response at more variable peak amplitudes

We calculated the AVREC traces (Figure 3.5A) to analyze the overall temporal columnar response profile. This showed a high AVREC peak amplitude response directly following tone onset in the ketamine-anesthetized group, in accordance with an induced increase in stimulus-locked cortical activity. Comparatively, the awake group response profile had a much lower amplitude of response over a broader time period. Single-trial peak detection within the first 100 ms of tone presentation revealed significantly higher peak amplitudes in response to the BF and surrounding octaves with large and medium effect sizes (Figure 3.5B *left*).

Due to the distinct temporal structure of the AVREC traces between groups, and the noticeably differently sized STD confidence intervals in peak amplitude and latency comparisons (Figure 3.5B *left, middle*, Figure 3.6A), we calculated a single trial Brown–Forsythe test of variance to observe differences in peak responses. In terms of response strength, the ketamine group peak amplitudes were significantly more variable, with a higher average peak response, than both

the awake group and muscimol condition (Figure 3.6B *left*). In the temporal domain, the awake group peak latency of stimulus induced activity was significantly more variable than the ketamine anesthetized group, which was significantly more variable than the muscimol silenced condition (Figure 3.6B *right*). The decreased peak latency variability in the ketamine group indicated a loss of probabilistic dynamics in the recruitment of cortical cell populations, confirming high stimulus-locking under ketamine in the cortical population.

Increased recurrent excitation in early granular activity under ketamine

Ketamine anesthesia caused a stronger recruitment of recurrent excitation in granular layers following thalamocortical input. We calculated layer-specific, early sink component, tuning curves (Figure 3.7) with a semi-automatic sink detection algorithm and compared them with repeated measures ANOVA and Cohen's d effect sizes over tone frequencies. There was a significant Group difference in response strength (represented as RMS) between the ketamine and awake subjects in layer III/IV specifically. This Group difference was, contrastingly, not found in the comparisons of RMS in the infragranular input layers Vb and VIa. From this result, we inferred that thalamic input was similar between awake and ketamine-anesthetized cortices, in agreement with a study conducted by Zhou et al. (2014) investigating whole-cell recordings with different sound levels and not finding differential thalamocortical input between conditions. To further support a noted similarity of thalamic input to the cortex, onset latencies were compared across ketamine anesthetized and awake groups. There was no difference in the onset tuning curves in layer IV and negligeable Cohen's d effect size at the BF for both groups. This means that there was a consistent onset latency within and across groups in the thalamic granular input layer at BF despite significantly different temporal current flow (Figure 3.2), and stronger activation in this layer (Figure 3.7) in the ketamine group. This is relevant as onset latencies are taken after activity has reached 1.5 standard deviation above a calculated baseline, which already happens within the first 15-20 ms and is contained entirely within the thalamocortical input sink time-window, meaning that the mechanism of onset latency would be almost entirely thalamic in origin.

Following that, the increased response strength in granular layers under ketamine is then likely cortically driven and may be a function of the disinhibition of recurrent excitation microcircuitry in this area. Single and multi-unit studies with ketamine anesthesia have also specifically implicated a lack of inhibitory modulations from supragranular populations to this recurrent excitation (Kato et al., 2017; Wehr & Zador, 2003). This is in line with influences of ketamine on the excitatory and inhibitory balance via selectively reducing activity of PV-releasing GABAergic interneurons. Our data therefore support the hypothesis of ketamine-driven cortical disinhibition (Miller et al., 2016) and are in support of previously revealed elevated levels of neural activity after ketamine due to increased cerebral blood flow (Långsjö et al., 2005).

Boosted recurrent excitation of granular inputs mediates gain enhancement

The increased strength of intracortical processing under ketamine was significant selectively in the granular layer (Group effects in Figure 3.7A and C). To further analyze laminar effects, we used continuous wavelet analysis (CWT) on center layer channels, for I/II, III/IV, Vb, and

VIa, in the single trial CSD profiles. CWT revealed spectral magnitude (Figure 3.8 and Figure 3.9) and phase coherence (Figure 3.10) profiles that contribute to the peak structure of evoked cortical responses. We then performed clustermass permutation tests between the ketamine and awake groups. The magnitude comparison at BF (Figure 3.8) demonstrated that the observed broadband magnitude response under ketamine was significantly increased compared to awake subjects selectively in the granular layer. This broad increase across spectral frequencies was less pronounce in other cortical layers and off-BF (Figure 3.9).

This finding was consistent with the prolonged and enhanced cortical response to the auditory stimulus found in granular layers under ketamine (Figure 3.1D) as well as the peak amplitude and latency distribution of the AVREC response (Figure 3.6A). The enhancement of stimulus-evoked AVREC peak amplitudes at lower peak latency variability reflected a highly stimulus-locked recruitment of the feedback loop circuits in layers III/IV, which then dominated the columnar response to the BF stimulus where thalamic input was most prevalent. Off-BF frequencies evoked less prominent differences in spectral magnitude, thus indicating a tonotopically tuned increase in granular recurrent excitation.

When comparing phase coherence, permutation clustermass revealed high significant group differences across all layers with an increase in phase coherence due to ketamine (Figure 3.10). Notable especially in the granular layer, ketamine induced a temporally increased area of cross-trial phase coherence across spectral frequencies compared to awake recordings and stronger phase coherence in lower spectral frequencies (low beta and below). During early thalamocortical input (~10–40 ms), granular layer processing showed no significant difference in phase coherence in the frequency range from high beta to high gamma (Figure 3.10A), even though a broadband significant increase in magnitude was seen (Figure 3.8A) between groups at this time point. This means that phase coherence was comparable at these spectral frequencies specifically at the time of tone onset and thalamocortical input. Therefore, we propose that the gain increase under ketamine due to magnitude effects and not to increased phase coherence. These findings are in accordance with gain enhancement due to an input-circuit-specific dephasing of recurrent excitation and inhibition—otherwise declared as GABAergic disinhibition of recurrent excitation—to incoming external stimuli most prominently seen in the gamma band (Miller et al., 2016; Morita et al., 2008; Wehr & Zador, 2003).

A within group awake vs anesthetized comparison yields comparable results

We have demonstrated characteristic spatiotemporal differences between awake, ketamine anesthetized, and muscimol diffused conditions. However, any reviewer would be completely right to question a lack of a within subject comparison (and in fact, all reviewers did). CSD distributions across subjects are a robust measure of synaptic current flow, which is a precondition that the data had to meet in order to allow meaningful averaging of CSD profiles across subjects to obtain grand mean CSD profiles (Figure 3.1). Nevertheless, we calculated AVREC traces and tuning curves also for the awake group's, called "chronic" for

A.

B.

C.
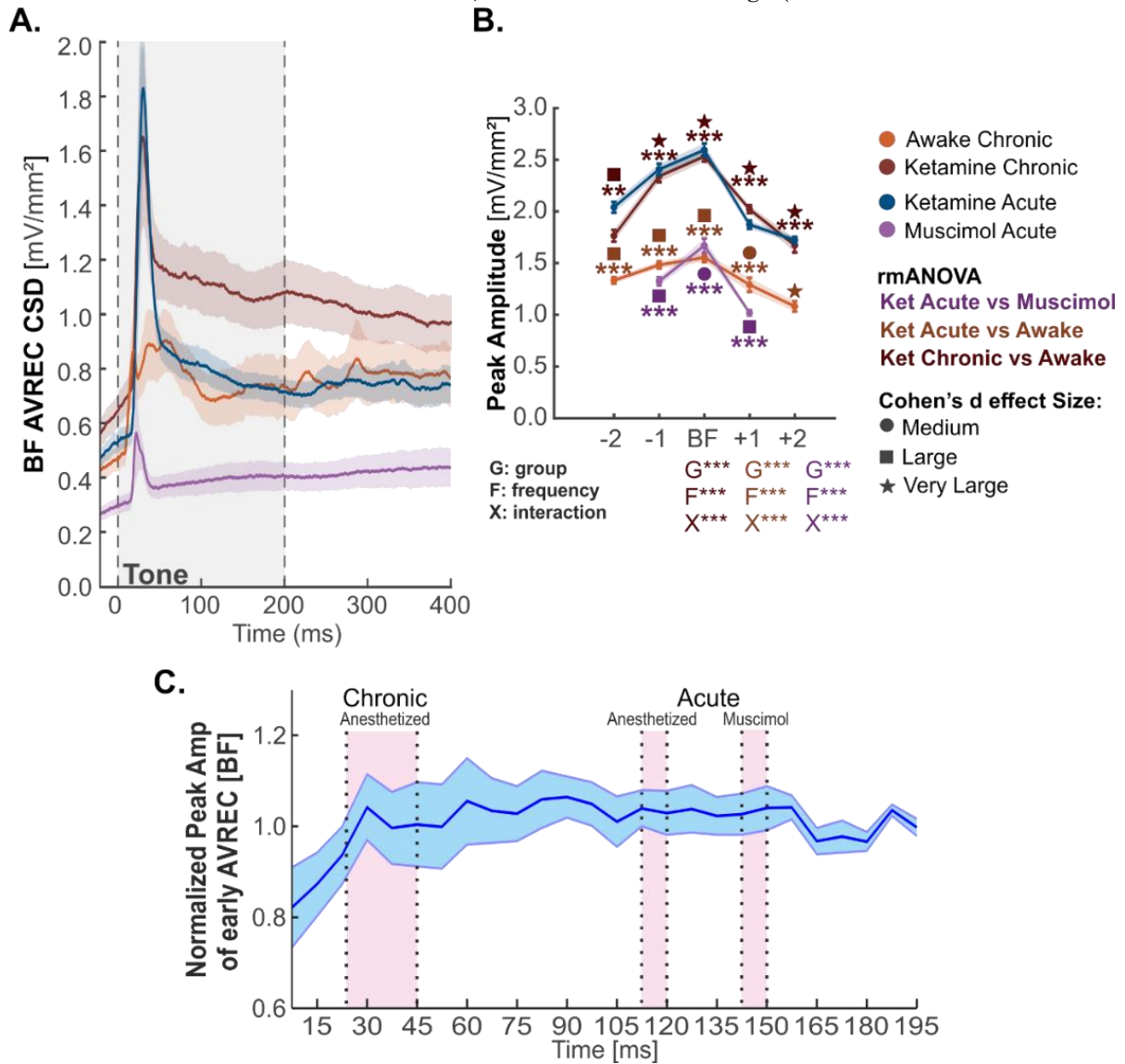
Figure 3.12A and B).

The AVREC waveform was not a perfect match between anesthetized groups, but it did reveal a characteristic similarity with a high peak amplitude synchronized to the stimulus onset. The anesthetized chronic peak amplitude tuning curve was a near match for the anesthetized acute (used in this study) peak amplitude tuning curve, though, and was similarly significantly different from the awake condition. However, this chronic group's

anesthetized recordings were ultimately not used due to practicality.
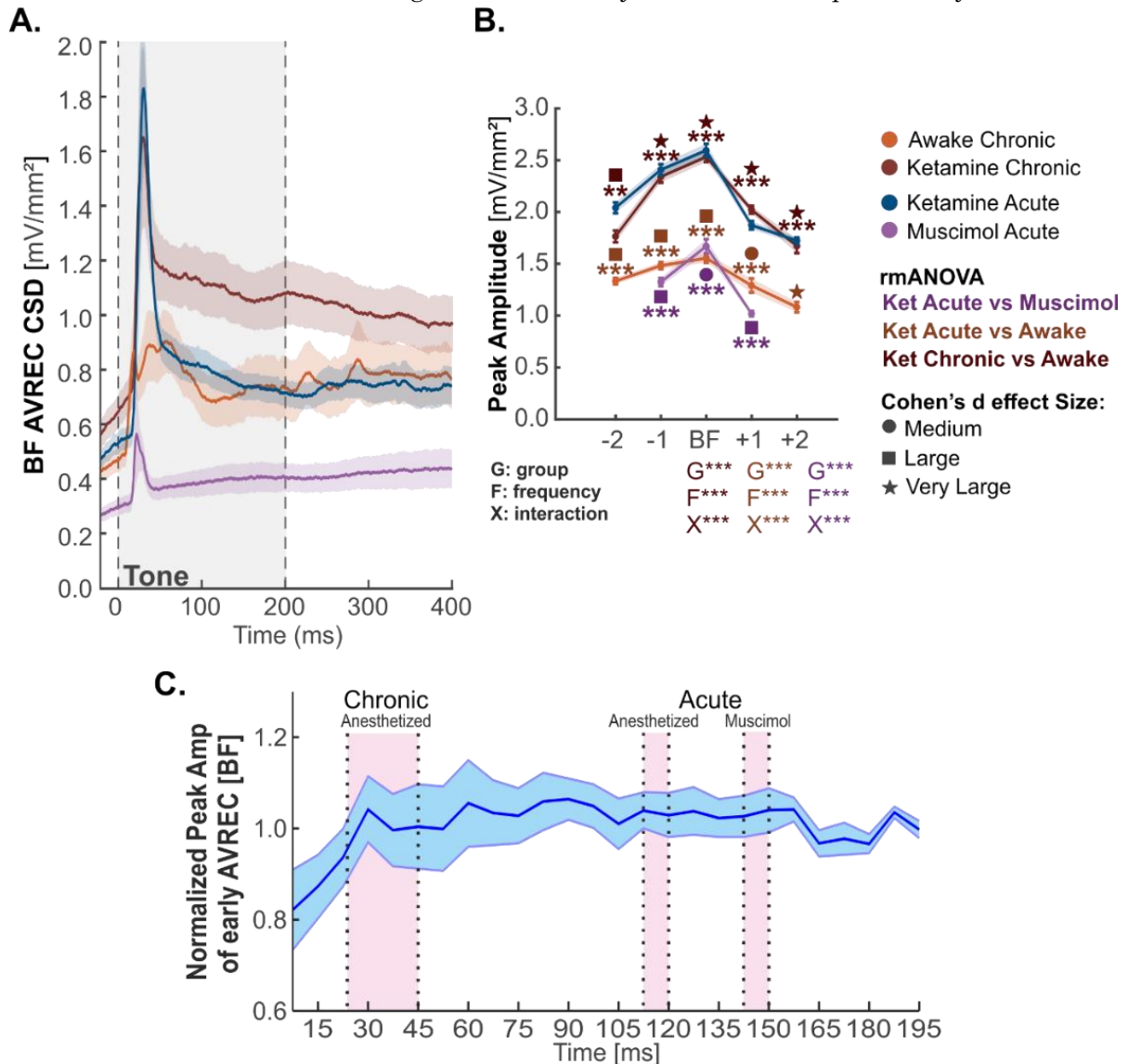
Figure 3.12C plots the normalized AVREC peak amplitude over the entire recording time of the acute anaesthetized group to highlight the reason for this omission. The evoked amplitudes increase over a period of up to 30 minutes and seemed to need approximately another 30 minutes to stabilize in variability (seen by a reduction of the error bar size). We assume this to be the time for cortical tissue to recover from the electrode implantation. In the initial ketamine-anesthetized group, we used data from recordings which exceeded 100 minutes after implantation of the electrode—a state where the cortical responses under anesthesia would have surely been stabilized. Such periods of recovery for recoding quality were not feasible during surgeries where electrodes were implanted chronically. A shorter time under anesthesia corresponds to better recovery of the subject. Therefore, we had only recorded for maximally 30-45 minutes under anesthesia for the chronic group. These subjects went on to be a part of the Zempeltzi et al. (2020) shuttle-box study after the initial passive recordings used in our work. Nevertheless, based on the AVREC-based tuning curves, we observed a strong similarity with the acute ketamine-anesthetized group which validates their between group comparison use.

Conclusion

We investigated the effects of anesthetic doses of ketamine (15 mg kg^{-1} h^{-1}) on synaptic population dynamics in the auditory cortex of Mongolian gerbils using layer-specific CSD analysis. Our data revealed a cortical gain increase under ketamine, robustly explained by a boosted recurrent excitation in granular input layers. This was ascribed to an increase in tone-evoked amplitude across spectral frequencies in a continuous wavelet (CWT) analysis rather than stimulus–response phase locking. Ketamine produced a temporally increased area of phase coherence to incoming stimuli mainly in granular layers in conjunction with a less variable temporal signal response, but this difference was not significant during early thalamocortical input processing. We observed higher stimulus-locked responses at more variable amplitudes under ketamine, specifically in granular thalamic input layers. The effect was most prominent in granular layers during best-frequency stimulation and less specific for other cortical layers and stimulation frequencies. Our findings therefore argue for an altered input processing due to an increase in recurrent feedback microcircuitry of thalamocortical inputs selectively in granular layers III/IV which may be attributed to a disinhibition of GABAergic interneurons, leading to a reduced coupling of excitatory and inhibitory input circuits under ketamine. A follow up study may selectively inhibit parvalbumin releasing interneurons optogenetically and record LFP to observe similar effects on the spatiotemporal flow of cortical activity. A broader discussion will follow in Chapter 6.

Chapter 4: Voltage gated calcium channel aggregation and its impact on A1 microcircuitry function

This chapter builds the basis for the recent pre-print publication, *Inhibiting presynaptic calcium channel mobility in the auditory cortex suppresses synchronized input processing* by Deane et al., 2022a. The current text contains parts of the pre-print and additional data and content.

Background

A key function of evolution is not only to select for successful adaptations, but to allow for random mutations. It turns out that flexibility is a harbinger of success, or as my high school choir teacher always put it: "a sign of greatness". This is because an organism or strategy that is perfectly suited for its current environment, may not be able to succeed in adapting to a change in that environment (see *Robby The Robot Genetic Algorithm* described in Mitchell, 2011). Variability in a population, along with dynamic, parallel pathways of exploitation and exploration, allows for a robustness not otherwise possible in a deterministic or static systems (see Figure 2.1). A large introduction of such variability in the brain is the motility of Cav2.1 voltage gated calcium channels (VGCCs). Neuronal communication is critically mediated by the release of chemical transmitters from presynaptic vesicles which is partly controlled by VGCCs. These highly motile channels trigger the influx of calcium ions to the presynaptic bouton upon action-potential-induced membrane depolarization. However, the transient and local action of calcium requires a close proximity between vesicular calcium sensors and the VGCC pore to efficiently initiate vesicle fusion and transmitter release. Previous to our study, it was shown *in vitro* that synapse-specific release properties depend on the molecular lateral mobility of Cav2.1 VGCCs within the presynaptic membrane (Heck et al., 2019). It has therefore been suggested that the regulation of presynaptic VGCC mobility and vesicle release-sites control synaptic release probability and short-term plasticity (Böhme et al. 2018; Heine et al. 2020). This probabilistic mechanism spans all neuronal architecture, which of course includes the primary auditory cortex (A1).

The A1 sits at the nexus of brain-wide systems that subsequently categorize sound and initiate potential auditory-guided behaviors (King et al, 2018; Nelken 2020). Coherent population activity within the A1 is primarily generated via recurrent microcircuits in granular layers (B. Liu et al., 2007) and sensory inputs recruit translaminar assemblies of synchronized neurons (Beltramo et al., 2013). Interplay between excitatory and inhibitory postsynaptic currents is considered a major origin for such input-derived population dynamics in the sensory cortex (Fu et al. 2014; Gabernet et al. 2005; Wu et al. 2008) and VGCC dynamics are interwoven therein. For example, neuromodulators like dopamine, released by calcium influx, can influence such circuit excitation (Brunk et al., 2019; Gao et al., 2001). Hay and Segev (2015) argued that dendritic backpropagating Ca^{2+}-spikes can coincide with tightly timed sensory inputs and contribute to sensory amplification. Synapses in the auditory brainstem show fast and repetitive synaptic vesicle release to encode sound information (Young & Veeraraghavan, 2021). Here, the availability of VGCCs in triggering action potential-mediated synaptic vesicle release, is an integral part of the temporal resolution of synaptic transmission and therefore a crucial component of sensory network dynamics.

Exactly how membrane motility of presynaptic VGCCs—at a cellular level—may influence the aforementioned gating of afferent inputs in the sensory cortex at a population level is the

subject of our investigation. We therefore targeted the N-termini of Cav2.1 channels in the right A1 of transgenic knock-in mice, Cacna1a^{Citrine} (Mark et al., 2011), with an optogenetically aggregating cryptochrome mutant, CRY2olig (Heck et al., 2019; Taslimi et al., 2014), via a feed-back-controlled anti-GFP intrabody (Figure 2.1). After lentiviral delivery and expression of CRY2olig in the A1 (Figure 2.2), we recorded local field potentials *in vivo* across all cortical layers of the A1 under ketamine-xylazine anesthesia and transformed signals into current source density (CSD) profiles (Brunk et al., 2019; Deane et al., 2020), before and after optogenetic-induced VGCC clustering. We compared responses to two different kinds of auditory stimulus sets—click trains and amplitude modulated (AM) tones (Figure 2.3).

Contrasting responses to these two stimulus types of spectral energy were hypothesized to reveal key differences in how a population with clustered VGCCs would internally synchronize and respond to sounds, whether more natural, with amplitude modulation, or more spectrally broad and dense, with click trains. Indeed, we found that population activity across the entire column was primarily affected in cases of higher synchronicity of incoming inputs: bottom-up dominated click train responses. That is to say, post-aggregation cortical responses were most significantly different between CRY2olig-treated and control groups, particularly in early input layers IV and V, in response to clicks trains, whereas effects on AM responses were more subtle in group comparisons. To both stimuli there was a consistently significant reduction of activity after clustering in the CRY2olig group across most layers but this reduction of cortical activity after aggregation was not represented to the same degree during spontaneous (without stimuli) activity. This indicated a suppression of accurate sensory encoding of synaptic inputs, dependent on level of synaptic recruitment, due to the reduced synaptic variability effectuated by presynaptic VGCC aggregation.

Results of project 2

Cortical activity during click train and amplitude modulation cortical responses reveal stimuli-dependent suppression during VGCC clustering

The mouse primary auditory cortex is generally around 1 mm deep, leaving less space for the microcircuitry shared between mammals than in the gerbil primary auditory cortex. Thalamic input to layers IV and the border of V and VI largely combine as a continuous sink across granular and upper thalamic layers. Figure 4.1 contains all group averaged CSD profiles for Cry2olig-treated, naïve control, and viral control across click trains and amplitude modulated pure tones of 5 and 10 Hz before and after laser presentation. Again, blue areas denote population activity due to the intake of positively charged ions from extracellular to intracellular space, called sinks.

Figure 4.1 A and B show the cortical response to click trains—a clear following response, or thalamocortical input per stimulus repetition, to 5 Hz clicks and a lightly visible following response to 10 Hz clicks. Clicks are a broadband high energy stimulus, activating hairs along the entire basilar membrane and subsequently the tonotopic map along the auditory pathway (Lu & Wang, 2000). The click carrier wave was set to the best frequency determine by a pseudorandomized series of pure tones at the beginning of each recording session, but clicks should theoretically equally activate the primary auditory cortex wherever the laminar probe is positioned. Figure 4.1 C and D are the cortical response to amplitude modulated pure tones, set to each animal's best frequency response. While the cortex was generally active across the 1 second time window that this stimulus was presented, there was no repetitive onset to initiate thalamocortical input in the same characteristic following response as in the click trains. Amplitude modulated pure tones cover only the spectrum of the best frequency of this area of the cortex and modulate volume at a fixed frequency. The click trains are fundamentally recruiting a much denser network of neurons than the amplitude modulated tones.

There is no clear difference before and after laser presentation between groups in the average CSD profiles. However, the difference between the control groups and the CRY2olig group, in which VGCCs initiated clustering during laser presentation, becomes more evident when the CSD spatial-temporal map is flattened into average rectified (AVREC) CSD and layer sink traces (Figure 4.2). These traces are normalized per animal to the first AVREC peak detected during the stimulus time window in the first measurement. Figure 4.2 A and C show the group averaged (±STD) AVREC and thalamic input layer traces, IV and V, before and after laser presentation in response to 5 and 10 Hz click trains (for defining channels to be averaged for layer-specific information, see Chapter 2 p 26). In Figure 4.2 A, arrows indicate the direction of change in cortical activity strength for CRY2olig and control groups. Specifically, in the click train cortical response profiles, activity decreased after the laser and VGCC clustering in the CRY2olig group and increased after the laser presentation in both control groups. One can see this also in the layer traces shown for click train cortical response, that there was a decrease in sink activity level after the VGCC clustering in the CRY2olig group and an increase after laser presentation in the control groups. For amplitude modulated pure tone cortical response traces, in Figure 4.2 B and D, this pre- to post-laser response strength difference is less clear and, in some cases, simply not present.
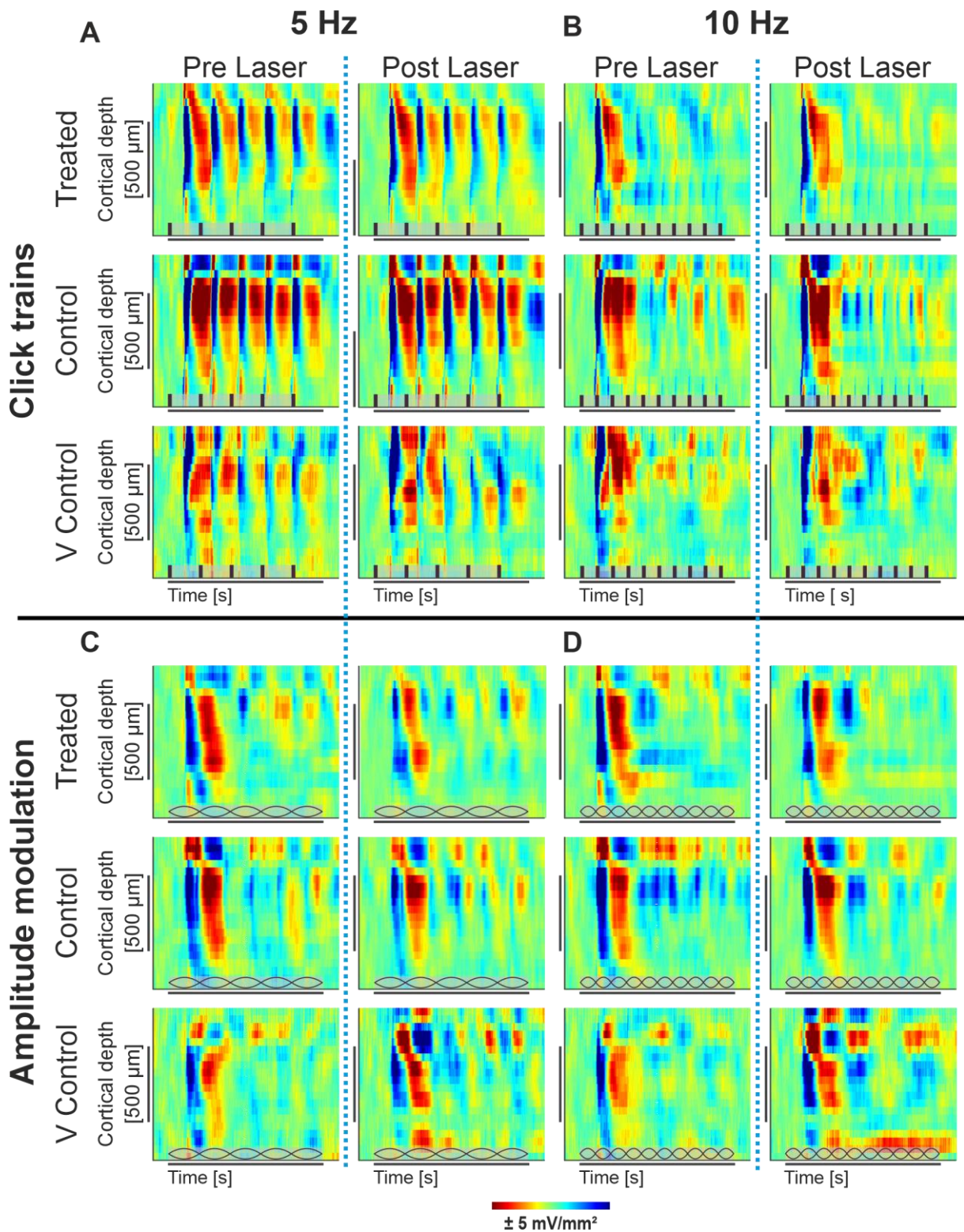
Figure 4.1 Grand Average Current Source Density Profiles. A: the group grand averaged CSD profiles of Cry2olig treated (top), naïve control (middle), and viral control (bottom) subjects in response to 5 Hz click trains over 1 second before (left) and after (right) laser presentation. **B, C,** and **D:** the same groups pre and post laser in response to 10 Hz click trains **(B)**, 5 Hz amplitude modulated pure tones **(C)**, and 10 Hz amplitude modulated pure tones **(D)**. Ticks and lemons in brown on the x-axis represent temporally accurate clicks and amplitude modulation respectively. Image in part published in Deane et al. 2022a.
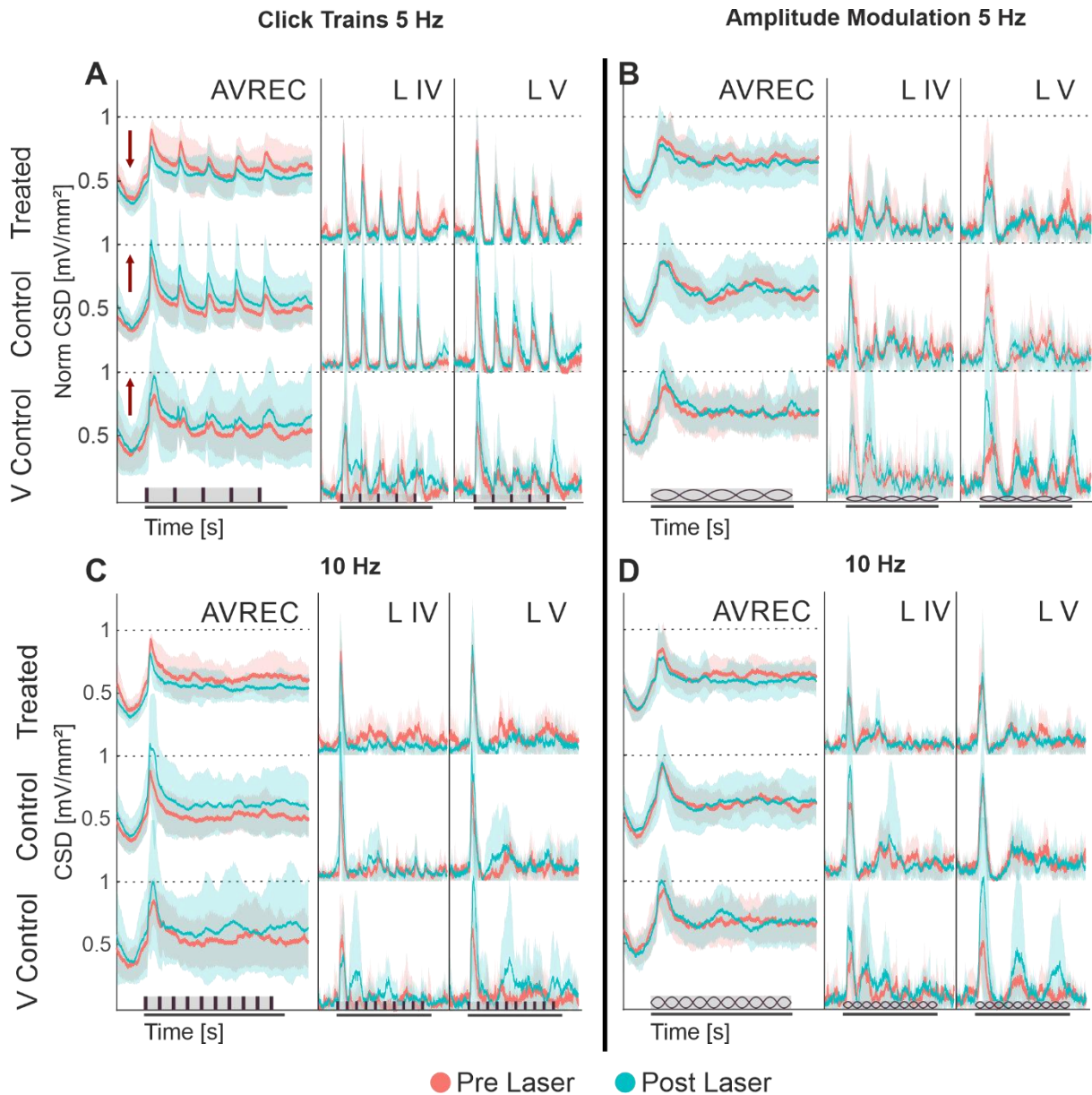
Figure 4.2 Average Rectified CSD and Layer Traces. A: the group grand averaged (±STD) AVREC (left), layer IV (middle), and layer V (right) traces of Cry2olig-treated (top), naïve control (middle), and viral control (bottom) subjects in response to 5 Hz click trains over 1 second before (peach) and after (cyan) laser presentation. **B, C, and D:** the same groups' traces pre and post laser in response to 5 Hz amplitude modulated pure tones (**B**), 10 Hz click trains (**C**), and 10 Hz amplitude modulated pure tones (**D**). Ticks and lemons in brown on the x-axis represent temporally accurate clicks and amplitude modulation respectively. Image in part published in Deane et al. 2022a.

Linear Mixed model indicated a consistent significant reduction after VGCC clustering

As a robust and conscientious statistical first pass, we performed a Linear Mixed Model (LMM) where the intercept, the point to which all else was compared, was the post-laser CRY2olig group cortical response strength. This intercept allowed all post-laser comparisons of CRY2olig to control groups and a pre- to post-laser comparison in the CRY2olig group. Response strength was taken as the RMS of AVREC or layer traces during the first 200 ms of stimulus presentation. RMS was transformed into logRMS as a standard protocol for LMM analysis. Comparisons were: CRY2olig vs naïve control group post-laser response strength, CRY2olig vs viral control group post-laser response strength, and CRY2olig pre- vs post-laser response

strength. Figure 4.3 shows the linear prediction of logRMS for each group pre- to post-laser and statistical results where p was found to be significant in these comparisons (see Table 4-1 for all click train LMM results and Table 4-2 for all amplitude modulated LMM results). Figure 4.3 A contains the linear prediction across the AVREC and all layer traces for cortical response to 5 Hz click trains and Figure 4.3 B contains the same for cortical response to 5 Hz amplitude modulated pure tones.

Here and in the following section I am primarily discussing 5 Hz click trains and amplitude modulated tones. The statistical results across are comparable across stimulus frequency within their stimulus type. See Figure 4.5 below to inspect this phenomenon.
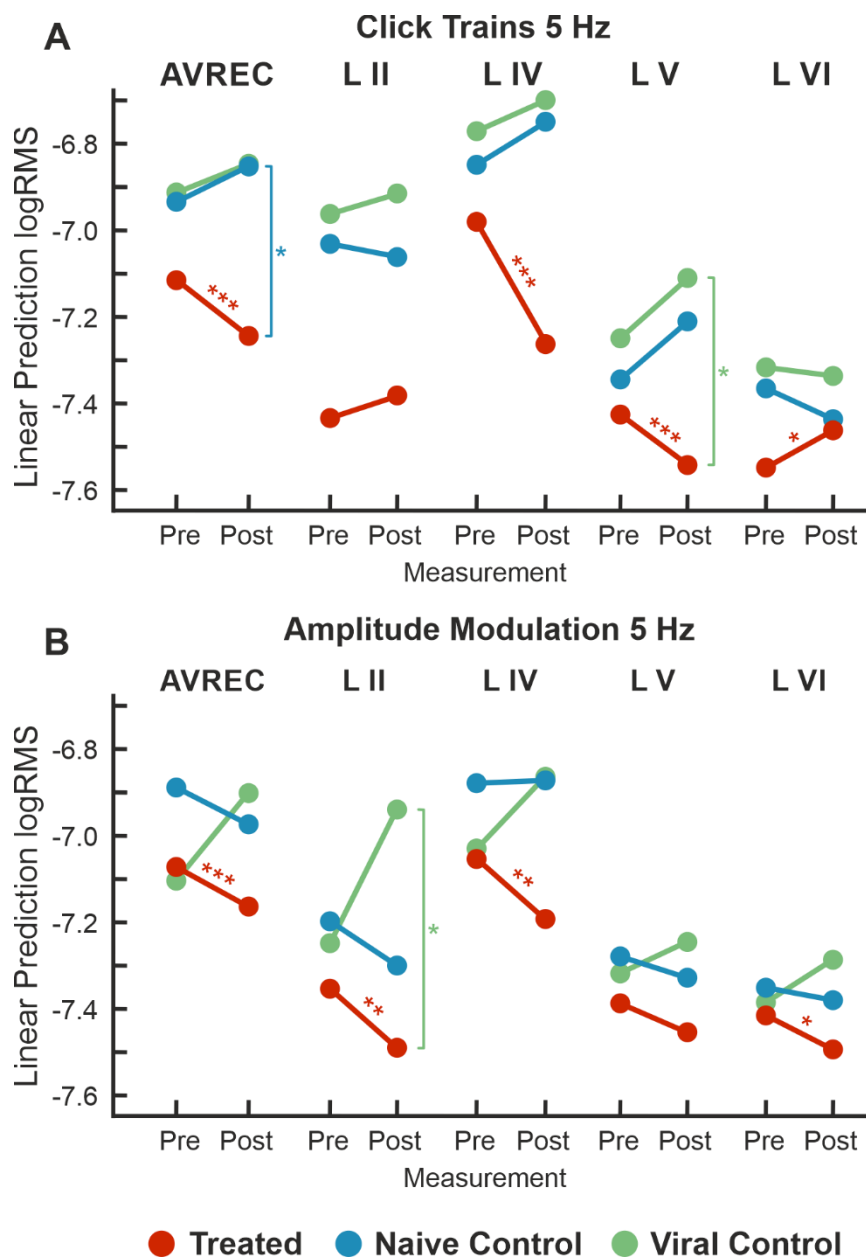
Figure 4.3 Linear Mixed Model Effects for 5 Hz. A: LMM effect plots for linear prediction over measurement (pre- to post-laser) for CRY2olig-treated (orange), naïve control (blue), and viral control (green) groups across the AVREC and all cortical layers in response to click trains. **B:** LMM effect plots for linear prediction over measurement (pre- to post-laser) for CRY2olig, naïve, and viral control groups across the AVREC and all cortical layers in response to amplitude modulation. Results for LMM comparisons—CRY2olig pre- vs CRY2olig post-laser (orange), CRY2olig vs naïve post-laser (blue), and CRY2olig vs viral post-laser (green)—are overlaid as significance stars. p < 0.05 *, <0.01 **, <0.001 ***. Figure and caption published in Deane et al. 2022a.

In the full cortical column, AVREC, and throughout the layers in response to both click trains and amplitude modulated pure tones, there was a fairly consistent decrease in response strength for the Cry2olig-treated group (orange). This most strongly significantly decreased in the AVREC of both stimulus types and in the thalamic input layers IV and V in response to clicks. It also significantly decreased in amplitude modulated tone response strength for layer II, IV, and VI. The exceptions are click train layer II, where there was a non-significant increase, and VI, where there was a significant increase in response strength.

In the LMM analysis, difference between groups post-laser were less robust. However, significant difference was found between the CRY2olig and naïve control groups post-laser at level of the AVREC in response to click trains. Difference was also found between the CRY2olig and viral control groups post-laser during click trains in layer V and amplitude modulation in layer II.

LMM Results: Click Trains

Predictors	Layer	Estimates	SE	Statistics	df	p
	AVREC	0.397	0.178	2.235	24	**0.035**
	II	0.327	0.222	1.475	23	0.154
CRY2olig vs Naïve-Control : Post-Laser	IV	0.508	0.26	1.953	24	0.063
	V	0.328	0.172	1.902	24	0.069
	VI	0.183	0.133	1.378	24	0.181
	AVREC	0.402	0.196	2.054	24	0.051
	II	0.478	0.423	1.961	23	0.062
CRY2olig vs Viral-Control : Post-Laser	IV	0.558	0.286	1.947	24	0.063
	V	0.425	0.190	2.239	24	**0.035**
	VI	0.232	0.147	1.581	24	0.127
	AVREC	0.13	0.025	5.121	702	**<0.001**
	II	-0.052	0.046	-1.132	729	0.258
CRY2olig : Post-Laser vs Pre-Laser	IV	0.281	0.044	6.362	758	**<0.001**
	V	0.115	0.038	-4.597	754	**0.003**
	VI	0.086	0.034	2.567	777	**0.044**

Table 4-1 LMM results for Click train stimulus: Comparisons run with the logRMS and the Intercept: CRY2olig-Treated:Post-Laser. Therefore the intercept, CRY2olig vs Naïve control post-laser, CRY2olig vs viral control post-laser, and CRY2olig pre-laser vs post laser are compared in the AVREC and layer traces. Significant results, p<0.05, are in bold. Table published in Deane et al. 2022a.

LMM Results: Amplitude Modulations

Predictors	Layer	Estimates	SE	Statistics	df	p
	AVREC	0.187	0.169	1.106	24	0.28
	II	0.188	0.195	0.964	23	0.35
CRY2olig vs Naïve-Control : Post-Laser	IV	0.322	0.239	1.349	24	0.19
	V	0.127	0.187	0.681	24	0.50
	VI	0.113	0.161	0.7	24	0.49
	AVREC	0.258	0.187	1.382	24	0.18
	II	0.543	0.214	2.924	23	**0.02**
CRY2olig vs Viral-Control : Post-Laser	IV	0.331	0.263	1.259	24	0.22
	V	0.211	0.206	1.787	24	0.32
	VI	0.205	0.177	1.155	24	0.26
	AVREC	0.08	0.025	3.632	657	**<0.001**
CRY2olig : Post-Laser vs Pre-Laser	II	0.134	0.046	2.924	693	**0.004**
	IV	0.138	0.044	3.147	743	**0.002**
	V	0.067	0.038	1.179	747	0.07

| | VI | 0.077 | 0.033 | 2.315 | 775 | **0.02** |

Table 4-2 LMM results for Amplitude modulated stimulus: Comparisons run with the logRMS and the Intercept: CRY2olig-Treated:Post-Laser. Therefore the intercept, CRY2olig vs Naïve control post-laser, CRY2olig vs viral control post-laser, and CRY2olig pre-laser vs post laser are compared in the AVREC and layer traces. Significant results, p<0.05, are in bold. Table published in Deane et al. 2022a.

Single trial tests indicate great increases in difference between groups after the laser in cases of strongest cortical recruitment

To further explore the difference between groups, we ran single-trial analyses on the first 200 ms RMS of AVREC and layer traces. Each measurement contained between 30 and 50 trials, giving minimum 210 (30 trials for 7 animals in the viral control group) and maximum 550 (50 trials for 11 animals in the CRY2olig group) for comparison. Single trial analysis is both more intuitive to explore variance in and between groups and more susceptible to false positive significant results. Therefore, we paired Cohen's d effect size to each Student's t test, looking for significant results in conjunction with at least medium effect sizes, and Bonferroni corrected our significance level by n=14. Higher effect size generally correlated with extreme significance.
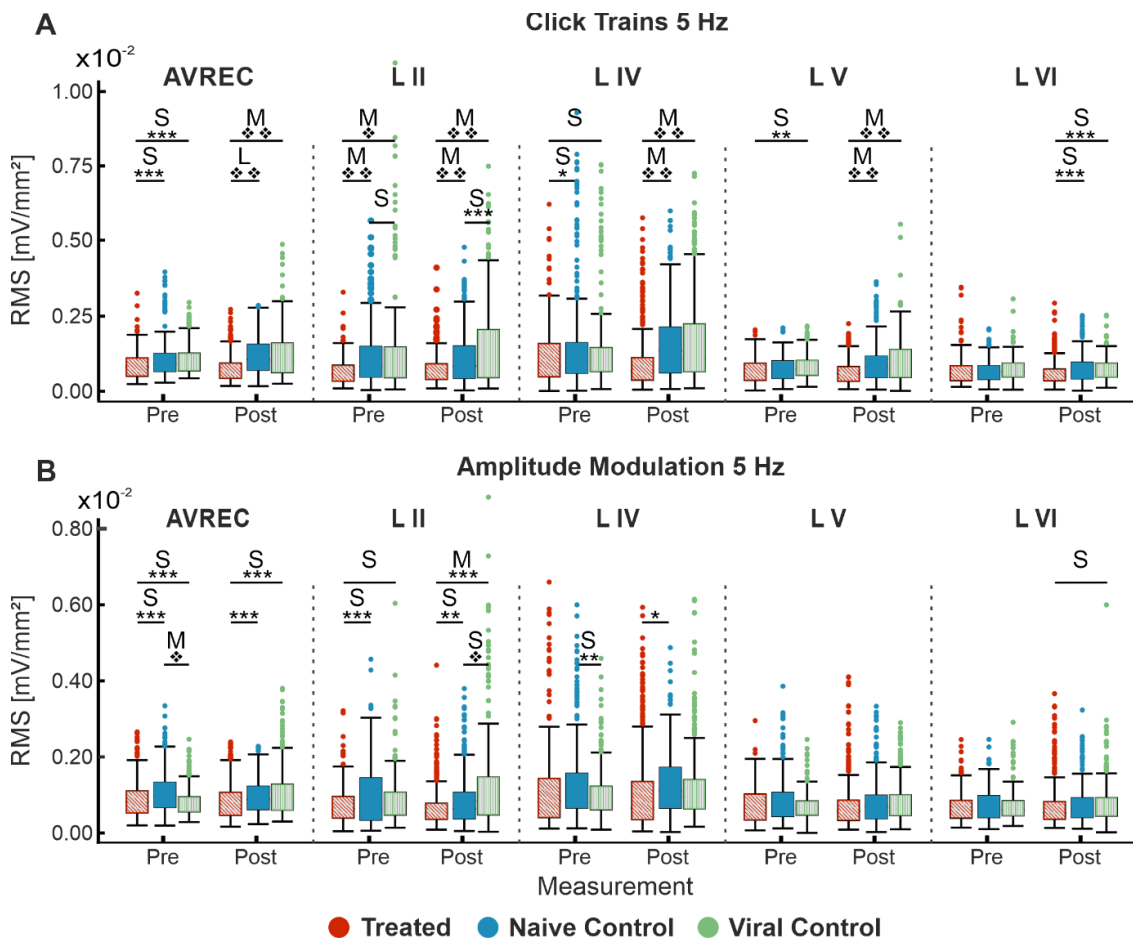
Figure 4.4 Single-trial box plots for 5 Hz. A: Single-trial box plots for CRY2olig-treated (orange), naïve (blue), and viral control (green) groups for the AVREC and layer traces (left to right) in response, measured by RMS, to the first 200 ms of 5 Hz click trains. **B:** Single-trial box plots for CRY2olig, naïve, and viral control groups for the AVREC and layer traces in RMS response to the first 200 ms of 5 Hz amplitude modulation. Student's t test and Cohen's d effect size results overlaid when significant or at least small, respectively. p < 0.05 *, <0.01 **, <0.001 ***, <0.000001❖, <1E-10❖❖, Bonferroni corrected in single-trial comparisons (n=14). Cohen's d 0.2-0.5 = small, 0.5-0.8 = medium, 0.8-1.2 = large. Figure and caption published in Deane et al. 2022a.

Within-group significant increases in activity were found in control groups pre- to post-laser in click train measurements (Table 4-4). This indicated possible amplification of ketamine-induced increase in recurrent excitation due to heat from the laser. This pre- to post-laser difference was not observed in control groups during amplitude modulated pure-tone recordings, attesting to the laser heat not being excessive and not affecting the less strongly synchronized cortical recruitment. Significant decreases in activity were found within the CRY2olig group pre- to post-laser which followed the LMM results in the click train cortical responses (Figure 4.3) of suppressed activity after VGCC clustering.

Between groups, significance was found in click train measurements between CRY2olig-treated and control groups pre-laser and post-laser in the AVREC, and all layers except pre-laser layer VI (Figure 4.4A, Table 4-3). The p value scale was dramatically increased in post-laser comparisons and the Cohen's d effect size increased from pre- to post-laser across the group comparisons by one or two effect sizes, except in layer II. Cohen's d was the most intuitive way to explore the relationships between groups pre- to post-laser and can be seen plotted, with statistical overlay, in Figure 4.5 A and B. There, the greater scale of post-laser group differences was revealed, in both 5 and 10 Hz click train measurements.

Cortical response to amplitude modulated pure tones was significantly different pre- and post-laser between the CRY2olig and at least one of the control groups for the AVREC and layer II (Figure 4.4B, Table 4-3). Only small effect sizes were found in CRY2olig and control group comparisons in the AVREC or thalamic input layers. The control group comparison revealed a medium effect size difference and significant p value pre-laser in the AVREC trace. Figure 4.5 C and D relays this relationship in Cohen's d effect sizes between group comparisons. This showed that even with the LMM-revealed pre- to post-laser suppression of activity in the CRY2olig group, population activity was more similar to controls in this condition for both 5 and 10 Hz amplitude modulation.

The viral control group appeared to be the most abnormal compared to the other groups for amplitude modulation. However, the directionality of change pre- to post-laser for the viral control group between click train and amplitude modulation was consistent (increase after laser) while the naïve control group had a slight decrease after laser in amplitude modulation measurements in contrast with its increase after laser in the click train measurements. Again, the CRY2olig group cortical activity consistently decreased after the laser, although the magnitude of significance was much less in the amplitude modulation pre- and post-laser comparisons.
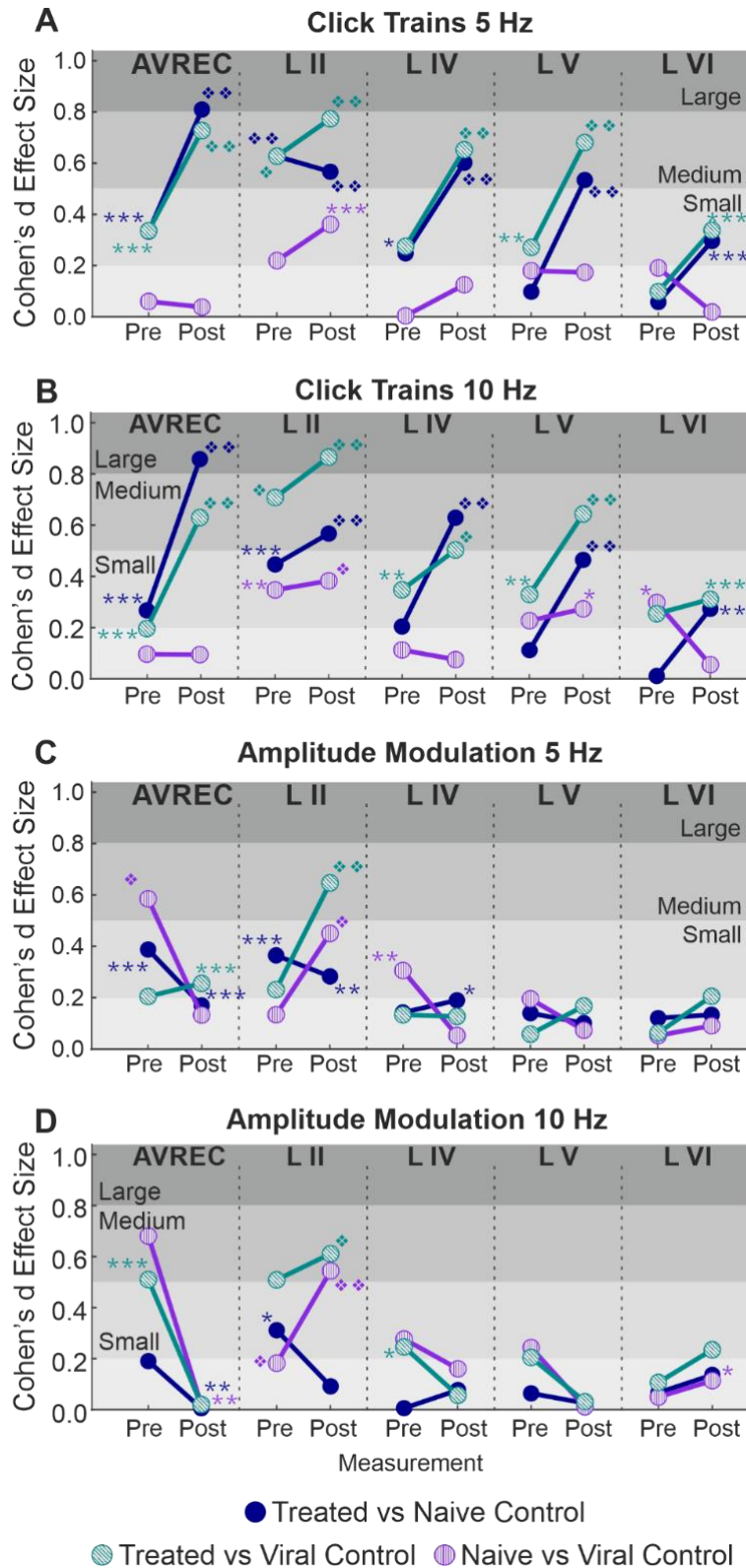
Figure 4.5 Cohen's d Effect Sizes for 5 and 10 Hz. A: 5 Hz click train Cohen's d effect sizes and overlaid student's t test p value results for comparison between CRY2olig and naïve control (blue), CRY2olig and viral control (green), and the naïve and viral control groups (purple) before and after the laser across the AVREC and layer traces (left to right). **B, C, and D:** the same comparison pre and post laser for 10 Hz click trains (**B**), 5 (**C**) and 10 (**D**) Hz amplitude modulated pure tones. Values compared were the RMS of the first 200 ms for 5 Hz and 100 ms for 10 Hz measurements. p < 0.05 *, <0.01 **, <0.001 ***, <0.000001❖, <1E-10❖❖, Bonferroni corrected. Cohen's d 0-0.2 = negligible, 0.2-0.5 = small, 0.5-0.8 = medium, 0.8-1.2 = large. Image in part published in Deane et al. 2022a.

Comparison	Measurement	Layer	Click Trains		Amplitude Modulation	
			RMS p value	RMS Cohen's d	RMS p value	RMS Cohen's d
CRY2olig vs. Naïve Control	**Pre-Laser**	**AVREC**	1.12E-05	0.33	3.91E-05	0.39
		I_II	**1.06E-12**	**0.63**	6.53E-05	0.37
		IV	2.47E-03	0.25	6.78E-02	0.14
		V	1.23E-01	0.10	4.66E-02	0.14
		VI	4.47E-01	-0.06	1.55E-01	0.12
	Post-Laser	**AVREC**	**3.58E-31**	*0.81*	6.69E-06	0.17
		I_II	**3.68E-17**	**0.57**	1.26E-04	0.28
		IV	**1.02E-19**	**0.60**	2.18E-03	0.19
		V	**8.96E-16**	**0.53**	1.12E-01	0.10
		VI	1.44E-05	0.30	4.76E-02	0.13
CRY2olig vs. Viral Control	**Pre-Laser**	**AVREC**	8.99E-06	-0.33	1.03E-01	0.21
		I_II	**9.67E-09**	**-0.63**	9.42E-03	-0.23
		IV	6.30E-03	-0.27	1.53E-01	0.13
		V	7.03E-04	-0.27	7.31E-01	0.06
		VI	2.76E-01	-0.10	4.48E-01	-0.06
	Post-Laser	**AVREC**	**3.32E-21**	**-0.72**	1.44E-07	-0.26
		I_II	**4.79E-20**	**-0.77**	**1.64E-13**	**-0.65**
		IV	**8.95E-17**	**-0.65**	2.58E-02	-0.13
		V	**5.39E-16**	**-0.68**	5.86E-03	-0.17
		VI	1.99E-06	-0.34	6.86E-03	-0.20
Control Comparison	**Pre-Laser**	**AVREC**	7.80E-01	0.06	**3.11E-08**	**0.58**
		I_II	2.17E-02	-0.22	2.92E-01	0.14
		IV	9.72E-01	0.00	3.57E-04	0.31
		V	3.44E-02	-0.18	2.02E-02	0.19
		VI	4.06E-02	-0.19	6.53E-01	0.05
	Post-Laser	**AVREC**	2.66E-01	-0.04	2.10E-02	-0.13
		I_II	2.60E-06	-0.36	**4.63E-08**	-0.45
		IV	7.90E-02	-0.12	7.17E-01	0.05
		V	3.20E-02	-0.17	1.66E-01	-0.07
		VI	6.62E-01	-0.02	2.37E-01	-0.09

Table 4-3 Between group AVREC and layer trace comparisons: CRY2olig vs Naïve control, CRY2olig vs. Viral control, and Naïve control vs Viral Control comparisons during measurements taken pre- and post-laser in the full AVREC and layer traces (top to bottom). *P* and Cohen's d results are shown for click train and amplitude modulated stimulations root mean square (RMS) for the first 200 ms. In bold are significance $p < 1.00E-7$ (Bonferroni corrected to 7.14E-08), corresponding to ❖ and ❖❖, as well as effect sizes over Medium d<0.5. Table published in Deane et al. 2022a.

Group	Layer	Click Trains		Amp Mod	
		RMS p value	RMS Cohen's d	RMS p value	RMS Cohen's d
CRY2olig	**AVREC**	**5.58E-04**	0.26	0.019	0.18
	I_II	0.266	-0.09	**0.001**	0.25
	IV	**0.0004**	0.27	0.109	0.12
	V	0.049	0.15	0.314	0.08
	VI	1.62E-01	0.10	0.227	-0.09
Naïve Control	**AVREC**	0.136	-0.11	0.297	0.08
	I_II	2.15E-01	0.09	0.888	0.01
	IV	0.630	-0.04	0.424	0.06
	V	**0.0003**	-0.27	0.377	0.07
	VI	0.021	-0.17	0.441	-0.06
Viral Control	**AVREC**	0.027	-0.19	4.234E-07	-0.45
	I_II	0.526	-0.06	**0.0004**	-0.32
	IV	0.297	-0.09	**0.0006**	-0.31
	V	2.12E-03	-0.27	0.016	-0.22
	VI	0.590	0.05	0.059	-0.17

Table 4-4 Within group AVREC and layer trace comparisons: Pre- vs post-laser comparison for CRY2olig, Naïve control, and Viral Control groups in the full AVREC and layer traces (top to bottom). *P* and Cohen's d results are shown for click train and amplitude modulated stimulations root mean square (RMS) for the first 200 ms. Table published in Deane et al. 2022a.

The relative contribution of the thalamocortical afferents were conserved through A1 VGCC clustering

We next asked the question: to what degree does thalamocortical vs intracortical contribution change after laser presentation or VGCC clustering? The motivation being that a weaker thalamic input in highly synchronized broad band click train measurements would account for the overall suppression of cortical activity. If the clustered VGCCs were actually enhancing corticothalamic feedback, it could have caused the suppression of subsequent thalamic signal in early trials which would then have lasted throughout the recording session.

Our lab has previously established relative CSD residues (RELRES) as a method of disentangling these two input streams and their relative contribution to the AVREC (Happel et al., 2010). Relative residues of CSD profiles reflect disbalance in sinks and sources (Harding, 1992). Because the neocortex is perpendicularly aligned and arranged in a laminar structure, signal from thalamic and cortical origins contribute differently to this signal, approaching each other orthogonally (Happel et al., 2010). In a neutral neuronal space, input to a population of cells would cause a sink, which would immediately transform into a source-sink-source pattern due to the movement of positive extracellular ions rushing into the newly negatively charged space. If the input was delivered vertically, as from the midbrain, the source-sink-source activity would be vertically aligned and sink source activity would be balanced in the column immediately surrounding the recording electrode. If, on the other hand, the input was laterally delivered, as from surrounding cortical circuitry, sink source activity would be laterally diffused, likely beyond the recording distance of the laminar probe (see Fig 5 in Happel 2010 for graphical clarification). Therefore, intracortical activity in our measurements would be disbalanced and not contribute to the RELRES trace.

We compared the RELRES traced before and after the laser between the 3 groups for both stimulus conditions (Figure 4.6) and only found significant difference between the CRY2olig vs naïve control group post-laser click train comparison and the control group pre-laser amplitude modulation comparison (Table 4-5). However, effect sizes were small or negligeable across all comparisons. We also ran *t* and Cohen's d tests for within group comparison between pre- and post-laser measurements. Here we did find a significant difference in the amplitude modulation pre- to post-laser conditions for the CRY2olig and naïve control groups (Table 4-6), but it again has only a small effect size. These results indicate that we did not observe profound differences of lateral intracortical processing across groups or treatments in our data set. More likely, we find largely conserved thalamocortical afferent input across groups and conditions, and hence, supporting evidence that the suppression effect observed after VGCC clustering is specific to local intracolumar processing, most likely via altered granular recurrent excitation (cf. Liu et al., 2007).
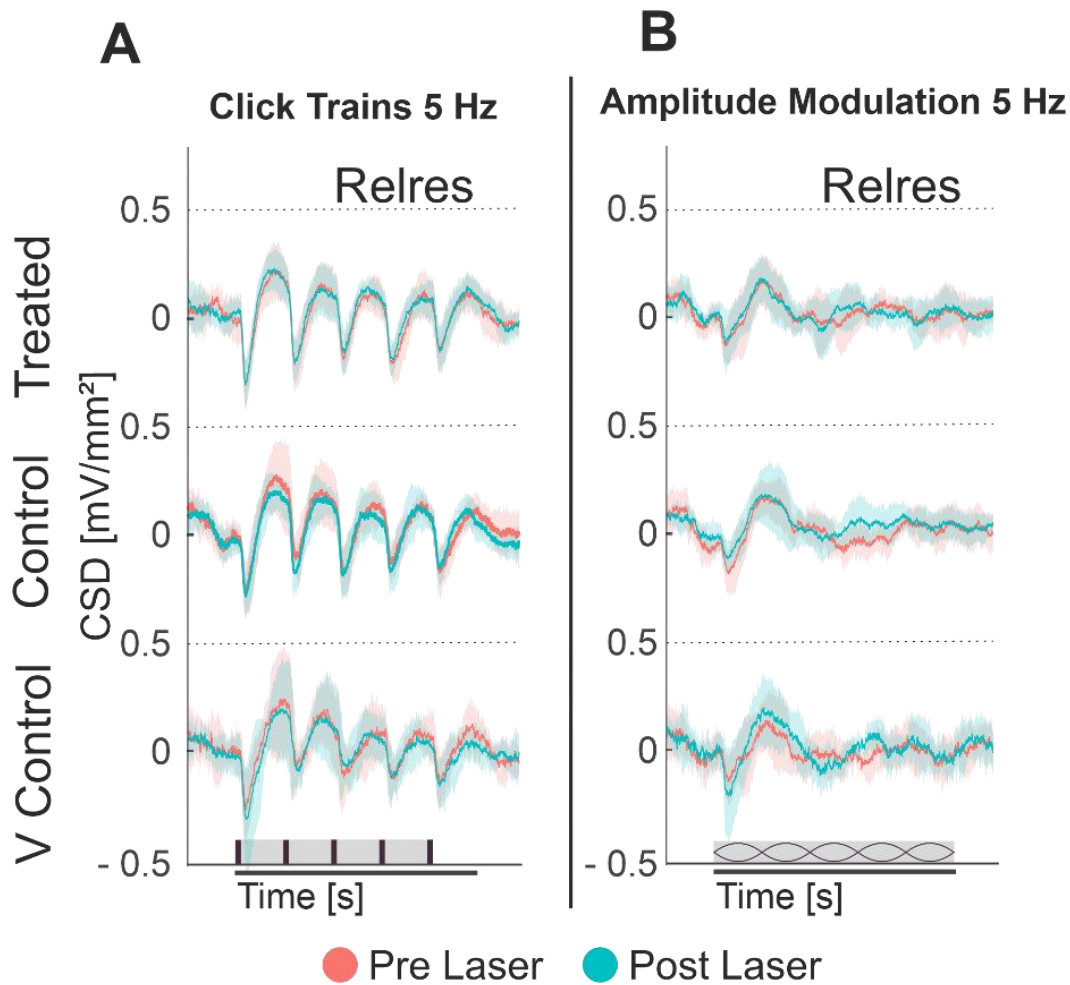
Figure 4.6 Relative Residual Traces. A: the group grand averaged (±STD) RELRES traces of Cry2olig-treated (top), naïve control (middle), and viral control (bottom) subjects in response to 5 Hz click trains over 1 second before (peach) and after (cyan) laser presentation. **B:** the same groups' traces pre and post laser in response to 5 Hz amplitude modulated pure tones. Ticks and lemons in brown on the x-axis represent temporally accurate clicks and amplitude modulation respectively.

Comparison	Measurement	Click Trains		Amp Mod	
		RMS p value	RMS Cohen's d	RMS p value	RMS Cohen's d
CRY2olig vs. Naïve Control	**Pre-Laser**	0.860	-0.02	0.011	-0.22
	Post-Laser	**0.0009**	-0.22	0.024	-0.16
CRY2olig vs. Viral Control	**Pre-Laser**	0.432	-0.07	0.053	-0.18
	Post-Laser	0.0084	0.19	0.009	0.19
Control Comparison	**Pre-Laser**	0.320	-0.09	**3.21E-05**	-0.41
	Post-Laser	0.862	-0.01	0.505	0.05

Table 4-5 Between group RELRES comparisons: CRY2olig vs Naïve control, CRY2olig vs. Viral control, and Naïve control vs Viral Control comparisons during measurements taken pre- and post-laser. p and Cohen's d results are shown for 5 Hz click train and amplitude modulated pure tone RMS for the first 200 ms. In bold are significance p < 0.05 (Bonferroni corrected to 0.0071), corresponding to *.

Group	Click Trains		Amp Mod	
	RMS p value	RMS Cohen's d	RMS p value	RMS Cohen's d
CRY2olig	0.072	-0.13	**8.38E-05**	-0.29
Naïve Control	0.345	0.07	**1.29E-07**	-0.39
Viral Control	0.143	0.13	0.4	0.08

Table 4-6 Within group 5 Hz RELRES comparisons: Pre- vs post-laser comparison for CRY2olig, Naïve control, and Viral Control groups. p and Cohen's d results are shown for 5 Hz click train and amplitude modulated pure tone RMS for the first 200 ms. In bold are significance $p < 0.05$ (Bonferroni corrected to 0.0071), corresponding to *.

The suppression of cortical activity after VGCC clustering was consistent over consecutive following responses

In the study by Heck et al. (2019), they showed a significant and reliable paired-pulse depression across consecutive responses in CRY2olig-treated cells. As mentioned previously, this was over a microscopic scale and within seconds. We looked for a similar effect in the mesoscopic and minute scale. An early hypothesis was, in fact, that we should also see an initially stronger cortical response to the first click in a train and then a pair-click suppression of following response. With 3 seconds in between each 1 second stimulus presentation, the aggregated VGCCs would theoretically have been able to reset from their refractory periods between presentations.

We checked for an effect across a series of frequency stimulations (2, 5, 10, 20, 40 Hz), 5 and 10 Hz are shown in Figure 4.7. RMS was calculated for the first and last 200 ms or 100 ms for 5 and 10 Hz respectively. Then the First RMS was divided by the Last at a single trial level. The CRY2olig and control groups were tested between groups at each pre- and post-laser measurement (Table 4-7) and within groups pre- vs post-laser for both stimulus conditions (Table 4-8). Across the board, Cohen's d effect sizes were small or negligeable. Some significant results were found: the CRY2olig vs viral control pre-laser comparison in both 5 and 10 Hz click train measurements, the CRY2olig vs naïve control post-laser comparison during 10 Hz click trains, the control group post-laser comparison for 10 Hz amplitude modulated pure tones, and the viral control pre- to post-laser comparison for both 5 and 10 Hz amplitude modulation measurements. Overall, these results do not agree with the proposed pair-click or pair-am suppression across consecutive stimuli that was observed *in vitro* for single cells.

Instead, we confirm with this analysis that the suppression seen after VGCC clustering in CRY2olig groups was systemic and that the effects lasted over a prolonged period beginning directly after clustering was initiated.
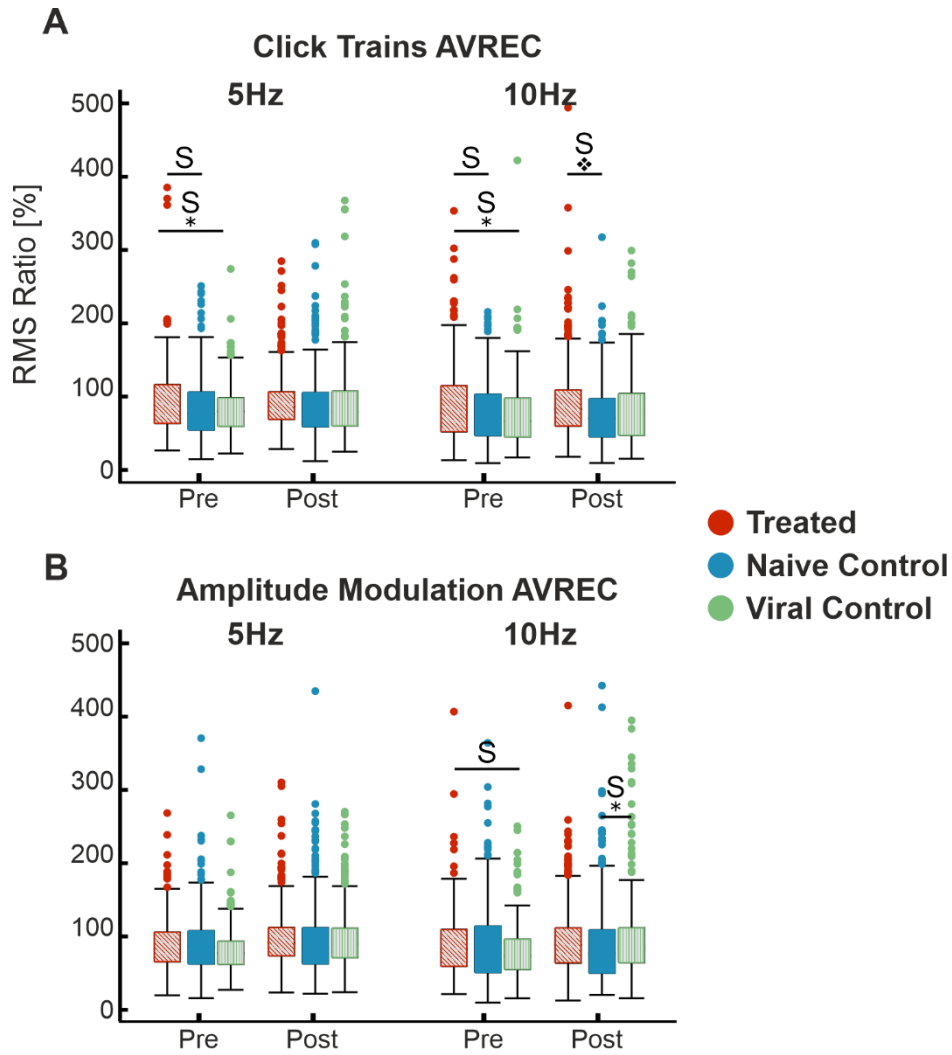
Figure 4.7 RMS Ratio; last to first response. A: Single-trial box plots for CRY2olig-treated (orange), naïve (blue), and viral control (green) groups for the AVREC trace's last 200 or 100 ms divided by the first 200 or 100 ms of stimulus presentation for 5 (left) or 10 (right) Hz click trains respectively. **B:** Single-trial box plots for CRY2olig-treated (orange), naïve (blue), and viral control (green) groups for the AVREC trace's last 200 or 100 ms divided by the first 200 or 100 ms of stimulus presentation for 5 (left) or 10 (right) Hz amplitude modulated pure tones respectively. Student's t test and Cohen's d effect size results overlaid when significant or at least small, respectively. p < 0.05 *, <0.01 **, <0.001 ***, <0.000001❖, Bonferroni corrected (n=14). Cohen's d 0.2-0.5 = small

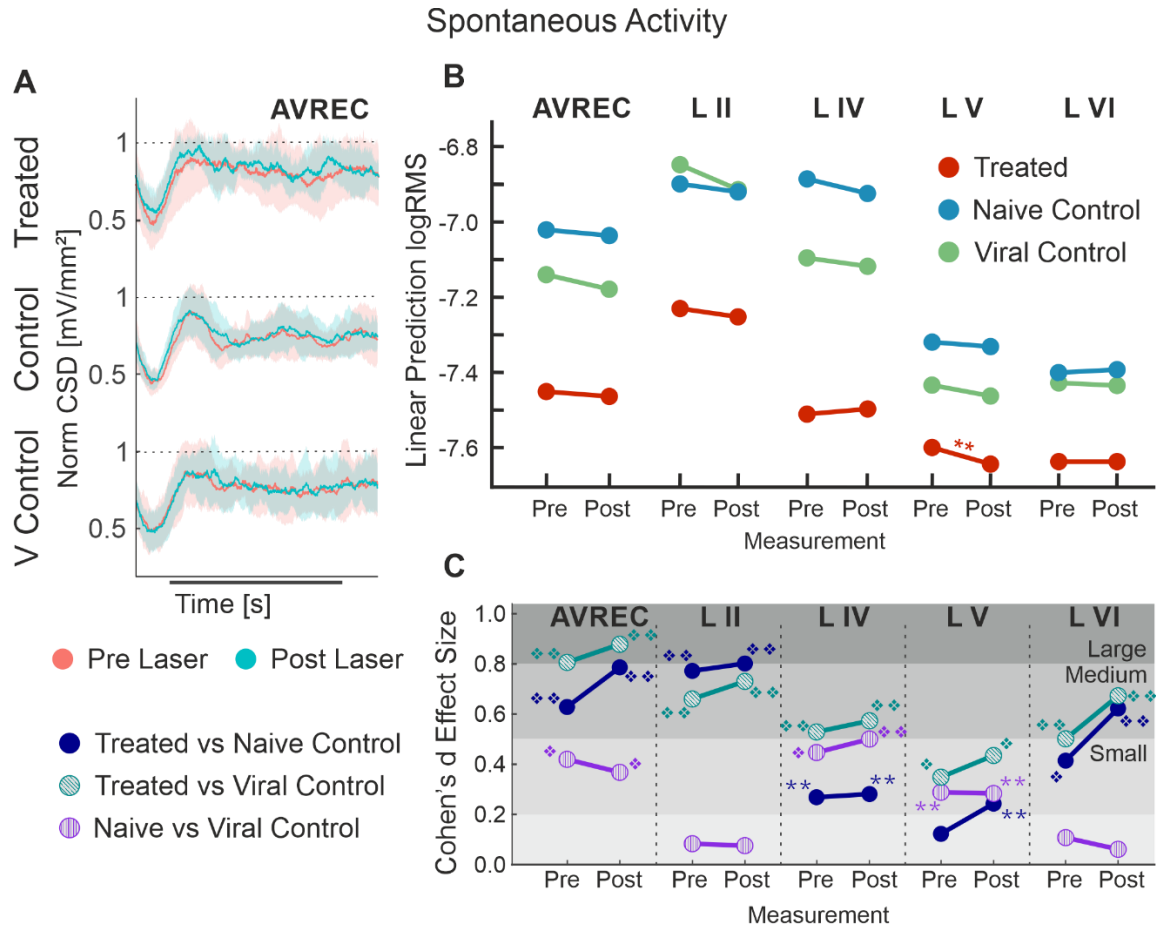| Comparison	Measurement	Click Trains 5 Hz		Click Trains 10 Hz	
		RMS % p value	RMS % Cohen's d	RMS % p value	RMS % Cohen's d
CRY2olig vs Naïve Control	**Pre-Laser**	0.004	-0.24	0.007	-0.22
	Post-Laser	0.028	-0.14	**2.30E-08**	-0.36
CRY2olig vs Viral Control	**Pre-Laser**	**0.0026**	0.26	**0.002**	0.27
	Post-Laser	0.517	0.05	0.011	0.18
Control Comparison	**Pre-Laser**	0.863	0.02	0.436	0.07
	Post-Laser	0.309	-0.07	0.020	-0.17
		Amp Mod 5 Hz		**Amp Mod 10 Hz**	
CRY2olig vs Naïve Control	**Pre-Laser**	0.779	0.02	0.820	0.02
	Post-Laser	0.211	-0.08	0.060	-0.12
CRY2olig vs Viral Control	**Pre-Laser**	0.075	0.16	0.025	0.20
	Post-Laser	0.411	-0.06	0.070	-0.14
Control Comparison	**Pre-Laser**	0.058	0.16	0.022	0.19
	Post-Laser	0.107	-0.12	**0.0019**	-0.23

Table 4-7 Between group AVREC RMS ratio comparisons: CRY2olig vs Naïve control, CRY2olig vs. Viral control, and Naïve control vs Viral Control comparisons during measurements taken pre- and post-laser. p and Cohen's d results are shown for 5 Hz (left) and 10 Hz (right) click train (top) and amplitude modulated pure tone (bottom). In bold are significance p < 0.05 (Bonferroni corrected to 0.0035), corresponding to *.

Group	Click Trains 5 Hz		Click Trains 10 Hz	
	RMS % p value	RMS % Cohen's d	RMS % p value	RMS % Cohen's d
CRY2olig	0.459	0.07	0.713	-0.04
Naïve Control	0.933	0.01	0.329	0.11
Viral Control	0.101	-0.14	0.630	-0.05
	Amp Mod 5 Hz		Amp Mod 10 Hz	
CRY2olig	0.056	-0.17	0.204	-0.14
Naïve Control	0.165	-0.11	0.720	0.04
Viral Control	**3.56E-05**	-0.35	**8.20E-05**	-0.39

Table 4-8 Within group AVREC RMS ratio comparisons: Pre- vs post-laser comparison for CRY2olig, Naïve control, and Viral Control groups. p and Cohen's d results are shown for 5 Hz (left) and 10 Hz (right) click train (top) and amplitude modulated pure tone (bottom). In bold are significance p < 0.05 (Bonferroni corrected to 0.0035), corresponding to *.

Spontaneous activity indicated systemic changes due to the presence of CRY2olig

We looked into the activity of the brain while no stimulus was playing, called spontaneous activity, to determine if effects were already visible without cortical response to stimuli. We hypothesized that the system-wide effect of voltage gated calcium channel aggregation should be noticeable also during the spontaneous brain activity which is constantly ongoing. At first glance at the pre- and post-laser AVREC traces for time window bins of 1400 ms (Figure 4.8A), there did not appear to be much difference. In fact, I dismissed this area of further analysis for over a year. However, when taking the RMS for these 1400 ms bins (of over 2 minutes of spontaneous activity), we found a massive group difference in single trial analysis, largely independent of laser stimulation (Figure 4.8B and C, between-group comparisons in Table 4-10). With a strong significant difference in the AVREC and layer traces between the CRY2olig and control groups, the only scale increase in significance pre- to post-laser was the CRY2olig and naïve control group in layer VI. Effect sizes were Large or Medium in most CRY2olig vs control comparisons, especially in the overall AVREC and in layer II. Control comparisons were also significantly different, with at most a Small effect size, in most cases but, notably, layer II and VI result in a negligeable effect size and no significant difference pre- or post-laser. Within-group comparisons of pre- to post-laser spontaneous activity (Table 4-11) found only one result of mild significance—in the naïve control group pre-laser—and negligeable effect size across the board. A linear mixed model (Figure 4.8B) over the same spontaneous activity time bins confirms that the CRY2olig group had a lower level of activity already before the laser in the AVREC, and layer traces II, IV, and VI, did not further suppress after laser presentation. Only in layer V, activity was significantly suppressed after laser stimulation in the CRY2olig group.

Figure 4.8 AVREC spontaneous activity. A: Grand averaged (±STD) AVREC traces of Cry2olig-treated (top), naïve control (middle), and viral control (bottom) subjects without stimulus presentation before (peach) and after (cyan) laser presentation. **B:** LMM effect plots for linear prediction over measurement (pre- to post-laser) for CRY2olig-treated (orange), naïve control (blue), and viral control (green) groups across the AVREC and all cortical layers without stimulus presentation. **C:** Cohen's d effect size plot for the AVREC and layer comparison CRY2olig vs naïve control (dark blue), CRY2olig vs viral control (teal), and naïve vs viral control (purple). p < 0.05 *, <0.01 **, <0.001 ***, <0.000001❖, <1E-10❖❖, Bonferroni corrected for single trial comparisons. Cohen's d 0-0.2 = negligible, 0.2-0.5 = small, 0.5-0.8 = medium, 0.8-1.2 = large.

LMM Results: Spontaneous Activity

Predictors	Layer	Estimates	SE	Statistics	df	p
	AVREC	0.312	0.230	1.358	19	0.190
	II	0.388	0.254	1.527	19	0.143
CRY2olig vs Naïve-Control : Post-Laser	IV	0.415	0.343	1.209	19	0.242
	V	0.164	0.297	0.552	19	0.587
	VI	0.208	0.179	1.159	19	0.261
	AVREC	0.431	0.242	1.779	19	0.091
	II	0.336	0.268	1.253	19	0.225
CRY2olig vs Viral-Control : Post-Laser	IV	0.625	0.363	1.723	19	0.101
	V	0.277	0.313	0.884	19	0.388
	VI	0.235	0.190	1.241	19	0.230
	AVREC	0.013	0.012	-1.085	1522	0.278
	II	-0.022	0.014	-1.538	1522	0.124
CRY2olig : Post-Laser vs Pre-Laser	IV	0.014	0.019	0.722	1522	0.470
	V	-0.044	0.016	-2.666	1522	**0.008**
	VI	-0.00	0.013	-0.015	1522	0.988

Table 4-9 LMM results for Spontaneous Activity: Comparisons run with the logRMS and the Intercept: CRY2olig-CRY2olig:Post-Laser. Therefore the intercept, CRY2olig vs Naïve control post-laser, CRY2olig vs viral control post-laser, and CRY2olig pre-laser vs post laser are compared in the AVREC and layer traces. Significant results, p<0.05, are in bold.

			Spontaneous Activity	
Comparison	Measurement	Layer	RMS p value	RMS Cohen's d
CRY2olig vs. Naïve Control	**Pre-Laser**	**AVREC**	**2.12E-22**	**0.63**
		I_II	**3.00E-39**	**0.77**
		IV	0.00012	0.27
		V	0.066	0.12
		VI	**1.18E-10**	0.41
	Post-Laser	**AVREC**	**1.81E-31**	**0.79**
		I_II	**9.60E-45**	**0.80**
		IV	0.00015	0.28
		V	0.00034	0.24
		VI	**1.41E-21**	**0.62**
CRY2olig vs. Viral Control	**Pre-Laser**	**AVREC**	**1.20E-34**	**-0.81**
		I_II	**1.04E-24**	**-0.66**
		IV	**2.78E-16**	**-0.53**
		V	9.52E-08	-0.35
		VI	**7.13E-14**	**-0.50**
	Post-Laser	**AVREC**	**2.26E-39**	**-0.88**
		I_II	**3.70E-29**	**-0.73**
		IV	**6.34E-18**	**-0.57**
		V	**5.29E-11**	-0.43
		VI	**1.43E-22**	**-0.67**
Control Comparison	**Pre-Laser**	**AVREC**	**6.53E-11**	-0.42
		I_II	0.173	-0.08
		IV	**1.83E-11**	-0.45
		V	5.16E-06	-0.29
		VI	0.074	-0.11
	Post-Laser	**AVREC**	**9.81E-09**	-0.37
		I_II	0.195	0.08
		IV	**9.18E-14**	-0.499
		V	8.65E-06	-0.28
		VI	0.312	-0.06

Table 4-10 Between group spontaneous AVREC and layer trace comparisons: CRY2olig vs Naïve control, CRY2olig vs. Viral control, and Naïve control vs Viral Control comparisons during measurements taken pre- and post-laser in the full AVREC and layer traces (top to bottom). *P* and Cohen's d results are shown for spontaneous activity root mean square (RMS) for 1400 ms bins. In bold are significance p < 1.00E-7 (Bonferroni corrected to 7.14E-08), corresponding to ❖ and ❖❖, as well as effect sizes over Medium d<0.5.

		Spontaneous Activity	
Group	Layer	RMS p value	RMS Cohen's d
CRY2olig	**AVREC**	0.368	0.06
	I_II	0.812	0.02
	IV	0.970	-0.00
	V	0.375	0.06
	VI	0.020	0.16
Naïve Control	**AVREC**	0.056	-0.11
	I_II	0.00039	-0.197
	IV	0.605	-0.03
	V	0.378	-0.05
	VI	0.924	-0.01
Viral Control	**AVREC**	0.896	-0.01
	I_II	0.778	-0.02
	IV	0.8	-0.02
	V	0.69	-0.02
	VI	0.485	0.04

Table 4-11 Within group AVREC and layer trace comparisons: Pre- vs post-laser comparison for CRY2olig, Naïve control, and Viral Control groups in the full AVREC and layer traces (top to bottom). *P* and Cohen's d results are shown for spontaneous activity root mean square (RMS) for 1400 ms bins.

An exploration of synchronization under ketamine anesthesia

Due to VGCC motility contributing to stochastic firing responses in neuronal populations, and the temporal nature of sound stimuli and auditory processing, we made several attempts at comparing neuronal synchronicity between groups. We presented two kinds of stimuli meant to differently approach temporal processing, namely the broadband, highly synchronized click trains, and the continuous but amplitude modulated pure tones, each at a range of frequencies: 2, 5, 10, 20, and 40 Hz. I will show examples of results in 5 or 10 Hz below because, under ketamine anesthesia, this was the difference between consistent click train impulse following response in 5 Hz and a more variable impulse or envelope following response in 10 Hz. Notably, ketamine anesthesia is a strong cortical synchronizer through disinhibition of recurrent feedback circuitry (Chapter 3, Deane et al., 2020). Hence, it is likely largely responsible for the non-significant results to follow and could cause speculation that effects of VGCC aggregation in awake subjects might be underestimated here. However, the suppression effects discussed above are present in this very dataset and therefore if synchronization, explored in the following ways, was not different between groups, it can be ruled out as an explanation for the changes observed after laser stimulation and VGCC clustering.

Frequency presentation was a determining factor on cortical activity synchronization to stimulus, not VGCC clustering

We recorded click train and amplitude modulation measurements for a full hour after their respective laser stimulation. These recordings were truncated into four bins with 15-minute durations containing 50 trials for each pseudorandomized frequency of stimulus presentation. With these one pre- and four post-laser measurements, we ran a vector strength analysis to determine the level to which cortical activity was synchronizing to the stimulus frequency. This was accomplished by expressing single trial peak latency times relative to the phase of the amplitude modulated pure tones, also in the click train recordings. A peak was detected within each time window of modulation—as in, within every 200 ms time bin during a 5 Hz stimulus and within every 100 ms time bin during 10 Hz. Results across groups (Figure 4.9) for 5 and 10 Hz were compared with ANOVA. There was a significant group difference in the 5 Hz click trains and 10 Hz amplitude modulation recordings over the hour of recording. However, there were not measurement or interaction effects indicating a difference of vector strength due to the laser or time period. The only clear determining factor of how well cortical activity synchronized to the stimulus was the frequency of modulation/train. 5 Hz stimuli caused a high level of synchronization of detected peaks of activity, centering around 80 % synchronization to stimuli. Click trains and amplitude modulation at 10 Hz caused only around 20 to 30 % synchronization of cortical activity to stimuli.
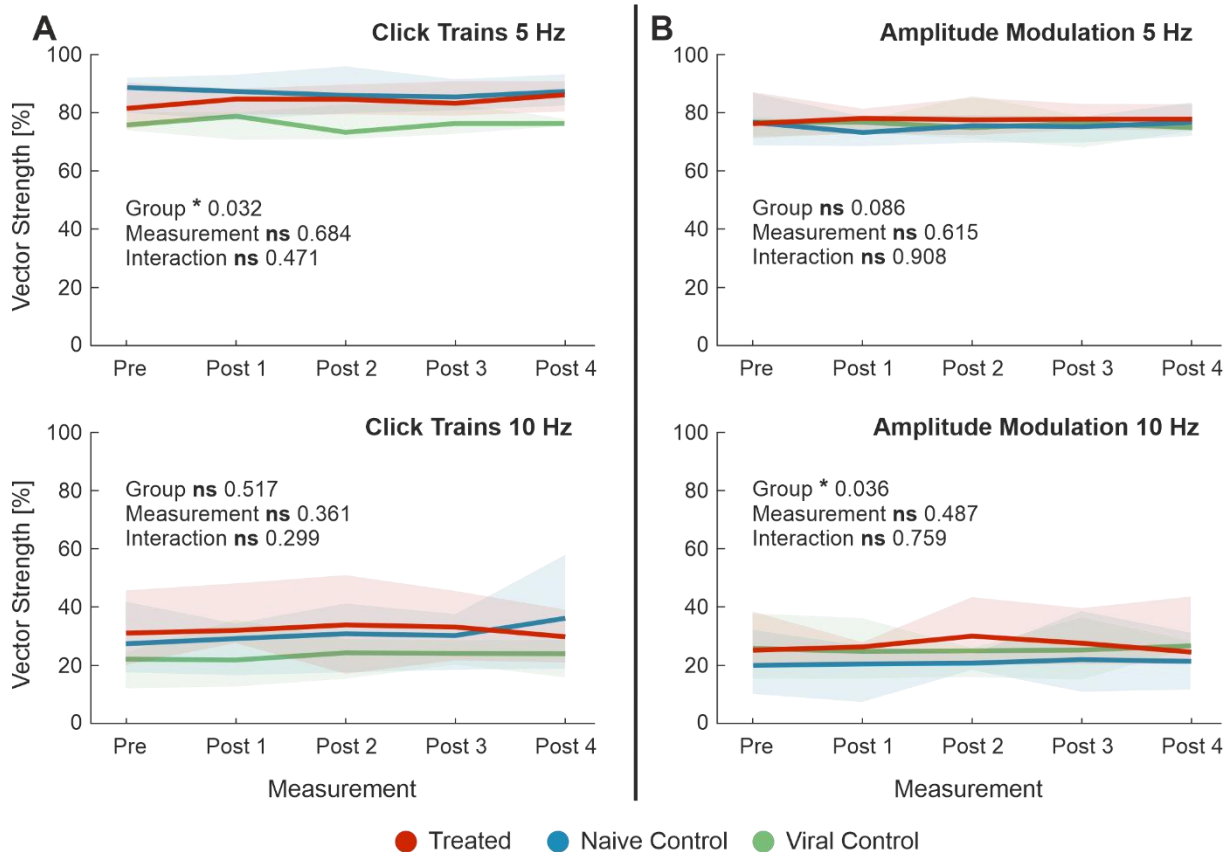
Figure 4.9 AVREC vector strength. A: 5 (top) and 10 (bottom) Hz click train AVREC vector strength for CRY2olig (orange), naïve control (blue), and viral control (green) groups across pre-laser and 4 post-layers measurements. Each post-laser measurement lasted for 15 minutes, creating an hour of post laser recording. **B:** 5 and 10 Hz amplitude modulation AVREC vector strength for CRY2olig, naïve control, and viral control groups across pre-laser and 4 post-layers measurements. Each post-laser measurement lasted for 15 minutes, creating an hour of post laser recording. ANOVA p value results of group, measurement, and interaction effects overlaid. * p < 0.05 and "ns" = not significant. Vector strength is taken by matching the latency of peak of cortical activity with the phase of the stimulus being presented to show cortical synchrony to stimulus. Note that the amplitude modulated phase was also used for click train measurements.

Spectral power and phase coherence were preserved across groups in all conditions

Next, we endeavored to explore the relationship between spectral frequencies' phase coherence and power between conditions through the cortical layers. Ketamine anesthesia, again, is known to cause a massively broadband spectral, especially in thalamic input layer IV (see previous chapter; Deane et al., 2020). Nonetheless, we expected to see a different level of spectral power representation in the gamma or possibly beta bands, reflecting the lower level of cortical activity in the CRY2olig group. Neuronal populations are a gamma oscillation generator and those along with beta oscillations are generally implicated in information processing (Gourévitch et al., 2020). Under ketamine, there was no difference between spectral bands in the power domain after a continuous wavelet analysis. Figure 4.10 contains the center layer IV channel of each group after continuous wavelet analysis for each stimulus (Figure 4.10A top row for click trains and Figure 4.10B top row for amplitude modulation). In Figure 4.10A and B bottom rows, there are the *t* value clustermaps, showing the point-wise Student's *t* test results between the CRY2olig group and both controls, where all non-significant results (p>0.05) were set to zero (black). Already here we see a very sparse clustermap with a low volume of significant results. Indeed, when performing clustermass permutation tests (500 permutations) on these comparisons, no observed clustermass was significant above chance across the spectral bands, alpha to high gamma (Figure 4.10A and B right bottom row, Table

4-12 for layer IV 5Hz post-laser; other layers, stim frequencies, and measurements not shown but had equivalent results).

We had expected to also see a difference in phase coherence between the CRY2olig and control groups. Our hypothesis was that suppressed cortical activity was a result of malfunctioning internal phase coherence dynamics (supported by the overall suppressed spontaneous activity above) due the aggregation of VGCCs disallowing normal stochastic-generating variability. However, the were no differences between groups across the phase coherence in spectral bands, alpha to high gamma, above chance (Table 4-13 for layer IV 5Hz post-laser; other layers, stim frequencies, and measurements not shown but had equivalent results).

We explored the phase coherence and power around different time windows, the first 200 ms or the full time window of stimulus presentation, as well as within all layers, the center channel or the center three channels averaged of each layer, and within all stimulation frequencies, 2, 5, 10, 20, and 40 Hz. No significant results were found between groups pre- or post-laser and no significant results were found within groups from pre- to post-laser. This may be due to the ketamine anesthesia. However, despite the utter lack of difference in spectral frequency power and phase coherence, cortical activity was suppressed due to VGCC clustering. Therefore, the suppression cannot be explained, under these conditions, to be due to power or phase coherence differences in response to stimuli presentation.
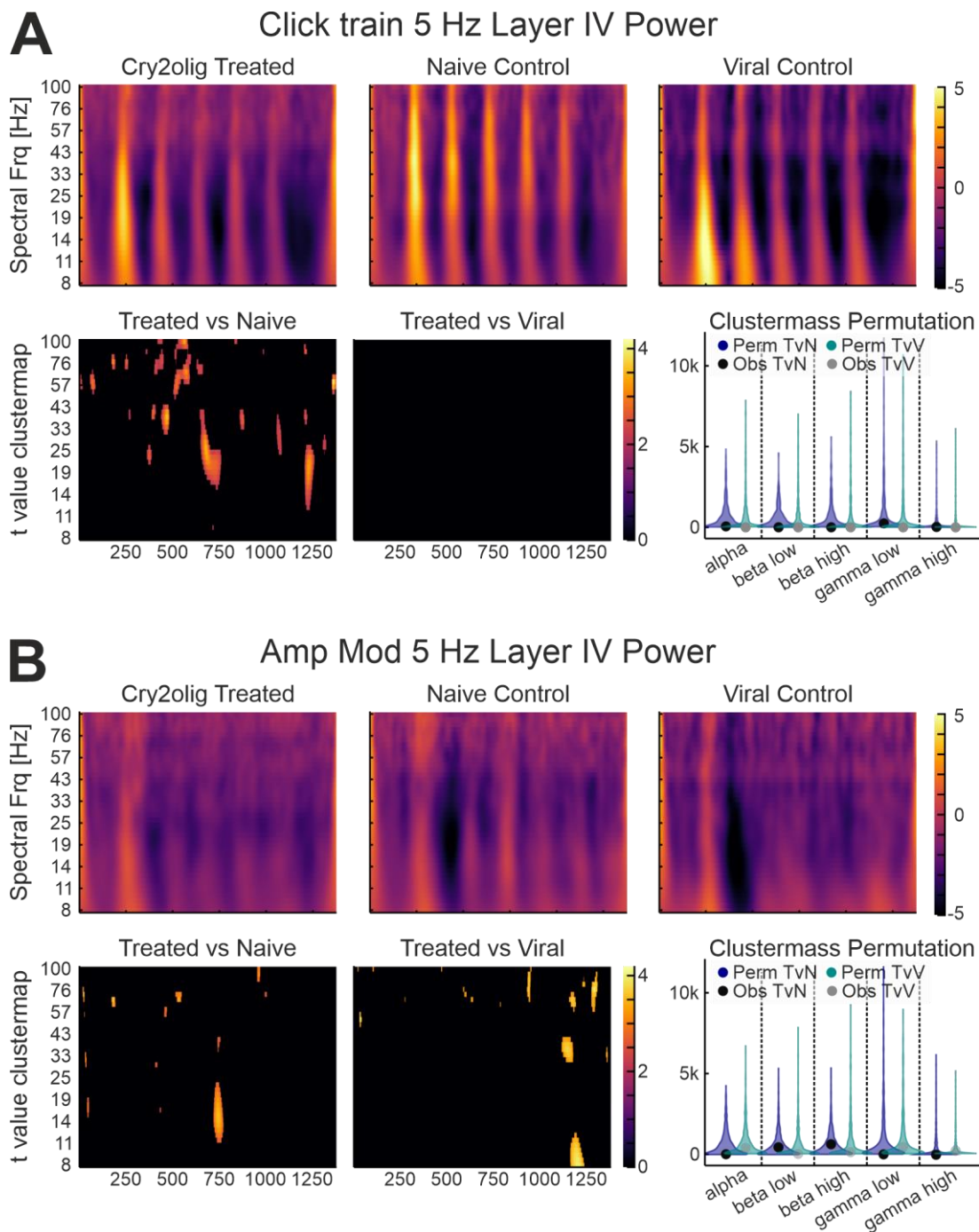
Figure 4.10 Example of Continuous Wavelet Transform, Power. A top row: Cry2olig-treated (left), naïve control (middle), and viral control (right) grand average power CWT heatmap of layer IV during 5 Hz click trains. The colormap denotes higher power in brighter areas. **A bottom row, left:** CRY2olig vs naïve control and CRY2olig vs viral control clustermap—result of point by point Student's t-test where are resulting non-significant points are set to zero (black), leaving only clusters of significance. **A bottom row, right:** violin plots showing clustermass permutation distribution (purple and teal per comparison) of randomized subjects into groups overlaid with observed count of clustermass (black and grey dots per comparison) per spectral band. Alpha: 8:12 Hz, beta low: 13:18 Hz, beta high: 19:30 Hz, gamma low: 31:60, gamma high: 61:30. **B:** the same groups, layer, comparison, and permutation tests for 5 Hz amplitude modulated pure tones.

		Power: Click Train 5 Hz			Power: Amp Mod 5 Hz		
		p value	mean	std	p value	mean	std
	alpha	0.648	578.68	839.58	0.729	577.12	757.89
	beta low	0.804	502.14	666.32	0.35	513.22	693.65
CRY2olig vs Naïve Control	**beta high**	0.78	554.78	875.70	0.291	559.12	738.54
	gamma low	0.434	809.76	1554.18	0.88	875.92	1484.95
	gamma high	0.541	347.07	819.15	0.781	386.29	818.345
	alpha	0.576	550.47	1121.30	0.422	566.99	850.10

		p value	mean	std	p value	mean	std
CRY2olig vs Viral Control	beta low	0.645	506.40	1023.64	0.73	488.65	869.72
	beta high	0.673	577.12	1264.28	0.506	585.09	1080.85
	gamma low	0.811	831.23	1756.32	0.379	831.31	1449.85
	gamma high	0.675	346.49	890.78	0.274	323.62	743.90
Control Comparison	alpha	0.625	475.88	843.80	0.788	500.00	665.28
	beta low	0.676	455.72	773.01	0.729	422.73	683.48
	beta high	0.709	546.11	942.58	0.249	483.84	972.84
	gamma low	0.743	915.06	1624.14	0.142	716.82	1394.48
	gamma high	0.668	389.71	840.16	0.129	301.52	600.87

Table 4-12 Between group Power CWT spectral band clustermass comparison. CRY2olig vs Naïve control, CRY2olig vs. Viral control, and Naïve control vs Viral Control comparisons during measurements taken post-laser. p value results and corresponding mean and std are shown for 5 Hz click trains (left) amplitude modulated pure tones (right).

		Phase: Click Train 5 Hz			Phase: Amp Mod 5 Hz		
		p value	mean	std	p value	mean	std
CRY2olig vs Naïve Control	alpha	0.49	461.494	839.58	0.729	577.12	757.89
	beta low	0.872	411.57	666.32	0.35	513.22	693.65
	beta high	0.693	473.39	875.70	0.291	559.12	738.54
	gamma low	0.273	705.12	1554.18	0.88	875.92	1484.95
	gamma high	0.954	298.81	819.15	0.781	386.29	818.345
CRY2olig vs Viral Control	alpha	0.974	474.07	1121.30	0.422	566.99	850.10
	beta low	0.987	408.83	1023.64	0.73	488.65	869.72
	beta high	0.969	452.30	1264.28	0.506	585.09	1080.85
	gamma low	0.982	724.71	1756.32	0.379	831.31	1449.85
	gamma high	0.652	299.64	890.78	0.274	323.62	743.90
Control Comparison	alpha	0.721	485.56	843.80	0.788	500.00	665.28
	beta low	0.184	422.72	773.01	0.729	422.73	683.48
	beta high	0.163	462.97	942.58	0.249	483.84	972.84
	gamma low	0.825	698.63	1624.14	0.142	716.82	1394.48
	gamma high	0.819	283.17	840.16	0.129	301.52	600.87

Table 4-13 Between group Phase Coherence CWT spectral band clustermass comparison. CRY2olig vs Naïve control, CRY2olig vs. Viral control, and Naïve control vs Viral Control comparisons during measurements taken post-laser. p value results and corresponding mean and std are shown for 5 Hz click trains (left) amplitude modulated pure tones (right).

Low phase, high amplitude cross frequency coupling did not reveal a difference in information propagation between groups

A final step into spectral analysis was to check the level of theta-gamma (not shown) and delta-gamma cross-frequency coupling between groups. Low oscillation phase coupled to high oscillation amplitude has been implicated in information transfer across neural tissue (Bonnefond et al., 2017; Gourévitch et al., 2020). This is partly due to the low oscillation frequencies having more power to travel through tissue, which is naturally a low-pass filter (Hindriks et al., 2016), and the higher oscillation frequencies, having more capacity for information content, riding those waves. While this experiment was conduction under ketamine anesthesia, we considered that the suppressed cortical activity might affect information transfer across the brain, especially in cases of highly synchronized cortical recruitment as with click trains.

Figure 4.11 demonstrates how Table 4-14 results were determined, which were then compared between-group (Table 4-15) and within-group (Table 4-16). That is, the single center channel to each layer per subject trial was filtered for delta, low gamma, and high gamma. The amplitude of each gamma band was taken and averaged at each phase of the delta band to

create an amplitude distribution. A value, h, was assigned as the maximum minus the minimum amplitude on this distribution. h was compared against a surrogate distribution created by randomizing the filtered signals per trial and calculating h for each surrogate test. Where the observed h fell on this distribution, the z score was taken and then z was averaged across groups for the final score and compared between and within groups pre- and post-laser.

In the 5 Hz click train and 5 Hz amplitude modulation measurements, there were several between-group comparisons where significance was found. However, the Cohen's d effect sizes were mostly negligeable and at most Small. The significant results were peppered through pre- and post-laser comparisons. There were two within-group comparisons found to be significant, CRY2olig group at 5 Hz amplitude modulation and viral control group at 5 Hz click train, but all Cohen's d results within groups were negligeable. These results reflect each frequency presentation, layer, and corresponding theta-gamma cross frequency results as well.

We found no difference in delta gamma or theta gamma coupling that would indicate differences in information propagation due to VGCC clustering, time, or laser presentation under ketamine anesthesia. I would suggest a follow-up study in awake animals with this analysis again because I believe the hypothesis would prove truer in the condition where cross-cortex information transfer is not suppressed with anesthesia.
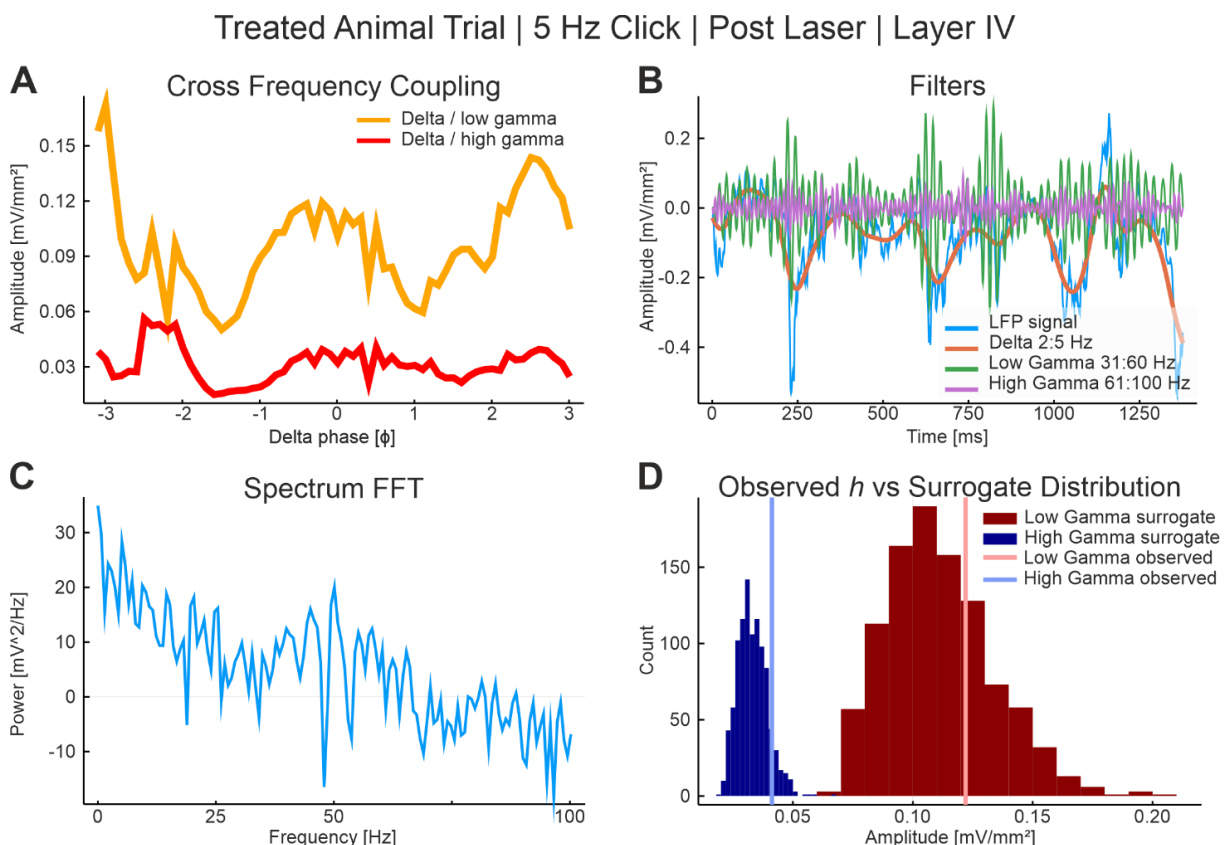

Figure 4.11 Example of a single animal trial Delta Gamma Cross Frequency Coupling. A: Low gamma (31:60 Hz) and high gamma (61:100 Hz) amplitude in relation to Delta (2:5 Hz) phase of the center channel of layer IV for one animal trial during a 5 Hz click train. **B:** the raw LFP signal from this channel and trial (blue) overlaid with the filtered signal for delta (orange), low gamma (green), and high gamma (purple). **C:** A fast Fourier transform (FFT) power spectrum for this channel and trial, power over spectral frequency. **D:** The observed h, or amplitude max-min over the cross frequency coupling analysis (light blue and red per gamma band) over a surrogate distribution of randomized trial gamma and delta bands (blue and red per gamma band).

Cross Frequency	Measurement	Stim Type	CRY2olig z	Naïve Control z	Viral Control z
Delta vs Low Gamma	Pre-Laser	Click Train 5 Hz	-6.083	-5.941	-6.042
	Post-Laser	Click Train 5 Hz	-6.115	-5.914	-5.896
	Pre-Laser	Amp Mod 5 Hz	-6.026	-6.082	-5.964
	Post-Laser	Amp Mod 5 Hz	-6.153	-6.132	-5.953
Delta vs High Gamma	Pre-Laser	Click Train 5 Hz	-6.096	-5.964	-6.050
	Post-Laser	Click Train 5 Hz	-6.115	-5.981	-5.928
	Pre-Laser	Amp Mod 5 Hz	-6.024	-6.154	-6.012
	Post-Laser	Amp Mod 5 Hz	-6.127	-6.152	-5.960

Table 4-14 Cross Frequency Coupling results per group in layer IV. For delta vs low gamma and delta vs high gamma cross frequency coupling pre- and post-laser of each 5 and 10 Hz click train and amplitude modulated measurements, Cry2olig-treated, naïve control, and viral control z values are given. Z corresponds to the mean distance of h to the mean of its surrogate distribution (see **Figure 4.11D**)

Comparison	Measurement	Cross Frequency	Click Train 5 Hz p value	Click Train 5 Hz Cohen's d	Amp Mod 5 Hz p value	Amp Mod 5 Hz Cohen's d
CRY2olig vs Naïve Control	Pre-Laser	Delta vs **Low** Gamma	**0.045**	-0.17	0.372	0.08
	Post-Laser		**0**	-0.27	0.666	-0.03
	Pre-Laser	Delta vs **High** Gamma	0.053	-0.17	**0.036**	0.18
	Post-Laser		**0.0057**	-0.18	0.607	0.03
CRY2olig vs Viral Control	Pre-Laser	Delta vs **Low** Gamma	0.5324	-0.06	0.371	-0.08
	Post-Laser		**0**	-0.30	**0.0002**	-0.27
	Pre-Laser	Delta vs **High** Gamma	0.479	-0.07	0.859	-0.02
	Post-Laser		**0.0003**	-0.26	**0.0019**	-0.22
Control Comparison	Pre-Laser	Delta vs **Low** Gamma	0.176	0.13	0.092	-0.16
	Post-Laser		0.762	-0.02	**0.0016**	0.23
	Pre-Laser	Delta vs **High** Gamma	0.233	0.11	**0.032**	-0.20
	Post-Laser		0.346	-0.07	**0.0005**	-0.26

Table 4-15 Between group CFC z value comparison in layer IV. CRY2olig vs Naïve control, CRY2olig vs. Viral control, and Naïve control vs Viral Control comparisons during measurements taken post-laser for delta vs low gamma and delta vs high gamma. p and Cohen's d effect size results shown for 5 Hz click trains (left) amplitude modulated pure tones (right). In bold are significance p < 0.05, corresponding to *.

Group	Cross Frequency	Click Train 5 Hz p value	Click Train 5 Hz Cohen's d	Amp Mod 5 Hz p value	Amp Mod 5 Hz Cohen's d
CRY2olig	Delta vs **Low** Gamma	0.547	0.05	**0.018**	0.18
	Delta vs **High** Gamma	0.718	0.03	0.060	0.14
Naïve Control	Delta vs **Low** Gamma	0.692	-0.03	0.384	0.07
	Delta vs **High** Gamma	0.787	0.02	0.978	-0.002
Viral Control	Delta vs **Low** Gamma	**0.029**	-0.19	0.872	-0.01
	Delta vs **High** Gamma	0.063	-0.17	0.443	-0.07

Table 4-16 Within group CFC z value comparison in layer IV. Pre- vs post-laser comparison for CRY2olig, Naïve control, and Viral Control groups. p and Cohen's d effect size results shown for 5 Hz click trains (left) amplitude modulated pure tones (right). In bold are significance p < 0.05, corresponding to *.

Staining procedures

Throughout the course of this study, many attempts were made to back up findings with histological results. The lentivirus containing CRY2olig could unfortunately not be successfully developed with a fluorescent protein and was provided to us with an EOS tag. We used an HE staining protocol to visualize EOS in the perfused and fixed slices of experimental animal brains and determined that it could not show the effectiveness of cross-linking *in vivo* due to the prolific presence of EOS in neural tissue (Figure 4.12; see Rieder et al. 2015 Figure 5). From that point, several CRY2olig lentiviruses were attempted by companies with mScarlet

but none were deemed fit for use. Therefore, we were unfortunately unable to provide evidence of cross-linking using IHC. This is a clear point of contention in our study and will be rectified in the future after the completion of this PhD.

Virus, containing Cry2olig, was injected 300 and 600 µm deep at the three sites across the A1, 1 mm apart. Each of the 6 injection sites received 207 nl of virus (23 nl x 9, every 3 seconds), totaling 1,242 nl across the A1. Lentiviruses have been shown as efficient in their role of infecting neurons *in vivo* in, amongst other species, rats (Naldini et al. 1996a; Naldini, et al. 1996b). While the spread of the virus is limited, it has been shown that 200 nl injection volumes diffuse within a spherical region with a diameter around 200-600 µm (Desmaris et al. 2001; Osten et al. 2006 see Figure 13.3). Therefore, between each subject, we assumed a large coverage of the A1 down the depth of the cortical column. We also assumed that cross-linking was at least minimally effective due to consistent effects in CRY2olig groups and confirmation of the CRY2olig/CaV2.1 N-terminus pairing in Heck et al. (2019).

Figure 4.12 shows endogenous Citrine in the perfused and fixed slices of the Citrine knock-in mouse line, confirming the presence of Citrine broadly distributed throughout neural tissue of our subject line. The same laser stimulation and intensity was provided to wild type slices, CRY2olig exactly the same as the knock-in slices, as a control.

We further endeavored to boost the endogenous Citrine with several types of nanobody GFP boosters, in order to visualize its presence in colocalization with both bassoon or CaV2.1 (Figure 4.12 features anti-BSN antibodies and GFP-Booster at 40x magnification). Our efforts led to largely unspecific staining, as seen here.
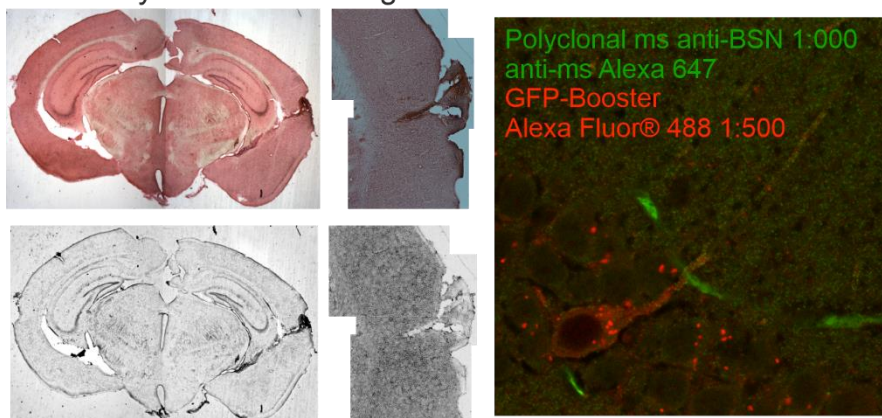
Figure 4.12 Overall Staining Results. A: Hematoxylin-eosin (HE) staining. **B:** Co-localization staining for polyclonal mouse against bassoon (BSN) 1:1000 with secondary anti-mouse Alexa 647 (green) and GFP-Booster Alexa Fluor 488 1:500 seen at 40x magnification. **C:** Confirmation of endogenous Citrine throughout hippocampus and A1 (not shown) compared to wild type mice, magnification 10x.
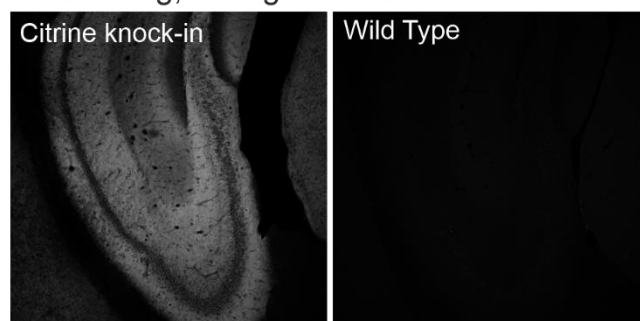
Discussion of project 2

VGCC clustering time course and laser-heat have opposing effects.

The overall activity level in the CRY2olig group was already suppressed compared to the controls before the laser, during stimulus presentation (Figure 4.3) and spontaneous activity (Figure 4.8). This pre-laser suppression compared to controls is potentially due to a light-activated clustering during the surgical and experimental procedures. However, additional and significant activity suppression after the laser presentation during experimentation was observed in in the CRY2olig-treated group. Contrastingly in the control groups, we often found increased activity after the laser illumination. Laser-induced increases in neuronal activity have been observed in multiple studies (Arias-Gil et al. 2016; Brunk et al. 2019; Owen et al. 2019; Stujenske et al. 2015). The systematic suppression effect of the VGCC clustering consistently counteracted this laser-induced increase. Therefore, our methodological approach, if anything, underestimates the effect strength of VGCC clustering on sound-evoked cortical responses.

The level of cortical activity during spontaneous recordings, significantly lower in the CRY2olig group, remained constant throughout experiments, with very little dependance on the laser. This indicates two things, although we would need to conduct further research to explore their reality. The first is that the CRY2olig, and presumably its clustering of VGCC, once initiated, results in a systemic, long-term change. In the click train and amplitude modulated pure-tone responses, we saw a clear decrease—the suppression effect—after laser stimulation. However, when not further exacerbated by the recruitment of microcircuitry in response to thalamocortical input, spontaneous activity did not further suppress after laser presentation and subsequently refreshed VGCC clustering. We have also observed a lack of recovery over 60 minutes, which mismatches *in vitro* microbiological results (see Taslimi et al., 2014 Fig. 1, Heck et al. 2019). This observation along with the current spontaneous activity findings suggest that baseline activity does not recover or recovers on a much slower timescale than the de-aggregation of VGCCs. The second observation was that the robust nature of neuronal population activity had been negatively affected and that stimulus response circuits using the affected networks where then suppressed to different levels depending on the amount of circuitry used. As in, in response to the highly synchronized, tonotopically activating, click trains, thalamic input layers IV and V were more strongly suppressed after the laser than in response to the narrow spectrum, amplitude modulated pure tone. Therefore, refreshing VGCC aggregation with laser presentation further suppressed responses to amplitude modulated pure tones and click trains in a level and laminar dependent way.

Columnar suppression of impulse responses due to VGCC clustering

We compared the CRY2olig group pre- to post-laser and between groups post-laser with a linear mixed model (LMM, Figure 4.3). Results indicated that pre- to post-laser suppression of activity was significant across most layers after VGCC clustering across both stimulus types. Contrasting the VGCC-induced suppression, there was an overall tendency in the control groups toward increased activity after laser stimulation, discussed above. The LMM analysis revealed significant between-group comparisons after the laser for some of the most pronounced effects on cortical layer activity. Specifically, VGCC clustering caused a significant reduction of the overall columnar response strength, compared to controls, measured by the

AVREC and sound-evoked synaptic activity in cortical layer V during the click train stimulation, and significantly lower activity in layer II during AM-stimulation. VGCC aggregation had differential effects on sensory processing of stimulus classes that cause broad spectral and highly synchronized thalamocortical synaptic input, compared to population activity, which relies more on temporal integration of intracortical synaptic inputs.

To further tease apart group differences, single-trial, Bonferroni corrected, Student's t tests were calculated pre- and post-laser between all groups (Figure 4.4). Results were contextualized with Cohen's d effect sizes (Figure 4.5). Responses to click trains were already significantly different between CRY2olig and control groups before laser-induced VGCC aggregation for the AVREC, and sound-evoked activity recorded in cortical layers IV and V. Effects increased in magnitude of significance as well as in effect size after laser presentation. Amplitude modulation comparisons yield much lower significance, when found, post-laser, and only had a medium effect size in post-laser layer II and in the pre-laser AVREC control comparison. The less strongly synchronized recruitment of synaptic populations with this stimulus class most likely explains the less prominent effects.

Our results indicate that the clustering presynaptic VGCC is detrimental to overall population activity—hence the suppression—which is exacerbated in circumstances of higher cortical recruitment. Such recruitment of recurrent excitation circuits is found particularly during the representation of salient and behaviorally relevant stimuli (Kato et al. 2017). Additionally, recurrent excitation in thalamic input layers of sensory cortex may play a central role especially for enhancing threshold-near stimuli (Happel & Ohl, 2017; X.-J. Wang, 2008). Our study now hints that the neural basis of such circuit-derived enhancement in the sensory cortex may be at least partly rooted in the presynaptic dynamics of VGCCs— and in light of Chapter 3, we may even underestimate the effects of VGCC aggregation in the awake subjects.

Amplification disruption of thalamic input layers.

Recurrent excitation in layer IV has been implicated as the dominant circuit activity contributing to the AVREC response under ketamine (Deane et al., 2020; Happel et al., 2010). It is henceforth unsurprising that this and thalamic input layer V most closely resembled the AVREC in the click train measurement cortical responses (Figure 4.3A). In single-trial group comparisons, there was a two-fold increase in effect size and an overwhelming increase in the magnitude of significance in the AVREC pre- to post-laser. This two-fold increase is reflected in as a one- or two-fold increase also in layers IV and V.

The reduction of impulse responses and ongoing responses after click train stimulation (Figure 4.2) can therefore be explained by the fact that the stochastic firing variability of individual synapses, reduced by the clustering of VGCCs, plays an important role in recurrent excitation in layer IV. By aggregating VGCCs we change the temporal resolution of recurrent excitation and, therefore, disrupt the gain function of cortical amplification circuits.

Dynamic supra- and infragranular responses

Click-train evoked responses in supragranular layers showed an opposing trend compared to the other layers: VGCC clustering led to a slight increase of activity. Pre-laser activity in the controls was generally lower in this layer during AM tones compared to click trains, owing

likely to a high volume of cross-columnar activity through the dense network in supragranular layers following click stimuli. While the heat from the laser, described above, would be most intense on the surface of the cortex, it did not cause an increase in activity across both types of stimulation in supragranular layers. This suggests that the effect of the laser, the VGCC clustering, and the higher recruitment of click trains coincide in a non-linear fashion. What might be concluded from this is that the network is more sensitive to light effects during high recruitment than clustering effects, therefore causing the increase in activity after clustering in the click train condition, but that suppression after clustering is more broadly consistent across different conditions (Figure 4.3).

Layer VI in the cortical microcircuit is largely seen as the main feedback to the thalamus, completing a cortico-thalamic loop that has been discussed with respect to cortical gain during sensory processing and perception (Alitto & Usrey, 2003; Homma et al., 2017; Saldeitis et al., 2021). While these layers are generally less active under anesthesia, during click train cortical responses, there was a significant increase in cortical activity after VGCC clustering (Figure 3A, LVI). Effects on aggregation in other layers may have caused a disinhibition of synaptic activity in deeper layers, explaining these opposing effects. Such disinhibitory feedback on the cortical gain has been related to Layer IV corticothalamic neurons in the auditory cortex (Williamson & Polley, 2019). Despite this possibly enhanced corticothalamic feedback, we confirmed thalamic contribution to the signal was largely unaltered between conditions (treatment or laser stimulation, Figure 4.6).

Undisrupted synchrony in the cortex

Due to the contribution of VGCC motility to stochastic population dynamics, several variations on the theme of analyzing cortical synchrony were performed. In conditions where activity was suppressed, we hypothesized that we would see some neuronal desynchronization, whether in phase coherence, spectral power (Figure 4.10), vector strength (Figure 4.9), or delta gamma cross-frequency-coupling (Figure 4.11). We found the synchronization dynamics, heavily influenced by strong cortical synchronizer, ketamine, to be preserved across groups and measurements. Very little significant difference and, at most, Small effect sizes were found in between- and within-group comparisons for each of these measures. This was a surprising finding, especially given the very significantly suppressed cortical activity in spontaneous recordings throughout the experiments and the already suppressed pre-laser activity in each stimulus condition for the CRY2olig group.

This suppression is therefore not explained by a lack of temporal precision, shown with vector strength analysis over two stimulation frequencies. It is not explained by a reduction of phase coherence or power, shown with continuous wavelet transform spectral analysis. This suppression also does not cause a difference in delta or theta phase and low or high gamma amplification, under anesthesia. However, the highly synchronized cortical recruitment of click trains led to a following impulse response in CRY2olig groups post-laser which clearly counteracted what would have been an increase in cortical response—seen in controls—and caused a more dramatic decrease in activity after the laser than with the less synchronized amplitude modulated input and during spontaneous activity. These analyses should be run again in an awake and behaving follow-up study, however suppression already exists in this dataset and therefore there must be some other feature explaining it – namely the loss of variability due to VGCC clustering.

Further steps in histology

Lentiviruses can deliver relatively large sequences to nearly all mammalian cell types and are efficient at infecting neurons *in vivo*. In our study so far, we were not able to procure a lentivirus with a fluorescent reporter gene and we were unable to provide evidence of cross-linking between the VGCC pores and the CRY2olig protein with the available EOS reporter.

We stand by the results demonstrated above in the neurophysiological recordings. We believe that the consistent observation of suppression of cortical response to stimuli after laser stimulation, and the fact that activity is equally suppressed in the CRY2olig group spontaneous activity through the duration of recording, belays the fact that the *in vitro* established CRY2olig VGCC cross-linking was at least partially successful—and this indicates that, if anything, our results are an underestimation of effects if cross-linking was indeed only minimally effective. However, we acknowledge the validity, that the lack of IHC confirmation may make our results less tenable for publication so far.

Regarding this, and as a future direction for this project, there are good prospects for the development of this lentivirus—with a protocol for visualizing it in slices after *in vivo* transfection—in the Heine Lab at the Johannes-Gutenberg University in Mainz. When cross-linking can be confirmed, our results have already been received with interest and will be published in a peer-reviewed journal. Until such a time, the work will rightly face criticism from the broader scientific community that we cannot, beyond a reasonable doubt, attribute the specific changes observed to VGCC aggregation in the auditory cortex. There is growing interest in moving findings through scales, micro- to meso- to macroscopic, in neuroscience and connecting single-neuron to neuronal population, brain-wide, and organism activity.

Conclusion

In this study, we used CRY2olig to aggregate VGCCs in the A1 of transgenic mice. By using laminar CSD analysis *in vivo,* we could show that manipulation of lateral membrane motility of VGCCs in the presynaptic terminals significantly modulates population activity in a laminar dependent manner. Our results indicate a more general loss of function in sensory processing due to the aggregation of these channels, despite an artificially created increase in initial firing response at a single-unit level (Heck et al., 2019; Heine et al., 2020). In comparing results between click train stimuli, amplitude modulated pure tones, and spontaneous activity, we argue that this loss of functionality is most critical in cases of strong cortical recruitment due to highly synchronized synaptic inputs—a key feature of recurrent excitation in sensory cortex during processing of salient, behaviorally relevant sensory cues.

Chapter 5: Complexity in neuroethology; comparing two auditory niches in bats and mice

This chapter builds the basis for the recent pre-print publication, *The auditory cortex of bats has a better signal to noise ratio and lower inter-trial variability in response to stimuli trains than mice* by Deane et al., 2022b. The current text contains parts of the pre-print and additional data and content.

Background

The brains and bodies of black 6 mice (*Mus musculus)* and seba's short-tailed bats (*Carollia perspicillata)* weigh roughly the same. In some places, bats are referred to as "flying mice" due to the visual similarity of many bat species and rodents. While they are both mammals—and many bats are small, bats make up the second largest mammal order, *Chiroptera* (Greek for "hand-wings"), after rodents, *Rodentia*. Bats are the only mammals that can achieve true flight, converging their evolution with that of birds, who have an entirely different brain structure to handle that niche. Instead, as mammals, they share neocortical laminar structures and microcircuitry with mice, and with us (Chang & Kawai, 2018; García-Rosales et al., 2019; Linden & Schreiner, 2003; Mountcastle, 1997). In their book chapter on cross-species comparisons, D.F. Sherry (2007) pointed out that these studies create a framework of understanding evolutionary adaptation through phenomena like selective pressure and generalized environmental needs.

Distinct size, nutritional needs, behavior, and society provide a jumping-off point for evolutionary particularity—even between more "comparable" animals, such as two rodents: mice and Mongolian gerbils. While classic response profiles from the auditory cortex (AC) seem to be extremely robust under anesthesia within species (See Chapter 3 & Deane et al., 2020), there are noticeable differences between them (see Figure 2.6). Often in studies of the AC, a host of species is listed in the literature review to belay known information such as oscillatory activity, local field potential (LFP) and spiking behavior, and cortical layer denomination. However, contradiction can commonly be seen across these results and—while this has to do with many complex factors—ambiguities may be specifically species-related in a way that hasn't been previously quantifiable through comparing across publications.

While there are some studies comparing the AC of several bat species (e.g. Hagemann et al., 2011), few compare the AC of bats to other mammals (see Kanwal & Rauschecker, 2007). Similarly, there are few studies quantitatively comparing the mouse AC against other species (see Hoglen et al., 2018). Bats have highly developed sonar calls and social communication (Beetz et al., 2017; Hechavarría et al., 2013; Thies et al., 1998; Weineck et al., 2020) and are an excellent non-standard animal model for auditory research which can be compared to the standard black 6 mouse model used frequently in auditory neuroscience. Investigating the potentially different development of general auditory processing principles would help to gain a better understanding of how the ecological needs of a species shape the development and function of the nervous system.

Therefore, we collaborated between the department of Systems Physiology of Learning in the Leibniz Institute for Neurobiology, Magdeburg, and the Auditory Computations Lab of Goethe University Frankfurt am Main to investigate the auditory cortex of awake, head-fixed, freely moving black 6 mice and awake, head-fixed seba's short-tailed bats. We attained A1 multichannel datasets across both species to perform comparative analyses aimed at

understanding fundamental auditory response profiles between them. The bat dataset included 5 bats with cortical windows from which 7 to 16 measurements, each with 50 trials, were taken from individual penetration sites. The mouse dataset included 2 mice with chronically implanted electrodes from which 14 measurements, each with 50 trials, were taken on consecutive days. Bats listened to a repeated distress syllable at 5.28 and 36.76 Hz and mice listened to a click trains at 5 and 40 Hz. To provide meaningful insight into auditory microcircuitry and to link evolutionary and behavioral need to specific auditory ability in these small brains, we used current source density (CSD) analysis to explore the laminar profiles. We performed a model fit analysis to better understand temporal response and background suppression over consecutively repeated stimuli trains. We computed phase amplitude coupling (PAC) over the LFP and CSD to investigate remote and local contributions to information transfer and spectral coupling profiles. We ran continuous wavelet transform (CWT) analysis to compare internal coherence dynamics and signal to noise ratio differences.

We found that while there are similarities between cortical response profiles in short-tailed bats and mice, there was a better signal to noise ratio in bats under these conditions, which allowed for a clearer following response and more accurate temporal resolution to stimuli trains. Overall, PAC profiles were fundamentally different between species and may indicate a better parsing strategy in bats. Phase coherence was far stronger in bats during stimulus response, indicating a more uniform inter-trial response profile—less variability—in bats. These results support that the shared laminar organization in mammalian species, even in brains that are very similarly sized, can adapt via differing recruitment of the microcircuitry to fill ecological niches.

Results of project 3

Shared microcircuitry but differing cortical response profiles

Seba's short-tailed bats and black 6 mice have a similarly sized auditory cortex, but it is slightly thicker in mice (~1 mm) than in bats (~750 µm; García-Rosales et al., 2019). Figure 5.1 shows the group averaged CSD profiles for bats and mice at ~5 and ~40 Hz stimulus presentation. Awake, head-fixed bats received a repeated species-specific distress call stimuli at a range of frequencies, including the 5.28 and 36.76 Hz contained in the following analysis, over 2 seconds for the publication by García-Rosales et al. (2020). Awake, head-fixed, freely moving mice were presented with click trains at a range of frequencies including 5 and 40 Hz over 1 second. Therefore, we must point out that the datasets were pre-made and not comprehensive with one another. However, we used the same recording equipment (Neuronexus probes with 50 µm channel distance and 177 µm² channel diameter) and we believe a comparison on basic functional circuitry differences is justified.
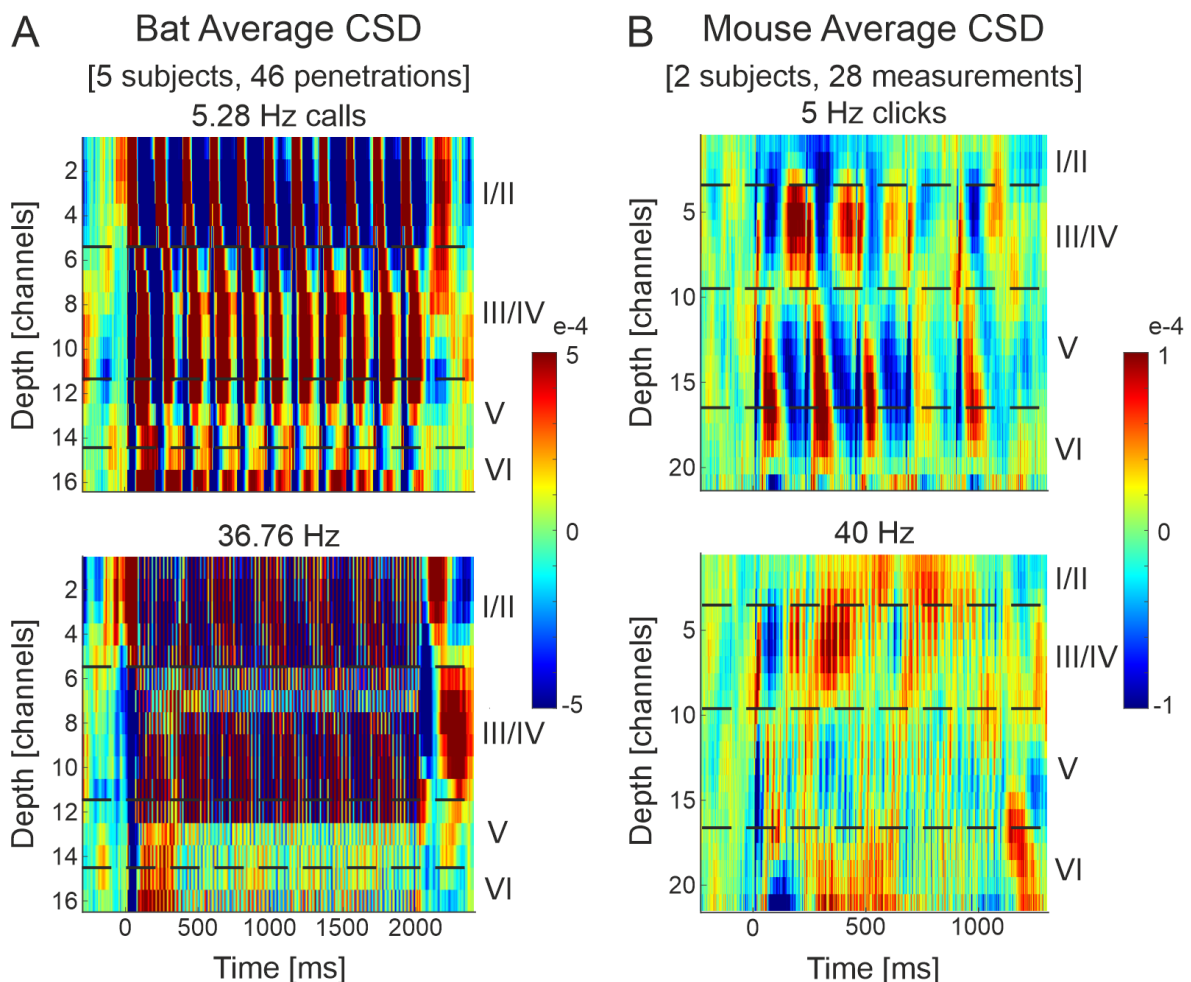
Figure 5.1 Grand average current-source density profiles. A: seba's short-tailed bats (n = 5, 47 separate penetrations) grand averaged cortical response to a click-like distress call presented repetitively at 5.28 Hz (top) and 36.76 Hz (bottom). **B:** black 6 mice (n = 2, 28 measurements from 2 penetrations) grand averaged cortical response to a click train presented at 5 Hz (top) and 40 Hz (bottom). The CSD profiles show the pattern of temporal processing (ms) within the cortical depth (channels are 50 µm apart). Representative layer assignment is indicated with horizontal dashed lines. Current sinks (blue), represent areas of excitatory synaptic population activity, while current sources reflect balancing currents (cf. Happel et al., 2010). Note the different c-axis scales: with much stronger signal from bats; the different time scales: 2 s stimuli for bats and 1 s stimuli for mice; and the different depth scales: slightly thicker cortex for mice, ~20 channels or ~1 mm, than bats 16 channels or ~750 µm. Modified image published in Deane et al., 2022b.

The supragranular layer at the penetration sites across the bat A1 was proportionally much thicker than that found across mice and had a very strong and consistent following response which lagged behind thalamocortical response. In the awake mice average CSD profile, the granular sink was very light in comparison to infragranular response. Where we saw very clear following responses down the depth of the cortex in bats at a lower (5.28 Hz) and higher (36.76 Hz) frequencies, the following response in mice was less clean and more relegated to thalamic input areas, with separate, repeated granular and infragranular sinks following the stimuli. The messier signal seen in awake mice, compared to their anesthetized signal seen in Chapter 4 (Deane et al., 2022a), is in line with the difference also observed between anesthetized and awake Mongolian gerbils in Chapter 3 (Deane et al., 2020). It also followed that the granular layer activity in awake mice was lower than that of anesthetized mice. Interestingly, the awake bat cortical activity was very clean compared to other awake datasets, in the sense of legible sinks far above the baseline cortical activity for each stimulus onset. The infragranular and granular sinks were smeared into one large cortical response sink in bats. That sink smearing might have been due to the individual penetration sites per measurement (as opposed to a single chronically implanted penetration in the 2 mouse subjects). Therefore, layer selection was done on a per-penetration or per-measurement basis. While it was not possible to perfectly match up layers in the CSD averages, those specific layer boundaries, seen as a representative layer selection in the profiles of Figure 5.1, were used for averaged traces (below) and further analysis.

Accurate cortical following responses through all layers in bats

Figure 5.2 and Figure 5.3 show the averaged AVREC and layer traces per group for ~5 and ~40 Hz respectively. Amplitude was normalized to each measurement's first AVREC peak detected in their 2 Hz conditions (not shown). This allowed us to see the relative contribution of the layers to the full cortical column activity. For both high and low frequency, in mice, layer V had the strongest contribution to columnar activity, and in bats, III/IV and V were roughly equivalent in amplitude.

Supragranular activity in mice and bats differed. Mouse granular sinks often smeared up into supragranular layers, causing a stimulus locked, small amplitude response at tone onset and following the lower frequency click trains. In the bats, the supragranular layer consistently lagged behind the stimulus-locked thalamic input activity of layers III/IV, V, and VI. Creating an accurate, yet lagged, following response to low and high frequency stimulus presentations. Not only did this confirm what was visible in the CSD profiles, that stimulus following response is very clear through the depth of the bat A1, but it also builds to the AVREC in a clear and concise way. In both bat and mouse ~5 Hz AVREC traces, there was an initial onset response in the full column and a second, smaller and broader peak after both the first and second stimulus responses. In the bats, that broader peak was driven almost exclusively by the supragranular lag. In the mice, a second, broader peak was seen in all layers, creating less specificity and causing the AVREC to build the second peak of activity from throughout the column.

Mouse cortical activity was also noisier than bat cortical activity. While bat averaged traces revealed clear, clean, and almost uniform following responses at high and low stimulus presentation frequencies, mouse cortical activity seemed to contain more high frequency jitter and more variable following response profiles across consecutive stimuli presentation.

Following responses at 40 Hz in mice were visible in the layers, especially layer III/IV, but not as clearly in the AVREC compared to bat following responses at 36.76 Hz..
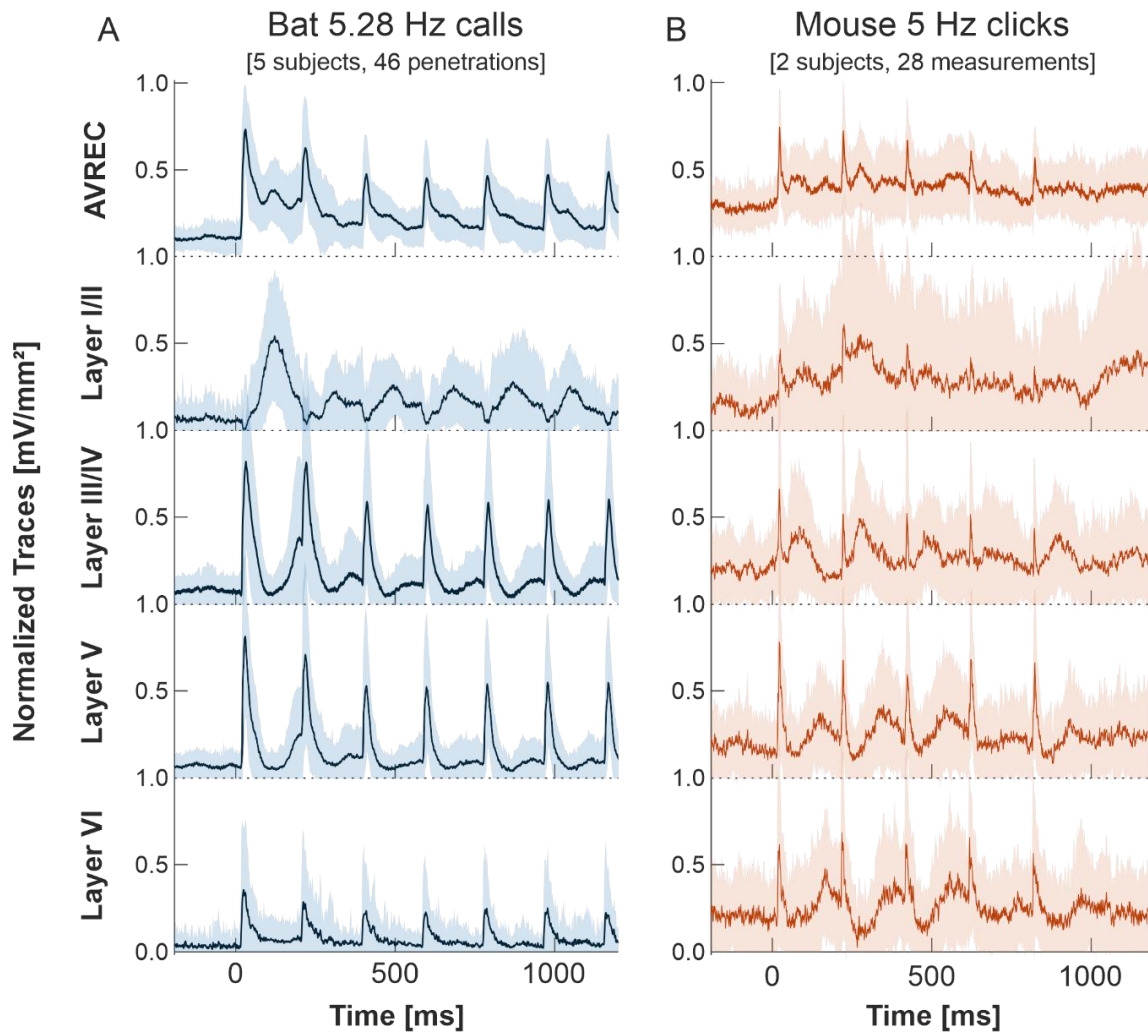

Figure 5.2 AVREC and layer traces at ~5 Hz. A: Bat averaged auditory cortex AVREC trace (top) and all layer traces (I/II, III/IV, V, VI in descending order), in response to 5.28 Hz click-like distress calls (blue). **B:** Mouse averaged auditory cortex AVREC layer traces, in response to 5 Hz click-trains (orange). Layer traces were calculated on sink activity only. Confidence intervals are shown in SEM. Traces were all normalized per measurement due to separate penetrations in bat group. Normalization was done according to the first detected peak of the AVREC at 2 Hz (not shown). Modified image published in Deane et al., 2022b.

Interestingly, even though layer III/IV had the clearest following response at 40 Hz in mice, layer V is where the onset signal was strongest. In bat layers IV and V, the onset response and following response was more equivalent. However, layer I/II in bats at 36.76 Hz had the highest amplitude consecutive following response compared to the AVREC and other layers. Here also, there was a slow wave buildup of activity over the first 200 ms which then came back down by 500 ms and remained fairly consistent in amplitude afterwards.

The base level of activity in mice during stimuli presentation stayed higher, seemingly in part due to the noisiness of the trace. This was clearest in the supragranular layer but also seen through the layers and in the AVREC after stimuli onset. Activity in bats, in comparison, began closer to relative 0 (as this is normalized to the peak of the AVREC at 2 Hz) and then sank back to near 0 in each layer after the onset response. The only exception was in the first

500 ms of the supragranular activity where there was the slow wave build-up and in the AVREC trace which included both sink and source activity rectified.
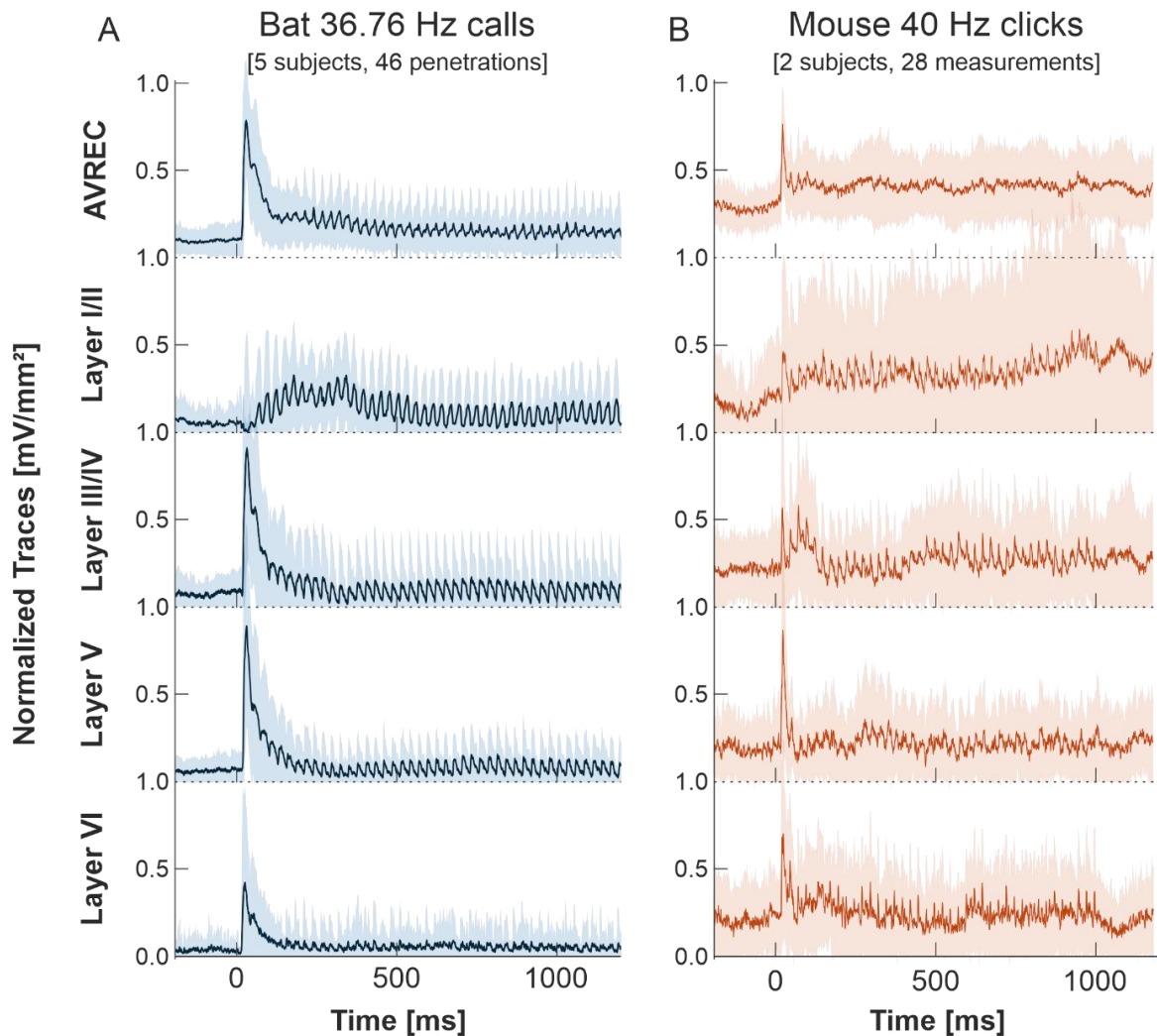

Figure 5.3 AVREC and layer traces at ~40 Hz. A: Bat averaged auditory cortex AVREC trace (top) and all layer traces (I/II, III/IV, V, VI in descending order), in response to 39.76 Hz click-like distress calls (blue). **B:** Mouse averaged auditory cortex AVREC layer traces, in response to 40 Hz click-trains (orange). Confidence intervals are shown in SEM. Traces were all normalized per measurement due to separate penetrations in bat group. Normalization was done according to the first detected peak of the AVREC at 2 Hz (not shown). Modified image published in Deane et al., 2022b.

Because we could see the following response riding the onset response in the bats at 36.76 Hz, we separated these two components with bandpass filters. We filtered +/- 3 Hz around the stimulus frequency (Figure 5.4) to reveal, more strictly, the following response components and we filtered from 1 to 4 Hz (Figure 5.5) to reveal the onset response. These were then normalized to the same AVREC first peak in each measurement's 2 Hz condition. In Figure 5.4, bats layer I/II showed the same response lag and then a fairly consistent amplitude following response. In each of the granular and infragranular layers, there was a relatively consistent higher amplitude following response in the first ~100 ms of tone presentation which then attenuated to a more even following response to consecutive stimuli. In mice at 40 Hz, the following response was more variable throughout the layers. Mouse layer V had the highest amplitude following response in the first 100 ms compared to the other layers but remained variable in amplitude in consecutive responses. The time it took for each layer to attenuate

was also less consistent than in bats. Where the initially increased amplitude in following response took roughly the same time in bats for layers III/IV-VI (and I/II at a delay), it attenuated more rapidly in layer VI than layer V in mice and didn't really adapt in layer III/IV at all.
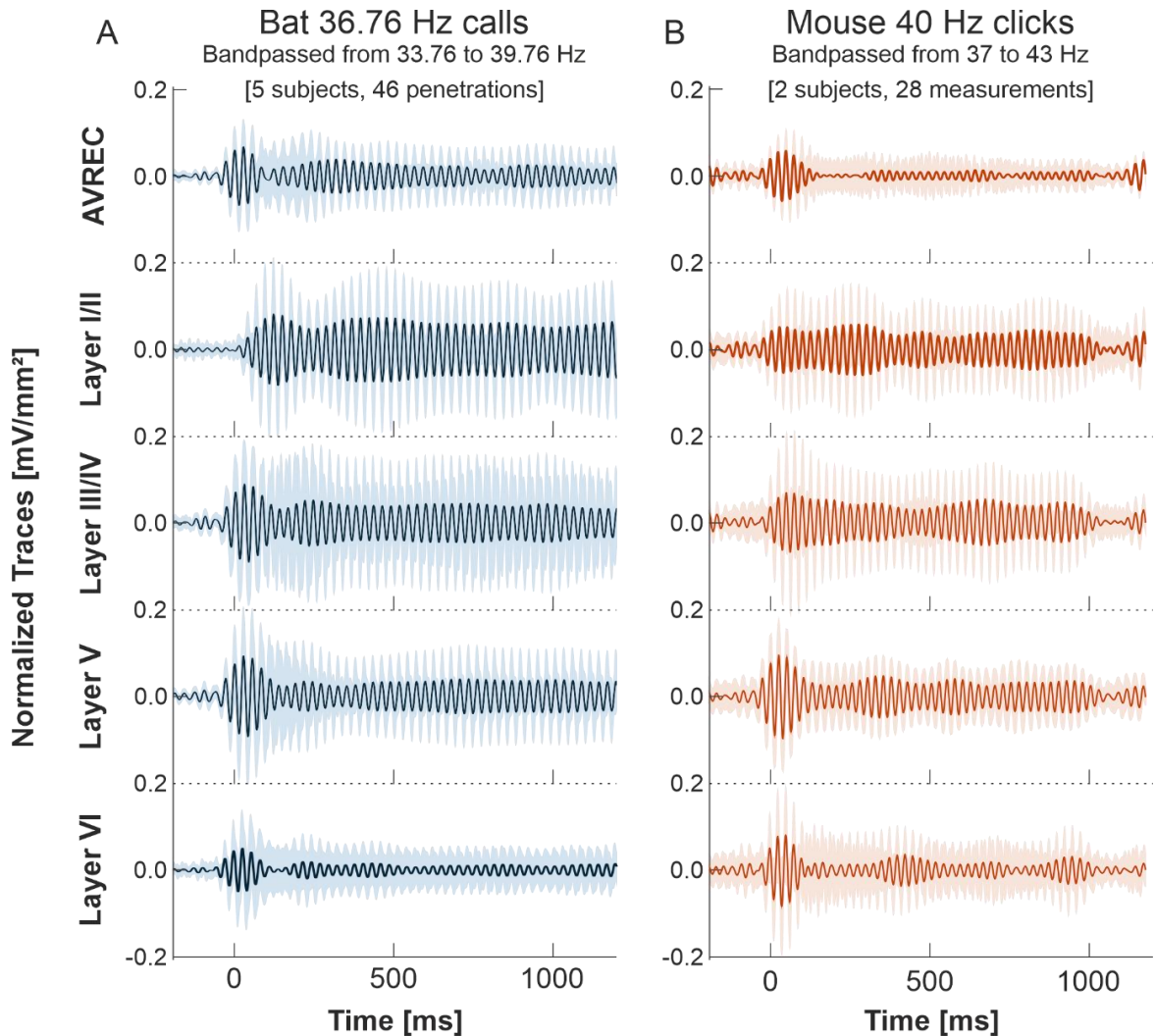

Figure 5.4 AVREC and layer traces at ~40 Hz, bandpass filtered at +/- 3 Hz around the stimulation frequency.
A: Bat averaged auditory cortex bandpass filtered AVREC (top) and all layer traces (I/II, III/IV, V, VI in descending order), in response to 39.76 Hz click-like distress calls (blue). **B:** Mouse averaged auditory cortex bandpass filtered AVREC and layer traces, in response to 40 Hz click-trains (orange). Confidence intervals are shown in SEM. Traces were all normalized per measurement due to separate penetrations in bat group. Normalization was done according to the first detected peak of the non-filtered AVREC at 2 Hz (the same normalization as in **Figure 5.3**). Modified image published in Deane et al., 2022b.

The onset components in Figure 5.5 showed generally a slower adaptation than the following response. The onset in bats was consistently relatively higher than mice in the AVREC, granular, and infragranular layer traces. The supragranular layer was nearly flat in bats but the previously described, lagged, slow wave was visible in both species with this filter. In the mouse granular trace, there was a somewhat singular onset wave. However, in infragranular layers, there were several slow waves throughout the signal. This was most evident in comparison between bats and mice in layer V, where bats had their highest relative amplitude onset response wave and mice had a lower onset response and a double-peak in the first 500 ms.
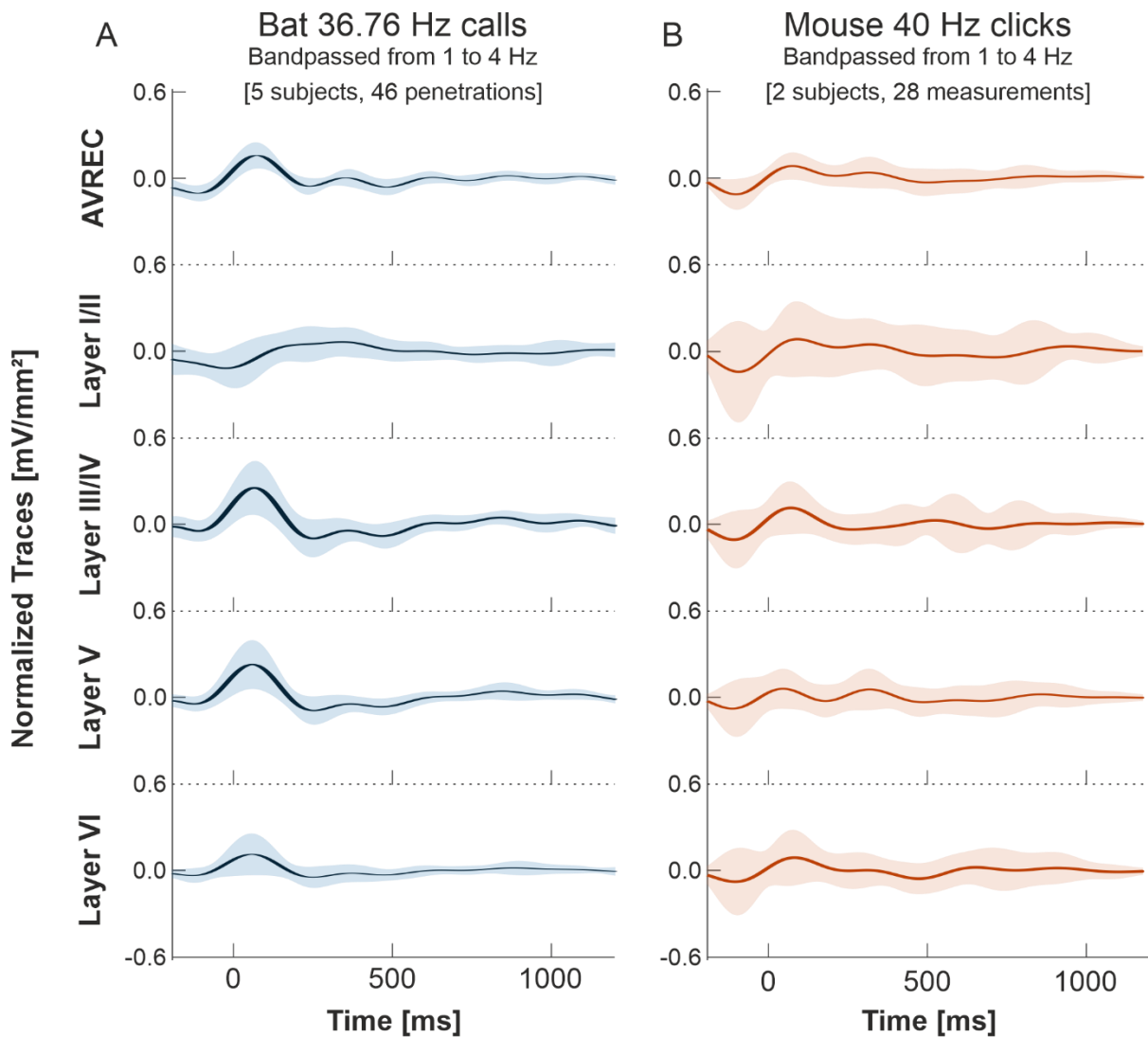
Figure 5.5 AVREC and layer traces at ~40 Hz, bandpass filtered from 1 to 4 Hz. A: Bat averaged auditory cortex bandpass filtered AVREC (top) and all layer traces (I/II, III/IV, V, VI in descending order), in response to 39.76 Hz click-like distress calls (blue). **B:** Mouse averaged auditory cortex bandpass filtered AVREC and layer traces, in response to 40 Hz click-trains (orange). Confidence intervals are shown in SEM. Traces were all normalized per measurement due to separate penetrations in bat group. Normalization was done according to the first detected peak of the non-filtered AVREC at 2 Hz (the same normalization as in **Figure 5.3**). Modified image published in Deane et al., 2022b.

A deeper decline of response amplitude to consecutive stimuli in bats

To characterize the response profile across consecutive stimuli presentations at a low (~5 Hz) or high (~40 Hz) frequency. We performed a model fit analysis, with 2 models to choose from algorithmically: exponential or linear. Figure 5.6 shows the peak amplitudes of responses after stimuli overlaid with the model selected and its fit value (root mean square error, RMSE) and parameters. The most common model selection was exponential decay. For bats, at both presentation frequencies, exponential decay was selected in all traces except the supragranular layer at 36.76 Hz, where a linear fit was selected. At 5 Hz in mice, layer III/IV and V were the only traces selected for exponential decay. In these layers, the exponential fit adjusted better to the mouse dataset, but it did not perform particularly well in either case to explain the dataset. The offset of 5 Hz layer III/IV was well below a possible peak amplitude due to how shallow the rate of decay was and the rate of decay in 5 Hz layer V was severely steep.
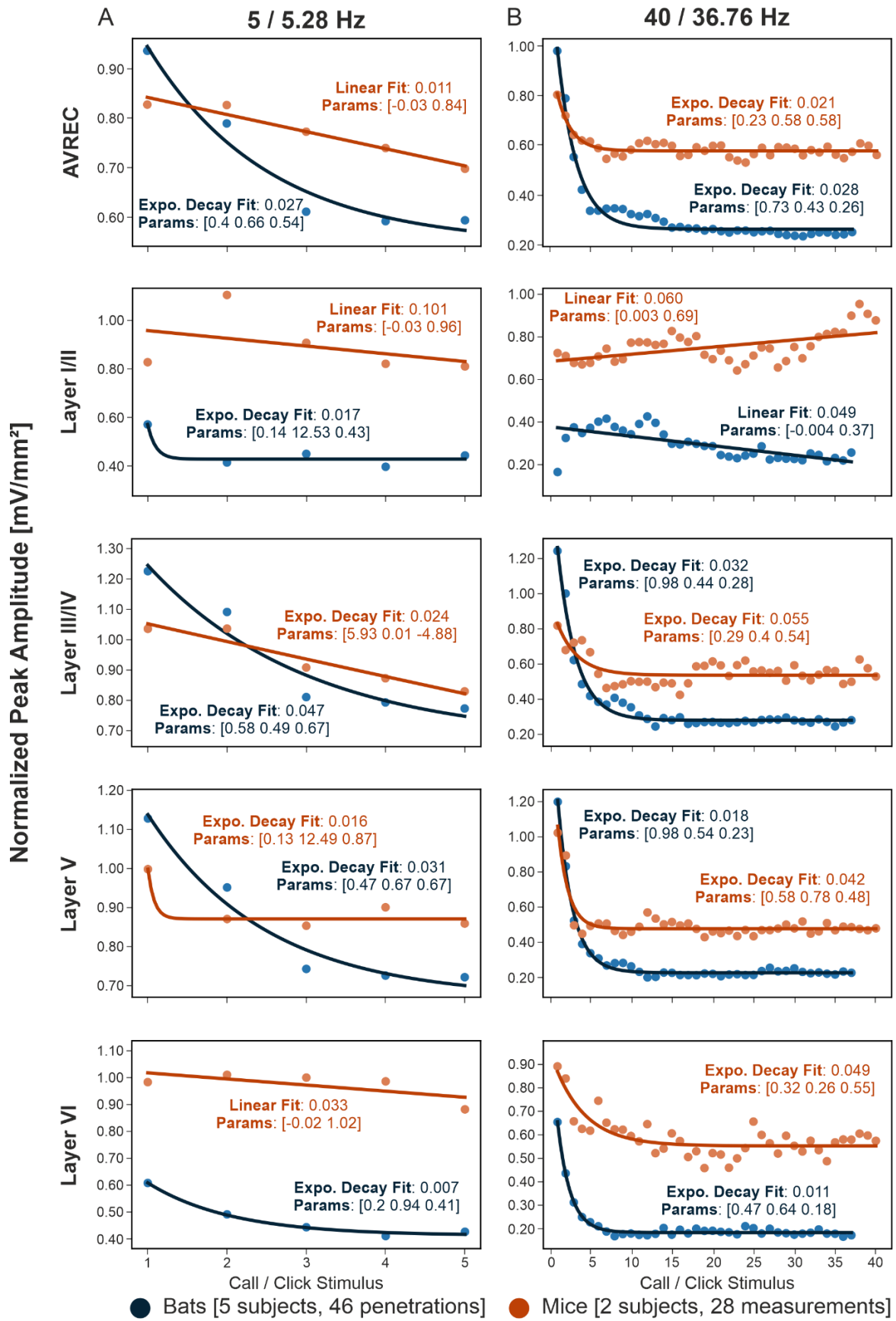
Figure 5.6 Model Fit Analysis. A: Bat (blue) and mouse (orange) group-averaged response peak amplitudes over consecutive stimulus repetition of 5 or 5.28 Hz with overlaid model fit. **B:** Bat and mouse group-averaged response peak amplitude over consecutive stimulus repetition of 40 or 36.76 Hz with overlaid model fit. The model selected, exponential or linear decay is overlaid, along with the fit value calculated by RMSE and the model parameters. The closer to zero that the model fit is, the better fit it is. For expo.: parameters are [depth, rate of decay, offset]. For linear: [slope, intercept]. Image published in Deane et al., 2022b.

The bat 5.28 Hz III/IV and V models were comparable to each other and spanned a greater depth (intercept – offset) than mouse 5 Hz V. In ~40 Hz, the exponential fit adapted better to the bat dataset in every case except the AVREC peak amplitudes. Importantly, bats had a greater depth parameter in the AVREC and layers III/IV through VI, indicating again a consistently deeper suppression of consecutive responses at this higher frequency presentation. In the AVREC, layer III/IV, and V, mice adapted faster (with a steeper decay rate) to repeated stimulus and vice versa in layer VI.
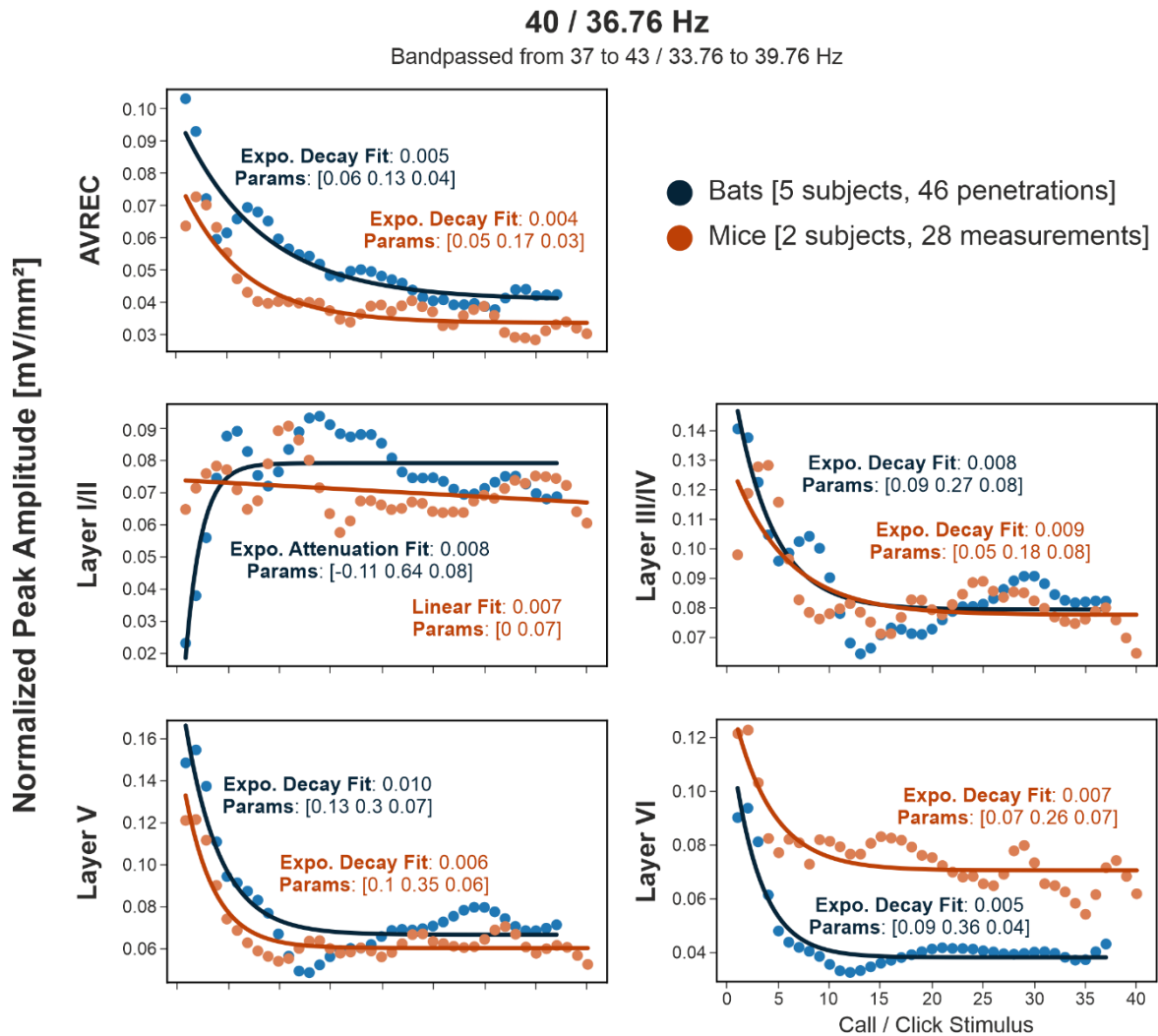
Figure 5.7 Model Fit Analysis on after bandpass filtering of +/- 3 Hz around stim frequency. Bat (blue) and mouse (orange) group-averaged response peak amplitudes from the filtered traces over consecutive stimulus repetition of 40 or 36.76 Hz with overlaid model fit. The model selected, exponential or linear decay is overlaid, along with the fit value calculated by RMSE and the model parameters. The closer to zero that the model fit is, the better fit it is. For expo.: parameters are [depth, rate of decay, offset]. For linear: [slope, intercept]. Image published in Deane et al., 2022b.

We performed the same model analysis on peaks detected from the ~40 Hz stimulus frequency bandpass filtered traces (shown in Figure 5.4). This was motivated to see if the model selection and relative parameters would change when the onset component, which was stronger than following response in both species, was removed. In Figure 5.7, the peak amplitudes are displayed with overlaid model fits. RMSE was closer to 0 across all fits, compared to the previous datasets, due to the difference in scale. Exponential decay was selected for all traces in bats and mice except for the outlying layer I/II where we had a linear regression model

selection for mice and exponential attenuation for bats. The exponential decay model adapted better to the mouse dataset in the AVREC and layer V traces compared to bats. The reverse was true for granular and layer VI traces. It's clear that the models in this analysis do not explain the data as well as when the onset response component is included as there is much more relative variability in amplitude around the model fit line. Regardless, the bat data still consistently showed a greater depth than mice throughout the AVREC, granular, and infragranular layers. This revealed that even without the large onset response component, cortical response to consecutive stimuli was more deeply suppressed in bats.

Fundamentally different local and global phase amplitude coupling profiles

As mentioned in the previous chapter, low oscillation phase coupled to high oscillation amplitude has been implicated in information transfer across neural tissue (Bonnefond et al., 2017; Gourévitch et al., 2020). Phase amplitude coupling (PAC) analysis is an increasingly common tool for exploring a range of possible coupling pairs. PAC is a well-established characteristic throughout the brain and neocortex (Esghaei et al., 2015; Helfrich & Knight, 2016; Lisman & Jensen, 2013; O'Connell et al., 2015; Sotero et al., 2015; Spaak et al., 2012; Xiao et al., 2019), and has been implicated in a variety of relevant functional tasks such as interareal communication and information binding (Colgin et al., 2009; Daume et al., 2017). Primary sensory processing may also rely on this coupling to parse ongoing stimuli by transferring local network activity, which exists in the gamma range, into slower timescales of lower-frequency activity (Giraud & Poeppel, 2012; Hyafil et al., 2015). Recently, García-Rosales et al., (2020) explored PAC coupling of the AC to the frontal auditory field during repetitive stimuli with this very bat dataset.

Here we performed PAC analysis within cortical layers of both species to differentiate coupling profiles. This analysis was done on low and high stimulus presentation frequencies on both LFP signal (Figure 5.8 and Figure 5.10) and CSD transformed signal (Figure 5.9 and Figure 5.11) to distinguish roughly between globally influenced and local network PAC contributions respectively. Overall, the strongest PAC was between delta and high gamma in mouse LFP signal at both stimulation frequencies. When computing a permutation clustermass test on this region of interest (ROI; Figure 5.8 and Figure 5.10, 3rd column), mice had consistently significantly stronger PAC with large to huge Cohen's d effect sizes (Table 5-1). Bat LFP PAC was generally weaker, with the species' stronger coupling in the 5.28 Hz stimulus presentation condition (Figure 5.8). There, a second ROI was chosen for the coupling in bats between, roughly, theta/alpha and low gamma. However, PAC was not significantly higher here than in mice according to permutation testing and was even significantly lower in the ~40 Hz comparison. The layers within both bat and mouse LFP PAC were comparable down the depth of the A1, with perhaps supragranular layers showing a slightly stronger PAC coupling profile than granular or infragranular layers.

When calculating PAC on the CSD profile channels, laminar differences were more profound. Mouse supragranular layers lost any noticeable PAC. Mouse layer III/IV through VI profiles revealed theta gamma (low and high) coupling at roughly equivalent levels in both high and low stimulus frequency conditions. CSD PAC in bats became much stronger than their LFP PAC. Bat PAC on CSD signal was also subsequently stronger than mouse CSD PAC across

layers in the ~5 Hz stimulus presentation condition but not in the ~40 Hz condition. In both species, the granular layer had the strongest PAC profile compared to other layers.
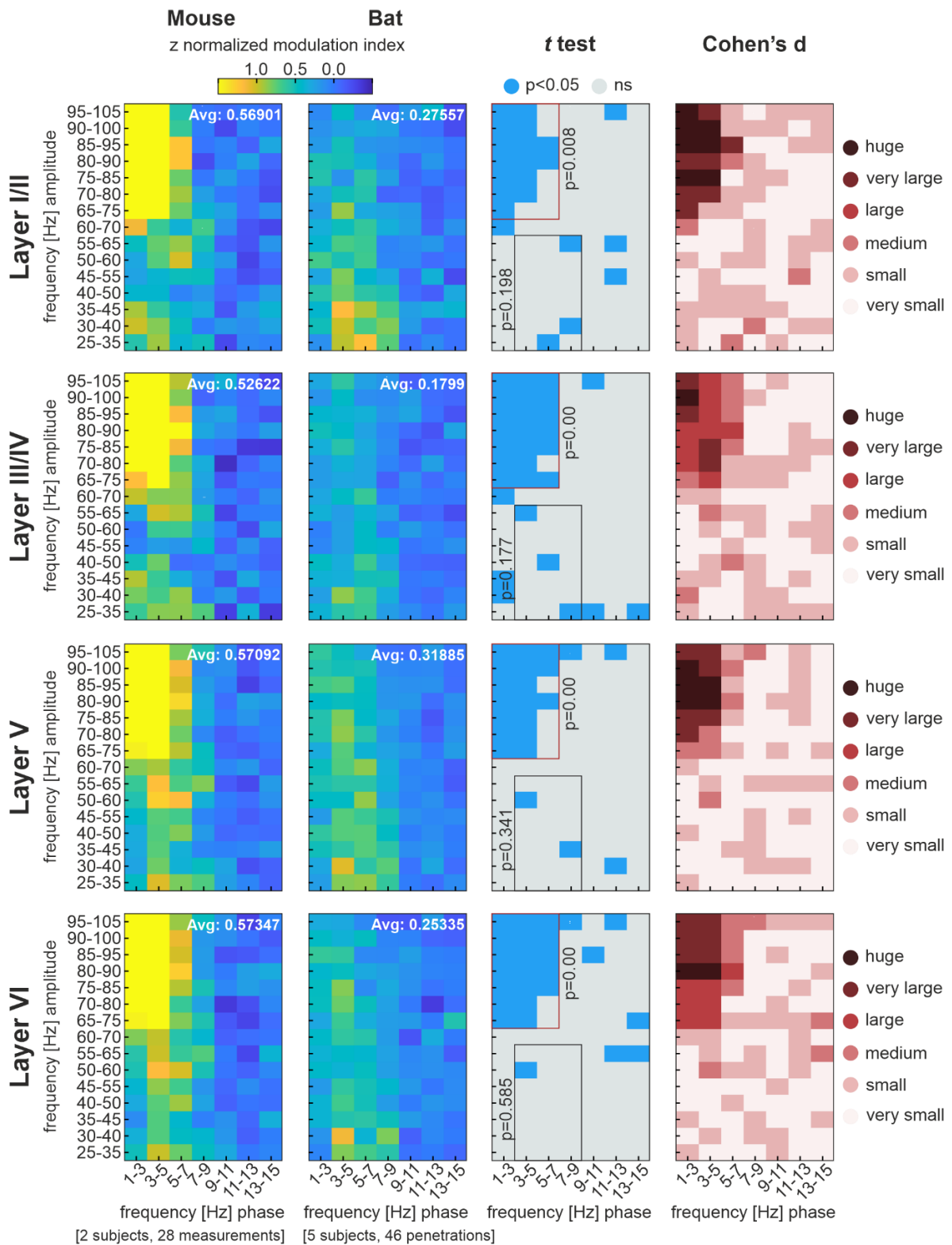
:)

Figure 5.8 Phase amplitude coupling profiles from LFP signal at ~5 Hz stim frequency. The PAC profiles, high frequency amplitude over low frequency phase, of mice and bats (left two columns) for each layer center channel (top to bottom). Color axis is in the z-score normalized MI for each phase-amp couple for each species. The higher the zMI, the better the coupling. Point-wise *t* test and Cohen's d effect size results show clustermass, where p < 0.05 (blue), and the range of effect size across results. Overlaid are regions of interest where permutation clustermass analysis was calculated. The regions are red where significantly different above chance and in black where not significant and the p value is displayed by its corresponding region. Regions were chosen based on the areas of best coupling in each species and were kept consistant between all PAC analyses. Cohen's d 0.2-0.5 = small, 0.5-0.8 = medium, 0.8-1.2 = large, 1.2-2.0 = very large, >2.0 = huge.
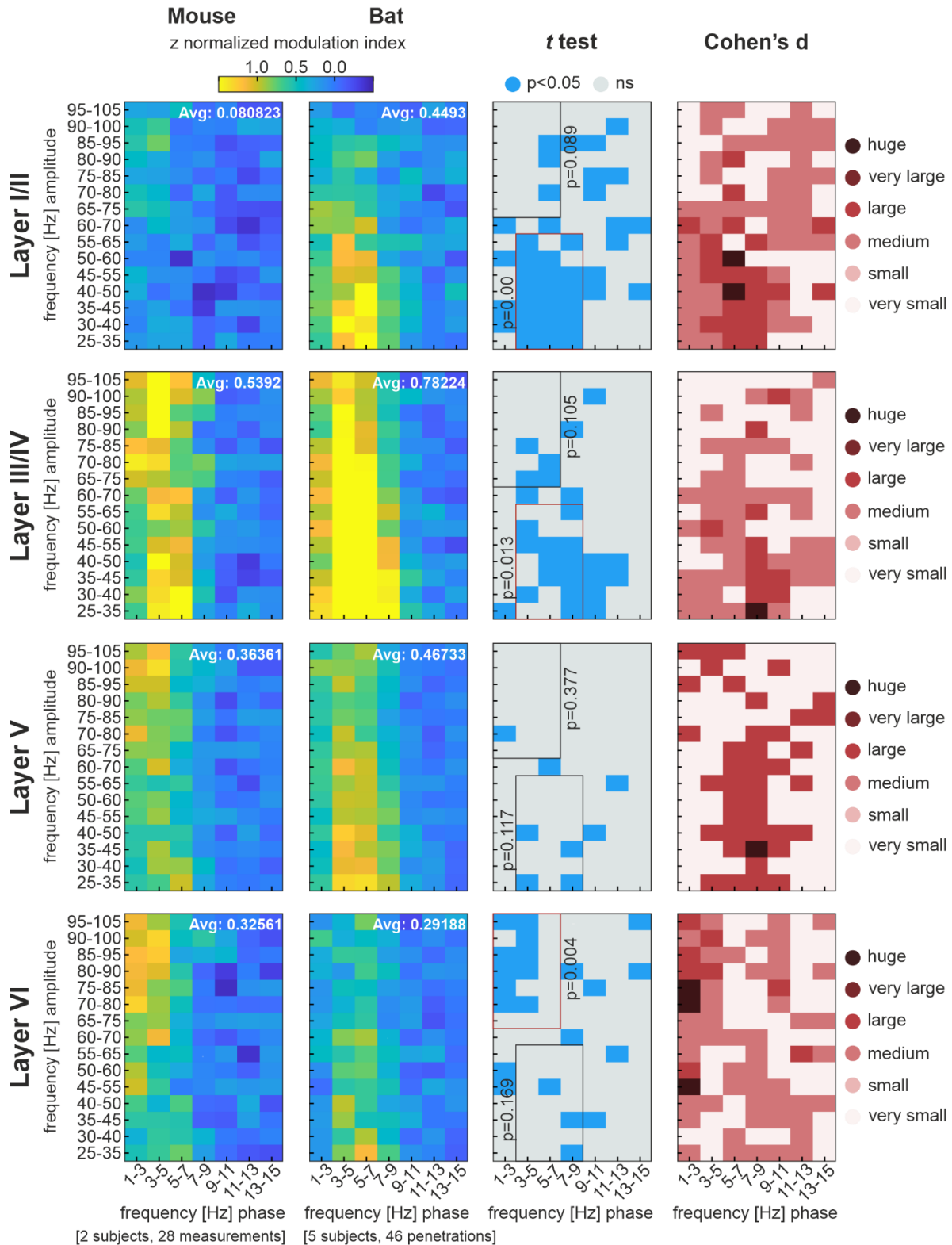
Figure 5.9 Phase amplitude coupling profiles from CSD signal at ~5 Hz stim frequency. The PAC profiles, high frequency amplitude over low frequency phase, of mice and bats (left two columns) for each layer center channel (top to bottom). Color axis is in the z-score normalized MI for each phase-amp couple for each species. The higher the zMI, the better the coupling. Point-wise *t* test and Cohen's d effect size results show clustermass, where p < 0.05 (blue), and the range of effect size across results. Overlaid are regions of interest where permutation clustermass analysis was calculated. The regions are red where significantly different above chance and in black where not significant and the p value is displayed by its corresponding region. Regions were chosen based on the areas of best coupling in each species and were kept consistant between all PAC analyses. Cohen's d 0.2-0.5 = small, 0.5-0.8 = medium, 0.8-1.2 = large, 1.2-2.0 = very large, >2.0 = huge. Modified image published in Deane et al., 2022b.
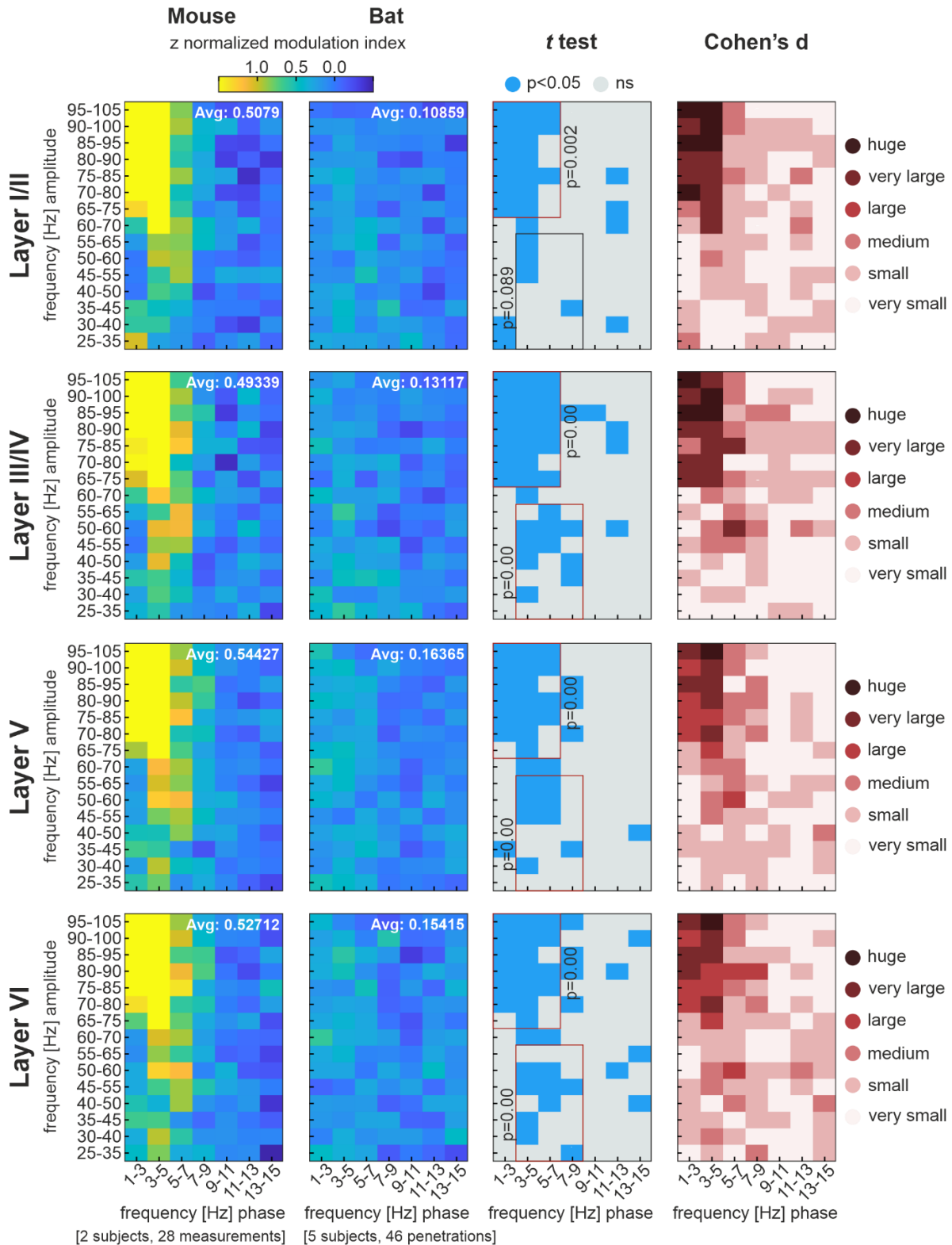
Figure 5.10 Phase amplitude coupling profiles from LFP signal at ~40 Hz stim frequency. The PAC profiles, high frequency amplitude over low frequency phase, of mice and bats (left two columns) for each layer center channel (top to bottom). Color axis is in the z-score normalized MI for each phase-amp couple for each species. The higher the zMI, the better the coupling. Point-wise *t* test and Cohen's d effect size results show clustermass, where p < 0.05 (blue), and the range of effect size across results. Overlaid are regions of interest where permutation clustermass analysis was calculated. The regions are red where significantly different above chance and in black where not significant and the p value is displayed by its corresponding region. Regions were chosen based on the areas of best coupling in each species and were kept consistant between all PAC analyses. Cohen's d 0.2-0.5 = small, 0.5-0.8 = medium, 0.8-1.2 = large, 1.2-2.0 = very large, >2.0 = huge.
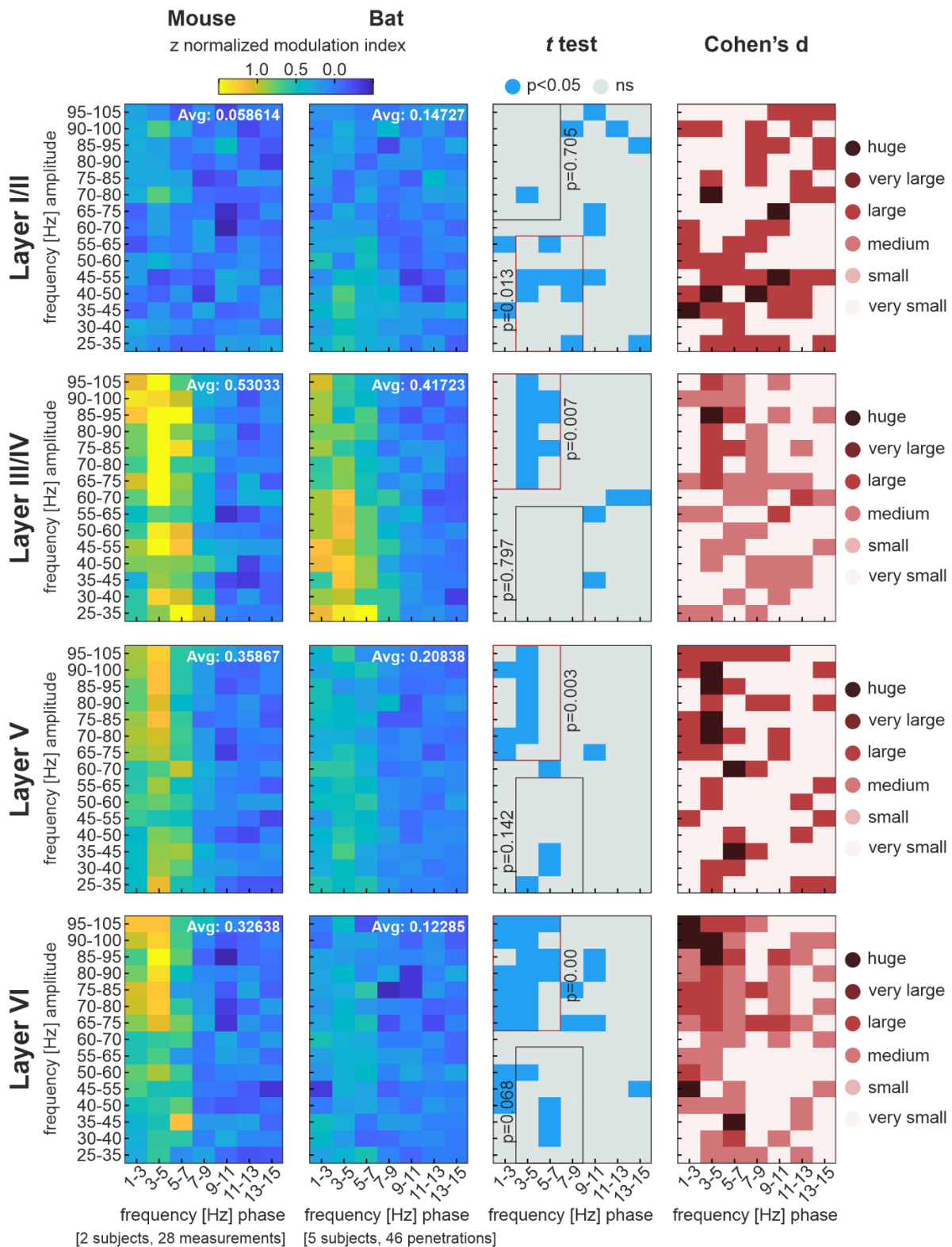
Figure 5.11 Phase amplitude coupling profiles from CSD signal at ~40 Hz stim frequency. The PAC profiles, high frequency amplitude over low frequency phase, of mice and bats (left two columns) for each layer center channel (top to bottom). Color axis is in the z-score normalized MI for each phase-amp couple for each species. The higher the zMI, the better the coupling. Point-wise *t* test and Cohen's d effect size results show clustermass, where p < 0.05 (blue), and the range of effect size across results. Overlaid are regions of interest where permutation clustermass analysis was calculated. The regions are red where significantly different above chance and in black where not significant and the p value is displayed by its corresponding region. Regions were chosen based on the areas of best coupling in each species and were kept consistant between all PAC analyses. Cohen's d 0.2-0.5 = small, 0.5-0.8 = medium, 0.8-1.2 = large, 1.2-2.0 = very large, >2.0 = huge. Modified image published in Deane et al., 2022b.

Frequency	Layer	Region of Interest	LFP Signal PAC Perm			CSD Signal PAC Perm		
			p	mean	std	p	mean	std
5 / 5.28	II	Delta vs high gamma	**0.008**	2.676	3.368	0.089	2.548	2.057
		Theta vs low gamma	0.198	2.202	2.196	**0.000**	2.300	2.925
	III/III/IV	Delta vs high gamma	**0.000**	2.555	2.958	0.105	2.350	2.438
		Theta vs low gamma	0.177	2.060	1.795	**0.013**	2.154	2.844
	V	Delta vs high gamma	**0.000**	2.358	2.384	0.377	2.327	2.213
		Theta vs low gamma	0.341	2.113	1.757	0.117	2.061	2.194
	VI	Delta vs high gamma	**0.000**	2.324	2.375	**0.004**	2.413	2.047
		Theta vs low gamma	0.585	2.146	1.735	0.169	2.070	1.989
40 / 36.75	II	Delta vs high gamma	**0.002**	2.572	3.485	0.705	2.485	1.563
		Theta vs low gamma	0.089	2.082	1.630	**0.013**	2.094	1.738
	III/III/IV	Delta vs high gamma	**0.000**	2.383	2.524	**0.007**	2.213	2.107
		Theta vs low gamma	**0.000**	2.101	1.614	0.797	2.106	2.094
	V	Delta vs high gamma	**0.000**	2.457	2.544	**0.003**	2.401	1.790
		Theta vs low gamma	**0.000**	2.141	1.549	0.142	1.951	1.544
	VI	Delta vs high gamma	**0.000**	2.508	2.514	**0.000**	2.390	1.843
		Theta vs low gamma	**0.000**	2.125	1.572	0.068	2.110	1.444

Table 5-1 Between group PAC region of interest comparison Bat vs Mouse PAC profiles at delta-high gamma (1-7 Hz phase vs 65-105 Hz amp) and theta-low gamma (3-9 Hz phase vs 25-65 Hz amp) phase-amp couplings. Regions were chosen based on the PAC profiles and not exact spectral frequency bins. Comparisons were done with the same regions across all layers and stimulus presentation frequencies. LFP and CSD signal PACs are both included (left and right respectively). p value results and corresponding mean and std are shown. In bold are p values where significant above chance p < 0.05. Table in part published in Deane et al., 2022b.

PAC analysis was performed also on spontaneous activity LFP and CSD signals. Several studies have found coupling that may assist remote activity across neuronal assemblies in the absence of a current stimuli to process (L. Wang et al., 2012; Weaver et al., 2016). The relation of LFP to CSD signal PAC were the same within each species—with mice having strong delta high gamma PAC in the LFP which was lost in the CSD PAC and with bats PAC increasing in strength from LFP to CSD. During spontaneous, or resting state, activity, bats had PAC at a wider range of low frequencies phases and high frequencies amplitudes. PAC was far stronger during spontaneous activity, regardless of signal source. Mice and bats were significantly different in the preselected ROIs. Mice had stronger delta high gamma coupling and bats had stronger theta low gamma coupling in the LFP PAC and bats had significantly higher PAC in both regions on the CSD signal. Especially in the CSD, there were chunks of large and huge effect sizes at delta/theta/alpha low gamma regions.
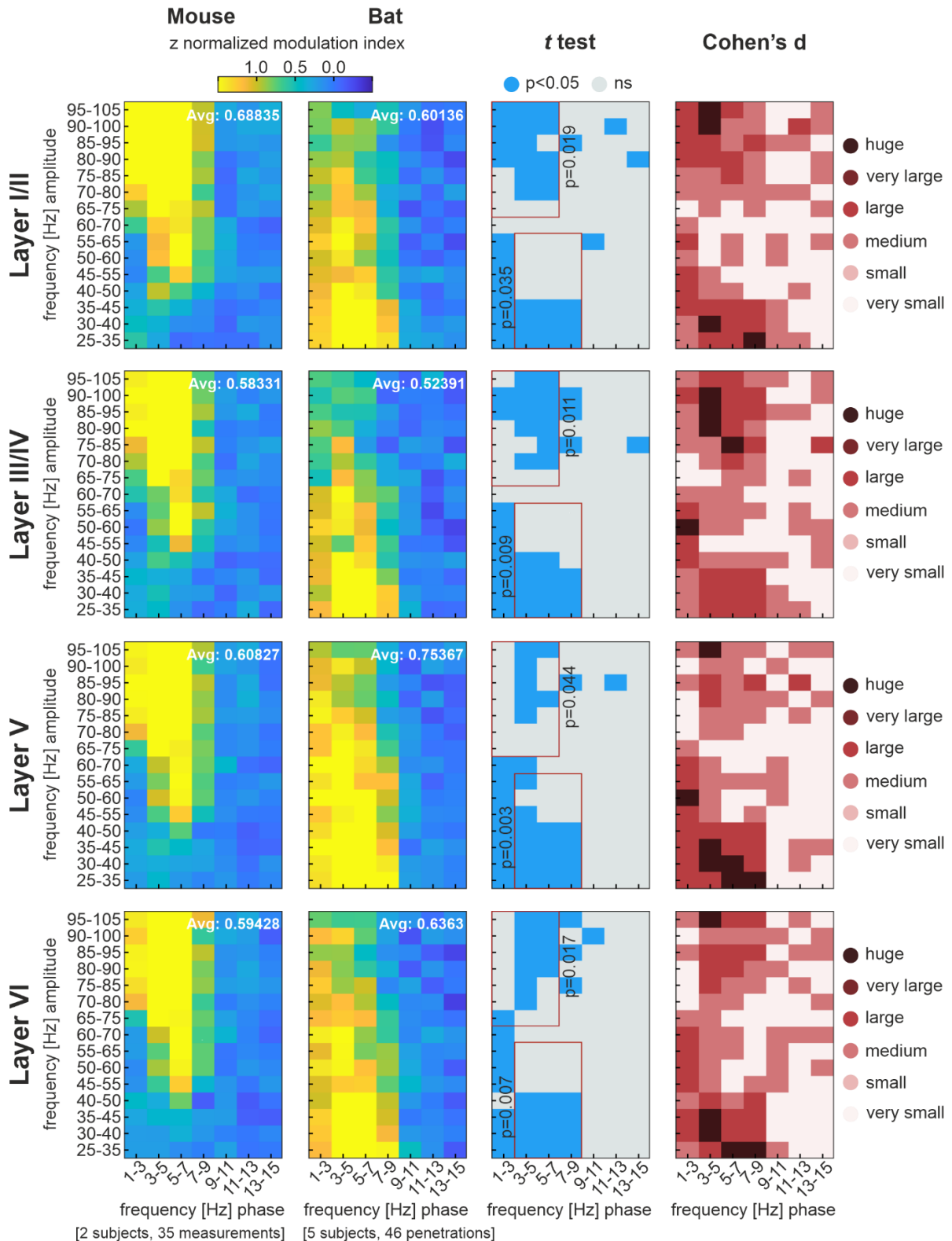
Figure 5.12 Phase amplitude coupling profiles from LFP during spontaneous activity. The PAC profiles, high frequency amplitude over low frequency phase, of mice and bats (left two columns) for each layer center channel (top to bottom). Color axis is in the z-score normalized MI for each phase-amp couple for each species. The higher the zMI, the better the coupling. Point-wise *t* test and Cohen's d effect size results show clustermass, where p < 0.05 (blue), and the range of effect size across results. Overlaid are regions of interest where permutation clustermass analysis was calculated. The regions are red where significantly different above chance and in black where not significant and the p value is displayed by its corresponding region. Regions were chosen based on the areas of best coupling in each species and were kept consistant between all PAC analyses. Cohen's d 0.2-0.5 = small, 0.5-0.8 = medium, 0.8-1.2 = large, 1.2-2.0 = very large, >2.0 = huge.
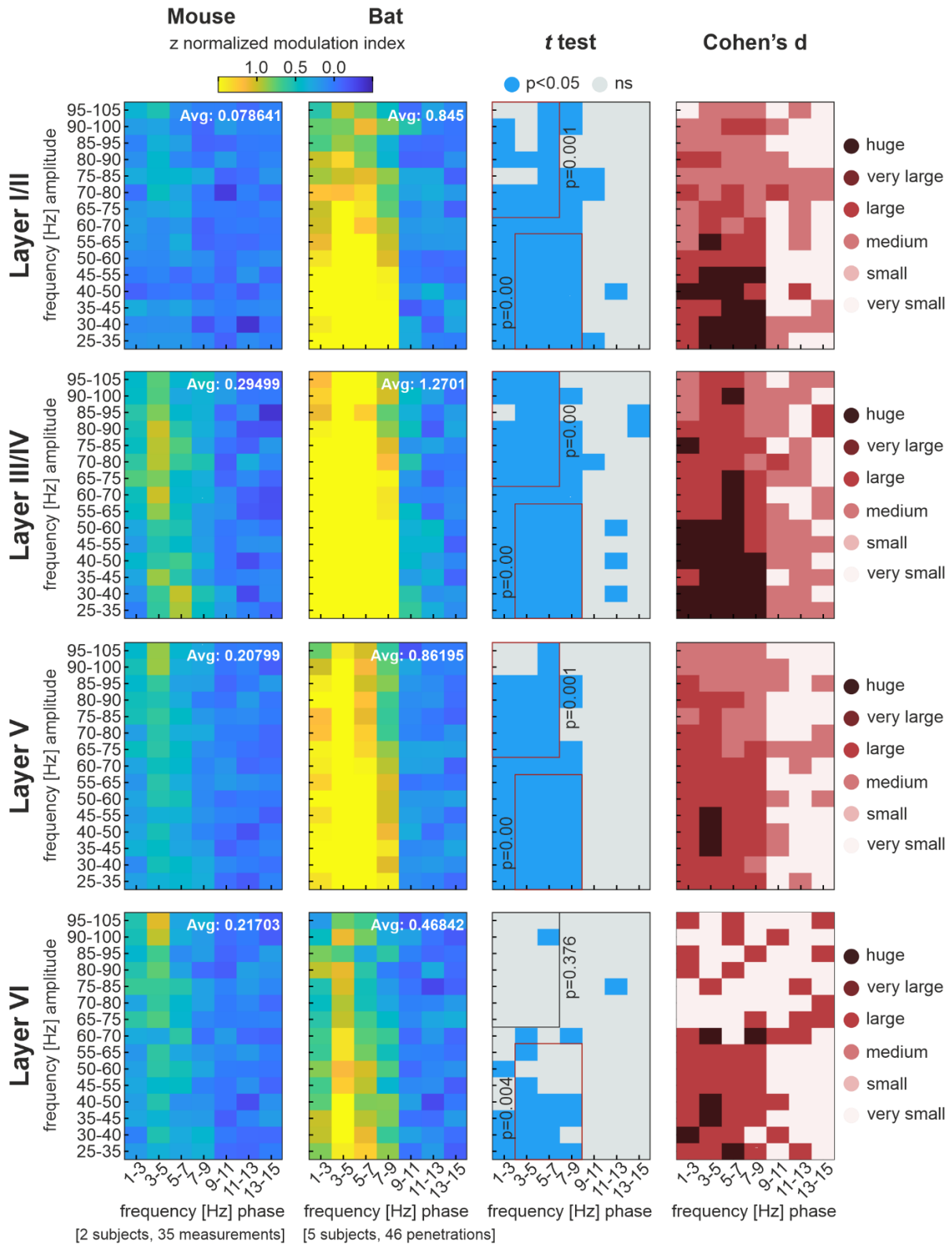
Figure 5.13 Phase amplitude coupling profiles from CSD during spontaneous activity. The PAC profiles, high frequency amplitude over low frequency phase, of mice and bats (left two columns) for each layer center channel (top to bottom). Color axis is in the z-score normalized MI for each phase-amp couple for each species. The higher the zMI, the better the coupling. Point-wise *t* test and Cohen's d effect size results show clustermass, where p < 0.05 (blue), and the range of effect size across results. Overlaid are regions of interest where permutation clustermass analysis was calculated. The regions are red where significantly different above chance and in black where not significant and the p value is displayed by its corresponding region. Regions were chosen based on the areas of best coupling in each species and were kept consistant between all PAC analyses. Cohen's d 0.2-0.5 = small, 0.5-0.8 = medium, 0.8-1.2 = large, 1.2-2.0 = very large, >2.0 = huge. Modified image published in Deane et al., 2022b.

Frequency	Layer	Region of Interest	LFP Signal PAC Perm			CSD Signal PAC Perm		
			p	mean	std	p	mean	std
~	II	Delta vs high gamma	**0.019**	2.627	3.939	**0.001**	2.445	2.766
		Theta vs low gamma	**0.035**	2.312	2.887	**0.000**	2.090	3.596
	III/III/IV	Delta vs high gamma	**0.011**	2.429	3.061	**0.000**	2.273	2.848
		Theta vs low gamma	**0.009**	2.059	2.535	**0.000**	2.273	3.671
	V	Delta vs high gamma	**0.044**	2.306	3.123	**0.001**	2.344	3.144
		Theta vs low gamma	**0.003**	2.095	2.691	**0.000**	2.082	3.311
	VI	Delta vs high gamma	**0.017**	2.235	2.993	0.376	2.364	2.201
		Theta vs low gamma	**0.007**	2.038	2.520	**0.004**	2.042	2.260

Table 5-2 Between group PAC region of interest comparison Bat vs Mouse PAC profiles at delta-high gamma (1-7 Hz phase vs 65-105 Hz amp) and theta-low gamma (3-9 Hz phase vs 25-65 Hz amp) phase-amp couplings. Regions were chosen based on the PAC profiles and not exact spectral frequency bins. Comparisons were done with the same regions across all layers and stimulus presentation frequencies. LFP and CSD spontaneous PACs are both included (left and right respectively). p value results and corresponding mean and std are shown. In bold are p values where significant above chance p < 0.05. Table in part published in Deane et al., 2022b.

Better signal to noise ratio in spectral power scalograms and stronger phase coherence in bats

In a final move to explore overarching species differences, we performed my favorite analysis: CWT analysis. After complex wavelet transforms were computed on center layer channels, power and phase coherence scalograms were extracted for both low (power: Figure 5.14 and phase coherence: Figure 5.16) and high (power: Figure 5.15 and phase coherence: Figure 5.17) stimulus frequency presentation conditions. Power was normalized to the maximum power in each measurement to result in a relative power of signal to background noise and to account for the large species difference in scale (bats had stronger unnormalized power by a factor of 3, not shown). Due to the stimulus presentation being unequal between datasets, permutation clustermass was run only on 200 ms of baseline activity and the time period from the onset of the stimulus train to the point of onset of the second stimulus (for 5 /5.28: -200 to 189 ms and for 36.76/40 Hz: -200 to 45 ms). Across both power and phase coherence at these time points for both stimulus conditions and across all spectral frequency bands, clustermass was significantly higher than chance according to permutation analysis (with one exception in the alpha frequency of layer III/IV power at ~40 Hz; Table 5-3). This attested to a reliability in the observed results pictured here.

In both ~5 and ~40 Hz comparisons of normalized spectral power (Figure 5.14 and Figure 5.15), the background around stimulus response was significantly different, with mice showing a higher level of spectral noise relative to signal response. In ~5 Hz, the time at which thalamic input entered the cortex had significantly higher power in bats around beta and low gamma. It was also higher in bats during thalamic input from alpha to low gamma at ~40 Hz. In both cases, a band of non-significant tests surrounded the higher spectral power of signal response to transition to the lower background spectral power in bats.

Phase coherence is a non-parametric result and was not normalized. Phase coherence was significantly stronger following each stimulus presentation in the ~5 Hz condition across a broadband of spectral frequencies. It was also significantly stronger as a broadband response at the onset of the stimulus presentation and in the spectral band within which the stimulus was presented in the ~40 Hz condition. In this higher frequency stimulus, there was also a significantly stronger high gamma phase coherence in bats.
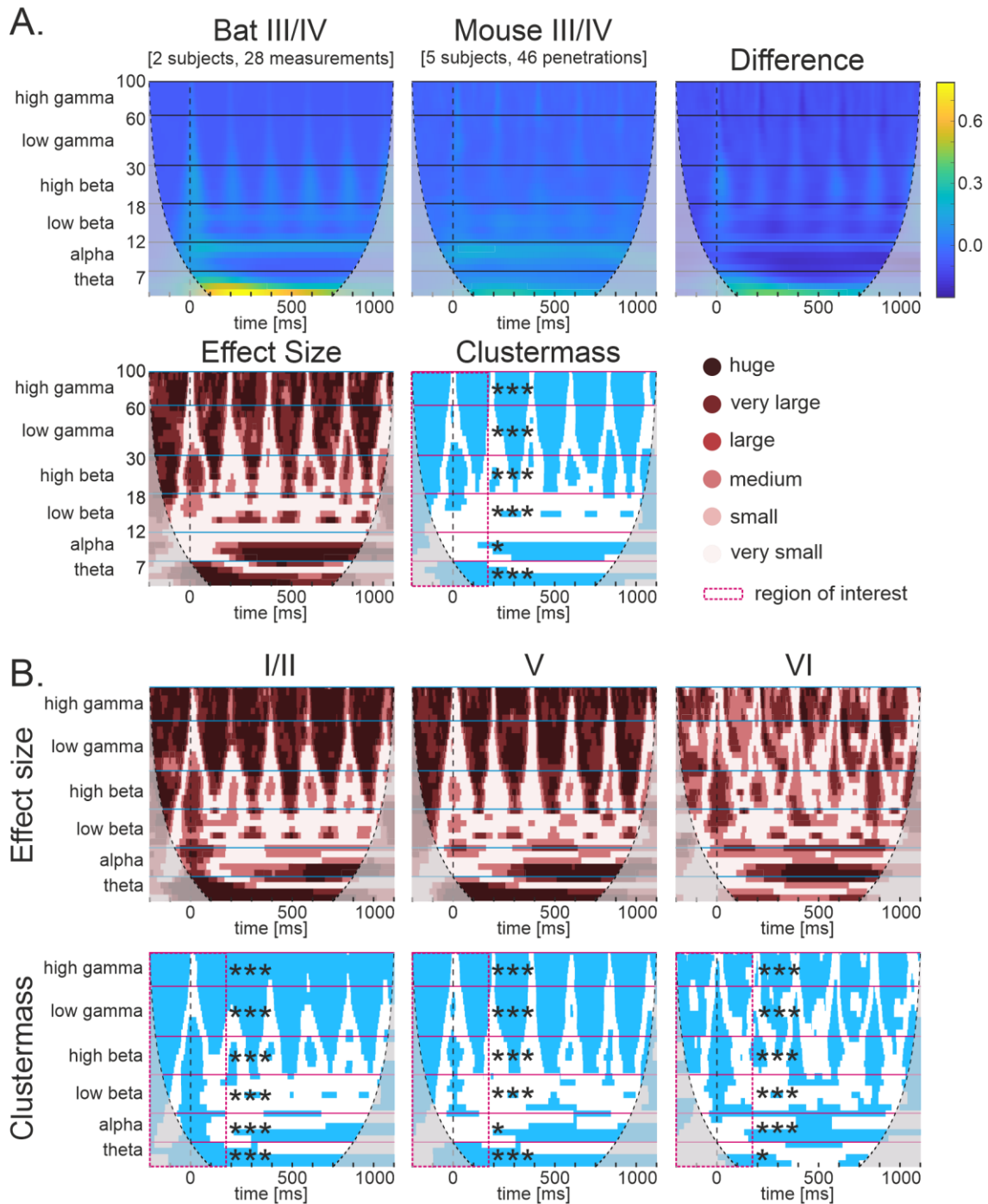
Figure 5.14 Power scalograms of continuous wavelet transform, ~5 Hz stimulus. A. top row: bat (left) and mouse (middle) grand average power CWT profile of layer III/III/IV during ~5 Hz stimuli presentation. The difference between them (bat – mouse) is on the right. **Bottom row:** bat vs mouse point-wise Cohen's d effect size results (left) and Student's t test result clustermass (right), where non-significant points, $p>=0.05$, are set to zero (white), leaving only clusters of significance ($p<0.05$, blue). **B:** bat vs mouse Cohen's d effect size profiles (top) and Student's t test clustermass results (bottom) for layers II, V, and VI (left to right). Horizontal borders designated spectral frequency bins: theta: 4-7 Hz (skipping delta in this analysis), alpha: 8:12 Hz, beta low: 13:18 Hz, beta high: 19:30 Hz, gamma low: 31:60, gamma high: 61:30. Overlaid on all clustermass plots are the results, where significant, of a permutation clustermass analysis at the baseline activity (200 ms before stimulus onset) to the time window of the first stimulus presentation (188 ms after stimulus onset) in each spectral frequency bin. *=p<0.05, **=p<0.01, ***=p<0.001. Modified image published in Deane et al., 2022b.
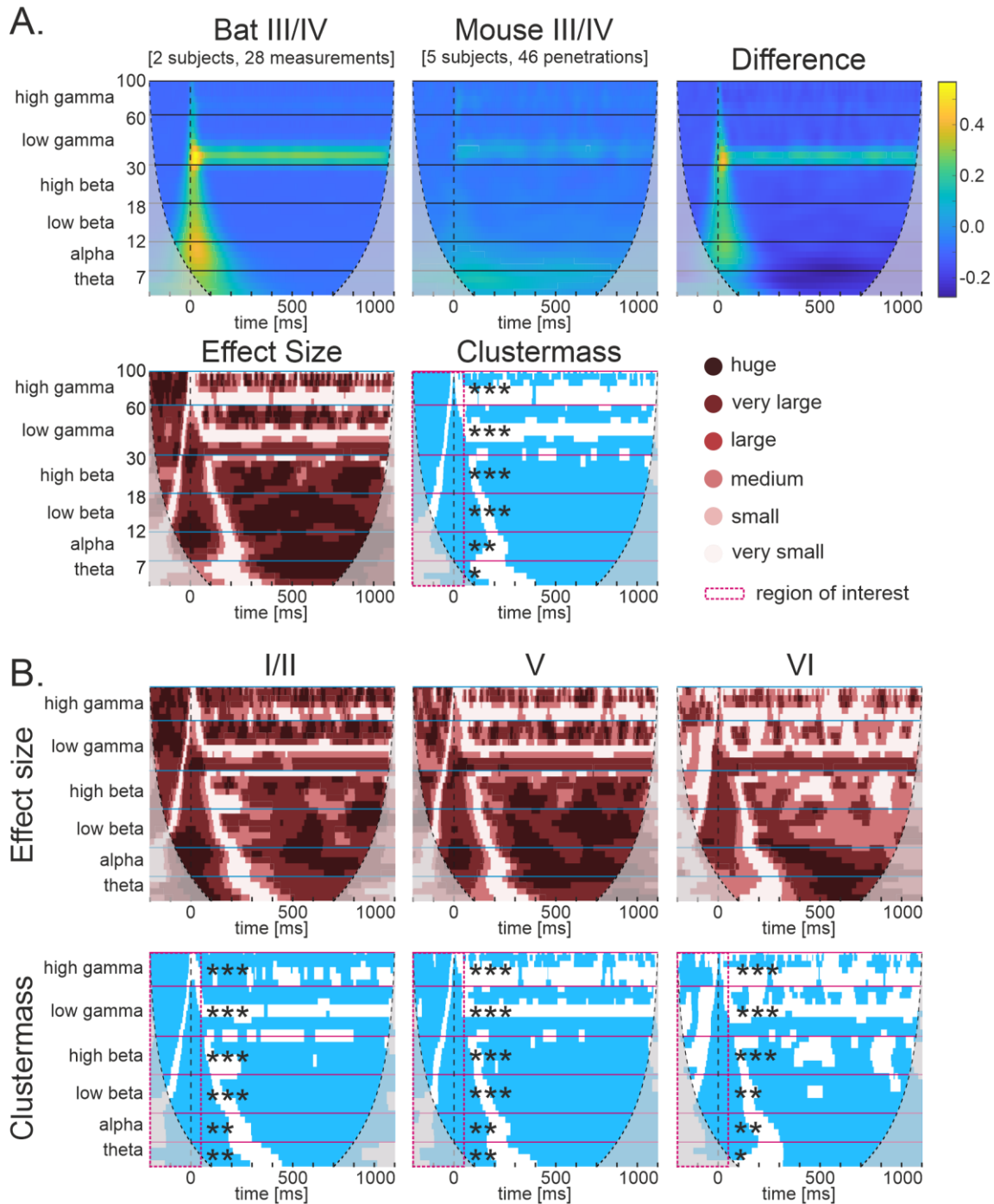
Figure 5.15 Power scalograms of continuous wavelet transform, ~40 Hz stimulus. A. top row: bat (left) and mouse (middle) grand average power CWT profile of layer III/III/IV during ~40 Hz stimuli presentation. The difference between them (bat – mouse) is on the right. **Bottom row:** bat vs mouse point-wise Cohen's d effect size results (left) and Student's *t* test result clustermass (right), where non-significant points, p>=0.05, are set to zero (white), leaving only clusters of significance (p<0.05, blue). **B:** bat vs mouse Cohen's d effect size profiles (top) and Student's *t* test clustermass results (bottom) for layers II, V, and VI (left to right). Horizontal borders designated spectral frequency bins: theta: 4-7 Hz (skipping delta in this analysis), alpha: 8:12 Hz, beta low: 13:18 Hz, beta high: 19:30 Hz, gamma low: 31:60, gamma high: 61:30. Overlaid on all clustermass plots are the results, where significant, of a permutation clustermass analysis at the baseline activity (200 ms before stimulus onset) to the time window of the first stimulus presentation (45 ms after stimulus onset) in each spectral frequency bin. *=p<0.05, **=p<0.01, ***=p<0.001. Modified image published in Deane et al., 2022b.
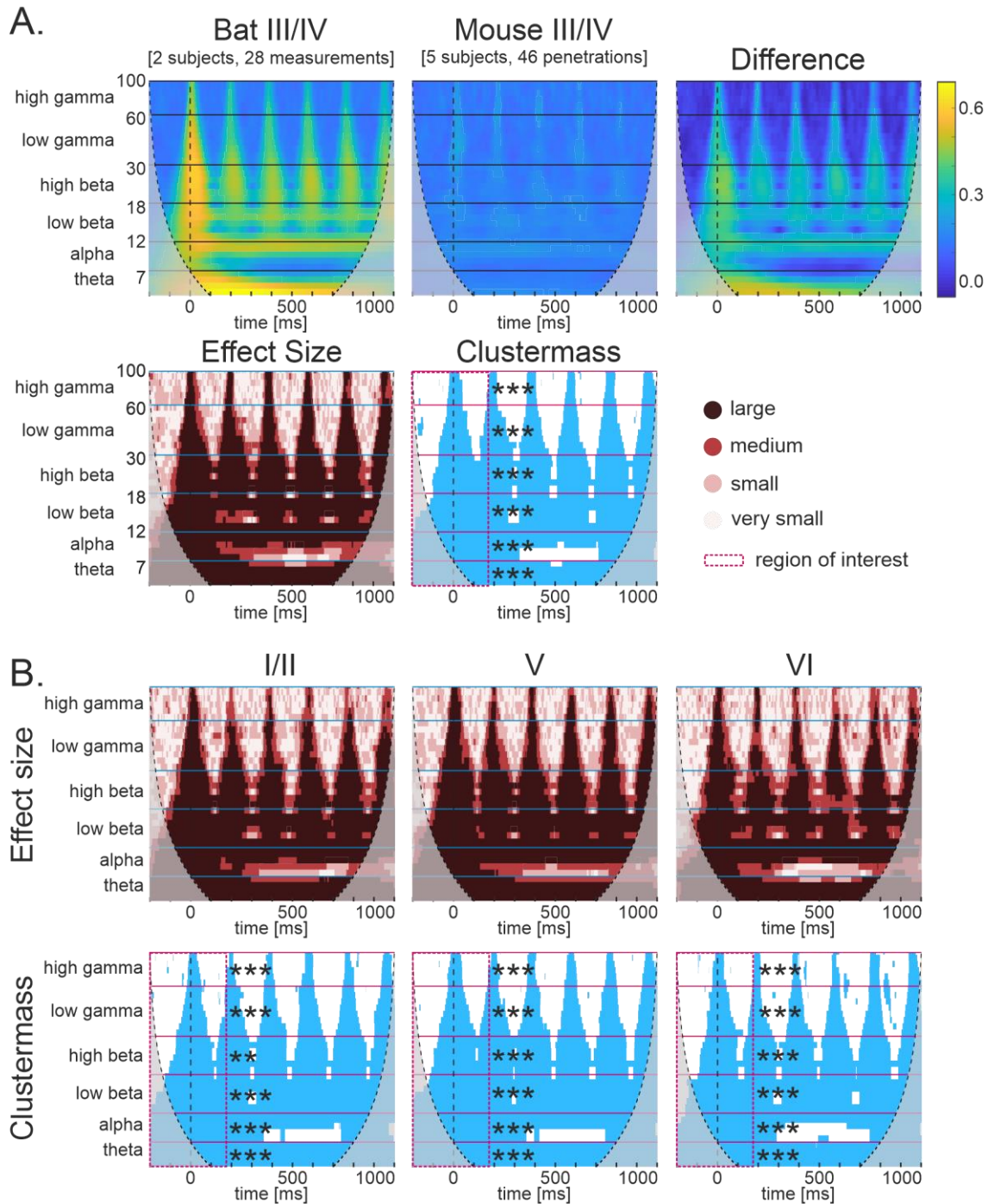
Figure 5.16 Phase coherence scalograms of continuous wavelet transform, ~5 Hz stimulus. A. top row: bat (left) and mouse (middle) grand average phase coherence CWT profile of layer III/III/IV during ~5 Hz stimuli presentation. The difference between them (bat – mouse) is on the right. **Bottom row:** bat vs mouse point-wise r effect size results (left) and Mann-Whitney U test result clustermass (right), where non-significant points, p>=0.05, are set to zero (white), leaving only clusters of significance (p<0.05, blue). **B:** bat vs mouse r effect size profiles (top) and Mann-Whitney U test clustermass results (bottom) for layers II, V, and VI (left to right). Horizontal borders designated spectral frequency bins: theta: 4-7 Hz (skipping delta in this analysis), alpha: 8:12 Hz, beta low: 13:18 Hz, beta high: 19:30 Hz, gamma low: 31:60, gamma high: 61:30. Overlaid on all clustermass plots are the results, where significant, of a permutation clustermass analysis at the baseline activity (200 ms before stimulus onset) to the time window of the first stimulus presentation (188 ms after stimulus onset) in each spectral frequency bin. *=p<0.05, **=p<0.01, ***=p<0.001. Modified image published in Deane et al., 2022b.
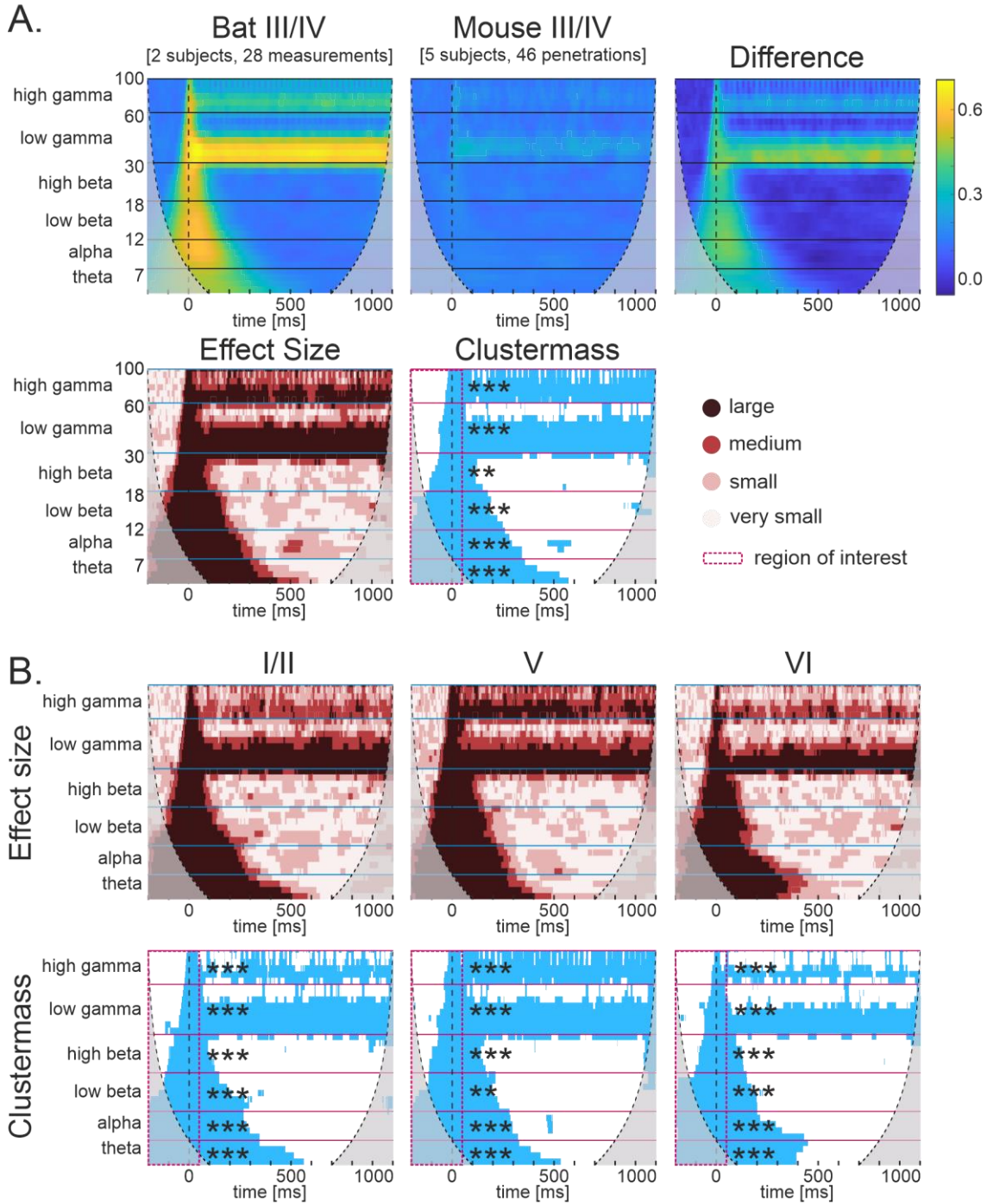
Figure 5.17 Phase coherence scalograms of continuous wavelet transform, ~40 Hz stimulus. A. top row: bat (left) and mouse (middle) grand average phase coherence CWT profile of layer III/IV during ~40 Hz stimuli presentation. The difference between them (bat – mouse) is on the right. **Bottom row:** bat vs mouse point-wise *r* effect size results (left) and Mann-Whitney U test result clustermass (right), where non-significant points, p>=0.05, are set to zero (white), leaving only clusters of significance (p<0.05, blue). **B:** bat vs mouse *r* effect size profiles (top) and Mann-Whitney U test clustermass results (bottom) for layers II, V, and VI (left to right). Horizontal borders designated spectral frequency bins: theta: 4-7 Hz (skipping delta in this analysis), alpha: 8:12 Hz, beta low: 13:18 Hz, beta high: 19:30 Hz, gamma low: 31:60, gamma high: 61:30. Overlaid on all clustermass plots are the results, where significant, of a permutation clustermass analysis at the baseline activity (200 ms before stimulus onset) to the time window of the first stimulus presentation (45 ms after stimulus onset) in each spectral frequency bin. *=p<0.05, **=p<0.01, ***=p<0.001. Modified image published in Deane et al., 2022b.

			Normalized Power			Phase Coherence		
			p value	mean	std	p value	mean	std
5 /5.28 Hz	II	theta	**0.000**	131.218	229.307	**0.000**	108.698	373.452
		alpha	**0.000**	97.514	173.180	**0.000**	87.212	246.840
		beta low	**0.000**	102.108	157.640	**0.000**	92.362	219.304
		beta high	**0.000**	92.496	150.770	**0.002**	88.138	175.845
		gamma low	**0.000**	149.660	178.927	**0.000**	149.122	146.197
		gamma high	**0.000**	116.752	144.497	**0.000**	131.186	67.101
	III/IV	theta	**0.000**	116.776	201.918	**0.000**	110.574	369.175
		alpha	**0.028**	94.676	176.134	**0.000**	94.714	265.334
		beta low	**0.000**	83.174	127.432	**0.000**	89.876	211.257
		beta high	**0.000**	86.382	134.406	**0.000**	87.820	181.234
		gamma low	**0.000**	157.592	212.520	**0.000**	145.158	166.716
		gamma high	**0.000**	130.882	205.087	**0.000**	125.694	71.814
	V	theta	**0.000**	131.484	236.421	**0.000**	114.956	359.558
		alpha	**0.010**	110.056	200.274	**0.000**	106.052	295.422
		beta low	**0.000**	104.466	161.433	**0.000**	91.080	215.649
		beta high	**0.000**	102.774	143.779	**0.000**	82.994	166.020
		gamma low	**0.000**	169.066	212.964	**0.000**	141.354	143.801
		gamma high	**0.000**	151.984	217.861	**0.000**	128.998	70.227
	VI	theta	**0.042**	111.344	217.676	**0.000**	131.896	371.271
		alpha	**0.000**	97.294	173.137	**0.000**	106.156	270.288
		beta low	**0.000**	94.464	144.153	**0.000**	97.940	199.283
		beta high	**0.000**	104.068	143.423	**0.000**	97.138	158.641
		gamma low	**0.000**	147.438	170.821	**0.000**	161.754	157.741
		gamma high	**0.000**	134.766	141.875	**0.000**	136.838	69.893
40 / 36.76 Hz	II	theta	**0.004**	70.496	176.558	**0.000**	64.418	195.627
		alpha	**0.002**	56.456	132.608	**0.000**	52.102	153.776
		beta low	**0.000**	58.520	118.183	**0.000**	49.800	75.338
		beta high	**0.000**	52.784	97.670	**0.000**	53.690	111.368
		gamma low	**0.000**	92.996	128.107	**0.000**	83.924	83.188
		gamma high	**0.000**	76.458	108.597	**0.000**	75.336	43.698
	III/IV	theta	**0.014**	72.490	162.299	**0.000**	62.692	186.233
		alpha	**0.008**	53.774	125.424	**0.000**	40.466	131.779
		beta low	**0.000**	58.204	116.705	**0.000**	47.138	102.103
		beta high	**0.000**	50.516	86.014	**0.002**	52.118	86.863
		gamma low	**0.000**	88.592	113.666	**0.000**	85.342	86.573
		gamma high	**0.000**	69.468	96.232	**0.000**	74.210	51.314
	V	theta	**0.008**	81.166	190.576	**0.000**	66.272	201.887
		alpha	**0.006**	60.426	133.991	**0.000**	51.592	152.009
		beta low	**0.000**	58.462	107.648	**0.000**	62.634	136.351
		beta high	**0.000**	47.114	83.609	**0.002**	55.520	93.465
		gamma low	**0.000**	85.062	112.553	**0.000**	92.212	107.622
		gamma high	**0.000**	76.046	98.973	**0.000**	78.158	59.692
	VI	theta	**0.010**	55.432	135.470	**0.000**	78.092	200.108
		alpha	**0.008**	67.270	147.863	**0.000**	55.574	148.022
		beta low	**0.002**	58.962	114.004	**0.000**	59.316	115.638
		beta high	**0.000**	56.724	99.520	**0.000**	60.592	83.472
		gamma low	**0.000**	92.646	109.561	**0.000**	86.642	78.144
		gamma high	**0.000**	81.128	94.222	**0.000**	75.170	47.197

Table 5-3 Between group CWT spectral band clustermass comparison. Bat vs Mouse region of interested comparisons of power and phase coherence scalograms for ~5 and ~40 Hz. ROI was the 200 ms before stimulus onset to 189 ms after stimulus onset in the 5/5.28 Hz stimulus condition or 45 ms after stimulus onset in the 40/36.76 Hz stimulus condition for each spectral band. p value results and corresponding mean and std are shown. In bold are p values where significant above chance $p < 0.05$. Table in part published in Deane et al., 2022b.

Discussion of chapter 3

Ecological niches and experimental considerations

Seba's short-tailed bats have sophisticated social communication and echolocate for navigation (Beetz et al., 2017; Hechavarría et al., 2013; Thies et al., 1998; Weineck et al., 2020), meaning that accurate and timely perception of auditory signals is paramount to successful social and flying behavior. Mice have a smaller repertoire of social verbal cues (Fonseca et al., 2021) and rely most heavily on their whiskers and olfaction for navigation (Gire et al., 2016), meaning that comparably precise cortical representation of auditory cues is not necessary for success in their environment. With this in mind, we compared the auditory response characteristics of two mammals from the kingdoms *Chiroptera* and *Rodentia*—with a similar body and brain mass—that either were or were not an auditory specialist. A cross species comparison can give us the basis for understanding neuroethology and evolutionary specialization, but such a comparison should be taken with caution for exactly the same reason—the niches of each animal require fundamentally different perception and decision algorithms.

The multichannel datasets of our subject species were taken from 2 projects; and while the recording equipment was shared between them, the stimuli and presentation frequencies were not precisely the same. Most importantly for consideration of this study: mice were listening to a repeated artificial click stimuli and bats were listening to a repeated, species-specific distress syllable. We would not like to make claims grander than we have the ability to, but rather to discuss overarching functional differences in auditory response profiles with the consideration of how their auditory system serves them in a behaviorally relevant environment.

Laminar structure overlap and differences

While the laminar structure of the neocortex is shared between mammals (Mountcastle, 1997), there were some differences between seba's short-tailed bat and black 6 mouse primary auditory cortex layers in histology (Chang & Kawai, 2018; García-Rosales et al., 2019) and in population activity. Two main differences stood out between species.

First, the supragranular layer of activity revealed by CSD analysis (Figure 5.1) was different in depth. Layer selection for bat CSD profiles was done per penetration. As seen in the grand-averaged CSD profile for these bats, supragranular activity was consistently thicker—taking up more channels on the probe relative to the full profile—than in mice. This distinction between supragranular and granular activity is clear in the bat CSD profiles, where the former had a definite lag behind the latter. In the mouse CSD profiles, supragranular activity was less divergent from granular activity and consistently proportionally thinner. In histological studies of the laminar profiles for each of these animals, either layer I and II were distinguished separately (García-Rosales et al., 2019) or layer I was separate and layer II was combined with III and IV (Chang & Kawai, 2018). It appears that layer I is proportionally thicker in the bat A1 than in the mouse A1. While this agrees with the population activity we observed in this study, it did not fully account for how much thicker supragranular CSD activity was. This may indicate differing recruitment of layer II neurons to either assist in layer I cross-columnar activity or in the layer III and IV excitation feedback circuitry between species.

Second, in the thinner bat A1 cortex, thalamic input to granular and infragranular layers appeared as more of a single sink. In the mouse A1, there were separable input sinks at the onset of a stimulus and both layer V and VI were thicker than in the bat CSD profiles. Following the histological references of Chang & Kawai, (2018) and García-Rosales et al., (2019), we found support for our layer designations. Layers III and IV in bats (~300 µm) are half-again as thick as both V (~100 µm) and VI (~100 µm). In mice, combined layers III and IV are more equivalent in size to layer V, and layer VI is around half the thickness of layer V. Therefore, despite the shared architecture, there were already differences as to the size of each layer and this likely contributed to the differing recruitment profile of microcircuitry across species.

Exploring these questions further is beyond the scope of this study, but a comparative histological review along with laminar activity profiles should be conducted to further understand the role of microcircuitry recruitment across layers.

A better signal to noise ratio in bats leads to lower resource cost on accurate stimuli response

The bat auditory cortex seems to be more readily primed for accurate perception due to a higher signal to noise ratio. We explored this with comparison of AVREC and layer traces in response to 2 stimuli frequencies, model fit analysis, and CWT analysis. Overall, in the comparison of signal traces at ~5 and ~40 Hz (Figure 5.2 and Figure 5.3), bat normalized cortical activity had less jitter around stimulus response. That is, the pre-stimulus baseline was closer to its relative 0 and cortical activity adapted back closer to relative 0 after the onset response component (first 200 ms) and each following response to consecutive stimuli. Mouse normalized activity was more variable, and contained more noise compared to signal. This caused higher amplitude following responses at ~40 Hz due to a continuously higher amplitude signal. Figure 5.4 shows that when the signal was bandpass filtered around the high frequency stimulus presentation, the higher level of activity was no longer represented in mice, indicating that the noise was not related to the stimulus frequency. This was then further reflected in the model fit analysis, which showed more similar response profiles between species.

In the ~40 Hz condition of the model fit analysis (Figure 5.6) bats had a higher intercept (first observed peak amplitude) in the AVREC and thalamic input layers III/IV and V. They subsequently had a deeper suppression of response amplitude to consecutive responses, reflected in the higher depth parameter. This was also generally true at the lower stimulus frequency condition, but less clear due to fewer data points. Due to the deeper suppression in bats, the response amplitude generally adapted slower to stimuli in these traces at ~40 Hz, reflected in the lower rate of decay parameter in the AVREC and layer V. As mentioned above, mice had a weaker onset response, a lower intercept, and a shallower rate of suppression to consecutive responses due to higher noise in the signal trace. When the onset component was removed from this analysis (Figure 5.7), the following component in bats still had a better signal to noise ratio in the same sense: that the depth was generally greater, meaning, consecutive responses reached a lower amplitude relative to the intercept.

This is further supported by the normalized power scalograms from the CWT analysis (run on CSD data; Figure 5.14 and Figure 5.15). In these results, there were two components to the significant difference between bats and mice. The bat spectral power was significantly stronger

at the timepoint of stimulus onset response, throughout the layers, especially in the ~40 Hz condition. However, the background spectral power was significantly stronger in mice, especially at higher oscillation frequencies where stimulus response was at a shorter time scale (due to temporally smaller wavelets at higher frequencies). The signal to noise relationship between each species was so different that little else could be understood from the CWT power analysis. In conjunction with the visually cleaner onset and following responses in the AVREC and layer traces for the bats, this suggests that the signal to noise ratio is significantly better in bats and that may create a cortical environment where stimulus processing is more temporally precise at a relatively lower activity cost to the neural populations.

Phase coherence revealed lower inter-trial variability in bat auditory response profiles

The phase coherence scalograms from CWT analysis revealed a significantly stronger inter-trial broadband phase coherence at the time of stimulus onset for both low and high frequencies and following response for the ~5 Hz condition. Phase coherence was also stronger in low gamma (around the frequency of the stimulus presentation) and high gamma spectral bands for the ~40 Hz condition. The difference was profound and held up very well to permutation testing. Given this result, it's clear that bats had more consistent response profiles across trials and measurements. We might have expected mice to have better coherence, because the probes were chronically implanted rather than having new penetration sites per measurement (as in the bat dataset) and there were more measurements per mouse than penetrations per bat. The greater variability was commonly seen, counterintuitively in that sense, in the mouse data. This was true of the level of background jitter in the AVREC and layer traces in the mice and in the better exponential decay model adaptations due to more variable peak amplitudes in the mice.

It is possible that these are purely a reflection of the difference in the stimuli presented. Mice heard a behaviorally irrelevant click stimulus in a passive-listening condition. The mice were habituated into their head-fixation setups but the level of anxiety (measured in increased corticosterone) in head-fixed mice never fully attenuates (Juczewski et al., 2020). Therefore, they may have either associated the click train to their stress-inducing fixation, or they may have been ignoring it completely (or any other guess as to the inner thoughts of mice). Bats, on the other hand, were listening to a behaviorally relevant syllable: a distress syllable from a recording of another of its species. Bat stress levels were monitored through movement, uneasiness, and vocalizations and recording was discontinued each day upon signs of overt stress in bats during recording. However, they were freshly separated from roost mates after the cortical window was made for access to their A1. Their level of stress was therefore not known and difficult to compare to the mice. It is possible that the single syllable is not as alarming as the full distress call message that it's taken from. It is also possible, that the repetition of such a syllable causes it to lose its behavioral relevance after a time (imagine hearing a recording of someone shouting "me" over and over again at different rates for 30 minutes while tied to a chair). The same may be said for the mice listening to clicks on repeat for days.

While this difference in stimuli may partly be the cause of less variability in cortical response profiles—due to difference in attention and stress—specialization in auditory perception also likely plays an important role. Bats require temporal precision in their auditory perception,

like we require spatial precision in vision to catch a ball, and mice require precision in their olfactory senses to forage. That a bat has more accurate and less variable auditory responses to consecutive stimuli than a mouse may be successful specialization of shared perceptual architecture for different ecological niches. It is also distinctly possible that the trade-off between flexibility and precision here is compensated for in a different way, unexplored by this analysis. Further cross-species comparisons may give us insight into the differential ways the mammalian cortex introduces or limits variability in populations of neurons based on behavioral or ecological need.

Phase amplitude coupling was fundamentally different between species

As discussed in García-Rosales et al., (2020), the functional use of PAC for information binding, segmentation of continuous stimuli into slower times scales of perceptual units, may be conserved through evolution as a shared mechanism in mammals. For example, in humans, theta gamma PAC has been implicated in efficient processing of speech phenomes into words and sentences (Gross et al., 2013; Lizarazu et al., 2019; Zion Golumbic et al., 2013). García-Rosales et al. suggested that bats could utilize this parsing strategy on echolocation to make sense of their auditory, and therefore spatial, scene. Vocalization and movement were not tracked in a way that they could be removed from the analysis of either species in this study. Therefore, conclusions drawn must be treated as largely speculative. We ran a PAC coupling analysis on the A1 datasets for bats and mice at low and high stimulus presentation conditions and during spontaneous activity. This analysis was run on the LFP signal, which reflected global inputs to the A1, and the CSD signal which revealed PAC of local activity (Happel, 2016; Happel et al., 2010, 2014).

The mouse LFP PAC had a consistently very strong area of PAC at delta high gamma. Mice were freely moving, and this may bias global coupling due to strong motor-cortex driven PAC during movement. Spontaneous LFP PAC was the strongest and largest area of coupling at this delta high gamma region in mice. When the analysis was run instead on CSD signal, this A1-deep PAC almost disappeared. Local PAC coupling in mice was similar in both stimulation frequencies and was strongest in layer III/IV. It was weakest during spontaneous activity. Local coupling therefore seemed to be dependent on a stimulus being present but was not sensitive to the frequency of presentation. Quite the opposite, the PAC coupling area in bats was centered around theta/alpha and low gamma and the local, CSD coupling profile was stronger in comparison to PAC analysis on the LFP signal. This was true of the stimulus presentation conditions and the spontaneous activity. However, PAC in the spontaneous activity was far stronger than during stimulus presentation on both signal types. Unlike in mice, bat PAC on CSD signal was different for low and high frequency presentation stimuli. Especially in layer III/IV, PAC was stronger at 5.28 Hz.

Bats and mice were most different in their spontaneous activity PAC, where each had a significantly stronger region of coupling in the LFP PAC, and bats had a significantly stronger and broader area of coupling in the CSD PAC. Mice had stronger PAC overall in the global signal and bats had stronger PAC in layer III/IV in the local signal at the lower stimulus frequency. It appeared that running the PAC on CSD profiles removed movement-driven biases, and other possible global influences, from the coupling profiles. However, PAC analysis is very sensitive to initial input conditions and surrogate testing. Therefore, further research would need to explore this phenomenon more directly to validate its interpretation. Regardless of signal frequency, or whether it was stimulus derived or during resting-state, coupling was

centered around delta high gamma in mice and theta low gamma in bats. The similarity in the bat PAC with human speech perception theta gamma coupling may support the hypothesized auditory scene parsing. This region may have had greater local A1 coupling because the repeated stimuli was specifically a bat vocalization phenome. It is also possible, though, that the delta high gamma coupling profile in mice were performing the same task but in a different temporal scale.

Further evidence to support the bat vocalization phenome or echolocation processing, specifically, was the slower adaptation of exponential decay in the overall signal and in thalamic input to layer V at higher frequency stimuli. In human research, a slower adaptation to repeated stimuli is implicated in the ability to parse continuous information into chunks, called sensory memory (Yu et al., 2018). Further experimentation with matched stimuli between species in a mismatched negativity condition would be needed to explore this.

Conclusion

When comparing two fundamentally different species, with alien subjective experiences, an analysis like this cannot say more than that these species have different interpretations of objective, external sound waves (Nagel, 1974). Nevertheless, cross-species comparisons can serve as valuable framework in consideration of shared, convergent, and divergent evolutionary adaptation (Sherry, 2007). Seba's short-tailed bats have adapted to an ecological niche which requires accurate temporal auditory perception during 3-dimensional navigation in flight and complex social communication—making them an auditory specialist. Mouse specialization lies in different perceptual regions, and they do not need as comparably accurate sound representation to find behavioral success in their environment. We have found, comparing these two mammals, that bats therefore have a significantly better signal to noise ratio, more accurate and less variable following responses to consecutive stimuli, far higher inter-trial phase coherence, and fundamentally different PAC profiles. These discrepancies do not stem from differing cortical architecture, though some variance has been noted there, but from the divergent recruitment of shared microcity and laminar organization seen in all mammalian species.

Chapter 6: Discussion

Abstracting neurophysiology

The term "physiology" was used in writing for the first time by a French physician, Jean Fernel (1497–1558), to explain function of the body in relation to the brain (Sherrington, 2014). The study of sensation and intellect was already over a thousand years old—with the view of thoughts originating from the brain, rather than the heart, generally accepted in the time of Galen, a physician to the Romans who demonstrated viscerally that behavior and emotion were connected to brain function only (Freemon, 1994). It would be another 150+ years, into the 1700s, before we could begin to study electrical signals in the brain. The mid 1800s saw a rapid growth in neuroanatomy, neurobiology, and neurophysiology with microscopes and new staining techniques. Santiago Ramón y Cajal used the Golgi staining method to bring the inside of the brain to the wider public in ways previously unseen (Finger, 2005). The case of Phineas Gage provided striking insight into brain function and anatomy in relation to emergent personality (Harlow, 1999; Sevmez et al., 2022). Seminal neurophysiology studies up through the 20th century have discovered important features of the cells, circuits, and regions of the brain. Classically, this has been done following the scientific convention of reductionism, such as the work done by Hodgkin and Huxley (1952) on the iconic squid axon action potential, by Hubel and Wiesel (1959) on visual receptive fields in partially anesthetized cats, and by Hebb (1949) on synaptic plasticity. Technology continues to improve, and schools of thought continue to develop and multiply. It has become more and more evident that studying the brain, as a whole, in awake and behaving animals is important to relate the studied phenomenon to wakeful behavior (cf Markicevic et al., 2021). For example, while it was revealed that neurons in awake primates behave similarly to those of anesthetized cats (Hubel & Wiesel, 1962; Wurtz, 1969), even being awake involves multisensory convergence (Lakatos et al., 2007), and motivation or emotional valence can actually shift cortical neural states (Fontanini & Katz, 2006). It is also slowly becoming more popular to contextualize results from our fields further out and to understand phenomena across temporal and spatial scales. Afterall, we can see how interdisciplinary neuroscience has already become and in what areas neuroscientists branch out to work in.

Therein, however, presents a relatively newer challenge. While the scientific method seems to require some amount of reductionism—one must control factors to say whether they had an effect, it is not simple to investigate only one thing in the brain, reducing all else. It is also not possible to relate that reduced target to a complex function or non-linearly related concept in a wholistic way. So far, that hasn't stopped scientific advancement; everything that came before has built a foundation of scientific fact that we largely take for granted and learn as children: the anatomy of neurons and their action potentials for example. The history of neurophysiology is one context that we function in and informs our decisions on how and what to investigate as neurophysiologists. It also provides us with a substantial set of findings that we can piece together into larger pictures with newer work aimed at connecting such things. However, the question posed here is how to structure scientific inquiry aimed at connecting across boundaries. It is the growing goal of a wider scientific community to lay the framework for incorporating larger contexts and becoming comfortable with being, living in, and studying complex systems. Systems neuroscience for example, the field in which I work, and complexity sciences were sown from the questions posed by cybernetics—so named and described as "the entire field of control and communication theory, whether in the machine or in the animal" by Norbert Wiener (Wiener, 2019). I would argue that future leaps in neuroscience will be in

collaboration with complexity science, as a framework for developing wholistic understandings, common elements across systems, and bridges between previously discriminated subjects of investigation.

On that note, my projects all seek to compare across certain established physiological boundaries: anesthetic states, micro- and mesoscopic scales, and mammalian species. Complex systems require a multifaceted approach, where researchers are coming at the problem from different directions and at different scales. The impact of my work can be explored in that context. Neuroscience is a highly topical, popular science and, every year, countless studies are published that further develop our picture of the brain. However, we are only beginning to understand how pieces of this complexity puzzle may fit together and how studies across domains may relate. How comparable is the auditory cortex across even the boundaries considered in this work? In the context of this dissertation, I have been able to demonstrate the need for systems-theoretic approaches that would accompany neuroscientists by looking at three subfields. I showed that anesthesia and brain states, sub-molecular dynamics of single molecules involved in signal transduction, as well as species-specific differences in brain functioning are all factors that need to be considered by systems neuroscientists studying this complex system. I subsequently argue that this validates a need for integration with complexity science or at least that the framework of complexity offers a ground to explore the broader context of our work. Our ability to create complex systems (e.g. economics), as a group of biological organisms, is a motif of nature repeating even her ability to develop them. As scientists, we are capable of building strategies to optimize how science comes together across disciplines, scales, and other boundaries to find a higher-order language of biological life. To accomplish that, it will take a conscious effort of at least a portion of the population to think and work toward that goal and to also apply the research of others under that umbrella. A complex system solution to understanding complex systems.

Research outcomes and wider connections

I cannot claim that the work I've done up to this point was for the intention of complexity research in neuroscience. The beauty of basic research is the application potential and the adaptive interpretations. This work has opened my eyes to an exciting field with the idealistic goal to unify fields. Here, I am providing insight into specific anesthetic usage, voltage gated calcium channel motility and its contribution to wider networks, and on differential processing across species with different ecological niches—all now within a wider context under the prism of complexity, that I would like to briefly summarize and connect with below.

Ketamine induces non-linear brain-state and microcircuitry changes

Ketamine, an NMDA antagonist, induces a gain increase in granular layer feedback in the primary auditory cortex of gerbils (Deane et al., 2020). This is likely accomplished by a biased suppression of PV-releasing interneurons, which normally inhibit the feedback circuitry that responds to granular thalamic input (Kato et al., 2017; Miller et al., 2016). These results showcased the balanced relationship of excitatory and inhibitory microcircuitry, which could potentially be offset to create cortical environments not suitable to successful auditory processing and filtering. That is to say, the feedback that should have dampened cortical response was not as active and may not have facilitated the proper corticothalamic feedback

to filter the stimulus appropriately. Schizophrenia is a disease linked to hypoactive NMDA receptors, partially due to ketamine and other NMDA antagonists inducing a psychotic state resembling the disorder (Lodge & Mercier, 2015). To be clear, the implication is then that hallucinations under the influence of ketamine and schizophrenia may be due to the same mechanism of disinhibition of cortical feedback and lack of appropriate cortical response to input. The increase in granular layer recurrent excitation that we explored in Deane et al. (2020) demonstrates mechanistically, at a mesoscopic scale, the unnecessary amplification of input which would underly such hallucinatory experiences. Ketamine has been used in other species and sensory systems and, for instance, also decreases the input selectivity and neuronal variability of sensory-evoked input processing in the visual system of the mouse and cat (Ouelhazi et al., 2019). The reduction of variability, a key feature in complex systems (Mitchell, 2011), may partly explain the maladaptive cortical response. Ketamine has the function of anti-depressant (Berman et al., 2000), psychotic, or anesthetic agent depending on dose, making it a complicated drug that acts non-linearly in the brain.

In neuronal population and cortical column studies of the A1, layer IV is classically implicated as the main thalamic input layer and is often used to characterize the columnar best frequency (Happel, 2016; B. Liu et al., 2007; Thomson & Bannister, 2003). The context of ketamine and its disproportionate action in this layer must be factored into interpretation of the results. This also includes, broadly, interpretation of earlier results from studies using ketamine at full or partial anesthetic dosage. Historical research, foundational or not, is subject to modern understanding—to recontextualize it for continued usefulness. The work that has been done to understand basic mechanisms under anesthesia is often foundational for studies of awake behavior, crossing brain state boundaries. The context of a non-linear psychotic state effects cannot be overstated when considering how studies might be interpreted between anesthetized and awake subjects. This is especially true when the exact same recording software can't be used, and one must work on assumptions that basically the same effect is happening inside the brain of an awake subject as seen under anesthesia.

Clustering P/Q VGCCs, critical to neuronal function, at the mesoscopic scale reduced cortical activity broadly and systemically

With an elegant method to cluster pre-synaptic VGCCs using CRY2olig optogenetic technology (Heck et al., 2019; Taslimi et al., 2014), it was demonstrated that we could reduce the firing variability of single neurons. We revealed that when VGCCs were clustered across the primary auditory cortex of mice, a transient and deterministic-inducing process at a single-cell level, it caused a systemic, lasting suppression to overall cortical activity (Deane et al., 2022a). This suppression was dependent on the level of neuronal recruitment—with clearer suppression in response to broadband click stimuli compared to amplitude modulated pure tones, compared to resting state. Altered calcium influx can lead to, amongst other things, migraine aura (Plomp et al., 2001) ataxia, and epilepsy (Ophoff et al., 1998). Calcium influx is a crucial mechanism of neuronal function, and it is difficult to study at higher scales as it is a molecular process. The study of it at microscopic scales, reducing to single cells and channels, has classically led to translational steps in understanding these disorders and is being positioned to find solutions to them. However, as my work demonstrates, interpretations from the microscopic to the whole brain are only possible in a limited capacity due to non-linear relationships across these scales. For example, common migraine prophylaxes are, at different doses, antidepressants and antiepileptics (Nimmrich & Gross, 2012) because these all have

pathologies that link to P/Q VGCCs; but there are not targeted drugs specific to preventing or curing migraines because the disease is still not wholistically understood. Our work here was to narrow the gap between pathology in whole organisms and the microscopic function of channels involved in signal transduction.

To that end, our results support the argument that the loss of variability at a single-cell level in the population, hurt its overall robustness and ability to adapt dynamically to different stimuli. Thus, our findings indicate that single molecular dynamics can indeed influence the behavior of populations in the cortex. However, the precise relationship between the roles of excitatory and inhibitory neurons, synaptic integration of inputs, circuit architecture, and neuronal dynamics that might be mutually influenced by our manipulation are not yet fully understood. In our collaboration, the first part of the study was done *in vitro* at a microscopic level. As stated above, assumptions need to be made when the recording equipment cannot be conserved across scales. The assumption here, was that the individual neurons *in vivo*, when infected with the lentivirus to receive CRY2olig tags on their VGCCs, would behave the same way as individual neurons *in vitro*. By taking a known effect at a cellular level, and infecting the wider A1 network with it, we aimed to establish the validity of this method to study channel dynamics at mesoscopic scales. In that regard, we had mixed results. While we did find a robust suppression of cortical activity, it clearly had a non-linear relationship to the effects found in smaller (e.g. molecular or microscopic) scales. We have no idea if we induced migraines, post lentivirus transduction, or set the mice on course for aging disorders and what that might mean in the context of translational work and what our results indicated. We did, however, find evidence of the consequence of reducing variability, but we are unable to relate it to other possible chain-reaction effects that may be responsible for its lasting effect on cortical activity despite the transient nature of the clustering protein. These cannot be overlooked in a wider conversation about the role of channel dynamics in pathologies that effect whole organisms. The results shown here were a valuable first step in filling in some of the space between channels and whole brains; a great deal more work will be required to approach an understanding of how the disordered calcium influx mechanic travels up through scales to cause disorder and disease.

Evolutionary adaptation causes divergent recruitment of shared microcircuitry or ecological specialization

"Species" as a physiological boundary is more abstract than internal brain states or spatial scales within one complex system. However, we are all related across evolution and our cognitive and perceptual abilities have seen many convergent and divergent pathways, all within a shared biological substrate of neural tissue. All mammals share laminar cortical architecture (Mountcastle, 1997), however we do not navigate or even experience our environments in ways congruous with each other. Our needs and which senses provide us with important navigational and societal information shape the way our neocortices, to say the least, have developed (Nagel, 1974). Therefore, in the comparison of a seba's short-tailed bat, an auditory specialist, and mouse primary auditory cortex, bats were shown to have a better signal to noise ratio and lower inter-trial phase variability. Bats also had a phase amplitude coupling profile that was stronger in local auditory circuits compared to global, which was the opposite for mice. The microcircuitry between these two species is largely shared, but the use of the auditory cortex for behavioral success has caused divergent adaptations. These findings fit into a neuroethological narrative: a better signal to noise ratio may allow for clearer and

more temporally precise cortical following to repetitive stimuli at a reduced metabolic cost compared to mice. However, the difference in variability between bats and mice was surprising.

In comparing awake and anesthetized auditory cortical activity, for both Mongolian gerbils (Deane et al., 2020) and mice (anesthetized in Deane et al., 2022a and awake in Deane et al., 2022b), the level of variability, or noise, was far higher in awake animals. As previously discussed, built-in variability creates a dynamic environment for an organism to adapt. This may mean on a shorter timescale, for example in assigning meaning to previously unimportant stimuli (Zempeltzi et al., 2020), or on a longer timescale as environments change and a species evolve. The awake bat cortical activity resembled anesthetized gerbils and mice in the clarity of signal response and lack of noise. For bats, temporal precision in auditory processing translates directly into accurate representation of their environment while flying. Failure to perform that task might be fatal in many cases. This is even more interesting when taking the recording methods into consideration. The bats from which we recorded had been expected to show higher variability because each measurement was taken at a separate penetration site from 5 bats. In contrast, 2 mouse subjects had chronically implanted electrodes which therefore recorded from the exact same place in each. A methodological consideration would have been to excuse lower variability in mice compared to bats due to the difference in electrode protocol, but the opposite was revealed.

What we cannot rule out is the prevalence of silent neurons in short-tailed bats' A1s compared to mice (cf. Shoham et al., 2006). In mice, we found that intrinsic noise was higher. Their species does not need to compute echo-delay as bats do, which requires very temporally precise neural circuitry (Hechavarría et al., 2013; Macías et al., 2013). It is possible that the level of specialization in bats required for this type of behavior leaves less room for flexibility in their population activity. Lower temporal variability likely represents an advantage in this scenario. It is also possible that the percentage of neurons active in response to repetitive stimuli is similar in bats and mice, but that bats have a higher proportion of silent to intrinsically active cells, allowing them to achieve the necessary precision and maintain the room for robust adaptation (cf. Ovsepian, 2019). Further cross-species examination would be needed to confirm or refute either of these possibilities. And in fact, the findings of dissimilarity within highly conserved laminar architecture in the auditory cortex, expected or not, indicate a need to develop a better understand of what neural mechanisms organisms have evolved to navigate their ecological niches. My work has already been able to show the influence that the role of transmitter equilibria, brain states or molecular dynamics, can have. What other subtle differences there may be in networking, number of excitatory and inhibitory synapses, or functionality of individual elements between species is the subject of further research.

Impact

The results of Deane et al., (2020), demonstrating the effect of ketamine on auditory cortical population activity, has impacts on the interpretation of work across micro- to macroscopic scales in studies where the drug is applied. It also provides a ground to recontextualize seminal findings under anesthesia for more well-rounded hypothesis about researching those mechanisms in different states of behavior. The pre-print, Deane et al., (2022a), revealing lasting cortical suppression after population wide VGCC clustering in the A1, is subject to a final histological investigation before it can be peer-reviewed. This will involve developing a

lentivirus that tags VGCCs with CRY2olig which can be visualized in histology and subsequently confirming and quantifying CRY2olig VGCC cross-linking. This will effectively provide a proof of concept for the clustering of VGCCs *in vivo* which can then be explored more thoroughly. We believe the study will be well-received because there is a growing interest for investigating the effect of channel dynamic changes across scales. Our collaborative research was one step in this process which will hopefully blossom into a series of these studies under different conditions to illuminate the mechanisms we began to glimpse here. Finally, the comparative study of seba's short-tailed bat and mouse A1 is available as a preprint (Deane et al., 2022b) and under review for publication. It will hopefully inspire others to further consider behavior and ecological context. It will be the first time a study is showing a comparison of mouse and bat auditory cortices, and the first time that this type of analysis has been published for either species. Because of that, interpretation was largely speculative. However, it impacts perception of the animal models we study and also how they relate to us. Given that we often relate clinical studies in mice to human pathologies, it is intrinsically valid to ask what kinds of biological and functional differences occur between species and why. Although all three of the projects laid out here have steps set for their continued investigations, the main topic that I will be carrying into my academic career is complexity explored through neuroethology of bat auditory cortices.

Conclusion; A modest synthesis

The discussion about how living organisms "compute" is pertinent to humans, who are organisms that "compute". This makes neuroscience and artificial intelligence fields intriguing and provides a fertile ground for interdisciplinary work between them and other complexity sciences. Finding a higher-order language to understand some universal processes by which pattern computing is possible and evolutionarily develops could link all of biology—as all computers are accessible through higher-order programming languages. The classic view of science has been to break things down to their simplest parts and understand them separately. Complexity necessarily means, however, that the whole is greater than the sum of its parts. As I have proposed several times already, the solution to understanding complexity may be through a multitude of scientists approaching complex systems from different angles and sharing their findings openly—all while considering greater contexts in their interpretations.

> All three of the projects I have developed are about mesoscopic population activity in the auditory cortex, meaning that they are all explorations of the same system in different mammals, states, and scales.

Populations of neurons in this area "compute" by processing, integrating, filtering, and signaling information (Bregman & McAdams, 1994; King et al., 2018; Ohl, 2015; Ohl & Scheich, 2005; Zempeltzi et al., 2020). I have explored changes to this "computation", read through auditory response profiles, under ketamine anesthesia, while changing single-unit probability dynamics, and across species evolved for different auditory niches. The circuitry and many of the analysis methods were shared between each study but the system was being affected in very different ways.

A synthesis of these topics with that of the auditory cortex as a complex system must be modest. This is because the scope of each of these studies was contained within their specific fields and lines of inquiry without the predetermined intention of quantifying how they relate. An organism is unlikely to have both hypoactive NMDA receptors and clustered voltage gated

calcium channels without an array of other related causes and effects. The important lesson that came from the first two studies was that

1. *balance intrinsically existed in the circuitry through nuanced excitatory and inhibitory population activity* and
2. *flexibility intrinsically existed through the introduction of variability at a single unit level that negatively impacted the population when reduced.*

These things were true of Mongolian gerbils, black 6 mice, and seba's short-tailed bats and they would likely be true of any other brain. However, we have further shown in the third section that

3. *evolution and adaptation can take shared features and specialize them for success in different ecological niches.*

A bat brain has a better auditory signal to noise ratio despite having nearly the same cortical structure and shared microcircuitry and this influences population variability dynamics across an entire species.

My explorations using these *in vivo* multichannel recording technologies and a subset of analysis tools shows just how complex this system is from the practical perspective of one researcher. *We can relate the primary auditory cortex to nested scales and across species, and of course, the results are non-linear and leave more questions than answers.* What exactly is causing the change from single cell to populations when we cluster VGCCs? Why is the suppression of the cortex stronger with increased cortical recruitment when there is reduced single-cell variability? What is the biological basis for the signal to noise ratio difference between bats and mice? Would we find the same phenomenon with another "better" auditory learner than mice, e.g., gerbils compared to bats? How does ketamine anesthesia exactly relate to disordered NMDA channels found in other diseases like Schizophrenia? Are we causing hallucinations under anesthesia and what would that even mean without the ability to perceive them due to the anesthetic-induced unconsciousness? Each study leads to another path of questions going further down their respective rabbit holes. We all know this to be "science". We are trained to be specialists, and only some focus then on generalism. Put another way, we are trained to practice reductionism and a few hubs of scientific discourse attempt to conceptualize wholistic reality based on findings from distributed groups. As specialists, we can do some of the work by trying to understand the broader system that our focus exists in. The action of VGCCs is related to the excitatory and inhibitory circuitry is related to the behavior of an organism is related to success in a habitat is related to etc., etc. Everything is connected and continuous. Future endeavors to reach across the physiological boundaries discussed here will benefit from intentionally attempting to answer the question of how they connect, to each other and their environment, and what purpose they serve together.

List of Abbreviations

A1	primary auditory cortex
AC	auditory cortex
AM	amplitude modulation measurements
ANOVA	analysis of variance
AVREC	average rectified (CSD)
BF	best frequency
BSA	bovine serum albumin
CFC	cross frequency coupling
CL	click train measurements
CSD	current source density analysis
CWT	continuous wavelet transform
FWER	familywise error rate
GFP	green fluorescent protein
H&E	Hematoxylin and Eosin
I/II	supragranular cortical layers
III/IV	granular cortical layers
L	layer
LFP	local field potential
LMM	linear mixed model
MWU	Mann-Whitney U
NMDA	N-methyl-D-aspartate
PAC	phase amplitude coupling
PBS	Phosphate-buffered saline
PV	Parvalbumin
RELRES	relative residues (CSD)
RMS	root mean square
RMSE	root mean square error
ROI	region of interest
STD	standard deviation
V/VI	infragranular cortical layers
VGCC	voltage gated calcium channels
YFP	yellow fluorescent protein
zMI	z-scored modulation index

References

Alday, P. M., Schlesewsky, M., & Bornkessel-Schlesewsky, I. (2017). Electrophysiology Reveals the Neural Dynamics of Naturalistic Auditory Language Processing: Event-Related Potentials Reflect Continuous Model Updates. *ENeuro*, *4*(6). https://doi.org/10.1523/ENEURO.0311-16.2017

Alitto, H. J., & Usrey, W. M. (2003). Corticothalamic feedback and sensory processing. *Current Opinion in Neurobiology*, *13*(4), 440–445. https://doi.org/10.1016/s0959-4388(03)00096-5

Anis, N. A., Berry, S. C., Burton, N. R., & Lodge, D. (1983). The dissociative anaesthetics, ketamine and phencyclidine, selectively reduce excitation of central mammalian neurones by N-methyl-aspartate. *British Journal of Pharmacology*, *79*(2), 565–575. https://doi.org/10.1111/j.1476-5381.1983.tb11031.x

Arias-Gil, G., Ohl, F. W., Takagaki, K., & Lippert, M. T. (2016). Measurement, modeling, and prediction of temperature rise due to optogenetic brain stimulation. *Neurophotonics*, *3*(4), 045007. https://doi.org/10.1117/1.NPh.3.4.045007

Atencio, C. A., & Schreiner, C. E. (2010). Columnar Connectivity and Laminar Processing in Cat Primary Auditory Cortex. *PLoS ONE*, *5*(3), e9521. https://doi.org/10.1371/journal.pone.0009521

Barth, D. S., & Di, S. (1990). Three-dimensional analysis of auditory-evoked potentials in rat neocortex. *Journal of Neurophysiology*, *64*(5), 1527–1536. https://doi.org/10.1152/jn.1990.64.5.1527

Beetz, M. J., Kordes, S., García-Rosales, F., Kössl, M., & Hechavarría, J. C. (2017). Processing of Natural Echolocation Sequences in the Inferior Colliculus of Seba's Fruit Eating Bat, Carollia perspicillata. *ENeuro*, *4*(6), ENEURO.0314-17.2017. https://doi.org/10.1523/ENEURO.0314-17.2017

Behrens, M. M., Ali, S. S., Dao, D. N., Lucero, J., Shekhtman, G., Quick, K. L., & Dugan, L. L. (2007). Ketamine-Induced Loss of Phenotype of Fast-Spiking Interneurons Is Mediated by NADPH-Oxidase. *Science*, *318*(5856), 1645–1647. https://doi.org/10.1126/science.1148045

Beltramo, R., D'Urso, G., Dal Maschio, M., Farisello, P., Bovetti, S., Clovis, Y., Lassi, G., Tucci, V., De Pietri Tonelli, D., & Fellin, T. (2013). Layer-specific excitatory circuits differentially control recurrent network dynamics in the neocortex. *Nature Neuroscience*, *16*(2), 227–234. https://doi.org/10.1038/nn.3306

Berman, R. M., Cappiello, A., Anand, A., Oren, D. A., Heninger, G. R., Charney, D. S., & Krystal, J. H. (2000). Antidepressant effects of ketamine in depressed patients. *Biological Psychiatry*, *47*(4), 351–354. https://doi.org/10.1016/S0006-3223(99)00230-9

Bidelman, G. (2013). The Role of the Auditory Brainstem in Processing Musically Relevant Pitch. *Frontiers in Psychology*, *4*. https://www.frontiersin.org/article/10.3389/fpsyg.2013.00264

Bidelman, G. M., & Krishnan, A. (2010). Effects of reverberation on brainstem representation of speech in musicians and non-musicians. *Brain Research*, *1355*, 112–125. https://doi.org/10.1016/j.brainres.2010.07.100

Böhme, M. A., Grasskamp, A. T., & Walter, A. M. (2018). Regulation of synaptic release-site Ca2+ channel coupling as a mechanism to control release probability and short-term plasticity. *FEBS Letters*, *592*(21), 3516–3531. https://doi.org/10.1002/1873-3468.13188

Bonnefond, M., Kastner, S., & Jensen, O. (2017). Communication between Brain Areas Based on Nested Oscillations. *ENeuro*, *4*(2), ENEURO.0153-16.2017. https://doi.org/10.1523/ENEURO.0153-16.2017

Borgstein, J., & Grootendorst, C. (2002). Half a brain. *The Lancet*, *359*(9305), 473. https://doi.org/10.1016/S0140-6736(02)07676-6

Bregman, A. S., & McAdams, S. (1994). Auditory Scene Analysis: The Perceptual Organization of Sound. *The Journal of the Acoustical Society of America*, *95*(2), 1177–1178. https://doi.org/10.1121/1.408434

Brunk, M. G. K., Deane, K. E., Kisse, M., Deliano, M., Vieweg, S., Ohl, F. W., Lippert, M. T., & Happel, M. F. K. (2019). Optogenetic stimulation of the VTA modulates a

frequency-specific gain of thalamocortical inputs in infragranular layers of the auditory cortex. *Scientific Reports*, *9*(1), 20385. https://doi.org/10.1038/s41598-019-56926-6

Buzsáki, G., Anastassiou, C. A., & Koch, C. (2012). The origin of extracellular fields and currents—EEG, ECoG, LFP and spikes. *Nature Reviews Neuroscience*, *13*(6), 407–420. https://doi.org/10.1038/nrn3241

Cardillo, G. (2009). *MWWTEST: Mann-Whitney-Wilcoxon non parametric test for two unpaired samples*. http://www.mathworks.com/matlabcentral/fileexchange/25830

Chang, M., & Kawai, H. D. (2018). A characterization of laminar architecture in mouse primary auditory cortex. *Brain Structure and Function*, *223*(9), 4187–4209. https://doi.org/10.1007/s00429-018-1744-8

Chen, C. M., Lakatos, P., Shah, A. S., Mehta, A. D., Givre, S. J., Javitt, D. C., & Schroeder, C. E. (2007). Functional anatomy and interaction of fast and slow visual pathways in macaque monkeys. *Cerebral Cortex*, *17*(7), 1561–1569. https://doi.org/10.1093/cercor/bhl067

Colgin, L. L., Denninger, T., Fyhn, M., Hafting, T., Bonnevie, T., Jensen, O., Moser, M.-B., & Moser, E. I. (2009). Frequency of gamma oscillations routes flow of information in the hippocampus. *Nature*, *462*(7271), Article 7271. https://doi.org/10.1038/nature08573

Daume, J., Gruber, T., Engel, A. K., & Friese, U. (2017). Phase-Amplitude Coupling and Long-Range Phase Synchronization Reveal Frontotemporal Interactions during Visual Working Memory. *Journal of Neuroscience*, *37*(2), 313–322. https://doi.org/10.1523/JNEUROSCI.2130-16.2016

David, S. V., Fritz, J. B., & Shamma, S. A. (2012). Task reward structure shapes rapid receptive field plasticity in auditory cortex. *Proceedings of the National Academy of Sciences of the United States of America*, *109*(6), 2144–2149. https://doi.org/10.1073/pnas.1117717109

Deane, K. E., Brunk, M. G. K., Curran, A. W., Zempeltzi, M. M., Ma, J., Lin, X., Abela, F., Aksit, S., Deliano, M., Ohl, F. W., & Happel, M. F. K. (2020). Ketamine anaesthesia induces gain enhancement via recurrent excitation in granular input layers of the auditory cortex. *Journal of Physiology*, *598*(13), 2741–2755. https://doi.org/10.1113/JP279705

Deane, K. E., Klymentiev, R., Heck, J., Mark, M. D., Ohl, F. W., Heine, M., & Happel, M. F. K. (2022a). *Inhibiting presynaptic calcium channel mobility in the auditory cortex suppresses synchronized input processing* (p. 2022.03.30.486338). bioRxiv. https://doi.org/10.1101/2022.03.30.486338

Deane, K. E., García-Rosales, F., Klymentiev, R., Hechavarria, J. C., & Happel, M. F. K. (2022b). *The auditory cortex of bats has a better signal to noise ratio and lower inter-trial variability in response to stimuli trains than mice* (p. 2022.10.28.514155). bioRxiv. https://doi.org/10.1101/2022.10.28.514155

Deliano, M., Brunk, M. G. K., El-Tabbal, M., Zempeltzi, M. M., Happel, M. F. K., & Ohl, F. W. (2018). Dopaminergic neuromodulation of high gamma stimulus phase-locking in gerbil primary auditory cortex mediated by D1/D5-receptors. *European Journal of Neuroscience*, *March*. https://doi.org/10.1111/ejn.13898

Desmaris, N., Bosch, A., Salaün, C., Petit, C., Prévost, M. C., Tordo, N., Perrin, P., Schwartz, O., de Rocquigny, H., & Heard, J. M. (2001). Production and neurotropism of lentivirus vectors pseudotyped with lyssavirus envelope glycoproteins. *Molecular Therapy: The Journal of the American Society of Gene Therapy*, *4*(2), 149–156. https://doi.org/10.1006/mthe.2001.0431

Deweese, M. R., & Zador, A. M. (2003). *Binary Coding in Auditory Cortex*. 8.

Douglas, R. J., & Martin, K. A. C. (2004). NEURONAL CIRCUITS OF THE NEOCORTEX. *Annual Review of Neuroscience*, *27*(1), 419–451. https://doi.org/10.1146/annurev.neuro.27.070203.144152

Duron, J., Monconduit, L., & Avan, P. (2020). Auditory Brainstem Changes in Timing may Underlie Hyperacusis in a Salicylate-induced Acute Rat Model. *Neuroscience*, *426*, 129–140. https://doi.org/10.1016/j.neuroscience.2019.11.038

Edeline, J.-M., Hars, B., Hennevin, E., & Cotillon, N. (2002). Muscimol Diffusion af-ter Intracerebral Microinjections: A Reevaluation Based on Electrophysiological and Autoradio-graphic Quantifications. *Neurobiology of Learning and Memory*, *78*, 100–124. https://doi.org/10.1006/nlme.2001.4035ï

Einevoll, G. T., Kayser, C., Logothetis, N. K., & Panzeri, S. (2013). Modelling and analysis of local field potentials for studying the function of cortical circuits. *Nature Reviews Neuroscience*, *14*(11), Article 11. https://doi.org/10.1038/nrn3599

Esghaei, M., Daliri, M. R., & Treue, S. (2015). Attention Decreases Phase-Amplitude Coupling, Enhancing Stimulus Discriminability in Cortical Area MT. *Frontiers in Neural Circuits*, *9*. https://www.frontiersin.org/article/10.3389/fncir.2015.00082

Feinberg, I. (1982). Schizophrenia: Caused by a fault in programmed synaptic elimination during adolescence? *Journal of Psychiatric Research*, *17*(4), 319–334. https://doi.org/10.1016/0022-3956(82)90038-3

Ferguson, K. A., & Cardin, J. A. (2020). Mechanisms underlying gain modulation in the cortex. *Nature Reviews Neuroscience*, *21*(2), 80–92. https://doi.org/10.1038/s41583-019-0253-y

Feuillet, L., Dufour, H., & Pelletier, J. (2007). Brain of a white-collar worker. *The Lancet*, *370*(9583), 262. https://doi.org/10.1016/S0140-6736(07)61127-1

Finger, S. (2005). Santiago Ramón y Cajal: From Nerve Nets to Neuron Doctrine. In *Minds Behind the Brain*. Oxford University Press. https://doi.org/10.1093/acprof:oso/9780195181821.003.0013

Fonseca, A. H., Santana, G. M., Bosque Ortiz, G. M., Bampi, S., & Dietrich, M. O. (2021). Analysis of ultrasonic vocalizations from mice using computer vision and machine learning. *ELife*, *10*, e59161. https://doi.org/10.7554/eLife.59161

Fontanini, A., & Katz, D. B. (2006). State-dependent modulation of time-varying gustatory responses. *Journal of Neurophysiology*, *96*(6), 3183–3193. https://doi.org/10.1152/jn.00804.2006

Freemon, F. R. (1994). Galen's ideas on neurological function. *Journal of the History of the Neurosciences*, *3*(4), 263–271. https://doi.org/10.1080/09647049409525619

Fritz, J., Shamma, S., Elhilali, M., & Klein, D. (2003). Rapid task-related plasticity of spectrotemporal receptive fields in primary auditory cortex. *Nature Neuroscience*, *6*(11), 1216–1223. https://doi.org/10.1038/nn1141

Fu, Y., Tucciarone, J. M., Espinosa, J. S., Sheng, N., Darcy, D. P., Nicoll, R. A., Huang, Z. J., & Stryker, M. P. (2014). A cortical circuit for gain control by behavioral state. *Cell*, *156*(6), 1139–1152. https://doi.org/10.1016/j.cell.2014.01.050

Gabernet, L., Jadhav, S. P., Feldman, D. E., Carandini, M., & Scanziani, M. (2005). Somatosensory integration controlled by dynamic thalamocortical feed-forward inhibition. *Neuron*, *48*(2), 315–327. https://doi.org/10.1016/j.neuron.2005.09.022

Gao, W.-J., Krimer, L. S., & Goldman-Rakic, P. S. (2001). Presynaptic regulation of recurrent excitation by D1 receptors in prefrontal circuits. *Proceedings of the National Academy of Sciences of the United States of America*, *98*(1), 295–300.

García-Rosales, F., López-Jury, L., González-Palomares, E., Cabral-Calderín, Y., Kössl, M., & Hechavarria, J. C. (2020). Phase-amplitude coupling profiles differ in frontal and auditory cortices of bats. *European Journal of Neuroscience*, *n/a*(n/a). https://doi.org/10.1111/ejn.14986

García-Rosales, F., Röhrig, D., Weineck, K., Röhm, M., Lin, Y.-H., Cabral-Calderin, Y., Kössl, M., & Hechavarria, J. C. (2019). Laminar specificity of oscillatory coherence in the auditory cortex. *Brain Structure and Function*, *224*(8), 2907–2924. https://doi.org/10.1007/s00429-019-01944-3

Giraud, A.-L., & Poeppel, D. (2012). Cortical oscillations and speech processing: Emerging computational principles and operations. *Nature Neuroscience*, *15*(4), Article 4. https://doi.org/10.1038/nn.3063

Gire, D. H., Kapoor, V., Arrighi-Allisan, A., Seminara, A., & Murthy, V. N. (2016). Mice develop efficient strategies for foraging and navigation using complex natural stimuli. *Current Biology : CB*, *26*(10), 1261–1273. https://doi.org/10.1016/j.cub.2016.03.040

Givre, S. J. J., Schroeder, C. E. E., & Arezzo, J. C. C. (1994). Contribution of extrastriate area V4 to the surface-recorded flash VEP in the awake macaque. *Vision Research*, *34*(4), 415–428. https://doi.org/10.1016/0042-6989(94)90156-2

González-Palomares, E., López-Jury, L., García-Rosales, F., & Hechavarria, J. C. (2021). Enhanced representation of natural sound sequences in the ventral auditory midbrain. *Brain Structure and Function*, *226*(1), 207–223. https://doi.org/10.1007/s00429-020-02188-2

Gourévitch, B., Martin, C., Postal, O., & Eggermont, J. J. (2020). Oscillations in the auditory system and their possible role. *Neuroscience and Biobehavioral Reviews*, *113*(April), 507–528. https://doi.org/10.1016/j.neubiorev.2020.03.030

Groppe, D. M., Urbach, T. P., & Kutas, M. (2011). Mass univariate analysis of event-related brain potentials/fields I: A critical tutorial review. In *Psychophysiology* (Vol. 48, Issue 12, pp. 1711–1725). Blackwell Publishing Inc. https://doi.org/10.1111/j.1469-8986.2011.01273.x

Gross, J., Hoogenboom, N., Thut, G., Schyns, P., Panzeri, S., Belin, P., & Garrod, S. (2013). Speech Rhythms and Multiplexed Oscillatory Sensory Coding in the Human Brain. *PLOS Biology*, *11*(12), e1001752. https://doi.org/10.1371/journal.pbio.1001752

Grundy, D. (2015). Principles and standards for reporting animal experiments in The Journal of Physiology and Experimental Physiology. In *Journal of Physiology* (Vol. 593, Issue 12, pp. 2547–2549). Blackwell Publishing Ltd. https://doi.org/10.1113/JP270818

Hagemann, C., Vater, M., & Kössl, M. (2011). Comparison of properties of cortical echo delay-tuning in the short-tailed fruit bat and the mustached bat. *Journal of Comparative Physiology A*, *197*(5), 605–613. https://doi.org/10.1007/s00359-010-0530-8

Happel, M. F. K. (2016). Dopaminergic impact on local and global cortical circuit processing during learning. *Behavioural Brain Research*, *299*, 32–41. https://doi.org/10.1016/j.bbr.2015.11.016

Happel, M. F. K., Deliano, M., Handschuh, J., & Ohl, F. W. (2014). Dopamine-Modulated Recurrent Corticoefferent Feedback in Primary Sensory Cortex Promotes Detection of Behaviorally Relevant Stimuli. *Journal of Neuroscience*, *34*(4), 1234–1247. https://doi.org/10.1523/JNEUROSCI.1990-13.2014

Happel, M. F. K., Jeschke, M., & Ohl, F. W. (2010). Spectral Integration in Primary Auditory Cortex Attributable to Temporally Precise Convergence of Thalamocortical and Intracortical Input. *The Journal of Neuroscience*, *30*(33), 11114–11127.

Happel, M. F. K., & Ohl, F. W. (2017). Compensating Level-Dependent Frequency Representation in Auditory Cortex by Synaptic Integration of Corticocortical Input. *PLOS ONE*, *12*(1), e0169461. https://doi.org/10.1371/journal.pone.0169461

Harding, G. W. (1992). The currents that flow in the somatosensory cortex during the direct cortical response. *Experimental Brain Research*, *90*(1). https://doi.org/10.1007/BF00229253

Harlow, J. M. (1999). Passage of an Iron Rod Through the Head. *The Journal of Neuropsychiatry and Clinical Neurosciences*, *11*(2), 281–283. https://doi.org/10.1176/jnp.11.2.281

Harrison, X. A., Donaldson, L., Correa-Cano, M. E., Evans, J., Fisher, D. N., Goodwin, C. E. D., Robinson, B. S., Hodgson, D. J., & Inger, R. (2018). A brief introduction to mixed effects modelling and multi-model inference in ecology. *PeerJ*, *6*, e4794. https://doi.org/10.7717/peerj.4794

Hay, E., & Segev, I. (2015). Dendritic Excitability and Gain Control in Recurrent Cortical Microcircuits. *Cerebral Cortex (New York, N.Y.: 1991)*, *25*(10), 3561–3571. https://doi.org/10.1093/cercor/bhu200

Hebb, D. (1949). *The Organization of Behavior*. Wiley.

Hechavarría, J. C., Macías, S., Vater, M., Mora, E. C., & Kössl, M. (2013). Evolution of neuronal mechanisms for echolocation: Specializations for target-range computation in bats of the genus Pteronotus. *The Journal of the Acoustical Society of America*, *133*(1), 570–578. https://doi.org/10.1121/1.4768794

Heck, J., Parutto, P., Ciuraszkiewicz, A., Bikbaev, A., Freund, R., Mitlöhner, J., Andres-Alonso, M., Fejtova, A., Holcman, D., & Heine, M. (2019). Transient Confinement of CaV2.1 Ca2+-Channel Splice Variants Shapes Synaptic Short-Term Plasticity. *Neuron*, *103*(1), 66-79.e12. https://doi.org/10.1016/j.neuron.2019.04.030

Heine, M., Heck, J., Ciuraszkiewicz, A., & Bikbaev, A. (2020). Dynamic compartmentalization of calcium channel signalling in neurons. *Neuropharmacology*, *169*, 107556. https://doi.org/10.1016/j.neuropharm.2019.02.038

Helfrich, R. F., & Knight, R. T. (2016). Oscillatory Dynamics of Prefrontal Cognitive Control. *Trends in Cognitive Sciences*, *20*(12), 916–930. https://doi.org/10.1016/j.tics.2016.09.007

Hindriks, R., Arsiwalla, X. D., Panagiotaropoulos, T., Besserve, M., Verschure, P. F. M. J., Logothetis, N. K., & Deco, G. (2016). Discrepancies between Multi-Electrode LFP and CSD Phase-Patterns: A Forward Modeling Study. *Frontiers in Neural Circuits*, *10*. https://www.frontiersin.org/article/10.3389/fncir.2016.00051

Hodgkin, A. L., & Huxley, A. F. (1952). A quantitative description of membrane current and its application to conduction and excitation in nerve. *The Journal of Physiology*, *117*(4), 500–544. https://doi.org/10.1113/jphysiol.1952.sp004764

Hoglen, N. E. G., Larimer, P., Phillips, E. A. K., Malone, B. J., & Hasenstaub, A. R. (2018). Amplitude modulation coding in awake mice and squirrel monkeys. *Journal of Neurophysiology*, *119*(5), 1753–1766. https://doi.org/10.1152/jn.00101.2017

Homayoun, H., & Moghaddam, B. (2007). NMDA Receptor Hypofunction Produces Opposite Effects on Prefrontal Cortex Interneurons and Pyramidal Neurons. *Journal of Neuroscience*, *27*(43), 11496–11500. https://doi.org/10.1523/JNEUROSCI.2213-07.2007

Homma, N. Y., Happel, M. F. K., Nodal, F. R., Ohl, F. W., King, A. J., & Bajo, V. M. (2017). A Role for Auditory Corticothalamic Feedback in the Perception of Complex Sounds. *The Journal of Neuroscience: The Official Journal of the Society for Neuroscience*, *37*(25), 6149–6161. https://doi.org/10.1523/JNEUROSCI.0397-17.2017

Houtsma, A. J. M., & Goldstein, J. L. (1972). The Central Origin of the Pitch of Complex Tones: Evidence from Musical Interval Recognition. *The Journal of the Acoustical Society of America*, *51*(2B), 520–529. https://doi.org/10.1121/1.1912873

Hu, B. (2003). Functional organization of lemniscal and nonlemniscal auditory thalamus. *Experimental Brain Research*, *153*(4), 543–549. https://doi.org/10.1007/s00221-003-1611-5

Hubel, D. H., & Wiesel, T. N. (1959). Receptive fields of single neurones in the cat's striate cortex. *The Journal of Physiology*, *148*(3), 574–591. https://doi.org/10.1113/jphysiol.1959.sp006308

Hubel, D. H., & Wiesel, T. N. (1962). Receptive fields, binocular interaction and functional architecture in the cat's visual cortex. *The Journal of Physiology*, *160*(1), 106–154. https://doi.org/10.1113/jphysiol.1962.sp006837

Hubel, D. H., & Wiesel, T. N. (1965). RECEPTIVE FIELDS AND FUNCTIONAL ARCHITECTURE IN TWO NONSTRIATE VISUAL AREAS (18 AND 19) OF THE CAT. *Journal of Neurophysiology*, *28*(2), 229–289. https://doi.org/10.1152/jn.1965.28.2.229

Hubel, D. H., & Wiesel, T. N. (1969). Visual area of the lateral suprasylvian gyrus (Clare-Bishop area) of the cat. *The Journal of Physiology*, *202*(1), 251–260. https://doi.org/10.1113/jphysiol.1969.sp008808

Huttenlocher, P. R. (1979). Synaptic density in human frontal cortex—Developmental changes and effects of aging. *Brain Research*, *163*(2), 195–205. https://doi.org/10.1016/0006-8993(79)90349-4

Hyafil, A., Fontolan, L., Kabdebon, C., Gutkin, B., & Giraud, A.-L. (2015). Speech encoding by coupled cortical theta and gamma oscillations. *ELife*, *4*, e06213. https://doi.org/10.7554/eLife.06213

Jaramillo, S., & Zador, A. M. (2011). The auditory cortex mediates the perceptual effects of acoustic temporal expectation. *Nature Neuroscience*, *14*(2), 246–251. https://doi.org/10.1038/nn.2688

Juczewski, K., Koussa, J. A., Kesner, A. J., Lee, J. O., & Lovinger, D. M. (2020). Stress and behavioral correlates in the head-fixed method: Stress measurements, habituation dynamics, locomotion, and motor-skill learning in mice. *Scientific Reports*, *10*(1), Article 1. https://doi.org/10.1038/s41598-020-69132-6

Kanwal, J. S., & Rauschecker, J. P. (2007). Auditory cortex of bats and primates: Managing species-specific calls for social communication. *Frontiers in Bioscience : A Journal and Virtual Library*, *12*, 4621–4640.

Kato, H. K., Asinof, S. K., & Isaacson, J. S. (2017). Network-Level Control of Frequency Tuning in Auditory Cortex. *Neuron*, *95*(2), 412-423.e4. https://doi.org/10.1016/j.neuron.2017.06.019

Kaur, S., Lazar, R., & Metherate, R. (2004). Intracortical Pathways Determine Breadth of Subthreshold Frequency Receptive Fields in Primary Auditory Cortex. *Journal of Neurophysiology*, *91*(6), 2551–2567. https://doi.org/10.1152/jn.01121.2003

Kelsch, W., Sim, S., & Lois, C. (2010). Watching synaptogenesis in the adult brain. *Annual Review of Neuroscience*, *33*, 131–149. https://doi.org/10.1146/annurev-neuro-060909-153252

Kikuchi, Y., Attaheri, A., Wilson, B., Rhone, A. E., Nourski, K. V., Gander, P. E., Kovach, C. K., Kawasaki, H., Griffiths, T. D., Howard, M. A., & Petkov, C. I. (2017). Sequence learning modulates neural responses and oscillatory coupling in human and monkey auditory cortex. *PLoS Biology*, *15*(4), e2000219. https://doi.org/10.1371/journal.pbio.2000219

King, A. J., Teki, S., & Willmore, B. D. B. (2018). Recent advances in understanding the auditory cortex. *F1000Research*, *7*, F1000 Faculty Rev-1555. https://doi.org/10.12688/f1000research.15580.1

Lachaux, J.-P., Rodriguez, E., Martinerie, J., & Varela, F. J. (1999). Measuring phase synchrony in brain signals. *Human Brain Mapping*, *8*(4), 194–208. https://doi.org/10.1002/(SICI)1097-0193(1999)8:4<194::AID-HBM4>3.0.CO;2-C

Lakatos, P., Chen, C. M., O'Connell, M. N., Mills, A., & Schroeder, C. E. (2007). Neuronal Oscillations and Multisensory Interaction in Primary Auditory Cortex. *Neuron*, *53*(2), 279–292. https://doi.org/10.1016/j.neuron.2006.12.011

Langner, G. (1997). Neural Processing and Representation of Periodicity Pitch. *Acta Oto-Laryngologica*, *117*(sup532), 68–76. https://doi.org/10.3109/00016489709126147

Långsjö, J. W., Maksimow, A., Salmi, E., Kaisti, K., Aalto, S., Oikonen, V., Hinkka, S., Aantaa, R., Sipilä, H., Viljanen, T., Parkkola, R., & Scheinin, H. (2005). S -Ketamine Anesthesia Increases Cerebral Blood Flow in Excess of the Metabolic Needs in Humans. *Anesthesiology*, *103*(2), 258–268. https://doi.org/10.1097/00000542-200508000-00008

Lilly, J. M., & Olhede, S. C. (2012). Generalized morse wavelets as a superfamily of analytic wavelets. *IEEE Transactions on Signal Processing*, *60*(11), 6036–6041. https://doi.org/10.1109/TSP.2012.2210890

Linden, J. F., & Schreiner, C. E. (2003). Columnar Transformations in Auditory Cortex? A Comparison to Visual and Somatosensory Cortices. *Cerebral Cortex*, *13*(1), 83–89. https://doi.org/10.1093/cercor/13.1.83

Lisman, J. E., & Jensen, O. (2013). The Theta-Gamma Neural Code. In *Neuron* (Vol. 77). https://doi.org/10.1016/j.neuron.2013.03.007

Liu, B., Wu, G. K., Arbuckle, R., Tao, H. W., & Zhang, L. I. (2007). Defining cortical frequency tuning with recurrent excitatory circuitry. *Nature Neuroscience*, *10*(12), 1594–1600. https://doi.org/10.1038/nn2012

Liu, J., Whiteway, M. R., Sheikhattar, A., Butts, D. A., Babadi, B., & Kanold, P. O. (2019). Parallel Processing of Sound Dynamics across Mouse Auditory Cortex via Spatially Patterned Thalamic Inputs and Distinct Areal Intracortical Circuits. *Cell Reports*, *27*(3), 872-885.e7. https://doi.org/10.1016/j.celrep.2019.03.069

Lizarazu, M., Lallier, M., & Molinaro, N. (2019). Phase−amplitude coupling between theta and gamma oscillations adapts to speech rate. *Annals of the New York Academy of Sciences*, *1453*(1), 140–152. https://doi.org/10.1111/nyas.14099

Lodge, D., & Mercier, M. S. (2015). Ketamine and phencyclidine: The good, the bad and the unexpected. *British Journal of Pharmacology*, *172*(17), 4254–4276. https://doi.org/10.1111/bph.13222

Lu, T., & Wang, X. (2000). Temporal discharge patterns evoked by rapid sequences of wide- and narrowband clicks in the primary auditory cortex of cat. *Journal of Neurophysiology*, *84*(1), 236–246. https://doi.org/10.1152/jn.2000.84.1.236

Luczak, A., & MacLean, J. N. (2012). Default activity patterns at the neocortical microcircuit level. *Frontiers in Integrative Neuroscience*, *6*, 30. https://doi.org/10.3389/fnint.2012.00030

MacDonald, J. F., Miljkovic, Z., & Pennefather, P. (1987). Use-dependent block of excitatory amino acid currents in cultured neurons by ketamine. *Journal of Neurophysiology*, *58*(2), 251–266. https://doi.org/10.1152/jn.1987.58.2.251

Macías, S., Hechavarría, J. C., Kössl, M., & Mora, E. C. (2013). Neurons in the inferior colliculus of the mustached bat are tuned both to echo-delay and sound duration. *NeuroReport*, *24*(8), 404–409. https://doi.org/10.1097/WNR.0b013e3283603f6d

Maris, E., Schoffelen, J.-M., & Fries, P. (2007). Nonparametric statistical testing of coherence differences. *Journal of Neuroscience Methods*, *163*(1), 161–175. https://doi.org/10.1016/j.jneumeth.2007.02.011

Mark, M. D., Maejima, T., Kuckelsberg, D., Yoo, J. W., Hyde, R. A., Shah, V., Gutierrez, D., Moreno, R. L., Kruse, W., Noebels, J. L., & Herlitze, S. (2011). Delayed postnatal loss of P/Q-type calcium channels recapitulates the absence epilepsy, dyskinesia, and ataxia phenotypes of genomic Cacna1A mutations. *Journal of Neuroscience*, *31*(11), 4311–4326. https://doi.org/10.1523/JNEUROSCI.5342-10.2011

Markicevic, M., Savvateev, I., Grimm, C., & Zerbi, V. (2021). Emerging imaging methods to study whole-brain function in rodent models. *Translational Psychiatry*, *11*(1), Article 1. https://doi.org/10.1038/s41398-021-01575-5

Marland, S., Ellerton, J., Andolfatto, G., Strapazzon, G., Thomassen, O., Brandner, B., Weatherall, A., & Paal, P. (2013). Ketamine: Use in Anesthesia. *CNS Neuroscience & Therapeutics*, *19*(6), 381–389. https://doi.org/10.1111/cns.12072

Metherate, R., Kaur, S., Kawai, H., Lazar, R., Liang, K., & Rose, H. J. (2005). Spectral integration in auditory cortex: Mechanisms and modulation. *Hearing Research*, *206*(1–2), 146–158. https://doi.org/10.1016/j.heares.2005.01.014

Middlebrooks, J. C. (2008). Auditory Cortex Phase Locking to Amplitude-Modulated Cochlear Implant Pulse Trains. *Journal of Neurophysiology*, *100*(1), 76–91. https://doi.org/10.1152/jn.01109.2007

Miller, O. H., Moran, J. T., & Hall, B. J. (2016). Two cellular hypotheses explaining the initiation of ketamine's antidepressant actions: Direct inhibition and disinhibition. *Neuropharmacology*, *100*, 17–26. https://doi.org/10.1016/j.neuropharm.2015.07.028

Mitani, A., Shimokouchi, M., Itoh, K., Nomura, S., Kudo, M., & Mizuno, N. (1985). Morphology and laminar organization of electrophysiologically identified neurons in the primary auditory cortex in the cat. *The Journal of Comparative Neurology*, *235*(4), 430–447. https://doi.org/10.1002/cne.902350403

Robby The Robot Genetic Algorithm. https://melaniemitchell.me/ExplorationsContent/RobbyTheRobot/

Mitchell, M. (2011). *Complexity A Guided Tour*. Oxford University Press.

Mitzdorf, U. (1985). Current source-density method and application in cat cerebral cortex: Investigation of evoked potentials and EEG phenomena. *PHYSIOLOGICAL REVIEWS*, *65*, 64.

Mongillo, G., Rumpel, S., & Loewenstein, Y. (2017). Intrinsic volatility of synaptic connections—A challenge to the synaptic trace theory of memory. *Current Opinion in Neurobiology*, *46*, 7–13. https://doi.org/10.1016/j.conb.2017.06.006

Morita, K., Kalra, R., Aihara, K., & Robinson, H. P. C. (2008). Recurrent Synaptic Input and the Timing of Gamma-Frequency-Modulated Firing of Pyramidal Cells during Neocortical "UP" States. *The Journal of Neuroscience*, *28*(8), 1871–1881. https://doi.org/10.1523/JNEUROSCI.3948-07.2008

Mountcastle, V. B. (1997). The columnar organization of the neocortex. *Brain*, *120*(4), 701–722. https://doi.org/10.1093/brain/120.4.701

Murrough, J. W., Iosifescu, D. V., Chang, L. C., Al Jurdi, R. K., Green, C. E., Perez, A. M., Iqbal, S., Pillemer, S., Foulkes, A., Shah, A., Charney, D. S., & Mathew, S. J. (2013). Antidepressant Efficacy of Ketamine in Treatment-Resistant Major Depression: A Two-Site Randomized Controlled Trial. *American Journal of Psychiatry*, *170*(10), 1134–1142. https://doi.org/10.1176/appi.ajp.2013.13030392

Nagel, T. (1974). What Is It Like to Be a Bat? *The Philosophical Review*, *83*(4), 435. https://doi.org/10.2307/2183914

Naldini, L., Blömer, U., Gage, F. H., Trono, D., & Verma, I. M. (1996). Efficient transfer, integration, and sustained long-term expression of the transgene in adult rat brains injected with a lentiviral vector. *Proceedings of the National Academy of Sciences of the United States of America*, *93*(21), 11382–11388.

Naldini, L., Blömer, U., Gallay, P., Ory, D., Mulligan, R., Gage, F. H., Verma, I. M., & Trono, D. (1996). In vivo gene delivery and stable transduction of nondividing cells by a lentiviral vector. *Science (New York, N.Y.)*, *272*(5259), 263–267. https://doi.org/10.1126/science.272.5259.263

Nelken, I. (2004). Processing of complex stimuli and natural scenes in the auditory cortex. *Current Opinion in Neurobiology*, *14*(4), 474–480. https://doi.org/10.1016/j.conb.2004.06.005

Nelken, I. (2020). From neurons to behavior: The view from auditory cortex. *Current Opinion in Physiology*, *18*, 37–41. https://doi.org/10.1016/j.cophys.2020.07.019

Nimmrich, V., & Gross, G. (2012). P/Q-type calcium channel modulators. *British Journal of Pharmacology*, *167*(4), 741–759. https://doi.org/10.1111/j.1476-5381.2012.02069.x

O'Connell, M. N., Barczak, A., Ross, D., McGinnis, T., Schroeder, C. E., & Lakatos, P. (2015). Multi-Scale Entrainment of Coupled Neuronal Oscillations in Primary Auditory Cortex. *Frontiers in Human Neuroscience*, *9*. https://www.frontiersin.org/article/10.3389/fnhum.2015.00655

Ohl, F. W. (2015). Role of cortical neurodynamics for understanding the neural basis of motivated behavior—Lessons from auditory category learning. *Current Opinion in Neurobiology*, *31*, 88–94. https://doi.org/10.1016/j.conb.2014.08.014

Ohl, F. W., & Scheich, H. (2005). Learning-induced plasticity in animal and human auditory cortex. *Current Opinion in Neurobiology*, *15*(4), 470–477. https://doi.org/10.1016/j.conb.2005.07.002

Olhede, S. C., & Walden, A. T. (2002). Generalized Morse wavelets. *IEEE Transactions on Signal Processing*, *50*(11), 2661–2670. https://doi.org/10.1109/TSP.2002.804066

Ophoff, R. A., Terwindt, G. M., Frants, R. R., & Ferrari, M. D. (1998). P/Q-type Ca2+ channel defects in migraine, ataxia and epilepsy. *Trends in Pharmacological Sciences*, *19*(4), 121–127. https://doi.org/10.1016/S0165-6147(98)01182-1

Osten, P., Dittgen, T., & Licznerski, P. (2006). Lentivirus-Based Genetic Manipulations in Neurons In Vivo. In J. T. Kittler & S. J. Moss (Eds.), *The Dynamic Synapse: Molecular Methods in Ionotropic Receptor Biology*. CRC Press/Taylor & Francis. http://www.ncbi.nlm.nih.gov/books/NBK2547/

Ouelhazi, A., Bharmauria, V., Chanauria, N., Bachatene, L., Lussiez, R., & Molotchnikoff, S. (2019). Effects of ketamine on orientation selectivity and variability of neuronal responses in primary visual cortex. *Brain Research*, *1725*, 146462. https://doi.org/10.1016/j.brainres.2019.146462

Ovsepian, S. V. (2019). The dark matter of the brain. *Brain Structure and Function*, *224*(3). https://doi.org/10.1007/s00429-019-01835-7

Owen, S. F., Liu, M. H., & Kreitzer, A. C. (2019). Thermal constraints on in vivo optogenetic manipulations. *Nature Neuroscience*, *22*(7), Article 7. https://doi.org/10.1038/s41593-019-0422-3

Pachitariu, M., Lyamzin, D. R., Sahani, M., & Lesica, N. A. (2015). State-Dependent Population Coding in Primary Auditory Cortex. *The Journal of Neuroscience*, *35*(5), 2058–2073. https://doi.org/10.1523/JNEUROSCI.3318-14.2015

Petersen, C. C. H., Grinvald, A., & Sakmann, B. (2003). Spatiotemporal Dynamics of Sensory Responses in Layer 2/3 of Rat Barrel Cortex Measured *In Vivo* by Voltage-Sensitive Dye Imaging Combined with Whole-Cell Voltage Recordings and Neuron Reconstructions. *The Journal of Neuroscience*, *23*(4), 1298–1309. https://doi.org/10.1523/JNEUROSCI.23-04-01298.2003

Pinheiro, J., Bates, D., DebRoy, S., Sarkar, D., & R Core Team. (2021). *Linear and Nonlinear Mixed Effects Models*. https://CRAN.R-project.org/package=nlme

Plomp, J. J., van den Maagdenberg, A. M., Molenaar, P. C., Frants, R. R., & Ferrari, M. D. (2001). Mutant P/Q-type calcium channel electrophysiology and migraine. *Current Opinion in Investigational Drugs (London, England: 2000)*, *2*(9), 1250–1260.

Rieder, S. A., Metidji, A., Glass, D. D., Thornton, A. M., Ikeda, T., Morgan, B. A., & Shevach, E. M. (2015). Eos Is Redundant for Regulatory T Cell Function but Plays an Important Role in IL-2 and Th17 Production by CD4 $^{+}$ Conventional T Cells. *The Journal of Immunology*, *195*(2), 553–563. https://doi.org/10.4049/jimmunol.1500627

Rothschild, G., Nelken, I., & Mizrahi, A. (2010). Functional organization and population dynamics in the mouse primary auditory cortex. *Nature Neuroscience*, *13*(3), 353–360. https://doi.org/10.1038/nn.2484

Sakata, S., & Harris, K. D. (2009). Laminar Structure of Spontaneous and Sensory-Evoked Population Activity in Auditory Cortex. *Neuron*, *64*(3), 404–418. https://doi.org/10.1016/j.neuron.2009.09.020

Saldeitis, K., Jeschke, M., Budinger, E., Ohl, F. W., & Happel, M. F. K. (2021). Laser-Induced Apoptosis of Corticothalamic Neurons in Layer VI of Auditory Cortex Impact on Cortical Frequency Processing. *Frontiers in Neural Circuits*, *15*. https://www.frontiersin.org/article/10.3389/fncir.2021.659280

Schaefer, M. K., Hechavarría, J. C., & Kössl, M. (2015). Quantification of mid and late evoked sinks in laminar current source density profiles of columns in the primary auditory cortex. *Frontiers in Neural Circuits*, *9*, 1–16. https://doi.org/10.3389/fncir.2015.00052

Schobel, S. A., Chaudhury, N. H., Khan, U. A., Paniagua, B., Styner, M. A., Asllani, I., Inbar, B. P., Corcoran, C. M., Lieberman, J. A., Moore, H., & Small, S. A. (2013). Imaging patients with psychosis and a mouse model establishes a spreading pattern of hippocampal dysfunction and implicates glutamate as a pathogenic driver. *Neuron*, *78*(1), 81–93. https://doi.org/10.1016/j.neuron.2013.02.011

Schroeder, C. E., Mehta, A. D., & Givre, S. J. (1998). A spatiotemporal profile of visual system activation revealed by current source density analysis in the awake macaque. *Cerebral Cortex*, *8*(7), 575–592. https://doi.org/10.1093/cercor/8.7.575

Sevmez, F., Adanir, S. S., & Ince, R. (2022). Legendary name of neuroscience: Phineas Gage (1823–1860). *Child's Nervous System*, *38*(5), 855–856. https://doi.org/10.1007/s00381-020-04595-6

Shatz, C. J. (1992). The Developing Brain. *Scientific American*, *267*(3), 60–67. https://doi.org/10.1038/scientificamerican0992-60

Sherrington, C. (2014). *The Endeavour of Jean Fernel*. Cambridge University Press.

Sherry, D. F. (2007). Cross-Species Comparisons. In *Ciba Foundation Symposium 208—Characterizing Human Psychological Adaptations* (pp. 181–194). John Wiley & Sons, Ltd. https://doi.org/10.1002/9780470515372.ch10

Shoham, S., O'Connor, D. H., & Segev, R. (2006). How silent is the brain: Is there a "dark matter" problem in neuroscience? *Journal of Comparative Physiology A*, *192*(8), 777–784. https://doi.org/10.1007/s00359-006-0117-6

Sotero, R. C., Bortel, A., Naaman, S., Mocanu, V. M., Kropf, P., Villeneuve, M. Y., & Shmuel, A. (2015). Laminar Distribution of Phase-Amplitude Coupling of Spontaneous Current Sources and Sinks. *Frontiers in Neuroscience*, *9*. https://www.frontiersin.org/article/10.3389/fnins.2015.00454

Spaak, E., Bonnefond, M., Maier, A., Leopold, D. A., & Jensen, O. (2012). Layer-Specific Entrainment of Gamma-Band Neural Activity by the Alpha Rhythm in Monkey Visual Cortex. *Current Biology*, *22*(24), 2313–2318. https://doi.org/10.1016/j.cub.2012.10.020

Steinschneider, M., Reser, D. H., Fishman, Y. I., Schroeder, C. E., & Arezzo, J. C. (1998). Click train encoding in primary auditory cortex of the awake monkey: Evidence for two mechanisms subserving pitch perception. *The Journal of the Acoustical Society of America*, *104*(5), 2935–2955. https://doi.org/10.1121/1.423877

Steinschneider, M., Tenke, C. E., Schroeder, C. E., Javitt, D. C., Simpson, G. V., Arezzo, J. C., & Vaughan, H. G. (1992). Cellular generators of the cortical auditory evoked potential initial component. *Electroencephalography and Clinical Neurophysiology/Evoked Potentials Section*, *84*(2), 196–200. https://doi.org/10.1016/0168-5597(92)90026-8

Stujenske, J. M., Spellman, T., & Gordon, J. A. (2015). Modeling the Spatiotemporal Dynamics of Light and Heat Propagation for In Vivo Optogenetics. *Cell Reports*, *12*(3), 525–534. https://doi.org/10.1016/j.celrep.2015.06.036

Szymanski, F. D., Garcia-Lazaro, J. A., & Schnupp, J. W. H. (2009). Current Source Density Profiles of Stimulus-Specific Adaptation in Rat Auditory Cortex. *Journal of Neurophysiology*, *102*(3), 1483–1490. https://doi.org/10.1152/jn.00240.2009

Taslimi, A., Vrana, J. D., Chen, D., Borinskaya, S., Mayer, B. J., Kennedy, M. J., & Tucker, C. L. (2014). An optimized optogenetic clustering tool for probing protein interaction and function. *Nature Communications*, *5*(1), 4925. https://doi.org/10.1038/ncomms5925

Thies, W., Kalko, E. K. V., & Schnitzler, H.-U. (1998). The roles of echolocation and olfaction in two Neotropical fruit-eating bats, Carollia perspicillata and C. castanea , feeding on Piper. *Behavioral Ecology and Sociobiology*, *42*(6), 397–409. https://doi.org/10.1007/s002650050454

Thomson, A. M., & Bannister, A. P. (2003). Interlaminar connections in the neocortex. *Cerebral Cortex (New York, N.Y.: 1991)*, *13*(1), 5–14. https://doi.org/10.1093/cercor/13.1.5

Tierney, A. L., & Nelson, C. A. (2009). Brain Development and the Role of Experience in the Early Years. *Zero to Three*, *30*(2), 9–13.

Virtanen, P., Gommers, R., Oliphant, T. E., Haberland, M., Reddy, T., Cournapeau, D., Burovski, E., Peterson, P., Weckesser, W., Bright, J., van der Walt, S. J., Brett, M., Wilson, J., Millman, K. J., Mayorov, N., Nelson, A. R. J., Jones, E., Kern, R., Larson, E., … Vázquez-Baeza, Y. (2020). SciPy 1.0: Fundamental algorithms for scientific computing in Python. *Nature Methods*, *17*(3), 261–272. https://doi.org/10.1038/s41592-019-0686-2

Wang, L., Saalmann, Y. B., Pinsk, M. A., Arcaro, M. J., & Kastner, S. (2012). Electrophysiological Low-Frequency Coherence and Cross-Frequency Coupling Contribute to BOLD Connectivity. *Neuron*, *76*(5), 1010–1020. https://doi.org/10.1016/j.neuron.2012.09.033

Wang, X.-J. (2008). Decision making in recurrent neuronal circuits. *Neuron*, *60*(2), 215–234. https://doi.org/10.1016/j.neuron.2008.09.034

Weaver, K., Wander, J., Ko, A., Casimo, K., Grabowski, T., Ojemann, J., & Darvas, F. (2016). Directional patterns of cross frequency phase and amplitude coupling within the resting state mimic patterns of fMRI functional connectivity. *NeuroImage*, *128*. https://doi.org/10.1016/j.neuroimage.2015.12.043

Wehr, M., & Zador, A. M. (2003). Balanced inhibition underlies tuning and sharpens spike timing in auditory cortex. *Nature*, *426*(6965), 442–446. https://doi.org/10.1038/nature02116

Weineck, K., García-Rosales, F., & Hechavarría, J. C. (2020). Neural oscillations in the fronto-striatal network predict vocal output in bats. *PLOS BIOLOGY*, *18*(3), 29. https://doi.org/10.1371/journal. pbio.3000658

Wiener, N. (2019). *Cybernetics or Control and Communication in the Animal and the Machine* (Reissue Of The 1961 Second Edition). MIT Press.

Wiesel, T. N., & Hubel, D. H. (1963). SINGLE-CELL RESPONSES IN STRIATE CORTEX OF KITTENS DEPRIVED OF VISION IN ONE EYE. *Journal of Neurophysiology*, *26*, 1003–1017. https://doi.org/10.1152/jn.1963.26.6.1003

Williamson, R. S., & Polley, D. B. (2019). Parallel pathways for sound processing and functional connectivity among layer 5 and 6 auditory corticofugal neurons. *ELife*, *8*, e42974. https://doi.org/10.7554/eLife.42974

Wu, G. K., Arbuckle, R., Liu, B., Tao, H. W., & Zhang, L. I. (2008). Lateral Sharpening of Cortical Frequency Tuning by Approximately Balanced Inhibition. *Neuron*, *58*(1), 132–143. https://doi.org/10.1016/j.neuron.2008.01.035

Wurtz, R. H. (1969). Visual receptive fields of striate cortex neurons in awake monkeys. *Journal of Neurophysiology*, *32*(5), 727–742. https://doi.org/10.1152/jn.1969.32.5.727

Xiao, Z., Martinez, E., Kulkarni, P. M., Zhang, Q., Hou, Q., Rosenberg, D., Talay, R., Shalot, L., Zhou, H., Wang, J., & Chen, Z. S. (2019). Cortical Pain Processing in the Rat Anterior Cingulate Cortex and Primary Somatosensory Cortex. *Frontiers in Cellular Neuroscience*, *13*. https://www.frontiersin.org/article/10.3389/fncel.2019.00165

Yamamura, D., Sano, A., & Tateno, T. (2017). An analysis of current source density profiles activated by local stimulation in the mouse auditory cortex in vitro. *Brain Research*, *1659*, 96–112. https://doi.org/10.1016/j.brainres.2017.01.021

Young, S. M., & Veeraraghavan, P. (2021). Presynaptic voltage-gated calcium channels in the auditory brainstem. *Molecular and Cellular Neuroscience*, *112*, 103609. https://doi.org/10.1016/j.mcn.2021.103609

Yu, Y. H., Shafer, V. L., & Sussman, E. S. (2018). The Duration of Auditory Sensory Memory for Vowel Processing: Neurophysiological and Behavioral Measures. *Frontiers in Psychology*, *9*. https://www.frontiersin.org/article/10.3389/fpsyg.2018.00335

Zempeltzi, M. M., Kisse, M., Brunk, M. G. K., Glemser, C., Aksit, S., Deane, K. E., Maurya, S., Schneider, L., Ohl, F. W., Deliano, M., & Happel, M. F. K. (2020). Task rule and choice are reflected by layer-specific processing in rodent auditory cortical microcircuits. *Communications Biology*, *3*(1), 345. https://doi.org/10.1038/s42003-020-1073-3

Zhang, Y., Wu, S., Xie, L., Yu, S., Zhang, L., Liu, C., Zhou, W., & Yu, T. (2019). Ketamine Within Clinically Effective Range Inhibits Glutamate Transmission From Astrocytes to Neurons and Disrupts Synchronization of Astrocytic SICs. *Frontiers in Cellular Neuroscience*, *13*, 240. https://doi.org/10.3389/fncel.2019.00240

Zhou, M., Liang, F., Xiong, X. R., Li, L., Li, H., Xiao, Z., Tao, H. W., & Zhang, L. I. (2014). *Laminar-specific Scaling Down of Balanced Excitation and Inhibition in Auditory Cortex by Active Behavioral States*. 31.

Zion Golumbic, E. M., Ding, N., Bickel, S., Lakatos, P., Schevon, C. A., McKhann, G. M., Goodman, R. R., Emerson, R., Mehta, A. D., Simon, J. Z., Poeppel, D., & Schroeder, C. E. (2013). Mechanisms Underlying Selective Neuronal Tracking of Attended Speech at a "Cocktail Party." *Neuron*, *77*(5), 980–991. https://doi.org/10.1016/j.neuron.2012.12.037

Declaration of Honor

I hereby declare that I prepared this thesis without the impermissible help of third parties and that none other than the aids indicated have been used; all sources of information are clearly marked, including my own publications.

In particular I have not consciously:

- fabricated data or rejected undesirable results,
- misused statistical methods with the aim of drawing other conclusions than those warranted by the available data,
- plagiarized external data or publications,
- presented the results of other researchers in a distorted way.

I am aware that violations of copyright may lead to injunction and damage claims by the author and also to prosecution by the law enforcement authorities.

I hereby agree that the thesis may be electronically reviewed with the aim of identifying plagiarism.

This work has not yet been submitted as a doctoral thesis in the same or a similar form in Germany, nor in any other country. It has not yet been published as a whole."

_____
(Place, date)

_____
(Signature)